

**Czech Technical University in Prague**  
**Faculty of Nuclear Sciences and Physical Engineering**

DISSERTATION THESIS

Combinatorial Development of Scintillators Based on Complex Halides

Prague 2022

Vojtěch Vaněček



## **Bibliografický záznam**

Autor: Ing. Vojtěch Vaněček  
České vysoké učení technické v Praze  
Fakulta jaderná a fyzikálně inženýrská  
Katedra jaderné chemie

Název Práce: Kombinatorický vývoj scintilátorů na bázi komplexních halogenidů

Studijní program: Aplikace přírodních věd

Studijní obor: Jaderná chemie

Školitel: prof. Ing. Martin Nikl, CSc.  
Fyzikální ústav Akademie věd České republiky

Školitel specialista: Ing. Robert Král, Ph.D.  
Fyzikální ústav Akademie věd České republiky

Akademický rok: 2022/2023

Počet stran: 118

Klíčová slova: Scintilátor, luminiscence, halogenidy, pěstování krystalů



## **Bibliographic Entry**

Author M.Sc. Vojtěch Vaněček  
Czech Technical University in Prague  
Faculty of Nuclear Sciences and Physical Engineering  
Department of Nuclear Chemistry

Title of Dissertation: Combinatorial Development of Scintillators Based on Complex Halides

Degree Programme: Applications of Natural Sciences

Field of Study: Nuclear Chemistry

Supervisor: prof. M.Sc. Martin Nikl, CSc.  
Institute of Physics of the Czech Academy of Sciences

Supervisor specialist: M.Sc. Robert Král, Ph.D.  
Institute of Physics of the Czech Academy of Sciences

Academic Year: 2022/2023

Number of Pages: 118

Keywords: Scintillator, luminescence, halides, crystal growth



## **Abstrakt**

Tato práce shrnuje autorovu vědeckou činnost v rámci doktorského studia zaměřenou na výzkum a vývoj nových scintilátorů na bázi komplexních halogenidů. Publikované výsledky jsou rozděleny do dvou kapitol. První kapitola se věnuje vývoji technologie pro růst vysoce kvalitních krystalů chloridu cesno-hafničitého, výzkumu jeho scintilačních vlastností a vlivu substituce zirkonia. Druhá kapitola se věnuje rozsáhlé studii nových cross-luminiscenčních scintilátorů perspektivních pro aplikace vyžadující vysoké časové rozlišení. Dosažené výsledky jsou prezentovány v kontextu výsledků publikovaných mezinárodní vědeckou komunitou.

## **Abstract**

This work summarizes the author's scientific activity in the doctoral study focused on the research and development of new scintillators based on complex halides. The published results are divided into two chapters. The first chapter deals with the development of technology for the growth of high-quality single crystals of cesium hafnium chloride, the investigation of its scintillation properties, and the effect of zirconium substitution. The second chapter deals with an extensive study of the new cross-luminescent scintillator's perspective for fast timing applications. The achieved results are presented in the context of the results published by the international scientific community.





## **Opening remarks**

This work is an annotated list of seven publications published during my Ph.D. studies at the Faculty of Nuclear Sciences and Physical Engineering of Czech Technical University in Prague (years 2018 – 2022) relevant to the topic of the dissertation thesis. The integrating text below summarizes the results published in the author's commented papers selection in the context of the results published by the international scientific community. Reprints of the selected papers can be found at the end of the document in the section "Reprints of commented author's paper selection". My work was focused on the development of novel halide single crystal scintillators. The research was done under the supervision of prof. Ing. Martin Nikl, CSc., and Ing. Robert Král, Ph.D. at the Institute of Physics of Czech Academy of Sciences in collaboration with domestic and international research institutions (Czech University of Chemistry and Technology in Prague, the European Center for Nuclear Research, Tohoku University, etc.). The funding was obtained through several grants including the ones from the international grant agencies.



## **Acknowledgement**

Here I would like to thank my supervisor and supervisor specialist for continuous support and leadership during my Ph.D. studies. Moreover, I would like to thank my colleagues from the Department of Optical Materials of the Institute of Physics and colleagues from other institutions. Finally, I would like to thank my wife and family for their continuous support and understanding.

Vojtěch Vaněček



## List of Acronyms

UV	Ultraviolet
BGO	$\text{Bi}_4\text{Ge}_3\text{O}_{12}$
R&D	Research and Development
e-h	Electron hole
LY	Light yield
Vis	Visible
PMT	Photomultiplier tube
mPD	micro-pulling-down
VB	Vertical Bridgman
CHC	$\text{Cs}_2\text{HfCl}_6$
CZC	$\text{Cs}_2\text{ZrCl}_6$
mVB	Modified vertical Bridgman
STE	self-trapped exciton
EPR	Electron paramagnetic resonance
TSL	Thermally stimulated luminescence
PL	Photoluminescence
PLE	Photoluminescence excitation
RL	Radioluminescence
XRF	X-ray fluorescence
CTR	Coincidence time resolution
VUV	Vacuum ultraviolet
NUV	Near ultraviolet
HD	high density



PDE	Photodetection efficiency
SiPM	Silicone photomultiplier
TOF	Time-of-flight
PET	Positron emission tomography
XRD	X-ray diffraction





## Table of Contents

1. Introduction .....	10
1.1. Scintillator .....	10
1.2. Scintillation detector.....	14
1.3. Single crystal growth.....	14
2. General discussion.....	17
2.1. Cs <sub>2</sub> HfCl <sub>6</sub> .....	17
2.2. Cross-luminescence scintillators.....	30
3. Conclusions.....	35
Literature - general.....	36
Literature - commented author's paper selection .....	42
Reprints of commented author's paper selection .....	44

# 1. Introduction

## 1.1. Scintillator

Scintillator is a material that converts the energy of ionizing radiation (alfa, beta, gamma, X-rays, etc.) into a large number of photons (i. e. flash of light), typically in the visible or ultraviolet (UV) spectral range. The scintillation process itself can be divided into three stages: conversion, transport, and luminescence (see Fig. 1).

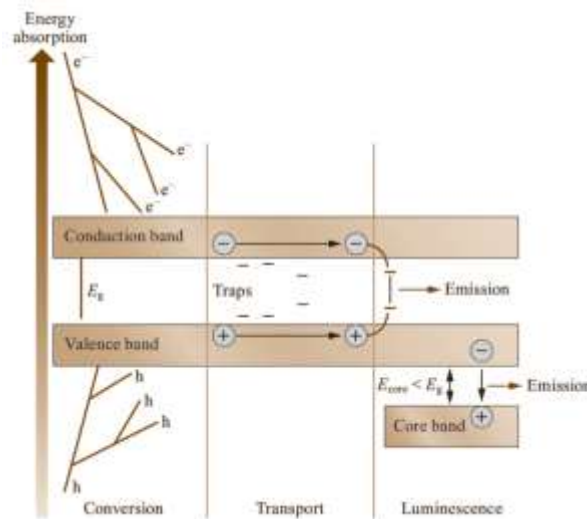


Fig. 1: Schematics of the scintillation process. Reprinted with permission from [1].

In the conversion stage, the ionizing radiation interacts with the scintillator resulting in the production of highly excited electron-hole (e-h) pairs. The mechanism of interaction depends on both the type and energy of the ionizing radiation and the composition of the absorbing material. On one hand, dense materials composed of heavy elements are required for the efficient detection of high-energy photons (X-ray or  $\gamma$ ). On the other hand, materials composed of light elements are required for the efficient detection of thermal and fast neutrons. The effect of the energy of ionizing radiation is illustrated in Fig. 2, which shows the diagram for the interaction cross-section of a photon with energy  $E$  with material with atomic number  $Z$ . The space is divided into three areas based on dominating channel of the interaction of a photon with the matter. It can be depicted from Fig. 2 that in the low  $Z$  materials photons from both  $^{57}\text{Co}$  (122 keV) and  $^{60}\text{Co}$  (1.17 and 1.33 MeV) will interact predominantly via Compton scattering. However, in high  $Z$

materials, the photoelectric effect will dominate for the 122 keV gamma photons of the  $^{57}\text{Co}$ , while the Compton scattering will still be the dominant type of interaction for the 1.17 and 1.33 MeV gamma photons of the  $^{60}\text{Co}$ . However, all interaction channels result in the formation of excited e-h pairs.

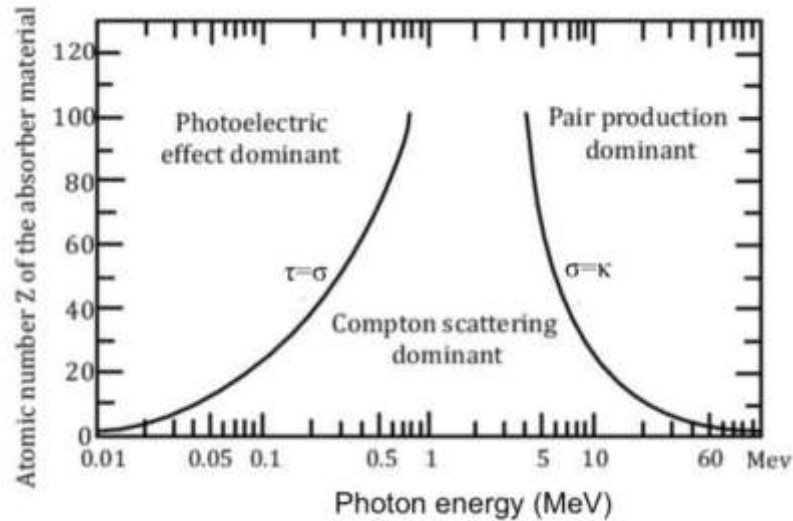


Fig. 2: Diagram of the cross-section for the interaction of a high-energy photon with the matter. Reprinted from [2].

Following the excitation, the highly excited electrons and holes relax to the bottom of the conduction band and top of the valence band, respectively. In the transport stage of the scintillation process, the relaxed charge carriers travel through the material to the luminescent center. During this stage, the charge carriers can interact with traps i. e. energy levels inside the band gap. This process, known as trapping of the charge carriers, usually results in deterioration of the scintillator performance. Depending on the trap depth (energy difference between trap level and respective band edge) and temperature, the detrapping time can vary by several orders of magnitude. The charge carrier can be trapped multiple times before reaching the luminescent center, resulting in slow components in the scintillation decay or even loss of the scintillation light. The origin of the traps can be any deviation from perfect crystal lattice e. g. vacancies, interstitial atoms, impurities, surface states, etc. During the luminescence stage, the e-h (e-h) pair undergoes radiative recombination at the luminescent center resulting in the emission of the desired scintillation photon.

Scintillators were first used for the detection of ionizing radiation already in early 1990s  $\text{CaWO}_4$  powder was used by Thomas Edison to increase the X-ray sensitivity of photographic film. Later  $\text{ZnS:Ag}$  fluorescent screen was used for the detection of  $\alpha$  particles in the experiments leading to Rutherford's model of the atomic nucleus. The first single-crystal scintillator  $\text{NaI:TI}$  was introduced by Hofstadter in 1948 [3], followed by the development of  $\text{CsI:TI}$  in 1951 [4]. Even today, more than 50 years after its discovery,  $\text{NaI:TI}$  is one of the most widespread single crystal scintillators. The success of  $\text{NaI:TI}$  motivated a significant effort in the development of new scintillating materials. In 1950  $\text{CaWO}_4$  and  $\text{CdWO}_4$  [5] were introduced as the first oxide single crystal scintillators. In the early years, the research and development were focused on heavy, high-density oxide materials with emission originating from the metal-oxide complexes including  $\text{Bi}_4\text{Ge}_3\text{O}_{12}$  (BGO) and  $\text{PbWO}_4$ . Later the R&D shifted towards host-activator concept. Resulting in the wide spectrum of single crystal scintillators (see reviews in [6,7]):

- Heavy oxide complexes (e. g.  $\text{CdWO}_4$ ,  $\text{PbWO}_4$ ,  $\text{Bi}_4\text{Ge}_3\text{O}_{12}$ )
- Rare-earth aluminum garnets and perovskites (e. g.  $\text{Y}_3\text{Al}_5\text{O}_{12}:\text{Ce}$ ,  $\text{YAlO}_3:\text{Ce}$ ,  $\text{Lu}_3\text{Al}_5\text{O}_{12}:\text{Pr}$ )
- Rare-earth silicates (e. g.  $\text{Y}_2\text{SiO}_5:\text{Ce}$ ,  $\text{Lu}_2\text{SiO}_5:\text{Ce}$ ,  $\text{Gd}_2\text{Si}_2\text{O}_7:\text{Ce}$ )
- Alkaline earth halides (e. g.  $\text{SrI}_2:\text{Eu}$ ,  $\text{CaI}_2:\text{Eu}$ ,  $\text{CsBa}_2\text{I}_5:\text{Eu}$ )
- Rare-earth halides ( $\text{LaBr}_3:\text{Ce}$ ,  $\text{CeBr}_3$ ,  $\text{LuI}_3:\text{Ce}$ )
- And many others

Most of the examples above are based on 5d-4f luminescence of  $\text{Ce}^{3+}$  and  $\text{Pr}^{3+}$ , the latter only in oxide hosts. Due to the allowed nature of the transition  $\text{Ce}^{3+}$  and  $\text{Pr}^{3+}$  exhibit fast decays in the range of 10 – 60 ns and show in most cases high quantum efficiency. The advances in research and development (R&D) of halide scintillators in the last decade have been recently reviewed in [P1].

A phenomenological model for the prediction of maximum efficiency of scintillation excited with gamma/X-ray photons was developed in 1980 [8]. The model allows calculation of the upper limit of (e-h) yield based on parameters of the ionization and thermalization process. This model was further refined in [9] allowing to calculate of the upper limit of photons produced by single gamma photon  $n_\gamma$  using three parameters  $\beta$ , S, and Q:

$$(1) \quad n_{ph} = \frac{E_{\gamma}}{2.3E_g} \times \beta SQ,$$

where  $E_{\gamma}$  is the energy of the gamma photon,  $E_g$  is the band gap,  $\beta$  is the conversion efficiency,  $S$  is the transport efficiency, and  $Q$  is the quantum efficiency of the luminescent center. The value of  $2.3 \cdot E_g$  is the minimum energy for the production of the e-h pair according to Robins [8]. However, this value can differ among materials. Therefore, the equation (1) is often rewritten in the form:

$$(2) \quad n_{ph} = \frac{E_{\gamma}}{\beta E_g} \times SQ,$$

where  $\beta$  is a dimensionless parameter with typical values from 2 to 3 for most scintillators. The relative efficiency of the scintillator  $\eta$  can be calculated as:

$$(3) \quad \eta = \frac{E_{hv} N_{hv}}{E_{\gamma}},$$

where  $N_{hv}$  is the number of emitted photons and  $E_{hv}$  is the energy of emitted photons. The efficiency  $\eta$  is far from 1 for all scintillators and phosphors. The most efficient material known today is ZnS:Ag with  $\eta$  close to 0.2 [6]. Both  $n_{ph}$  and  $\eta$  can be used as a benchmark to evaluate the performance of real scintillators.

Many characteristics of the material play a role in its performance as a scintillator. The most important characteristics include [6]:

- Scintillation efficiency
- Light yield (LY)
- Energy resolution and nonproportionality
- Stopping power
- Scintillation response in time
- Spectral matching between scintillator and photodetector
- Chemical and mechanical stability
- Radiation resistance
- Price

The relative importance of the above-mentioned material characteristic differs according to the field of application of the scintillation detector. Choice of a suitable scintillator requires careful consideration of all the parameters.

## 1.2. Scintillation detector

The scintillator detector can be schematically divided into three parts (see Fig. 3): scintillator, photodetector, and read-out electronics. The scintillator converts the energy of the ionizing radiation into a flash of light in the UV/Vis range e. g. the scintillation pulse. The scintillation pulse is converted into an electric signal via a photodetector. The electric signal is then processed (discrimination, amplification, etc.) and digitalized via read-out electronics. The selection of the scintillator (NaI:TI, SrI<sub>2</sub>:Eu, Y<sub>3</sub>Al<sub>5</sub>O<sub>12</sub>:Ce etc.), photodetector (photomultiplier tube, avalanche photodiode, charged coupled device etc.), and read-out electronics (digital counter, multichannel analyzer, coincidence circuit, etc.) depend on the target application.

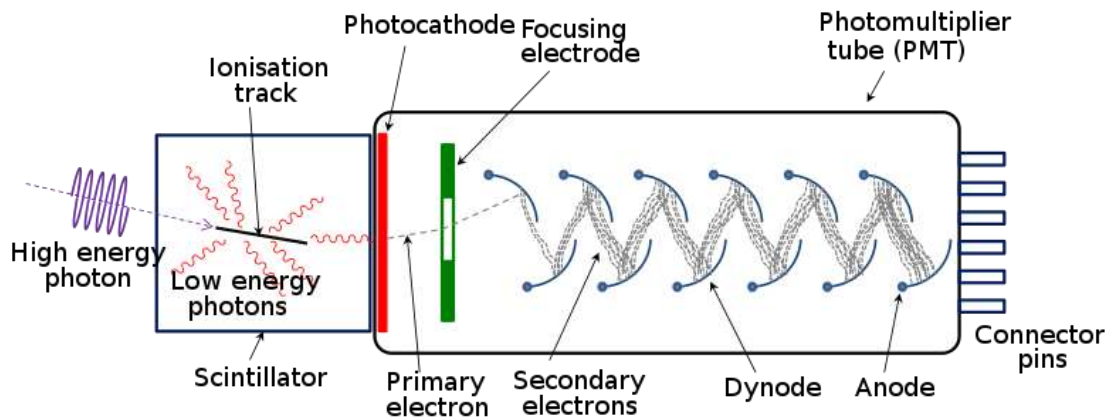


Fig. 3: Schematics of the scintillation detector with photomultiplier tube (PMT) as the photodetector. Reproduced under terms of the CC BY-SA license [10].

## 1.3. Single crystal growth

A crystal is a solid material with its components arranged in a highly ordered microscopic structure, forming a crystal lattice. Crystalline materials are used in almost every area of human activity due to their irreplaceable properties. Single crystals can be prepared (grown) from the solid phase, solutions, melt, and gas phase. However, the crystal growth from the melt is most common for the growth of bulk single crystals for industrial applications. Many methods were developed for crystal growth from melt including Czochralski, Bridgman, Kyropoulos, film-fed edge growth, micro-pulling-down, etc. The growth of halide crystals is complicated

due to the hygroscopic nature of most of the halide compounds. For a review of methods used for the growth of halide single crystals see [P1] and references therein. Methods used in this work, namely micro-pulling-down (mPD) and vertical Bridgman (VB) method, will be briefly introduced below.

Bridgman method is the most widely used technique for single crystal growth of hygroscopic halide materials. It was developed by Bridgman in 1925 [11] and later improved by Stockbarger [12] (so-called Bridgman-Stockbarger method). In the typical vertical Bridgman-Stockbarger growth the material is sealed in an ampoule (usually made of silica) and placed into a two-zone furnace (See Fig. 4). The upper zone is heated to the temperature above the melting point of the material and the lower zone is heated to a temperature below the melting point of the material. This creates a temperature gradient in the volume between the zones. The ampoule is then slowly pulled through the temperature gradient which results in nucleation and following crystallization.

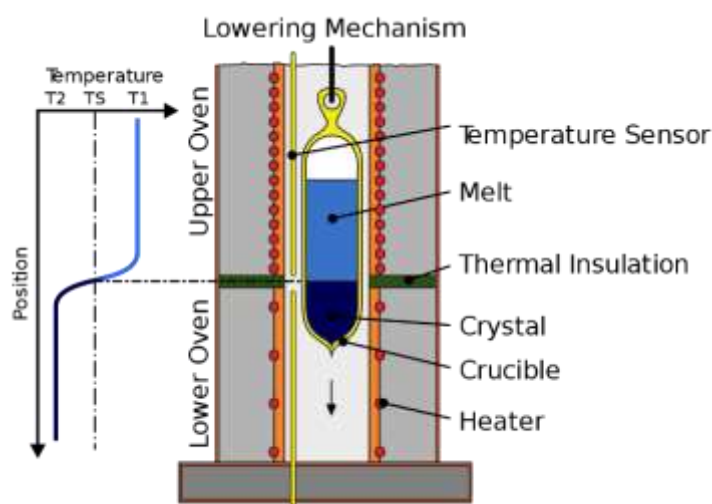


Fig. 4: Schematics of crystal growth using two-zone vertical Bridgman-Stockbarger method. The shape of the vertical temperature gradient is illustrated on the left. Reproduced under terms of the CC BY-SA license [13].

The micro-pulling-down method was developed in the 1990s [14] for the growth of crystal fibers of  $\text{LiNbO}_3$ . Later it was modified for the growth of metals and alloys [15], semiconductors [16], and halides [17]. In typical micro-pulling-down growth, the material is melted in a crucible with an opening (capillary or small hole)

at the bottom. The resulting melt flows down through the opening to the bottom of the crucible, where it is connected to a cooled seed. The undercooling formed by thermal gradient results in crystallization. The seed is then pulled down, forcing the melt through the temperature gradient until the entire (or majority) volume of the melt in the crucible is depleted. The main advantages of the mPD method are high growth rates (up to 1 mm/min) and low material consumption (~0.1 – 1 g). For detailed description of the mPD method see [18].

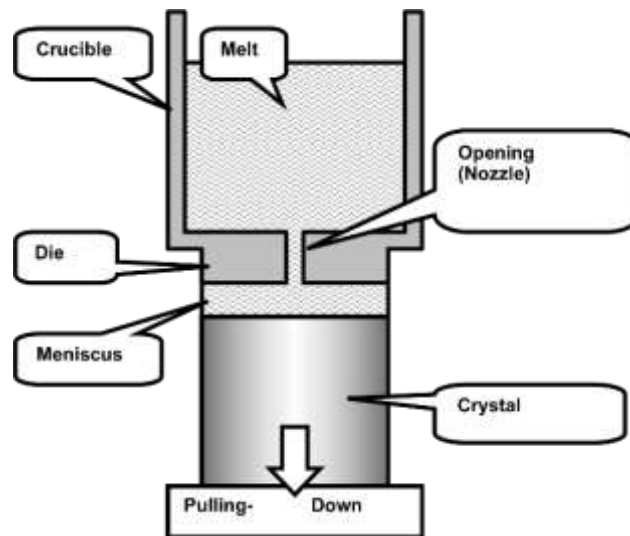


Fig. 5: Schematics of crystal growth by the micro-pulling-down method.



## 2. General discussion

The publications discussed in this work focus on two main topics: Cs<sub>2</sub>HfCl<sub>6</sub> based scintillators and cross-luminescence scintillators. In the first section, the development of high-quality Cs<sub>2</sub>HfCl<sub>6</sub> based scintillators and an investigation of their scintillation properties is discussed. In the second section, a systematic study of materials perspective as cross-luminescence scintillators is introduced.

### 2.1. Cs<sub>2</sub>HfCl<sub>6</sub>

The first studies investigating optical [19,20] and magnetic [21,22] properties of transition metal ions in Cs<sub>2</sub>HfCl<sub>6</sub> (CHC) and Cs<sub>2</sub>ZrCl<sub>6</sub> (CZC) crystals were reported in the early 1970s. However, in those studies, CHC and CZC were used only as host material. First studies investigating crystal structure [23], thermodynamic properties [24], and luminescence [25,26] of CHC and CZC were reported in the late 70s and 80s. The study by Ackerman [25] reported intrinsic luminescence in all of the Cs<sub>2</sub>HfX<sub>6</sub> (X = Cl, Br, I) materials. However, the study was focused on the identification of new hosts with K<sub>2</sub>PtCl<sub>6</sub> structure suitable for the investigation of optical properties of transition metal ions. Therefore, intrinsic luminescence was undesirable, and it was not investigated further. Bryan and Ferranti [26] report high quantum efficiency of luminescence and high radioluminescence intensity (compared to CaWO<sub>4</sub> standard) in both CHC and CZC and suggested further plans for investigation of those materials. However, to the best of my knowledge, no further studies were published.

The CHC was rediscovered as a promising scintillator by Burger et al. [27] in 2015. They reported a high LY of 54 000 [27], excellent energy resolution of 3.3 % [27] (at 662 keV of <sup>137</sup>Cs), high proportionality, and low hygroscopicity. In addition, CHC has a high stopping power for high-energy photons due to the combination of high  $Z_{eff}$  of 58 [27] and moderate density of 3.86 g/cm<sup>3</sup> [27]. These results inspired significant R&D of CHC-based materials.

The Cs<sub>2</sub>HfCl<sub>6</sub> crystalizes in K<sub>2</sub>PtCl<sub>6</sub> like cubic crystal structure (space group  $Fm\bar{3}m$ , no. 225). This so-called “vacancy ordered double perovskite” structure can be derived from a regular perovskite structure (space group  $Pm\bar{3}m$ , no. 221, phase prototype CaTiO<sub>3</sub>) with general (halide) formula  $A^+B^{2+}X_3^-$  by doubling the structure

unit and replacing one  $B^{2+}$  cation with  $M^{4+}$  and the other  $B^{2+}$  cation with vacancy. Resulting in a charge-neutral formula  $A_2MX_6$  with  $[MX_6]^{2-}$  octahedra at the corners and face centers of the cube separated by  $A^+$  (See fig. 6). This matrix offers high compositional flexibility with  $A = Na, K, Rb, Cs, Tl$ ,  $M = Ti, Zr, Hf, Sn, Se, Te, Pt$ , and  $X = F, Cl, Br, I$ . Most of the resulting compositions keep the cubic  $K_2PtCl_6$  like crystal structure. Only compositions with smaller alkali metals on the A site undergo distortion to the lower crystal symmetry [28]. This creates a large compositional space for exploration and optimization of CHC based scintillators.

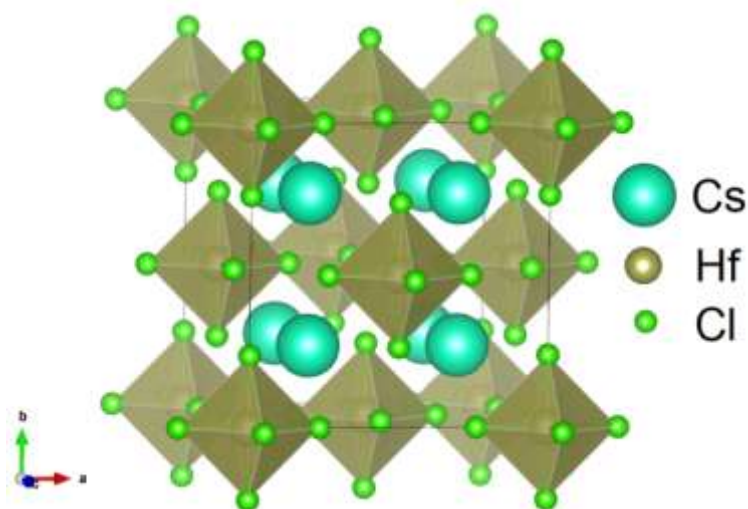


Fig. 6: Crystal structure of  $Cs_2HfCl_6$ .

In recent years many scintillators with general formula  $A_2MX_6$  were reported. Including chlorides:  $Rb_2HfCl_6$  [29],  $Cs_2HfCl_6$  [27,30,31][P2,P3],  $Cs_2ZrCl_6$  [31],  $Tl_2HfCl_6$  [32,33],  $Tl_2ZrCl_6$  [33,34], bromides:  $Cs_2HfBr_6$  [35],  $Cs_2ZrBr_6$  [35], iodides:  $Rb_2HfI_6$  [36],  $Cs_2HfI_6$  [37,38] and mixed anion solid solutions [30,39–41]. Such a broad compositional spectrum allows fine-tuning properties of  $A_2MX_6$  scintillators for specific application. Substitution of chlorine with heavier halides decreases the value of band gap which results in redshift of the emission and increase in LY (see equation no. 2). This was demonstrated in [38], where  $Cs_2HfI_6$  was chosen as a perspective scintillator for remote high-dose dosimetry due to match of  $Cs_2HfI_6$  ( $\lambda_{em,max} = 700\text{ nm}$ ) emission and window of high transparency of silica optical fibers. Scintillators with emission in red/near IR are also perspective for coupling with avalanche photodiode to increase detection efficiency [42].

Doping of  $A_2MX_6$  with conventional activators including  $Tl^+$  [43],  $Eu^{2+}$  [44], and  $Ce^{3+}$  [43,44] or unconventional doping with alkaline earth metals [45] was unsuccessful so far. On the other hand, the substitution of  $Hf^{4+}$  with  $Te^{4+}$  results in a broad emission band with maxima at 575 nm [46]. However, even the best  $Cs_2HfCl_6:Te$  samples exhibit a light yield of only 13 100 ph/MeV [46].

The  $A_2MCl_6$  crystals exhibit an excellent  $\alpha/\gamma$  pulse shape discrimination [32,34,47,48]. This enables the use of  $A_2MCl_6$  scintillators for the detection of rare events. However, sufficient radiopurity is necessary for such applications [49]. The use of CHC for the detection of rare events was demonstrated in [50] where authors measured the half-life of alpha decay of  $^{174}Hf$  ( $T_{1/2} \sim 10^{16}$  years). It was also suggested that CZC is a perspective candidate for the detection of neutrinoless double beta decay, due to the high concentration of Zr [51]. Isotope  $^{96}Zr$  with 2.80 % abundance in natural zirconium is one of the candidates for the detection of neutrinoless double-beta decay [52].

For all the applications mentioned above, high-quality crystals with optimized performance are required. This comprises mainly two prerequisites: optimization of the crystal growth technology and a good understanding of the scintillation mechanism. The optimized crystal growth results in high-quality crystals with a low concentration of defects. This improves the overall performance of the scintillator and allows investigation of the scintillation mechanism without interfering effects that complicate data evaluation. A good understanding of the scintillation mechanism is required for the effective engineering of a high-performance scintillator. This involves methods such as the use of activators, defect engineering, band-gap engineering, etc.

The growth of CHC single crystals has three main complications:

- Purification of starting materials
- Hygroscopicity of  $HfCl_4$
- Sublimation of  $HfCl_4$ .

Impurities present in the starting materials can create heterogeneous nucleation centers, lattice defects, traps in the band gap, etc. Therefore, high purity of starting materials (usually 99.99 % or higher) are required for the growth of high-quality single crystals suitable for use in scintillator detectors. However, such a high purity

HfCl<sub>4</sub> is not available on the market. Therefore, the purification step must precede the synthesis and crystal growth. Multiple resublimation [53][P3], introduction of halogenation agents [54][P2], zone refining [P2], and filtration [54] were successfully used for purification of CsCl and/or HfCl<sub>4</sub>.

The metal tetrahalides MX<sub>4</sub> (M = Hf, Zr, Ti, X = Cl, Br, I) are highly hygroscopic due to the strong affinity of M<sup>4+</sup> cation to oxygen. The metal tetrahalides react spontaneously with water or water vapor to produce oxyhalides and their hydrates MOX<sub>2</sub>·nH<sub>2</sub>O [55]. Upon heating above 200 °C under an inert atmosphere, the MOX<sub>2</sub>·nH<sub>2</sub>O decomposes into MO<sub>2</sub>. The resulting oxides act as high melting (> 1800 °C) impurities in the melt. Forming heterogenous nucleating centers and inclusions in the grown crystals [54] [P3].

To avoid exposure of the material to air the Cs<sub>2</sub>MCl<sub>6</sub> crystals are grown (similarly to most hygroscopic halides) in enclosed silica ampoules via the vertical Bridgman – Stockbarger (VB) method. Due to technical reasons, the growth ampoules are usually sealed under vacuum [53][P3,P4]. Therefore, the investigation of the thermodynamic properties of Cs<sub>2</sub>MCl<sub>6</sub> under vacuum is of interest.

The study of Král et al. [P5] investigated the thermodynamic properties of CHC under an inert atmosphere (N<sub>2</sub>) and vacuum (~ 100 Pa). The study showed that CHC is stable up to the Cs<sub>2</sub>HfCl<sub>6</sub>-CsCl eutectic point (586 °C) under an inert atmosphere. However, it decomposes continuously above ~300 °C under vacuum according to:



The decomposition can result in non-stoichiometry of the grown crystals and therefore deteriorate the scintillation performance. Furthermore, deposition of the sublimated HfCl<sub>4</sub> on the surface of the crystal during cooling could explain the translucent/non-transparent surface of the as-grown crystals [30,54][P3,P4].

Optimization of CHC in terms of purification of starting materials [53,54] and optimization of growth conditions [41,54] resulted in improvement of energy resolution down to 2.8 % (at 662 keV of <sup>137</sup>Cs) [41] and LY of 27 000 ph/MeV [41]. Furthermore, CHC with a diameter up to 23 mm was successfully grown [56]. It is important to note here that the best reported LY of 54 000 ph/MeV in [27] was never

reproduced, even by the same authors, and the value of LY of CHC in most of the other publications is around 30 000 ph/MeV. Thus, the value of 54 000 ph/MeV is probably an overestimation caused by the evaluation method. It is also difficult to compare the reported light yields because the value of the shaping time is varying among the publications and in some publications, it is not specified at all.

Even though high-quality  $A_2MX_6$  crystals can be grown via the standard two-zone vertical Bridgman method in closed silica ampoules, the slow growth rates usually used for vertical Bridgman growth of halide crystals (0.1 – 0.5 mm/h) result in long growth times. For example, the growth of a 100 mm long CHC crystal lasts approximately 20 days, depending on the growth and cooling rates. Therefore, composition screening of the  $A_2MX_6$  matrix can be extremely time-consuming. This can be solved by simultaneous growth in a large number of furnaces, which is demanding in terms of cost, personnel, and workspace, or by modification of the growth procedure. The modification of vertical Bridgman growth using the so-called “multi-ampoule growth station” was successfully used for simultaneous growth of four  $\varnothing 25$  mm x 25 mm crystals of  $KCaI_3$  in one furnace [57]. In [P3] we reported modification of halide micro-pulling-down (H-mPD) apparatus for inductively heated vertical Bridgman growth in closed silica ampoules. The components of the “hot-zone” used for H-mPD consisting of the afterheater, the crucible, and shielding (See fig. 7A) were replaced with a graphite tube heater and single alumina shielding to create a small (inner  $\varnothing 14$  mm) one-zone furnace (See fig. 7B). This so-called “modified vertical Bridgman growth” (mVB) can be used for the growth of halide crystals with a diameter of 7 mm and length up to 50 mm. The temperature gradient can be modified via an adjustment in the position of the induction coil relative to the heater and by perforation of the heater which results in suppression of heat generation and conduction. The entire growth (stabilization, growth, and cooling) takes from 5 to 7 days. This is a significant reduction of growth time which allows more effective screening of halide scintillators including members of the  $A_2MX_6$  family.

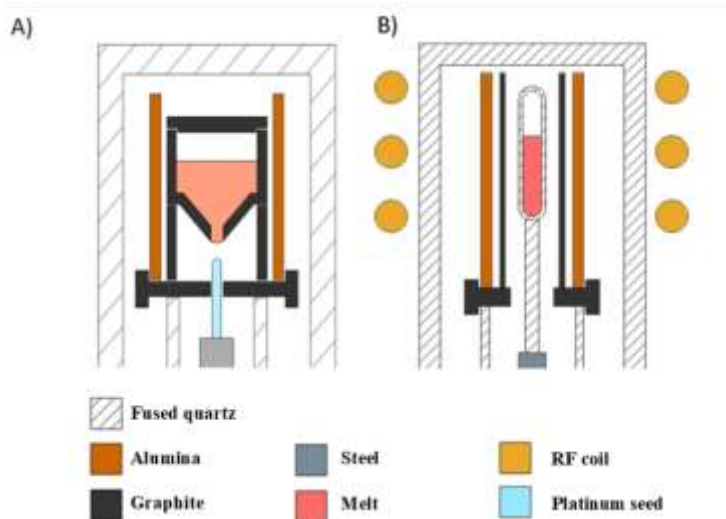


Fig. 7: Schematics of hot zones used for a) H-mPD and b) mVB single crystal growth.

To ensure that the quality of the crystals grown by the mVB method is sufficient for the evaluation of the scintillation properties of the material, the structural and optical properties of CHC crystals grown by the mVB, and the standard VB method were compared. The X-ray powder diffraction (XRD) confirmed that the grown crystals were phase-pure cubic CHC [P3]. Moreover, optical characterization including absorption, PL, PL kinetics, radioluminescence (See fig. 8), and scintillation kinetics confirmed that the optical quality of CHC crystals grown by the mVB method is comparable to the crystals grown by the standard VB method. Therefore, the mVB method can be used for the time-effective screening of scintillation properties of  $A_2MX_6$  crystals [P3].

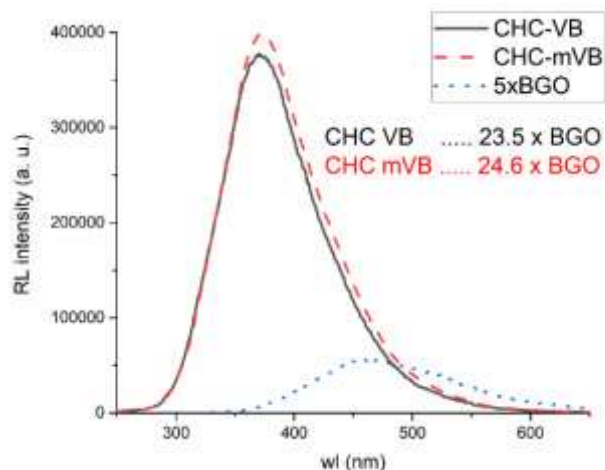


Fig. 8: Comparison of radioluminescence spectra of CHC crystals grown by mVB and VB methods. Reprinted with permission from [P3].

Despite a large number of publications focusing on  $A_2MX_6$  scintillators, only a few of them investigate the scintillation mechanism itself. In most of the publications emission in  $A_2MX_6$  is ascribed to radiative recombination of the self-trapped exciton (STE). This assumption is based on large Stokes shift, broad emission spectrum, and PL decays in order of  $\mu\text{s}$ . The assumption was further supported by first-principle calculations [58], where the emission was ascribed to STE formed by a hole trapped on neighboring Cl atoms ( $\text{Cl}_2^-$  molecular ion, known as  $V_k$  center) and electron trapped on  $\text{Hf}^{4+}$  [58]. However, experimental confirmation and deeper investigation of the scintillation mechanism were still missing.

In [59] authors investigated the scintillation mechanism in CHC using a combination of PL and electron paramagnetic resonance (EPR). Photoluminescence revealed the presence of two emission bands which were ascribed to STE and defect-related emission. A phenomenological model with three excited state levels was proposed to explain the temperature dependence of PL intensity and decay kinetics. Moreover, EPR measurements showed the formation of two types of  $V_k$  centers after X-ray irradiation. One formed by two neighboring Cl atoms, which was predicted by first-principle calculations [58], and the second involving interstitial  $\text{Cl}^-$  ion. Therefore, non-stoichiometry and crystal quality could play a role in the formation of the second  $V_k$  center.

The influence of non-stoichiometry and crystal quality on the presence and nature of defects in CHC was further studied in [P2]. In this paper, the authors investigated three CHC (See fig. 9) crystals with different phase purity via correlated photoluminescence, radioluminescence, thermally stimulated luminescence (TSL), and electron paramagnetic resonance.

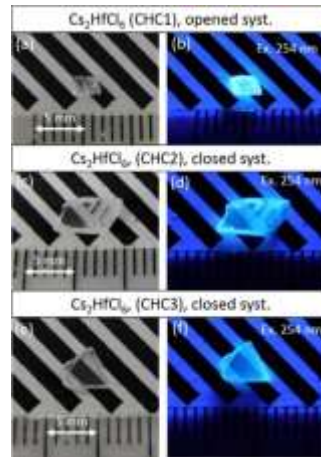


Fig. 9: Cut and polished samples from three CHC crystals under a) daylight and b) UV illumination (CHC1 – high non-stoichiometry, CHC2 – slight non-stoichiometry, and CHC3 – phase pure).

Reprinted with permission from [P2].

The TSL glow curves were very complex with 8 peaks in the temperature range of 10 – 320 K. However, the intensity of the TSL signal was decreasing significantly with increasing crystal quality (See fig. 10).

The EPR measurements confirmed the presence of the regular  $V_k$  (denoted  $V_k(a)$  in the publication) center reported in [59], together with the  $V_k$  center perturbed by a defect (denoted  $V_k'(b)$  in the publication). The intensity of the EPR signal of the regular  $V_k$  center was significantly lower in the phase pure sample, in accordance with results from TSL. It was concluded that the number of both trapping and recombination centers is decreasing with increasing crystal quality. Moreover, the decomposition of RL spectra into gaussian-shaped components revealed the presence of at least two components. The components were assigned to exciton trapped at regular  $[HfCl_6]^{2-}$  octahedra and exciton trapped at Zr impurity forming  $[ZrCl_6]^{2-}$  octahedron. Zirconium is a common impurity in hafnium



compounds due to the difficult separation of Hf and Zr. The role of Zr impurity was suggested already by Burger et al. [27].

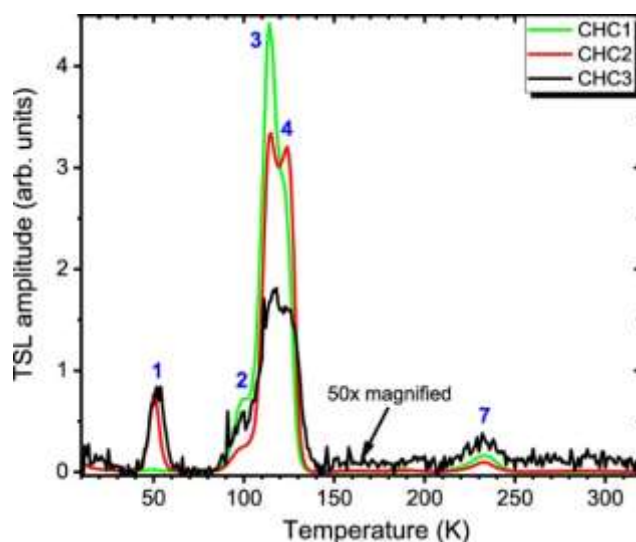


Fig. 10: TSL glow curves of three  $\text{Cs}_2\text{HfCl}_6$  crystals (CHC1 – high non-stoichiometry, CHC2 – slight non-stoichiometry, and CHC3 – phase pure).

Reprinted with permission from [P2].

The study of charge trapping and recombination was extended to CZC in [P6]. Samples from phase-pure CHC and CZC were studied by a combination of RL, TSL, and EPR similar to Král et al. [59] and Buryi et al. [P2]. The X-ray fluorescence (XRF) confirmed the presence of Zr in CHC. However, the presence of Hf in CZC was not confirmed by XRF. This is expected since the majority of hafnium is produced as a by-product of the purification of nuclear-grade zirconium. The EPR revealed the presence of a regular  $V_k$  center in CZC similar to the one reported for CHC [59][P2]. This corroborates the similarity of the electronic structure of Zr and Hf and the crystal structure of CZC and CHC. The TSL glow curves exhibited a complex shape for both samples with up to 8 distinguishable peaks. However, several peaks in the glow curves could be identified in both CZC and CHC at the same temperature. Pointing toward the formation of similar defect in both crystals. The RL spectra of CZC and CHC were decomposed into Gaussian-shaped components (See fig. 11). The RL spectrum of CZC was well approximated with a single component, while two components were needed for a good approximation of CHC emission. Moreover, the position of the CZC band and

low energy component of CHC coincide very well pointing toward the significant influence of Zr impurity in CHC crystals. It was suggested that Zr impurity participates in energy transfer in CHC crystals.

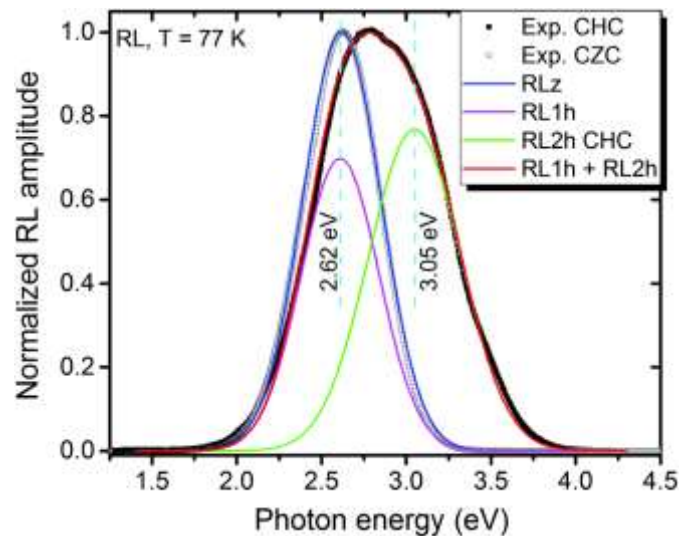


Fig. 11: RL spectra of Cs<sub>2</sub>HfCl<sub>6</sub> (CHC) and Cs<sub>2</sub>ZrCl<sub>6</sub> (CZC) and their decomposition into gaussian-shaped components. Reprinted with permission from [P6].

Considering the results above which pointed to a significant role of Zr impurity on the scintillation properties of CHC, the influence of low-level intentional doping of Zr into CHC was investigated by Vanecek et al. in [P4]. In this publication four Cs<sub>2</sub>HfCl<sub>6</sub>:Zr (x %) crystals with x = 0, 0.1, 0.5 and 1.0 were investigated. The RL spectra exhibit a red shift with Zr doping (See fig. 12), which is more prominent on the low-energy edge of the emission band. This could be explained in terms of the two-component decomposition of RL spectra suggested in [P6]. The Zr doping results in a higher contribution of the low energy band, which is forming the low energy edge of the emission spectra. The high energy edge of the emission spectra is affected only slightly because it is formed by the high energy component of exciton trapped at [HfCl<sub>6</sub>]<sup>2-</sup>.

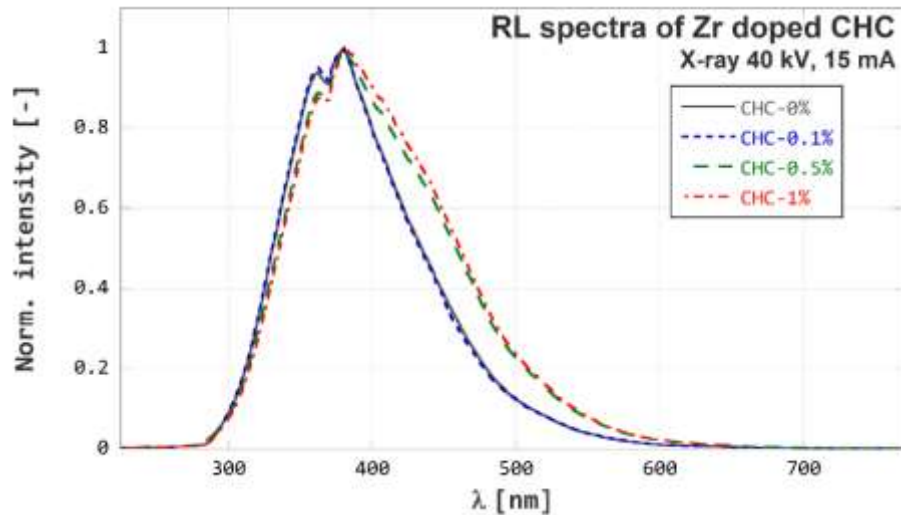


Fig. 12: Normalized RL spectra of  $\text{Cs}_2\text{HfCl}_6:\text{Zr}(x\%)$  crystals. Reprinted with permission from [P4].

The influence of the Zr doping can be observed also in scintillation decay kinetics. The scintillation decay profiles of  $\text{Cs}_2\text{HfCl}_6:\text{Zr}$  samples were approximated using a three exponential model. It can be seen from a comparison of undoped sample and sample with 0.5 % of zirconium (See fig. 13), that Zr doping results in a higher contribution of the slow ( $12\ \mu\text{s}$ ) component. It is expected to observe a slower decay time for a transition of the same type but with a lower energy of emission. Moreover, a decrease in the afterglow (intensity of slow light emitted by the scintillator after cut off of the excitation source) with increasing Zr concentration was observed.

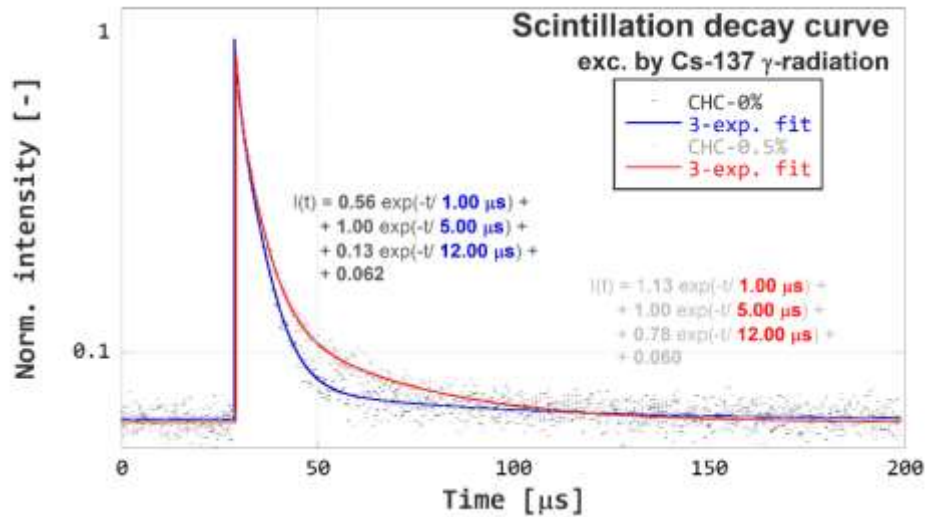


Fig. 13: Scintillation decay curves of the undoped CHC:Zr (0%) and CHC:Zr (0.5%) and the corresponding 3-exponential fit functions. Reprinted with permission from [P4].

We have decided to study the influence of Zr in  $\text{Cs}_2\text{HfCl}_6$  beyond the scope of [P4] to get deeper insights into the interplay of Hf and Zr-related emission centers in CHC. For this study, fourteen crystals were grown using the mVB method [P3] with composition covering the whole range of  $\text{Cs}_2\text{Hf}_{1-x}\text{Zr}_x\text{Cl}_6$  solid solution (i. e.  $0 \leq x \leq 1$ ). Cut and polished samples were prepared from each crystal and their structural and optical properties were investigated. The RL spectra show a smooth transition from the RL spectrum of CHC to CZC upon Zr substitution (see Fig. 14).

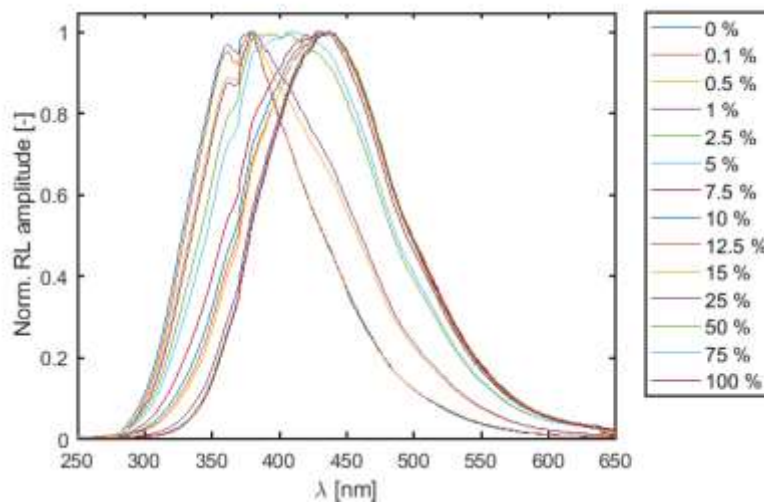


Fig. 14: RL spectra of  $\text{Cs}_2\text{Hf}_{1-x}\text{Zr}_x\text{Cl}_6$  samples.

This corroborates with the results reported in [P4,P6]. Such effect could be explained by competition of the  $[\text{HfCl}_6]^{2-}$  and  $[\text{ZrCl}_6]^{2-}$  trapping centers. Moreover, the data suggest preferential trapping of excitons at  $[\text{ZrCl}_6]^{2-}$  since the RL spectra of  $\text{Cs}_2\text{Hf}_{1-x}\text{Zr}_x\text{Cl}_6$  closely resemble the RL spectrum of pure  $\text{Cs}_2\text{ZrCl}_6$  already at 25 % of Zr substitution. This can be seen from the dependence of RL emission band maxima on Zr content (See fig. 15). The redshift or RL emission band maxima “saturates” already at 10 % of Zr.

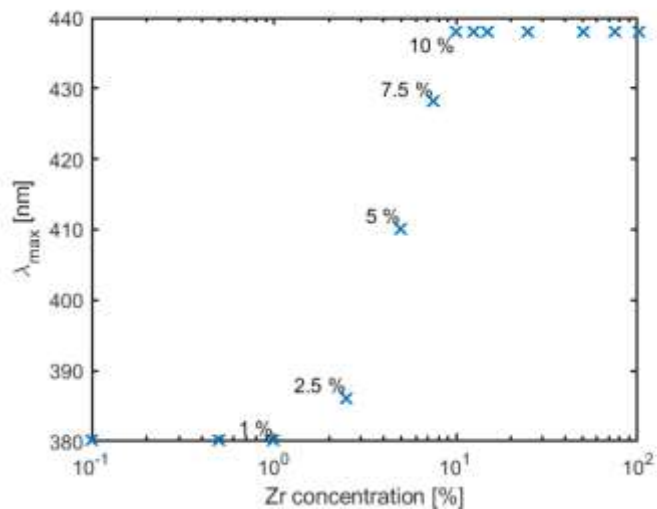


Fig. 15: Dependence of RL emission band maxima of  $\text{Cs}_2\text{Hf}_{1-x}\text{Zr}_x\text{Cl}_6$  on Zr concentration.

Zirconium substitution into the CHC matrix also heavily influences the afterglow. The RL intensity 1 second after the excitation source cut-off decreases significantly up to 7.5 % of Zr and then levels off and fluctuates around the same level for higher Zr concentrations (See fig. 16). However, the value of afterglow in  $\text{Cs}_2\text{Hf}_{0.925}\text{Zr}_{0.075}\text{Cl}_6$  is almost 30 times lower compared to pure CHC. This points again to the suggestion that  $[\text{ZrCl}_6]^{2-}$  can trap excitons more effectively than  $[\text{HfCl}_6]^{2-}$ . Therefore,  $[\text{ZrCl}_6]^{2-}$  can compete for charge carriers with traps more effectively than  $[\text{HfCl}_6]^{2-}$ . Considering the very small difference in bond lengths of  $[\text{HfCl}_6]^{2-}$  and  $[\text{ZrCl}_6]^{2-}$  octahedra ( $a_{\text{Hf-Cl}} = 2.46 \text{ \AA}$ ,  $a_{\text{Cl-Cl}} = 3.48 \text{ \AA}$  for CHC and  $a_{\text{Zr-Cl}} = 2.45 \text{ \AA}$ ,  $a_{\text{Cl-Cl}} = 3.46 \text{ \AA}$  for  $\text{Cs}_2\text{ZrCl}_6$ ) we assume that higher trapping efficiency of  $[\text{ZrCl}_6]^{2-}$  compared to  $[\text{HfCl}_6]^{2-}$  is caused by the higher binding energy of electron polaron at Zr compared to Hf. Rather than by higher binding energy of hole trapped at  $\text{Cl}_2^- V_k$  center in CZC compared to CHC. This assumption is supported by the

results of EPR [P6] and first-principle calculations [58]. These results show, that Zr substitution into the CHC matrix can be utilized to achieve a redshift of the emission band and decrease of the afterglow, without a significant decrease of effective atomic number (at 7.5% of Zr substitution). However, at the cost of slower scintillation decay kinetics. Although, the afterglow of CHC can be significantly decreased by Zr substitution even the best  $\text{Cs}_2\text{Hf}_{1-x}\text{Zr}_x\text{Cl}_6$  samples exhibit high afterglow (approx. two orders of magnitude higher than BGO). Therefore, elimination of the influence of traps by the methods of the defect and/or band gap engineering should result in a significant increase in light output of  $\text{Cs}_2\text{HfCl}_6$  and possibly other scintillators from the  $\text{A}_2\text{MX}_6$  family. However, better knowledge of the nature of the traps is required for their effective suppression.

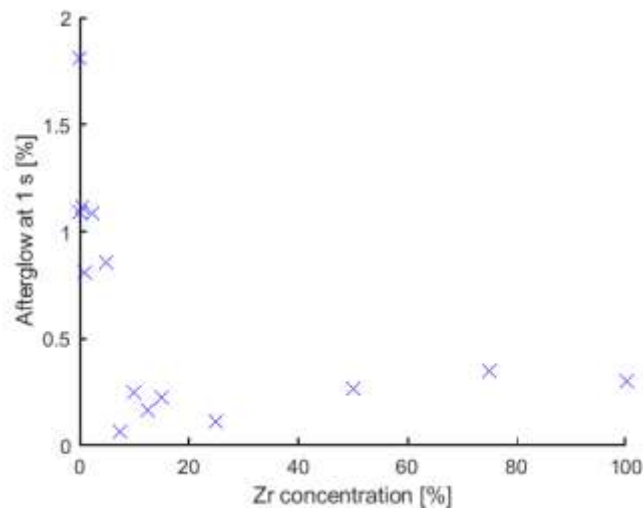


Fig. 16: Dependence of afterglow of  $\text{Cs}_2\text{Hf}_{1-x}\text{Zr}_x\text{Cl}_6$  on Zr concentration.

## 2.2. Cross-luminescence scintillators

A Cross-luminescence (also known as core-valence luminescence or Auger-free luminescence) is the radiative recombination of an electron in the valence band with a hole in the uppermost core band (see Fig. 17). This type of luminescence is observed in materials where the energy between the top of the uppermost core band and the bottom of the valence band (sometimes denoted as  $E_{g2}$ ) is smaller than the band gap (usually denoted  $E_g$ ). Otherwise, the recombination of core holes is dominated by the Auger recombination i. e. process where the energy of the recombination of the hole in the core band and electron in

the valence band is transferred to another electron which is excited to the conduction band (see Fig. 17).

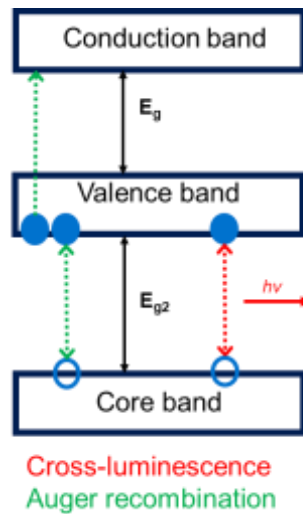


Fig. 17: Schematics of band structure with an indication of cross-luminescence and Auger recombination.

After the discovery of cross-luminescence in  $\text{BaF}_2$  crystals in 1982 [60] a large number of cross-luminescence scintillators were investigated (see review [61]). However, most of the works were focused on basic research and didn't result in a significant application for scintillation detectors. The cross-luminescence scintillators exhibit fast decay kinetics ( $\sim$  ns) with rather low light output ( $\sim 10^3$  ph/MeV). Moreover, cross-luminescence emission lies in the VUV - deep UV region (190 nm + 220 nm for  $\text{BaF}_2$ ) which is not suitable for commonly used photodetectors. These aspects were detrimental for use of cross-luminescence scintillators. As a result,  $\text{BaF}_2$  is the only commercially available cross-luminescence scintillator, besides the  $\text{Cs}_2\text{LiYCl}_6:\text{Ce}$  in which cross-luminescence is used for  $n^0/\gamma$  discrimination [62]. However, recent development in high-energy physics and medical imaging [63] created a new demand for ultra-fast scintillators resulting in a renewed interest in cross-luminescence scintillators further supported by the development of UV-sensitive semiconductor photodetectors. In [64] a coincidence time resolution (CTR) of  $51 \pm 5$  ps was reported for  $\text{BaF}_2$  crystal using vacuum ultraviolet high density (VUV-HD) silicon photomultiplier (SiPM). To the best of my knowledge, this is currently the lowest CTR value reported for an inorganic scintillator. This result was achieved despite low spectral matching of

BaF<sub>2</sub> emission and VUV SiPM sensitivity, resulting in a photodetection efficiency (PDE) of 22 %. It was estimated that if the PDE for BaF<sub>2</sub> reached that of (Lu,Y)<sub>2</sub>SiO<sub>5</sub>:Ce (LYSO:Ce) standard i. e. 59 % of the CTR should reach 24 ps [64]. Such a low CTR is a perspective for time-of-flight positron emission tomography (TOF PET) and is very close to the desired 10 ps benchmark [63]. The increase in PDE can be achieved via a redshift of the CL emission. The energy of cross-luminescence emission depends on the energy difference between the uppermost core band (composed of the p states of alkali or alkaline earth metal) and the valence band (composed mostly of the p state of the respective halide). Therefore, materials composed of light halides and heavy alkali metals are the most perspective for the redshift of cross-luminescence emission. For example, CsF exhibits cross-luminescence with a maximum at 400 nm [65] which is close to the PDE maximum of near-ultraviolet (NUV) HD SiPMs [66] reaching PDE up to 63 %. However, high hygroscopicity of CsF together with the complicated technology of fluoride single crystals growth hinders its application potential. Therefore, recent R&D of NUV cross-luminescence scintillators focused mostly on Cs containing ternary chlorides. Compositions including (Cs,Rb)CaCl<sub>3</sub> [67,68], Cs(Mg,Ca)Cl<sub>3</sub> [69], Cs<sub>2</sub>BaCl<sub>4</sub> [70], Cs<sub>2</sub>ZnCl<sub>4</sub> [71], and Cs<sub>3</sub>ZnCl<sub>5</sub> [71] were investigated. In [P7] we reported an extensive study of selected ternary chlorides of alkali metals and alkaline earth metals. Crystals (see fig. 18) from two composition groups were grown via mVB [P3] method: (Cs,Rb)MeCl<sub>3</sub> (Me = Mg, Ca, Sr) and A<sub>2</sub>BaCl<sub>4</sub> (A = K, Rb, Cs). All Cs containing crystals exhibit a two-band emission with maxima around 260 nm and 290 nm which we ascribed to cross-luminescence. This ascription is in agreement with values reported in the literature [61] and supported by measurements of scintillation decay kinetics.



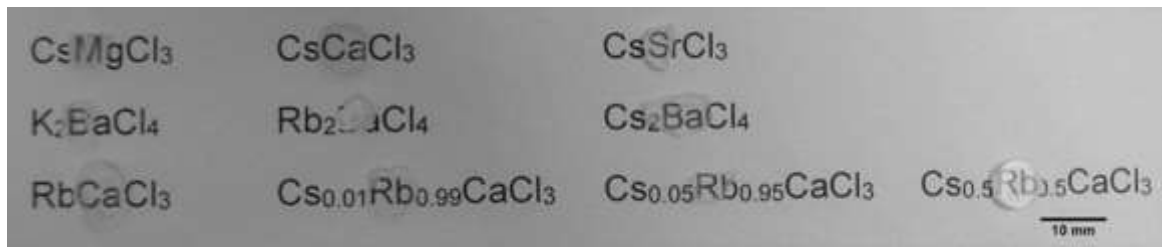


Fig. 18: Cut and polished samples from crystals of  $(\text{Cs,Rb})\text{MeCl}_3$  ( $\text{Me} = \text{Mg, Ca, Sr}$ ) and  $\text{A}_2\text{BaCl}_4$  ( $\text{A} = \text{K, Rb, Cs}$ ). Reproduced under terms of the CC-BY license [P7].

The radioluminescence spectra of  $\text{CsMeCl}_3$  samples (See fig. 19) showed cross-luminescence emission partially overlapped with emission bands at longer wavelengths. The emission bands at the long-wavelength region (approximately 350 – 750 nm) differ significantly in both shape and intensity among the  $\text{CsMeCl}_3$  samples. Those bands are most probably caused by exciton or defect-related emissions.

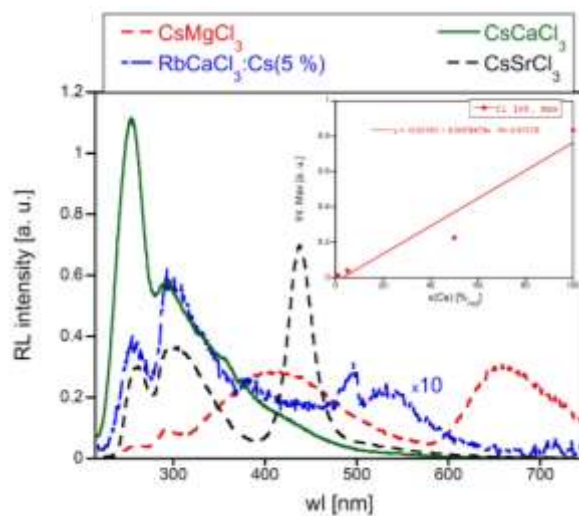


Fig. 19: RL spectra of  $(\text{Cs,Rb})\text{MeCl}_3$  ( $\text{Me} = \text{Mg, Ca, Sr}$ ) samples. The spectrum of  $\text{RbCaCl}_3:\text{Cs}$  (5 %) was multiplied by 10 for better clarity. Inset shows the dependence of the intensity of high energy CL band with Cs concentration. Reproduced under terms of the CC-BY license [P7].

The  $\text{CsCaCl}_3$  exhibits both the highest intensity of cross-luminescence and the lowest intensity of long wavelength emissions from the  $\text{CsMeCl}_3$  crystals. Therefore,  $\text{CsCaCl}_3$  was chosen for a detailed study of timing properties. The measurements of fast scintillation decay kinetics (see Fig. 20) revealed two main

components with decays of 150 ps (6.5 %) and 2.21 (94.5 %) ns and rise time below the resolution of the system (i. e.  $t_r < 50$  ps). Based on spectrally resolved scintillation decay measurements and comparison with values reported in the literature the 2.212 ns component was ascribed to cross-luminescence and the 151 ps component was ascribed to heavily quenched excitonic or defect-related emission. A 3x3x2 mm CsCaCl<sub>3</sub> sample exhibited a CTR of  $148 \pm 12$  ps. However, the measurement conditions were not optimal, because the CTR apparatus is not designed for the measurement of hygroscopic samples. Based on a comparison with BaF<sub>2</sub> measured under the same conditions it was estimated that CsCaCl<sub>3</sub> could achieve CTR below 50 ps. These results make the CsCaCl<sub>3</sub> a perspective candidate for fast timing applications. Moreover, it was shown that scintillation decay kinetics of CsCaCl<sub>3</sub> can be accelerated through quenching of cross-luminescence via Auger recombination in (Rb,Cs)CaCl<sub>3</sub> solid solution. However, it is achieved at the cost of lower radioluminescence intensity (See inset of Fig. 19).

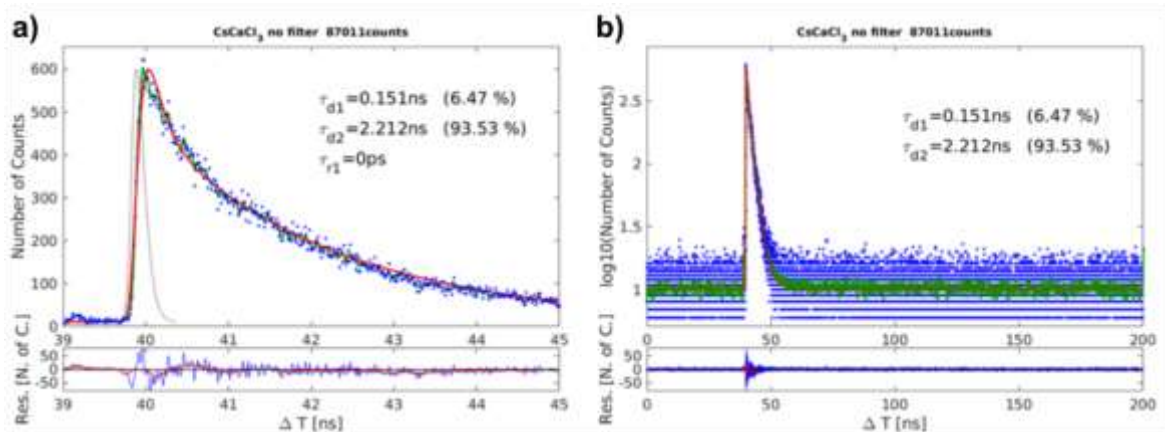


Fig. 20: Fast scintillation decay kinetics of CsCaCl<sub>3</sub> sample in a) short and b) long time window. Reproduced under terms of the CC-BY license [P7].

The radioluminescence spectra of the last composition group A<sub>2</sub>BaCl<sub>4</sub> reported in [P7] exhibit broadband emission centered at 400 nm. The cross-luminescence bands were observed only for the Cs<sub>2</sub>BaCl<sub>4</sub> which is in accordance with results reported in the literature [61]. However, Cs<sub>2</sub>BaCl<sub>4</sub> is not a perspective candidate for fast timing application due to the presence of slow components ( $\sim \mu\text{s}$ ) in the scintillation decay originating from the broad emission band centered at 400 nm and complicated crystal growth.

### 3. Conclusions

The work during my Ph.D. studies was focused on the research and development of novel single crystal scintillators based on complex halides. Such effort can be very time-consuming due to the necessity to prepare and study a large number of samples to cover a relevant compositional space of materials perspective for a specific application together with time requirements for the growth of high-quality single crystals. To overcome this obstacle, I have developed a method for time and cost-effective growth of halide single crystals via the vertical Bridgman method using micro-pulling-down apparatus. This method allowed me to perform extensive studies of materials of interest.

A significant effort was focused on the development of  $\text{Cs}_2\text{HfCl}_6$  based scintillators. The early work focused on the optimization of crystal growth technology including the purification of starting materials. Later on, the scintillation mechanism was investigated via correlation of several experimental techniques which resulted in the identification of trapping centers in  $\text{Cs}_2\text{HfCl}_6$  and  $\text{Cs}_2\text{ZrCl}_6$ . Moreover, the results suggested the important role of Zr impurity in the scintillation mechanism of  $\text{Cs}_2\text{HfCl}_6$ . The role of Zr was further investigated in a series of  $\text{Cs}_2\text{Hf}_{1-x}\text{Zr}_x\text{Cl}_6$  solid solution crystals. The results showed a possibility of significant afterglow suppression and spectral tunability in the  $\text{Cs}_2\text{Hf}_{1-x}\text{Zr}_x\text{Cl}_6$  solid solution.

The second main topic was the development of novel cross-luminescence scintillators for fast timing applications. The research was focused on the combinatorial investigation of cesium-containing halides. Through investigation of structural and optical properties, the  $\text{CsCaCl}_3$  emerged as the most perspective candidate. The further evaluation confirmed the potential of  $\text{CsCaCl}_3$  to surpass the timing properties of  $\text{BaF}_2$  and achieve coincidence time resolution below 50 ps. This shows the potential of cesium-containing cross-luminescence scintillators for fast timing applications.

I have used the knowledge in the field of halide scintillators, gathered during my Ph.D. studies, in writing the review paper "Advanced Halide Scintillators: From the Bulk to Nano".

## Literature - general

- [1] R.L. Leonard, J.A. Johnson, Scintillator Glasses, in: J.D. Musgraves, J. Hu, L. Calvez (Eds.), Springer Handbook of Glass, Springer International Publishing, Cham, 2019: pp. 1555–1584. [https://doi.org/10.1007/978-3-319-93728-1\\_46](https://doi.org/10.1007/978-3-319-93728-1_46).
- [2] G.F. Knoll, Radiation Detection and Measurement, John Wiley & Sons, 2010.
- [3] R. Hofstadter, Alkali Halide Scintillation Counters, Phys. Rev. 74 (1948) 100–101. <https://doi.org/10.1103/PhysRev.74.100>.
- [4] W. Van Sciver, R. Hofstadter, Scintillations in Thallium-Activated CaI<sub>2</sub> and CsI, Phys. Rev. 84 (1951) 1062–1063. <https://doi.org/10.1103/PhysRev.84.1062.2>.
- [5] R.H. Gillette, Calcium and Cadmium Tungstate as Scintillation Counter Crystals for Gamma-Ray Detection, Review of Scientific Instruments. 21 (1950) 294–301. <https://doi.org/10.1063/1.1745567>.
- [6] M. Nikl, A. Yoshikawa, Recent R&D Trends in Inorganic Single-Crystal Scintillator Materials for Radiation Detection, Advanced Optical Materials. 3 (2015) 463–481. <https://doi.org/10.1002/adom.201400571>.
- [7] C. Dujardin, E. Auffray, E. Bourret-Courchesne, P. Dorenbos, P. Lecoq, M. Nikl, A.N. Vasil'ev, A. Yoshikawa, R.-Y. Zhu, Needs, Trends, and Advances in Inorganic Scintillators, IEEE Transactions on Nuclear Science. 65 (2018) 1977–1997. <https://doi.org/10.1109/TNS.2018.2840160>.
- [8] D.J. Robbins, On Predicting the Maximum Efficiency of Phosphor Systems Excited by Ionizing Radiation, J. Electrochem. Soc. 127 (1980) 2694. <https://doi.org/10.1149/1.2129574>.
- [9] A. Lempicki, A.J. Wojtowicz, E. Berman, Fundamental limits of scintillator performance, Nuclear Instruments and Methods in Physics Research Section A: Accelerators, Spectrometers, Detectors and Associated Equipment. 333 (1993) 304–311. [https://doi.org/10.1016/0168-9002\(93\)91170-R](https://doi.org/10.1016/0168-9002(93)91170-R).
- [10] Qwerty123uiop, Schematic view of a photomultiplier coupled to a scintillator, illustrating detection of gamma rays, 2013. <https://commons.wikimedia.org/wiki/File:PhotoMultiplierTubeAndScintillator.svg> (accessed July 14, 2022).
- [11] P.W. Bridgman, Various Physical Properties of Rubidium and Caesium and the Resistance of Potassium under Pressure, Proceedings of the American Academy of Arts and Sciences. 60 (1925) 385–421. <https://doi.org/10.2307/25130061>.
- [12] D.C. Stockbarger, The Production of Large Single Crystals of Lithium Fluoride, Review of Scientific Instruments. 7 (1936) 133–136. <https://doi.org/10.1063/1.1752094>.
- [13] Cepheiden, Bridgman-Stockbarger Technique, 2018. <https://commons.wikimedia.org/wiki/File:Bridgman-Stockbarger-Technique.svg> (accessed July 14, 2022).

- [14] D.-H. Yoon, I. Yonenaga, T. Fukuda, N. Ohnishi, Crystal growth of dislocation-free LiNbO<sub>3</sub> single crystals by micro pulling down method, *Journal of Crystal Growth*. 142 (1994) 339–343. [https://doi.org/10.1016/0022-0248\(94\)90342-5](https://doi.org/10.1016/0022-0248(94)90342-5).
- [15] K. Oikawa, R. Saito, K. Anzai, H. Ishikawa, Y. Sutou, T. Omori, A. Yoshikawa, V.A. Chernenko, S. Besseghini, A. Gambardella, R. Kainuma, K. Ishida, Elastic and Superelastic Properties of NiFeCoGa Fibers Grown by Micro-Pulling-Down Method, *Mater. Trans.* 50 (2009) 934–937. <https://doi.org/10.2320/matertrans.M2009013>.
- [16] S. Uda, J. Kon, K. Shimamura, T. Fukuda, Analysis of Ge distribution in Si<sub>1-x</sub>Gex single crystal fibers by the micro-pulling down method, *J. Cryst. Growth*. 167 (1996) 64–73. [https://doi.org/10.1016/0022-0248\(96\)00237-0](https://doi.org/10.1016/0022-0248(96)00237-0).
- [17] A.M.E. Santo, B.M. Epelbaum, S.P. Morato, N.D. Vieira, S.L. Baldochi, Growth and characterization of LiF single-crystal fibers by the micro-pulling-down method, *J. Cryst. Growth*. 270 (2004) 121–123. <https://doi.org/10.1016/j.jcrysgro.2004.05.110>.
- [18] T. Fukuda, V.I. Chani, *Shaped crystals: micro-pulling-down technique and growth*, Springer, Berlin ; New York, 2007.
- [19] A.R. Reinberg, S.G. Parker, Sharp-Line Luminescence of Re 4 + in Cubic Single Crystals of Cs<sub>2</sub>ZrCl<sub>6</sub> and Cs<sub>2</sub>HfCl<sub>6</sub>, *Phys. Rev. B*. 1 (1970) 2085–2088. <https://doi.org/10.1103/PhysRevB.1.2085>.
- [20] A.R. Reinberg, Sharp-Line Luminescence from Os 4 + and Mo 3 + in Cs<sub>2</sub>HfCl<sub>6</sub>, *Phys. Rev. B*. 3 (1971) 41–46. <https://doi.org/10.1103/PhysRevB.3.41>.
- [21] S. Maniv, W. Low, A. Gabay, EPR spectrum of W<sup>5+</sup> in single crystals of Cs<sub>2</sub>ZrCl<sub>6</sub> and Cs<sub>2</sub>HfCl<sub>6</sub>, *Journal of Physics and Chemistry of Solids*. 32 (1971) 815–817. [https://doi.org/10.1016/0022-3697\(71\)90044-8](https://doi.org/10.1016/0022-3697(71)90044-8).
- [22] S. Maniv, W. Low, A. Gabay, EPR sites of molybdenum ions in single crystals of Cs<sub>2</sub>HfCl<sub>6</sub> and Cs<sub>2</sub>ZrCl<sub>6</sub>, *Journal of Physics and Chemistry of Solids*. 35 (1974) 373–381. [https://doi.org/10.1016/S0022-3697\(74\)80030-2](https://doi.org/10.1016/S0022-3697(74)80030-2).
- [23] S. Maniv, Crystal data for Cs<sub>2</sub>HfCl<sub>6</sub>, *Journal of Applied Crystallography*. 9 (1976) 245. <https://doi.org/10.1107/S0021889876011114>.
- [24] D.A. Asvestas, P. Pint, S.N. Flengas, Some thermodynamic properties of the solutions of ZrCl<sub>4</sub> and HfCl<sub>4</sub> in CsCl melts, *Can. J. Chem.* 55 (1977) 1154–1166. <https://doi.org/10.1139/v77-162>.
- [25] J.F. Ackerman, Preparation and luminescence of some [K<sub>2</sub>PtCl<sub>6</sub>] materials, *Materials Research Bulletin*. 19 (1984) 783–791. [https://doi.org/10.1016/0025-5408\(84\)90036-9](https://doi.org/10.1016/0025-5408(84)90036-9).
- [26] P.S. Bryan, S.A. Ferranti, Luminescence of Cs<sub>2</sub>ZrCl<sub>6</sub> and Cs<sub>2</sub>HfCl<sub>6</sub>, *Journal of Luminescence*. 31–32 (1984) 117–119. [https://doi.org/10.1016/0022-2313\(84\)90220-5](https://doi.org/10.1016/0022-2313(84)90220-5).
- [27] A. Burger, E. Rowe, M. Groza, K. Morales Figueroa, N.J. Cherepy, P.R. Beck, S. Hunter, S.A. Payne, Cesium hafnium chloride: A high light yield, non-hygroscopic cubic crystal scintillator for gamma spectroscopy, *Appl. Phys. Lett.* 107 (2015) 143505. <https://doi.org/10.1063/1.4932570>.

- [28] E.A. Kravchenko, V.G. Morgunov, Z.B. Mukhametshina, V.V. Chibrikin, G.A. Yagodin, Temperature Dependence of NQR Spectra and Phase Transitions in Alkali Metal Hexaiodozirconates and Hafnates (IV), *Zeitschrift Für Naturforschung A*. 41 (1986) 294–298. <https://doi.org/10.1515/zna-1986-1-254>.
- [29] K. Saeki, Y. Wakai, Y. Fujimoto, M. Koshimizu, T. Yanagida, D. Nakauchi, K. Asai, Luminescence and scintillation properties of Rb<sub>2</sub>HfCl<sub>6</sub> crystals, *Jpn. J. Appl. Phys.* 55 (2016) 110311. <https://doi.org/10.7567/JJAP.55.110311>.
- [30] S. Lam, C. Gugushev, A. Burger, M. Hackett, S. Motakef, Crystal growth and scintillation performance of Cs<sub>2</sub>HfCl<sub>6</sub> and Cs<sub>2</sub>HfCl<sub>4</sub>Br<sub>2</sub>, *Journal of Crystal Growth*. 483 (2018) 121–124. <https://doi.org/10.1016/j.jcrysgro.2017.11.013>.
- [31] K. Saeki, Y. Fujimoto, M. Koshimizu, T. Yanagida, K. Asai, Comparative study of scintillation properties of Cs<sub>2</sub>HfCl<sub>6</sub> and Cs<sub>2</sub>ZrCl<sub>6</sub>, *Appl. Phys. Express*. 9 (2016) 042602. <https://doi.org/10.7567/APEX.9.042602>.
- [32] P.Q. Vuong, M. Tyagi, S.H. Kim, H.J. Kim, Crystal growth of a novel and efficient Ti<sub>2</sub>HfCl<sub>6</sub> scintillator with improved scintillation characteristics, *CrystEngComm*. 21 (2019) 5898–5904. <https://doi.org/10.1039/C9CE01202H>.
- [33] R. Hawrami, E. Ariesanti, V. Buliga, A. Burger, S. Lam, S. Motakef, Ti<sub>2</sub>HfCl<sub>6</sub> and Ti<sub>2</sub>ZrCl<sub>6</sub>: Intrinsic Ti-, Hf-, and Zr-based scintillators, *Journal of Crystal Growth*. 531 (2020) 125316. <https://doi.org/10.1016/j.jcrysgro.2019.125316>.
- [34] P.Q. Vuong, H. Kim, H. Park, G. Rooh, S. Kim, Pulse shape discrimination study with Ti<sub>2</sub>ZrCl<sub>6</sub> crystal scintillator, *Radiation Measurements*. 123 (2019) 83–87. <https://doi.org/10.1016/j.radmeas.2019.02.007>.
- [35] K. Saeki, Y. Fujimoto, M. Koshimizu, D. Nakauchi, H. Tanaka, T. Yanagida, K. Asai, Luminescence and scintillation properties of Cs<sub>2</sub>HfBr<sub>6</sub> and Cs<sub>2</sub>ZrBr<sub>6</sub> crystals, *Jpn. J. Appl. Phys.* 57 (2018) 030310. <https://doi.org/10.7567/JJAP.57.030310>.
- [36] S. Kodama, S. Kurosawa, Y. Morishita, H. Usami, T. Torii, M. Hayashi, M. Sasano, T. Azuma, H. Tanaka, V. Kochurikhin, J. Pejchal, R. Kral, M. Yoshino, A. Yamaji, S. Toyoda, H. Sato, Y. Ohashi, Y. Yokota, K. Kamada, M. Nikl, A. Yoshikawa, Growth and Scintillation Properties of a New Red-Emitting Scintillator Rb<sub>2</sub>HfI<sub>6</sub> for the Fiber-Reading Radiation Monitor, *IEEE Trans. Nucl. Sci.* 67 (2020) 1055–1062. <https://doi.org/10.1109/TNS.2020.2976695>.
- [37] S. Kodama, S. Kurosawa, M. Ohno, A. Yamaji, M. Yoshino, J. Pejchal, R. Král, Y. Ohashi, K. Kamada, Y. Yokota, M. Nikl, A. Yoshikawa, Development of a novel red-emitting cesium hafnium iodide scintillator, *Radiation Measurements*. 124 (2019) 54–58. <https://doi.org/10.1016/j.radmeas.2019.03.005>.
- [38] S. Kodama, S. Kurosawa, M. Ohno, Y. Morishita, H. Usami, M. Hayashi, M. Sasano, T. Azuma, H. Tanaka, V. Kochurikhin, A. Yamaji, M. Yoshino, S. Toyoda, H. Sato, Y. Ohashi, K. Kamada, Y. Yokota, A. Yoshikawa, T. Torii, Fiber-read radiation monitoring system using an optical fiber and red-emitting scintillator for ultra-high-dose conditions, *Appl. Phys. Express*. 13 (2020) 047002. <https://doi.org/10.35848/1882-0786/ab77f7>.

- [39] E. Rowe, W.B. Goodwin, P. Bhattacharya, G. Cooper, N. Schley, M. Groza, N.J. Cherepy, S.A. Payne, A. Burger, Preparation, structure and scintillation of cesium hafnium chloride bromide crystals, *Journal of Crystal Growth*. 509 (2019) 124–128. <https://doi.org/10.1016/j.jcrysgro.2018.08.033>.
- [40] S. Kodama, S. Kurosawa, K. Fujii, T. Murakami, M. Yashima, J. Pejchal, R. Král, M. Nikl, A. Yamaji, M. Yoshino, S. Toyoda, H. Sato, Y. Ohashi, K. Kamada, Y. Yokota, A. Yoshikawa, Single-crystal growth, structure and luminescence properties of Cs<sub>2</sub>HfCl<sub>3</sub>Br<sub>3</sub>, *Optical Materials*. 106 (2020) 109942. <https://doi.org/10.1016/j.optmat.2020.109942>.
- [41] E. Ariesanti, R. Hawrami, A. Burger, S. Motakef, Improved growth and scintillation properties of intrinsic, non-hygroscopic scintillator Cs<sub>2</sub>HfCl<sub>6</sub>, *Journal of Luminescence*. 217 (2020) 116784. <https://doi.org/10.1016/j.jlumin.2019.116784>.
- [42] W. Wolszczak, K.W. Krämer, P. Dorenbos, CsBa<sub>2</sub>I<sub>5</sub>:Eu<sup>2+</sup>,Sm<sup>2+</sup>—The First High-Energy Resolution Black Scintillator for  $\gamma$ -Ray Spectroscopy, *Physica Status Solidi (RRL) – Rapid Research Letters*. 13 (2019) 1900158. <https://doi.org/10.1002/pssr.201900158>.
- [43] K. Saeki, Y. Fujimoto, M. Koshimizu, D. Nakauchi, H. Tanaka, T. Yanagida, K. Asai, Luminescence and scintillation properties of Tl- and Ce-doped Cs<sub>2</sub>HfCl<sub>6</sub> crystals, *Jpn. J. Appl. Phys.* 56 (2017) 020307. <https://doi.org/10.7567/JJAP.56.020307>.
- [44] S. Kodama, S. Kurosawa, A. Yamaji, J. Pejchal, R. Král, Y. Ohashi, K. Kamada, Y. Yokota, M. Nikl, A. Yoshikawa, Growth and luminescent properties of Ce and Eu doped Cesium Hafnium Iodide single crystalline scintillators, *Journal of Crystal Growth*. 492 (2018) 1–5. <https://doi.org/10.1016/j.jcrysgro.2018.03.033>.
- [45] S. Kodama, S. Kurosawa, J. Pejchal, R. Král, A. Yamaji, Y. Ohashi, Y. Yokota, K. Kamada, M. Nikl, A. Yoshikawa, Growth and Luminescent Properties of Cs<sub>2</sub>HfCl<sub>6</sub> Scintillators Doped With Alkaline Earth Metals, *IEEE Transactions on Nuclear Science*. 65 (2018) 2169–2173. <https://doi.org/10.1109/TNS.2018.2848474>.
- [46] Y. Fujimoto, K. Saeki, D. Nakauchi, H. Fukada, T. Yanagida, H. Kawamoto, M. Koshimizu, K. Asai, Photoluminescence, photoacoustic, and scintillation properties of Te<sup>4+</sup>-doped Cs<sub>2</sub>HfCl<sub>6</sub> crystals, *Materials Research Bulletin*. 105 (2018) 291–295. <https://doi.org/10.1016/j.materresbull.2018.04.050>.
- [47] C. Cardenas, A. Burger, B. Goodwin, M. Groza, M. Laubenstein, S. Nagorny, E. Rowe, Pulse-shape discrimination with Cs<sub>2</sub>HfCl<sub>6</sub> crystal scintillator, *Nuclear Instruments and Methods in Physics Research Section A: Accelerators, Spectrometers, Detectors and Associated Equipment*. 869 (2017) 63–67. <https://doi.org/10.1016/j.nima.2017.06.041>.
- [48] Q.V. Phan, H.J. Kim, G. Rooh, S.H. Kim, Tl<sub>2</sub>ZrCl<sub>6</sub> crystal: Efficient scintillator for X- and  $\gamma$ -ray spectroscopies, *Journal of Alloys and Compounds*. 766 (2018) 326–330. <https://doi.org/10.1016/j.jallcom.2018.06.349>.
- [49] C. Cardenas, A. Burger, M.L. DiVacri, B. Goodwin, M. Groza, M. Laubenstein, S. Nagorny, S. Nisi, E. Rowe, Internal contamination of the Cs<sub>2</sub>HfCl<sub>6</sub> crystal scintillator, *Nuclear Instruments and Methods in Physics Research Section A*:

- Accelerators, Spectrometers, Detectors and Associated Equipment. 872 (2017) 23–27. <https://doi.org/10.1016/j.nima.2017.08.006>.
- [50] V. Caracciolo, S.S. Nagorny, P. Belli, R. Bernabei, F. Cappella, R. Cerulli, A. Incicchitti, M. Laubenstein, V. Merlo, S. Nisi, P. Wang, Search for  $\alpha$  decay of naturally occurring Hf-nuclides using a Cs<sub>2</sub>HfCl<sub>6</sub> scintillator, Nuclear Physics A. 1002 (2020) 121941. <https://doi.org/10.1016/j.nuclphysa.2020.121941>.
- [51] S. Nagorny, Novel Cs<sub>2</sub>HfCl<sub>6</sub> Crystal Scintillator: Recent Progress and Perspectives, Physics. 3 (2021) 320–351. <https://doi.org/10.3390/physics3020023>.
- [52] A. Giuliani, A. Poves, Neutrinoless Double-Beta Decay, Advances in High Energy Physics. (n.d.) 39.
- [53] R. Hawrami, E. Ariesanti, V. Buliga, S. Motakef, A. Burger, Latest Progress on Advanced Bridgman Method-Grown K<sub>2</sub>PtCl<sub>6</sub> Cubic Structure Scintillator Crystals, IEEE Transactions on Nuclear Science. 67 (2020) 1020–1026. <https://doi.org/10.1109/TNS.2020.2971859>.
- [54] C. Delzer, M. Zhuravleva, L. Stand, C. Melcher, N. Cherepy, S. Payne, R. Sanner, J.P. Hayward, Observations regarding inclusions in the growth of Cs<sub>2</sub>HfCl<sub>6</sub> single crystal scintillators, Journal of Crystal Growth. 531 (2020) 125336. <https://doi.org/10.1016/j.jcrysgro.2019.125336>.
- [55] E. Barraud, S. Bégin-Colin, G. Le Caër, F. Villieras, O. Barres, Thermal decomposition of HfCl<sub>4</sub> as a function of its hydration state, Journal of Solid State Chemistry. 179 (2006) 1842–1851. <https://doi.org/10.1016/j.jssc.2006.02.027>.
- [56] R. Hawrami, E. Ariesanti, V. Buliga, L. Matei, S. Motakef, A. Burger, Advanced high-performance large diameter Cs<sub>2</sub>HfCl<sub>6</sub> (CHC) and mixed halides scintillator, Journal of Crystal Growth. 533 (2020) 125473. <https://doi.org/10.1016/j.jcrysgro.2019.125473>.
- [57] A.C. Lindsey, Y. Wu, M. Zhuravleva, M. Loyd, M. Koschan, C.L. Melcher, Multi-ampoule Bridgman growth of halide scintillator crystals using the self-seeding method, Journal of Crystal Growth. 470 (2017) 20–26. <https://doi.org/10.1016/j.jcrysgro.2017.03.038>.
- [58] By. Kang, K. Biswas, Carrier Self-trapping and Luminescence in Intrinsically Activated Scintillator: Cesium Hafnium Chloride (Cs<sub>2</sub>HfCl<sub>6</sub>), J. Phys. Chem. C. 120 (2016) 12187–12195. <https://doi.org/10.1021/acs.jpcc.6b02496>.
- [59] R. Král, V. Babin, E. Mihóková, M. Buryi, V.V. Laguta, K. Nitsch, M. Nikl, Luminescence and Charge Trapping in Cs<sub>2</sub>HfCl<sub>6</sub> Single Crystals: Optical and Magnetic Resonance Spectroscopy Study, J. Phys. Chem. C. 121 (2017) 12375–12382. <https://doi.org/10.1021/acs.jpcc.7b02327>.
- [60] N. ERSHOV, N. ZAKHAROV, P. RODNYI, SPECTRAL-KINETIC STUDY OF INTRINSIC LUMINESCENCE CHARACTERISTICS FOR A FLUORITE-TYPE CRYSTAL, OPTIKA I SPEKTROKOPIYA. 53 (1982) 89–93.
- [61] C.W.E. van Eijk, Cross-luminescence, Journal of Luminescence. 60–61 (1994) 936–941. [https://doi.org/10.1016/0022-2313\(94\)90316-6](https://doi.org/10.1016/0022-2313(94)90316-6).



- [62] D.W. Lee, L.C. Stonehill, A. Klimentko, J.R. Terry, S.R. Tornga, Pulse-shape analysis of Cs<sub>2</sub>LiYCl<sub>6</sub>:Ce scintillator for neutron and gamma-ray discrimination, *Nuclear Instruments and Methods in Physics Research Section A: Accelerators, Spectrometers, Detectors and Associated Equipment*. 664 (2012) 1–5. <https://doi.org/10.1016/j.nima.2011.10.013>.
- [63] P. Lecoq, C. Morel, J.O. Prior, D. Visvikis, S. Gundacker, E. Auffray, P. Križan, R.M. Turtos, D. Thers, E. Charbon, J. Varela, C. de La Taille, A. Rivetti, D. Breton, J.-F. Pratte, J. Nuyts, S. Surti, S. Vandenberghe, P. Marsden, K. Parodi, J.M. Benloch, M. Benoit, Roadmap toward the 10 ps time-of-flight PET challenge, *Phys. Med. Biol.* 65 (2020) 21RM01. <https://doi.org/10.1088/1361-6560/ab9500>.
- [64] S. Gundacker, R.H. Pots, A. Nepomnyashchikh, E. Radzhabov, R. Shendrik, S. Omelkov, M. Kirm, F. Acerbi, M. Capasso, G. Paternoster, A. Mazzi, A. Gola, J. Chen, E. Auffray, Vacuum ultraviolet silicon photomultipliers applied to BaF<sub>2</sub> cross-luminescence detection for high-rate ultrafast timing applications, *Phys. Med. Biol.* 66 (2021) 114002. <https://doi.org/10.1088/1361-6560/abf476>.
- [65] M. Moszyński, R. Allemand, M. Laval, R. Odru, J. Vacher, Recent progress in fast timing with CsF scintillators in application to time-of-flight positron tomography in medicine, *Nuclear Instruments and Methods in Physics Research*. 205 (1983) 239–249. [https://doi.org/10.1016/0167-5087\(83\)90194-1](https://doi.org/10.1016/0167-5087(83)90194-1).
- [66] A. Gola, F. Acerbi, M. Capasso, M. Marcante, A. Mazzi, G. Paternoster, C. Piemonte, V. Regazzoni, N. Zorzi, NUV-Sensitive Silicon Photomultiplier Technologies Developed at Fondazione Bruno Kessler, *Sensors*. 19 (2019) 308. <https://doi.org/10.3390/s19020308>.
- [67] M. Koshimizu, N. Yahaba, R. Haruki, F. Nishikido, S. Kishimoto, K. Asai, Scintillation and luminescence properties of a single CsCaCl<sub>3</sub> crystal, *Optical Materials*. 36 (2014) 1930–1933. <https://doi.org/10.1016/j.optmat.2014.04.004>.
- [68] K. Takahashi, M. Koshimizu, Y. Fujimoto, T. Yanagida, K. Asai, Auger-free luminescence characteristics of Rb<sub>1-x</sub>Cs<sub>x</sub>CaCl<sub>3</sub>, *J. Ceram. Soc. Japan*. 126 (2018) 755–760. <https://doi.org/10.2109/jcersj2.18051>.
- [69] K. Takahashi, M. Koshimizu, Y. Fujimoto, T. Yanagida, K. Asai, Auger-free luminescence characteristics of Cs(Ca 1 - x Mg<sub>x</sub>)Cl<sub>3</sub>, *Nuclear Instruments and Methods in Physics Research Section A: Accelerators, Spectrometers, Detectors and Associated Equipment*. 954 (2020) 161842. <https://doi.org/10.1016/j.nima.2019.01.068>.
- [70] K. Takahashi, M. Arai, M. Koshimizu, Y. Fujimoto, T. Yanagida, K. Asai, Luminescence characteristics of Cs<sub>2</sub>BaCl<sub>4</sub>, *Jpn. J. Appl. Phys.* 59 (2020) 032003. <https://doi.org/10.35848/1347-4065/ab762b>.
- [71] K. Takahashi, M. Arai, M. Koshimizu, Y. Fujimoto, T. Yanagida, K. Asai, Luminescence and scintillation properties of Cs<sub>2</sub>ZnCl<sub>4</sub> and Cs<sub>3</sub>ZnCl<sub>5</sub>, *Jpn. J. Appl. Phys.* 59 (2020) 072002. <https://doi.org/10.35848/1347-4065/ab9655>.

## Literature - commented author's paper selection

- [P1] V. Vaněček, K. Děcká, E. Mihóková, V. Čuba, R. Král, M. Nikl, Advanced Halide Scintillators: From the Bulk to Nano, *Advanced Photonics Research*. n/a (2022) 2200011. <https://doi.org/10.1002/adpr.202200011>.
- [P2] M. Buryi, R. Král, V. Babin, J. Páterek, V. Vaněček, P. Veverka, M. Kohoutková, V. Laguta, M. Fasoli, I. Villa, F. Cova, A. Vedda, M. Nikl, Trapping and Recombination Centers in Cesium Hafnium Chloride Single Crystals: EPR and TSL Study, *J. Phys. Chem. C*. (2019) acs.jpcc.9b05760. <https://doi.org/10.1021/acs.jpcc.9b05760>.
- [P3] V. Vanecek, R. Kral, J. Paterrek, V. Babin, V. Jary, J. Hybler, S. Kodama, S. Kurosawa, Y. Yokota, A. Yoshikawa, M. Nikl, Modified vertical Bridgman method: Time and cost effective tool for preparation of Cs<sub>2</sub>HfCl<sub>6</sub> single crystals, *Journal of Crystal Growth*. 533 (2020) 125479. <https://doi.org/10.1016/j.jcrysgr.2020.125479>.
- [P4] V. Vaněček, J. Páterek, R. Král, M. Buryi, V. Babin, K. Zloužeová, S. Kodama, S. Kurosawa, Y. Yokota, A. Yoshikawa, M. Nikl, Cs<sub>2</sub>HfCl<sub>6</sub> doped with Zr: Influence of tetravalent substitution on scintillation properties, *Journal of Crystal Growth*. 573 (2021) 126307. <https://doi.org/10.1016/j.jcrysgr.2021.126307>.
- [P5] R. Král, P. Zemenová, V. Vaněček, A. Bystřický, M. Kohoutková, V. Jarý, S. Kodama, S. Kurosawa, Y. Yokota, A. Yoshikawa, M. Nikl, Thermal analysis of cesium hafnium chloride using DSC–TG under vacuum, nitrogen atmosphere, and in enclosed system, *J Therm Anal Calorim*. 141 (2020) 1101–1107. <https://doi.org/10.1007/s10973-019-09087-7>.
- [P6] M. Buryi, V. Babin, R.A.M. Ligthart, S.S. Nagorny, V.B. Mikhailik, V. Vaněček, L.P. Prochazková, R. Kandel, V.V. Nahorna, P. Wang, Correlation of emission, scintillation and charge trapping properties in Cs<sub>2</sub>HfCl<sub>6</sub> and Cs<sub>2</sub>ZrCl<sub>6</sub> single crystals, *J. Mater. Chem. C*. 9 (2021) 2955–2968. <https://doi.org/10.1039/D0TC05482H>.

- [P7] V. Vaněček, J. Páterek, R. Král, R. Kučerková, V. Babin, J. Rohlíček, R. Cala', N. Kratochwil, E. Auffray, M. Nikl, (INVITED) Ultraviolet cross-luminescence in ternary chlorides of alkali and alkaline-earth metals, *Optical Materials: X.* 12 (2021) 100103. <https://doi.org/10.1016/j.omx.2021.100103>.

Reprints of commented author's paper selection

# Advanced Halide Scintillators: From the Bulk to Nano

Vojtěch Vaněček,\* Kateřina Děcká, Eva Mihóková, Václav Čuba, Robert Král, and Martin Nikl\*

Halide scintillators have been playing a crucial role in the detection of ionizing radiation since the discovery of scintillation in NaI:Tl in 1948. The discovery of NaI:Tl motivated the research and development (R&D) of halide scintillators, resulting in the development of CsI:Tl, CsI:Na, CaF<sub>2</sub>:Eu, etc. Later, the R&D shifted toward oxide materials due to their high mechanical and chemical stability, good scintillation properties, and relative ease of bulk single-crystal growth. However, the development in crystal growth technology allows for the growth of high-quality single crystals of hygroscopic and mechanically fragile materials including SrI<sub>2</sub> and LaBr<sub>3</sub>. Scintillators based on these materials exhibit excellent performance and push the limits of inorganic scintillators. These results motivate intense research of a large variety of halide-based scintillators. Moreover, materials based on lead halide perovskites find applications in the fields of photovoltaics, solid-state lighting, and lasers. The first studies show also the significant potential of lead halide perovskites as ultrafast scintillators in the form of nanocrystals. The purpose of this review is to summarize the R&D in the field of halide scintillators during the last decade and highlight perspectives for future development.

recently by needs of homeland security techniques to counterfight illicit traffic of radioisotope materials, explosives, and drugs, and to prevent the population from terrorist attacks. Last but not least, there are specific fields in the industry (defectoscopy, particle beam detection and diagnostics, geophysical and environmental applications, to name a few), the progress of which is also based on the R&D of tailored scintillators for each application. Such a broad variety of applications results in rich and specific demands on scintillation parameters in tailored material structures which explain a long-lasting R&D coming all the time with new issues to solve.

Scintillation material works as a transformer of high-energy photons, accelerated particles, or even neutrons into a bunch of UV/VIS/NIR photons (a flash of light), Figure 1, which are easily detectable by existing photodetectors (photomultipliers, semiconductor-based devices). The scintillation mechanism, that is, the physical

scheme behind this transformation process, consists of three consecutive stages, namely, the conversion, transfer, and luminescence, described in more detail in numerous existing reviews which are also focused on various application fields, material groups, or specific parameters.<sup>[1–6]</sup>

In the 1990s, R&D was focused mainly on oxide-based materials due to the development of PbWO<sub>4</sub> single crystals for high-energy physics and Ce-doped orthosilicates and perovskites for medical imaging. Around the beginning of the new millennium, attention has also been paid to new families of halide scintillators based on rare earth (RE) halides, see the study by Kramer et al.,<sup>[7]</sup> followed by the search for efficient and high-energy-resolution materials in Eu<sup>2+</sup>-doped bromides and iodides,<sup>[6]</sup> high-Z<sub>eff</sub> halide materials, the composition of which includes Hf<sup>[8]</sup> and Tl<sup>[9]</sup> elements, and the most recent extension of classical CsI scintillator toward ternary Cs–Cu–I compositions<sup>[10]</sup> with advanced characteristics. A survey of scintillation parameters of the bulk halide single crystals is summarized in Table S1, Supporting Information.


In addition to the bulk single-crystal form of these materials, microstructured halide materials in eutectic form with light-guiding property, nanocrystals (NCs), nanostructures, and nanocomposites were reported, which further enriched the halide scintillator material family. Probably, the most intense R&D in recent years is devoted to halide perovskites including especially the nanomorphological materials. Luminescence of

## 1. Introduction

Research and development (R&D) of solid-state scintillation materials has been an intense research topic in the past three decades. It was launched by the needs of high-energy physics at the beginning of 1990s which needed radiation-resistant materials for the new generation of accelerators (Large Hadron Collider in CERN) and further intensified by the search for heavy, fast, and efficient scintillators to be applied in medical imaging (CT, positron emission tomography [PET], SPECT) and most

V. Vaněček, K. Děcká, E. Mihóková, R. Král, M. Nikl  
FZU Institute of Physics  
Czech Academy of Sciences  
Cukrovarnicka 10, 16200 Prague, Czech Republic  
E-mail: vanecekv@fzu.cz; nikl@fzu.cz

V. Vaněček, K. Děcká, E. Mihóková, V. Čuba  
FNSPE  
Czech Technical University in Prague  
Brehova 7, 11000 Prague, Czech Republic

 The ORCID identification number(s) for the author(s) of this article can be found under <https://doi.org/10.1002/adpr.202200011>.

© 2022 The Authors. Advanced Photonics Research published by Wiley-VCH GmbH. This is an open access article under the terms of the Creative Commons Attribution License, which permits use, distribution and reproduction in any medium, provided the original work is properly cited.

DOI: 10.1002/adpr.202200011

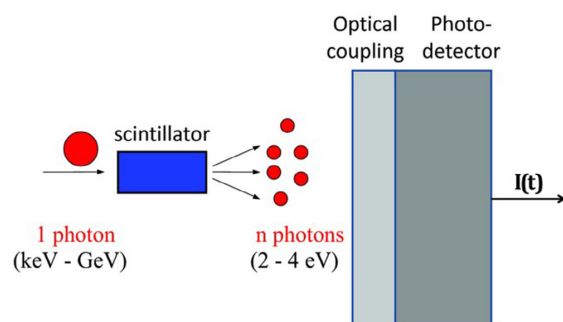


**Figure 1.** A sketch of the scintillation detector. Reproduced with permission.<sup>[5]</sup> Copyright 2021, John Wiley and Sons.

classical halide perovskites, CsPbX<sub>3</sub> (X = Cl, Br) single crystals prepared by the Bridgman method, was studied a few decades ago including the luminescence decay kinetics.<sup>[11,12]</sup> Even the luminescence of nanosized quantum dots (QDs) of these compounds was reported in the 1990s, spontaneously created after thermal annealing of Pb-doped CsX (X = Cl, Br) single crystals.<sup>[13,14]</sup> Their intrinsic emission is due to the Wannier exciton characterized by subnanosecond lifetimes and small Stokes shift of several tens of meV, which disables guiding the luminescence light out of bulk elements. Recently, a family of halide perovskites has emerged as an interesting class of semiconductors, highly promising for a variety of applications. Single crystals and polycrystalline thin films have been extensively investigated in photovoltaic cells and photodetectors thanks to their strong light absorption, high charge carrier mobility, and exceptional defect tolerance. However, resulting from mobile ionic defects and small exciton binding energy, their PL quantum yields (PLQYs) at room temperature (RT) are low, limiting thus their light-emitting applications.<sup>[15,16]</sup>

The way to significantly improve PLQY appears in the preparation of halide perovskites in the form of self-standing NCs (NCs), having higher exciton binding energy and lesser defects.

Nanostructured perovskite materials are of great interest due to multiple quantum-confinement effects. The most widely known perovskite NCs are the perovskite QDs which have sizes in the nanometer scale that are less than or close to the exciton Bohr radius. In terms of emission, perovskite QDs have a higher color purity, a wider color gamut, and lower cost of processing compared with traditional QDs.

Starting from the first reports on colloidal solutions of organic–inorganic (hybrid) perovskite NCs<sup>[17]</sup> and especially fully inorganic perovskite NCs,<sup>[18]</sup> immense research efforts have been devoted to the study and development of these materials. Due to their excellent luminescence properties, they became instantly identified as highly promising for a number of applications, such as solar cells,<sup>[19–23]</sup> photodetectors,<sup>[24–26]</sup> light-emitting diode (LEDs),<sup>[27–32]</sup> displays,<sup>[33–36]</sup> and lasers.<sup>[37–39]</sup> Recently, a body of studies on lead halide perovskites has also been focused on their application in scintillation detectors; see recent review papers.<sup>[40–43]</sup>

The aim of this review is to provide a broad overview in the field of halide scintillators studied in the past decade focusing on

material composition and its scintillation performance and also on new trends in nonsingle-crystal systems' R&D trying to explain the added value which they might bring if their manufacturing technology will advance enough.

## 2. Bulk Crystal Growth of Halide Materials

An important part of the R&D of halide scintillators is their preparation in the form of single crystals. Throughout history, various technologies and methods for crystal growth of halide materials have been developed. However, the hygroscopic nature of halides complicates the manufacturing process contributing to the formation of various oxidic impurities and thus influencing the behavior of halide's melt (e.g., wetting the growth container, cracking of crystal or the container) and degrading the final optical and physical properties of prepared scintillators. Generally, the hygroscopicity of halide salts is an ability to absorb moisture from ambient atmosphere,<sup>[44]</sup> depending on the temperature, relative humidity, and time of exposure.<sup>[45]</sup> The hygroscopicity of halide salts can be roughly estimated by the salt's solubility in water.<sup>[46]</sup>

The origin of oxidic impurities comes from reactions of halides with ambient atmosphere, moisture, and oxygen under the formation of, for example, hydrates, carbonates, hydroxy- and oxy-halides, and oxides.<sup>[44,46–49]</sup> Removal of such impurities is absolutely essential before the growth to prepare high-quality and pure single crystals. Thus, multiple techniques were developed to achieve such a goal consisting for instance of introduction of halogenation agents into molten halides,<sup>[46,48–50]</sup> implementation of vacuum to the raw material in a container under thermal treatment,<sup>[51–53]</sup> application of zone refining,<sup>[54–56]</sup> or their combination.<sup>[47,50]</sup>

Interestingly, the technology of introducing halogenation agents into molten halides was independently developed and presented in similar period in 1960s' and 1970s' by Lebl and Trnka,<sup>[48]</sup> Rosenberger,<sup>[46]</sup> and Kanzaki and Sakuragi.<sup>[57]</sup> Generally, the process is based on the multiple step reactions of various reagents such as hydrogen halides (HCl, HBr),<sup>[46,48,56]</sup> halogens (Cl<sub>2</sub>, Br<sub>2</sub>, I<sub>2</sub>),<sup>[46,48]</sup> organic halides (e.g., COCl<sub>2</sub>, CCl<sub>4</sub>, CHCl<sub>3</sub>),<sup>[48]</sup> silicon tetrachloride,<sup>[49]</sup> and others, with oxidic impurities in molten halides and their replacements with the required halide anion. Other purification techniques may be used as well such as 1) filtration of solutions as a basic removal of insoluble particles; 2) extraction of certain constituents based on preferential dissolution in a solvent; 3) liquid–liquid extraction based on the distribution of a solute (i.e., impurity in a dissolved matrix) between two essentially immiscible solvents; 4) ion exchange by running a solution through an inert tube filled with a resin enabling cationic separation in alkali halide solutions, as well as 5) precipitation of insoluble compounds from certain constituents in a solution by introduction of a selectively reacting agent. For more details, see the study by Rosenberger.<sup>[46]</sup>

The most widely used technique for bulk crystal growth of halides from their melt is the vertical Bridgman (VB) method. This technique was developed by Bridgman and published in 1925<sup>[58]</sup> belonging into a group of directional solidification methods. It is based on placing a container (crucible or ampoule) with the raw material into a tubular vertical furnace heated above the melting point of the material. Afterward, the container is pulled down out

of the furnace, where solidification appears. Further, a very important modification was suggested by Stockbarger<sup>[59]</sup> for the growth of LiF using two independently heated tubular and vertically arranged furnaces separated with an annular baffle. The upper furnace (or a so-called zone) was heated above the material's melting point and the lower one below creating a well-defined temperature gradient between them. The growth itself proceeded similarly by lowering the container with molten LiF from the upper furnace through the gradient into the lower furnace. Such a technique with minor changes (e.g., number of furnaces/zones, heating elements, etc.) is used up to now and it is most commonly referred to as the VB–Stockbarger method or simply the Bridgman method. Recently, the design of the technique was adjusted for simultaneous multiple-ampoule growth of  $\text{KCaI}_3$  using the so-called multiampoule growth station (MAGS).<sup>[60,61]</sup> Such multiampoule furnace designs incorporating an inductively or resistively heated crucible for growth of GaAs as well as fluoride-based materials have been proposed for instance in other studies.<sup>[62,63]</sup> Importantly, the Bridgman technique enables to select the type of the container used for the growth procedure. Depending on the properties of the grown material (such as melting point, reactivity, hygroscopicity, etc.), the container can be either opened, for example, alumina, platinum, graphite crucible, or closed, for example, sealed quartz ampoule. However, only the latter one is perfectly suitable for growth of hygroscopic halides as it prevents any contact with ambient atmosphere. In this way, various single crystals of halide scintillators were prepared, for instance,  $\text{NaI:Tl}$ ,<sup>[64]</sup>  $\text{SrI}_2\text{:Eu}$ ,<sup>[51,65,66]</sup>  $\text{LaBr}_3\text{:Ce}$ , and<sup>[67,68]</sup> various ternary and mixed halides and eutectics:  ${}^6\text{LiCl}/{}^6\text{Li}_2\text{SrCl}_4$ ,<sup>[69]</sup>  $\text{Tl}_2\text{LaCl}_5\text{:Ce}$ ,<sup>[70]</sup>  $\text{KSr}_2\text{I}_5\text{:Eu}$ ,<sup>[71]</sup>  $\text{Cs}_2\text{HfCl}_6$ ,<sup>[8,72,73]</sup>  $\text{Cs}_3\text{Cu}_2\text{I}_5$ ,<sup>[53,74]</sup>  $\text{Ba}_2\text{CsI}_5\text{:Eu}$ ,<sup>[75]</sup>  $\text{BaBrI:Eu}$ .<sup>[76]</sup>

The Czochralski (CZ) method is another crystal growth technique widely used in the R&D and commercial production of large-sized single crystals. It was developed by J. CZ in 1918<sup>[77]</sup> and since then it was applied for the production of various single crystals such as semiconductors (Si, Ge),<sup>[78]</sup> sapphire,<sup>[79]</sup> multicomponent oxides (YAG:Ce, GGAG:Ce),<sup>[80,81]</sup> and many others. Originally, the method was invented for measuring the crystallization velocity of metals by preparing them in the form of single-crystalline wires.<sup>[77,82]</sup> However, significant improvements based on the CZ method to produce controlled bulk semiconductor single crystals of germanium were proposed by Teal and Little.<sup>[83,84]</sup> Since then, the method remained unchanged with minor modifications until today. In summary, the CZ technique consists of placing a starting charge into a crucible (e.g., metals, ceramics, graphite, etc.), heating it above its melting point, tipping the melt with a seed (e.g., parent material, metal wire, etc.) from above, and slowly pulling the seed up again and rotating it, while crystallization takes place and the new crystalline phase is grown at the melt's surface. Even if this method was discovered about 100 years ago, its application for the growth of halide crystals was introduced only recently. Apart from using an air-tight CZ system, the procedure requires additional modifications due to hygroscopicity of halides such as baking of the growth chamber prior to the experiment or treating it by a high-purity carrier gas (e.g., Ar) through a molecular sieve; for more details, see, e.g., an article related to the preparation of mixed halides  $\text{BaBrCl}$  and  $\text{BaBrCl:Eu}$ .<sup>[85]</sup> A similar procedure was applied in the case of  $\text{PbI}_2$ ,<sup>[86]</sup> eutectics  $\text{CsI/CsCl/NaCl}$ ,<sup>[87]</sup>

or halides with higher hygroscopicity such as  $\text{CsCe}_2\text{Cl}_7$ ,  $\text{Cs}_2\text{NaCeCl}_6$ ,<sup>[88]</sup> and  $\text{SrI}_2\text{:Eu}$ .<sup>[89]</sup>

The Kyropoulos method is a growth technique derived from the CZ technique and is up to now frequently used for industrial production of large-sized single crystals. It was developed by Kyropoulos<sup>[90]</sup> and it is based on a similar arrangement as in the CZ method, that is, a crucible with starting charge is heated above its melting point, seed touched at its surface from above, and afterward the crystal growth is commenced. However, the growth is conducted with following differences from the CZ method<sup>[91]</sup>: 1) complete crystallization of the melt in the crucible is carried out; 2) the final shape of the crystal is defined by the shape of the crucible; 3) the seed is water cooled; 4) rotation of the seed takes part only at the beginning of the growth; 5) a slow pulling of the seed up is performed only at the initial part of the growth followed by controlled cooling of the system; and 6) pulling is stopped when the crystal reaches bottom of the crucible. In this way, the single crystals of various sizes (small to large) of semiconductors, for example,  $\text{ZnTe}$ ,<sup>[92]</sup> sapphire,<sup>[93]</sup> including halides such as  $\text{CsBr}$  (9 inch diam.),<sup>[94]</sup>  $\text{KX:Cu}$  ( $\text{X} = \text{Cl, Br, I}$ ),<sup>[95]</sup> or  $\text{LiF}$ ,<sup>[96]</sup> were prepared.

The edge-defined film-fed growth or simply edge-defined film-fed growth (EFG) method is a technique developed by H. LaBelle<sup>[97]</sup> for the growth of sapphire fibers used as reinforcements in metal matrix composites. This technique is similar to the CZ method as it is based on melting the starting charge in a crucible and placing a floating capillary die (made of e.g., refractory metal, carbon, etc.) with multiple channels on the melt's surface. Then, the melt is brought to the top of the die by capillary forces, where it is often spread over the die. Afterward, a seed touch is performed and the seed is pulled up. The crystal/melt interface is stabilized at the die and fed by a thin film of the melt coming out of the capillaries. Due to the melt's wetting of the die toward its edge, the final shape of the crystal is defined by the shape of the die.<sup>[91]</sup> Thus, EFG is a suitable and widely used technique for the production of shaped crystals (e.g., tubes, rods – circular or rectangular, sheets, etc.) of various materials (dielectric, semiconductors, etc.) of different sizes. Nevertheless, the origin of a shaped crystal growth can be tracked even to earlier times to Stepanov,<sup>[98]</sup> who suggested a similar technological approach. The differences between EFG and Stepanov method, as mentioned by LaBelle,<sup>[99]</sup> can be simplified to that the EFG process must use a wettable die and the Stepanov technique generally uses a nonwetted shaper. This is not entirely true as the key to Stepanov's technique is shaping a melt column in the die, which also defines the final shape of the grown crystal. On the contrary, in EFG the shape of the die controls the shape of the crystal.<sup>[99]</sup> Apart from the growth of sapphire fibers,<sup>[97,99]</sup> and for instance of  $\text{Mn}_2\text{SiO}_4$ ,<sup>[100]</sup> EFG was used for the growth of halide materials such as mixed ternary  $\text{CsSr}_{1-x}\text{Eu}_x\text{I}_3$ ,<sup>[101]</sup> eutectics (e.g.,  $\text{NaCl-LiF}$ ,  $\text{LiF-NaF}$ ),<sup>[102]</sup>  $\text{SrI}_2$ ,<sup>[103,104]</sup>  $\text{TlBr}$ ,<sup>[105]</sup> or  $\text{CsI}$ .<sup>[106,107]</sup>

The micropulling-down method ( $\mu\text{-PD}$ ) is a modern technique proposed by Ohnishi et al.<sup>[108]</sup> for fiber crystal growth of  $\text{LiNbO}_3$ . Afterward, the technique was adjusted for the growth of different materials such as mixed  $\text{Si-Ge}$ ,<sup>[109]</sup>  $\text{PbWO}_4$ ,<sup>[110]</sup> multicomponent garnets,<sup>[111,112]</sup>  $\text{LiF}$ ,<sup>[113]</sup> or metals and alloys.<sup>[114]</sup> In the case of hygroscopic halides, an important modification of  $\mu\text{-PD}$  was reported by Yokota et al.<sup>[115]</sup> for the growth of  $\text{NaCl:Ce,Pr}$ .

The method was modified and equipped with a removable growth chamber enabling its transport from the apparatus into an oxygen and moisture-free atmosphere-controlled glovebox, where a setup of a hotzone, weighing of starting materials, and other handling procedures were performed. The growth itself was performed after the transport of the chamber back to the  $\mu$ -PD apparatus in a similar way as for other materials mentioned earlier. The starting charge, placed in a crucible with a hole in its bottom, was heated above its melting point, touched with a seed from underneath (e.g., Pt wire), see Figure 2a, and pulled down below the crucible, where crystallization took place. Since then  $\mu$ -PD was used for growth of, for example,  $\text{SrI}_2:\text{Eu}$ ,<sup>[116]</sup>  $\text{CeCl}_3$ , and  $\text{LaBr}_3:\text{Ce}$ ,<sup>[117]</sup> or ternary  $\text{RbPb}_2\text{Cl}_5:\text{RE}$ <sup>[118]</sup>. Due to high pulling rates ( $0.03\text{--}1.0\text{ mm min}^{-1}$ ), low starting charges (up to 1 g), short experimental time (1–3 days), the  $\mu$ -PD technique is ideal for an initial R&D and materials screening as it is significantly more cost effective than traditional growth techniques (VB, CZ, etc.). Recently, reports about modifications of  $\mu$ -PD to grow halide crystals via the VB method of, for example,  $\text{Eu}:\text{SrI}_2$ <sup>[119]</sup> or  $\text{Cs}_2\text{HfCl}_6$ <sup>[120,121]</sup> were presented. This is the so-called miniaturized VB method (mVB), see Figure 2b. Such a setup combines advantages of both  $\mu$ -PD and Bridgman methods, that is, fast experiment and cost effectivity and closed container using sealed ampoules, respectively.

Vertical gradient freeze method (VFG) is derived from the Bridgman technique by assembling a dynamically controlled multiple-zone furnace. The crystal growth is then performed by moving a thermal gradient through the container with the material instead of any mechanical translation mechanism of the container or the crystal like in the traditional methods (e.g., VB or CZ).<sup>[122]</sup> Such a setup minimizes thermal stress generation of dislocations using low thermal gradients, low growth rates, and controlling postsolidification cooling rates below the yield point for the stress-induced dislocation generation.<sup>[123]</sup> Initially, this technique was used for crystal growth of semiconductors and many publications were devoted to CdTe applying both the vertical<sup>[124]</sup> and horizontal<sup>[125]</sup> arrangements. On the contrary, the reports on the vertical gradient freeze (VGF) growth

of halide crystals were limited to few publications regarding preparation of  $\text{KGd}_2\text{Cl}_7:\text{Ce}$ ,<sup>[126]</sup>  $\text{Cs}_3\text{EuI}_5$ ,<sup>[127]</sup> and  $\text{CsI}:\text{Tl}$ .<sup>[128]</sup>

The skull method is another technique belonging to the directional solidification ones developed in 1960s.<sup>[129–131]</sup> It is based on melting a material with inductive heating (contact-free) and keeping it in a cooled solid shell (skull) from the parent material, that is, with a chemical composition identical to that of the melt. Thus, such a method provides following advantages: no limit on the heating temperature (up to  $3000\text{ }^\circ\text{C}$  and higher), variability of the growth atmosphere (including an oxidizing one), growth of large-sized crystals, crystallization conducted by moving an inductive heat source or gradual reduction of power, and waste-free method (possibility of remelting unused scraps), for more details see the study by Osiko.<sup>[130]</sup> The method was widely used for purification and growth of refractory semiconductors and metals (e.g., Ge, Si, Zr),<sup>[132,133]</sup> growth of multicomponent oxides  $(\text{ZrO}_2)_{0.89}(\text{Sc}_2\text{O}_3)_{0.1}(\text{CeO}_2)_{0.01}$  crystals,<sup>[134]</sup> as well as halide crystals such as large-sized  $\text{NaI}:\text{Tl}$ .<sup>[135,136]</sup>

### 3. Divalent Rare-Earth-Activated High LY and ER Halide Scintillators

In the last decade, there was an intense R&D of the  $\text{Eu}^{2+}$ -activated scintillators to discover a scintillator with an ultimate light yield (LY) and energy resolution (ER) mainly for the nuclear nonproliferation applications. Fewer reports also deal with the  $\text{Yb}^{2+}$ - and  $\text{Sm}^{2+}$ -doped halides. All these centers' luminescence is based on the  $5d\text{--}4f$  transitions. In the case of  $\text{Yb}^{2+}$ , given its electronic configuration in the  $4f$  shell, the spin-allowed (low spin: LS) and spin-forbidden (high spin: HS) transitions can be resolved in the excitation and emission spectra in which the HS-related ones are always low energy shifted compared with LS ones; see the study by Dorenbos et al.<sup>[137]</sup> The lifetimes of HS-based emissions are of the order of tenths of ms, while those related to LS ones are about two orders of magnitude faster; see systematic reports made on the  $\text{Yb}^{2+}$ -doped  $\text{CsCaX}_3$  and  $\text{CsSrX}_3$  ( $X = \text{Cl, Br, and I}$ ).<sup>[138–140]</sup> The decay times of LS-based transitions are strongly temperature dependent and appear as a result of a delicate interplay of symmetry and also nonradiative relaxation pathways interconnecting the excited HS and ground states of the  $\text{Yb}^{2+}$  center. In the case of  $\text{Sm}^{2+}$ , instead, the interplay of the  $5d^1\text{--}4f$  emission transition and  ${}^7F_{0,1} \rightarrow D_{0,1}$  absorption lines can change the emission pattern considerably depending on the temperature, crystal field strength, and splitting.<sup>[141]</sup> The configurational coordinate diagram of  $\text{Sm}^{2+}$  in  $\text{BaBrI}$  is depicted in Figure 3, showing the thermal repopulation between  $4f$  and  $5d$  levels of  $\text{Sm}^{2+}$ , which can result in either the fast  $5d \rightarrow 4f$  or slow  $4f \rightarrow 4f$  emissions. The reason for using the  $\text{Sm}^{2+}$  dopant consists of lower energy of its  $5d\text{--}4f$  transitions, situated in the red/near-infrared spectral region, in the same host when compared with  $\text{Eu}^{2+}$  or  $\text{Yb}^{2+}$ ,<sup>[137]</sup> which enables efficient use of semiconductor detectors. Most of the research was focused on the exploration of the compositional space formed by ternary halides of alkali and alkaline earth metals, that is,  $A_x^+ B_y^{2+} X_{x+2y}^-$  (where  $A$  stands for an alkali metal or thallium,  $B$  for alkaline earth metal, and  $X$  for halogen). Alkaline earth metals are isovalent with  $\text{Eu}^{2+}$  ( $\text{Yb}^{2+}$ ,  $\text{Sm}^{2+}$ ) and have similar ionic radii (1.00, 1.18, 1.35, and  $1.17\text{ \AA}$  for  $\text{Ca}^{2+}$ ,  $\text{Sr}^{2+}$ ,  $\text{Ba}^{2+}$ , and  $\text{Eu}^{2+}$ , respectively, in VI

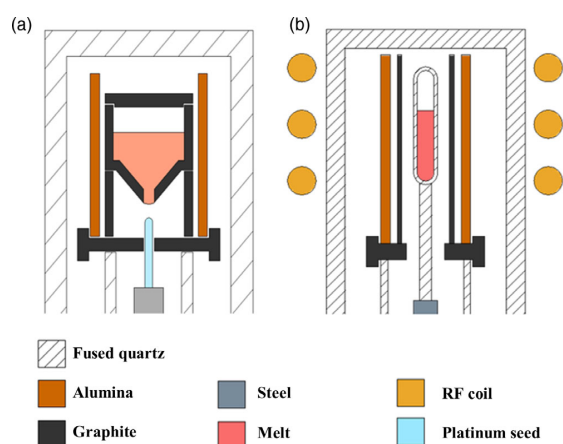
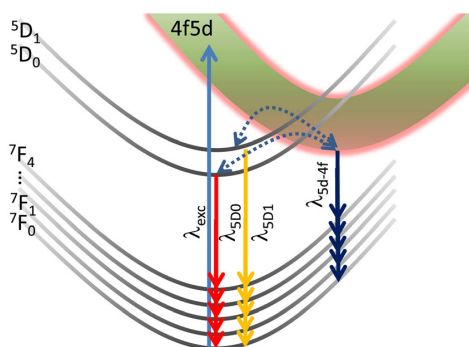


Figure 2. Scheme of halide crystal growth by a)  $\mu$ -PD and b) mVB methods.





**Figure 3.** Configurational coordinate diagram of  $\text{Sm}^{2+}$  in BaBrI. Solid arrows indicate radiative and dotted arrows non-radiative processes. Reproduced under terms of the CC-BY license.<sup>[141]</sup> Copyright 2020, The Authors, Published by Elsevier.

coordination<sup>[142]</sup>. This makes them the best candidates for  $\text{Eu}^{2+}$  ( $\text{Yb}^{2+}$ ,  $\text{Sm}^{2+}$ ) substitution. Divalent lead cation is another suitable candidate for the  $\text{Eu}^{2+}$  substitution. However,  $\text{Pb}^{2+}$  is undesirable due to its toxicity. A suitable crystal lattice site is essential for the  $\text{Eu}^{2+}$ -activated scintillators, because of the high doping levels often required for optimal scintillation performance.<sup>[143]</sup> Several compositions with different A:B ratios form congruently melting compounds which can be explored for use as bulk single-crystal scintillators, namely, the  $\text{AB}_2\text{X}_5$ ,  $\text{ABX}_3$ ,  $\text{A}_2\text{BX}_4$ ,  $\text{A}_3\text{BX}_5$ , and  $\text{A}_4\text{BX}_6$  ones

The number of photons  $N_{\text{ph}}$  emitted after absorption of a photon with energy  $E_\gamma$  is given by the equation<sup>[144]</sup>

$$N_{\text{ph}} = \frac{E_\gamma}{E_g} YSQ \quad (1)$$

where  $E_g$  is the bandgap of the scintillator, parameters  $Y$ ,  $S$ , and  $Q$  are related to the conversion, transfer, and luminescence stages of scintillation mechanism, namely,  $Y$  is the conversion efficiency,  $S$  is the transfer efficiency, and  $Q$  is the QL of the luminescent process. Due to the inverse correlation between the number of emitted photons and bandgap, materials with a narrow bandgap are prospective for achieving high light yield. Therefore, iodides were the most extensively investigated halide scintillators for high-LY applications.

### 3.1. $\text{AB}_2\text{X}_5$

All the compounds of interest from the  $\text{AB}_2\text{X}_5$  family crystallize in  $\text{TiPb}_2\text{Cl}_5$ -type monoclinic ( $P2_1/c$ , space group no. 14) crystal structure with two crystallographic lattice sites of the  $\text{B}^{2+}$  cation (coordination numbers 7 and 8). First-principle calculations predict a random distribution of  $\text{Eu}^{2+}$  among the two  $\text{B}^{2+}$  lattice sites in  $\text{ASr}_2\text{I}_5$  compounds and a preferential occupation of the crystal site with CN 7 in  $\text{ABa}_2\text{I}_5$  compounds.<sup>[145]</sup> The preferential occupation of  $\text{Eu}^{2+}$  may result in the formation of Eu-rich domains in  $\text{ABa}_2\text{I}_5$  crystals.<sup>[145]</sup>

$\text{CsBa}_2\text{I}_5:\text{Eu}^{2+}$  exhibits LY up to  $102\,000\text{ ph MeV}^{-1[76]}$  and energy resolution down to  $2.3\%[146]$  (at  $662\text{ keV }^{137}\text{Cs}$ ). Pulse

height spectra are shown in **Figure 4**. Both the photopeak with ER  $2.3\%$  full width at half maximum (FWHM) and escape peak are well resolved. The  $\text{Sm}^{2+}$  codoping of  $\text{CsBa}_2\text{I}_5:\text{Eu}^{2+}$  was reported as the first attempt to prepare a “black scintillator” where an efficient  $\text{Eu}^{2+}$ – $\text{Sm}^{2+}$  energy transfer occurs, and in the energy of the resulting  $5d^1$ – $4f$  transition of  $\text{Sm}^{2+}$ , the emission peak is situated at around  $755\text{ nm}$ . Scintillation response shows a high-energy resolution of  $3.2\%$  ( $662\text{ keV }^{137}\text{Cs}$  excitation) and a leading decay time of  $2.1\text{ }\mu\text{s}$ .<sup>[147]</sup> The bromide analog  $\text{CsBa}_2\text{Br}_5:\text{Eu}^{2+}$  also exhibits a very high LY of  $92\,000\text{ ph MeV}^{-1}$  with an advantage of lower hygroscopicity.<sup>[148]</sup>  $\text{CsBa}_2\text{I}_5$  is also a prospective material for activation with monovalent cations.<sup>[149]</sup>  $\text{KSr}_2\text{I}_5$ <sup>[150]</sup> and  $\text{KSr}_2\text{Br}_5$ <sup>[151]</sup> were introduced as other promising scintillators from the  $\text{AB}_2\text{X}_5$  family showing high LY of  $94\,000$  and  $75\,000\text{ ph MeV}^{-1}$  and ER of  $2.4\%$  and  $3.5\%$  (at  $662\text{ keV }^{137}\text{Cs}$ ), respectively. These materials were further developed with regard to growth conditions,<sup>[71,152,153]</sup>  $\gamma$  detection capabilities,<sup>[154,155]</sup> and mixed  $\text{KSr}_2\text{Br}_x\text{I}_{5-x}$  compositions<sup>[156]</sup> resulting in high quality, large-volume ( $\text{Ø}1 \times 1\text{ in.}$ ) crystals for  $\gamma$  spectrometry.<sup>[71]</sup> Results on rubidium<sup>[157]</sup> and barium<sup>[158]</sup> analogs were also reported to have similar parameters.

Substitution of an alkali metal with thallium results in better stopping power for high-energy  $\gamma$  quanta due to higher  $Z_{\text{eff}}$  while keeping high performance. Therefore, analogs based on chlorides,<sup>[159]</sup> bromides,<sup>[160]</sup> and iodides<sup>[70,161–163]</sup> were investigated. However, similarly to other  $\text{Eu}^{2+}$ -doped scintillators mentioned, the iodides exhibit the best performance with LY up to  $72\,000\text{ ph MeV}^{-1[63]}$  and energy resolution below  $3\%$  (at  $662\text{ keV }^{137}\text{Cs}$ ).<sup>[162,163]</sup>

### 3.2. $\text{ABX}_3$

Iodides from the  $\text{ABX}_3$  family crystallize in either  $\text{NH}_4\text{CdCl}_3$ -type ( $Pnma$ , space group no. 62) or  $\text{UFeS}_3$  ( $Cmcm$ , space group no. 63)-type orthorhombic crystal structure. Both crystal structures have a single octahedral  $\text{B}^{2+}$  lattice site available for  $\text{Eu}^{2+}$  doping. Scintillation properties of a large number of  $\text{Eu}^{2+}$ -doped crystals from the  $\text{ABX}_3$  family were reported. However, most of the crystals does not exceed LY of  $50\,000\text{ ph MeV}^{-1}$  and ER of  $5\%$  (at  $662\text{ keV }^{137}\text{Cs}$ ) except for  $\text{CsSrI}_3$  and  $\text{KCaI}_3$ . For  $\text{CsSrI}_3$ , the LY value up to  $65\,000\text{ ph MeV}^{-1[64]}$  and ER down to

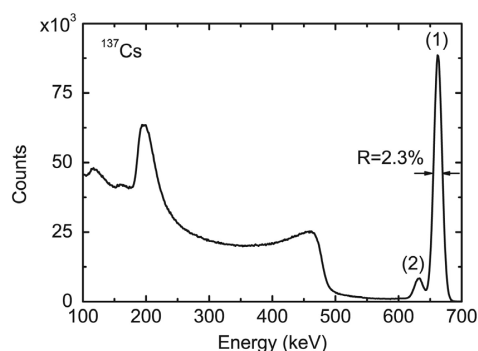


**Figure 4.** Pulse height spectrum of  $\text{CsBa}_2\text{I}_5:\text{Eu}(0.5\%)$ . Reproduced with permission.<sup>[146]</sup> Copyright 2013, Elsevier.

3.4%<sup>[165]</sup> (at 662 keV <sup>137</sup>Cs) were reported. However, the growth of large-volume single crystals of CsSrI<sub>3</sub> has proven very complicated. KCaI<sub>3</sub> has emerged as the most promising candidate from the ABX<sub>3</sub> family having LY of 72 000 ph MeV<sup>-1</sup> and ER of 3%<sup>[55]</sup> for a small crystal (Ø 2 mm). Further improvement was achieved via Sr substitution.<sup>[166,167]</sup> Moreover, codoping with RE<sup>3+</sup> results in significant suppression of the afterglow,<sup>[168]</sup> while Zr<sup>4+</sup> codoping results in improvement of energy resolution.<sup>[169]</sup> Growth of large volume crystals (up to Ø50 mm) is possible without significant deterioration of the scintillation performance.<sup>[61]</sup> The Yb<sup>2+</sup>-doped ACaCl<sub>3</sub> (A = Cs, Rb, K) crystals show emission bands centered at ≈445 nm with two decay time constants of ≈10 and 200 μs in the PL and scintillation decays attributed to fast (LS) and slow (HS) 5*d*–4*f* transition of Yb<sup>2+</sup>, respectively.<sup>[170]</sup> LY values of ACaCl<sub>3</sub>:Yb<sup>2+</sup> were estimated at about 3,600–5,200 ph MeV<sup>-1</sup> based on the pulse height spectra, that is., much lower compared with the aforementioned KMeI<sub>3</sub>:Eu (Me = Ca, Sr), which can be explained by the presence of a very slow decay component due to the involvement of the HS 5*d* state of Yb<sup>2+</sup> in the decay mechanism.

### 3.3. A<sub>4</sub>BX<sub>6</sub>

All the compounds of interest from the A<sub>4</sub>BX<sub>6</sub> family crystallize in the K<sub>4</sub>CdCl<sub>6</sub> type (*R*-3*c*, space group no. 167) with a single octahedral B<sup>2+</sup> lattice site. The scintillation properties were reported for Cs<sub>4</sub>CaI<sub>6</sub> and Cs<sub>4</sub>SrI<sub>6</sub> with LY up to 69 000 and 71 000 ph MeV<sup>-1</sup> and ER down to 3.6% and 3.2% (at 662 keV <sup>137</sup>Cs) respectively.<sup>[171,172]</sup> The effect of alkali metal substitution<sup>[172]</sup> was investigated. In the case of Yb<sup>2+</sup> activator, the best scintillation performance was achieved with Cs<sub>4</sub>CaI<sub>6</sub>:Yb (1%<sub>mol</sub>), which had a 3.5% energy resolution at 662 keV and 43 000 ph MeV<sup>-1</sup> light yield.<sup>[173]</sup> Lower light yield compared with the Eu<sup>2+</sup>-doped Cs<sub>4</sub>CaI<sub>6</sub> might be due to worse timing characteristics of the scintillation response because of the involvement of HS 5*d* level of Yb<sup>2+</sup> as mentioned above. Moreover, this matrix allows complete substitution of B<sup>2+</sup> cation with Eu<sup>2+</sup>. Single crystals of Cs<sub>4</sub>EuBr<sub>6</sub> and Cs<sub>4</sub>EuI<sub>6</sub> exhibit LY of 78 000 and 53 000 ph MeV<sup>-1</sup> and ER of 4.3% and 5.0% (at 662 keV <sup>137</sup>Cs) respectively.<sup>[174]</sup>

### 3.4. Srl<sub>2</sub>

Even though Srl<sub>2</sub>:Eu was patented by Hofstadter,<sup>[51]</sup> it regained the interest of the scientific community at the beginning of the last decade due to technological advancements that allowed large-volume high-quality single-crystal growth of this high-performance scintillator. In the last decade, the R&D of Srl<sub>2</sub> was focused on the improvement of its properties via codoping,<sup>[66,175,176]</sup> optimizing the growth conditions,<sup>[65,103,177,178]</sup> and packaging.<sup>[179]</sup> Moreover, Yb<sup>2+</sup> doping was also suggested as prospective due to the faster scintillation kinetics.<sup>[180]</sup>

## 4. Ce<sup>3+</sup>-Activated Fast Scintillators

Similarly to the Eu<sup>2+</sup>-activated halide scintillators, the search for new Ce<sup>3+</sup>-activated halide ones was focused on the exploration of compositional space formed by ternary halides involving alkali

metals (or thallium). The motivation for Ce<sup>3+</sup> doping is due to its at least 20 times faster luminescence lifetime compared with Eu<sup>2+</sup> even if it is based on the same type of 5*d*–4*f* transition and somewhat bigger Stokes shift which decreases unwanted reabsorption. In the case of Ce<sup>3+</sup> activation, the alkali earth metals were replaced by RE metals to create a crystal lattice site suitable for Ce<sup>3+</sup> doping.

It is worth explaining here an absence of reports in bromide and iodide hosts dealing with Pr<sup>3+</sup> emission center and its 5*d*–4*f* luminescence which is typically two times faster compared with that of Ce<sup>3+</sup>. The reason is that in bromides and iodides the Pr<sup>3+</sup> ground state becomes immersed in the valence band, see **Figure 5**, which results in its preferential excitation through the charge transfer absorption band followed with emission from the lower-lying 4*f*<sup>3</sup>P<sub>1</sub> state, which occurs with the lifetime of the order of ten microseconds. Even in the chloride host, namely, LuCl<sub>3</sub>, where both the 4*f* ground-state <sup>3</sup>H<sub>4</sub> and excited-state 5*d*<sup>1</sup> are located in the forbidden gap and the transition 4*f*(<sup>3</sup>H<sub>4</sub>)–5*d*<sup>1</sup> of Pr<sup>3+</sup> is located at lower energy compared with the charge transfer one, the band-to-band excitation results in energy transfer from the exciton state right to lower-lying 4*f*<sup>3</sup>P<sub>1</sub> and <sup>1</sup>D<sub>2</sub> levels and their much slower luminescence so that the fast 5*d*<sup>1</sup>–4*f* radiative transition is avoided.<sup>[181]</sup>

### 4.1. CeBr<sub>3</sub>

To this date, lanthanum bromide doped with cerium and codoped with strontium (LaBr<sub>3</sub>:Ce,Sr) exhibits the best energy resolution (2.0% at 662 keV of <sup>137</sup>Cs) among bulk single-crystal inorganic scintillators.<sup>[182]</sup> However, the attention in R&D shifted from LaBr<sub>3</sub>:Ce to CeBr<sub>3</sub> due to internal contamination with <sup>138</sup>La (0.089% abundance, T<sub>1/2</sub> = 1.05 · 10<sup>11</sup> y) radionuclide and a high tendency for cracking during crystal growth. Based on the knowledge of LaBr<sub>3</sub>:Ce, the influence of aliovalent doping (mainly by alkaline earth metals) was investigated,<sup>[183–185]</sup> suggesting that codoping with Sr<sup>2+</sup> results in the best energy resolution in both

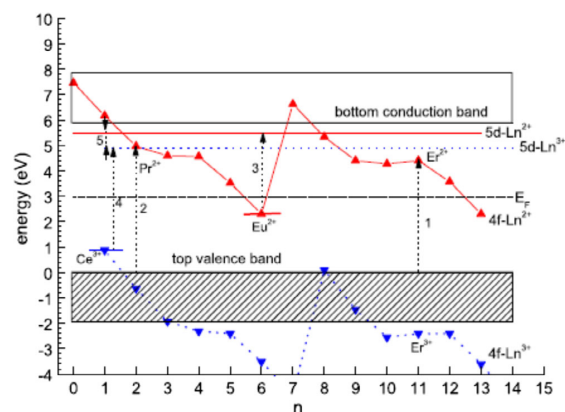


**Figure 5.** Location of divalent and trivalent lanthanide energy levels in LaBr<sub>3</sub> as a function of the number *n* of electrons in the 4*f* shell of the trivalent lanthanide. Note, *n* is the number of electrons in the 4*f* shell of the divalent lanthanide. Reproduced with permission.<sup>[354]</sup> Copyright 2005, Elsevier.

LaBr<sub>3</sub>:Ce and CeBr<sub>3</sub>.<sup>[184]</sup> The influence of codoping on the non-proportionality of the scintillation response in CeBr<sub>3</sub> is illustrated in **Figure 6**. Moreover, the influence of CeBr<sub>3-x</sub>Cl<sub>x</sub><sup>[186]</sup> or CeBr<sub>3-x</sub>I<sub>x</sub><sup>[187]</sup> solid solutions on scintillation properties was investigated.

#### 4.2. A<sub>2</sub>A'LnX<sub>6</sub>

The successful development of Cs<sub>2</sub>LiYCl<sub>6</sub>:Ce (CLYC) as a thermal neutron detector with excellent  $n^0/\gamma$  discrimination<sup>[65]</sup> initiated extensive research in scintillators from the elpasolite family. These materials offer a combination of high proportionality, resulting in a good energy resolution and a suitable site for Ce<sup>3+</sup> doping. Moreover, cesium-containing chloride elpasolites exhibit crossluminescence which can be used for discrimination of neutron/alpha radiation from beta and gamma one.

Substitution of Cs with Tl results in a material with higher stopping power while keeping comparable energy resolution and light yield.<sup>[188,189]</sup> However, the substitution of chlorine with heavier halides results in improvement of the light yield and energy resolution.<sup>[190–193]</sup> However, heavy halide analogs of CLYC do not exhibit fast CL emission. First-principle calculations suggest that Ag substitution on A' position should further improve scintillation properties.<sup>[194]</sup>

#### 4.3. A<sub>3</sub>LnX<sub>6</sub>

Materials from this family are mostly monoclinic with either K<sub>3</sub>MoCl<sub>6</sub> (*P2<sub>1</sub>/c*, space group no. 14) or Cs<sub>3</sub>BiCl<sub>6</sub> (*C2/c*, space group no. 15)-type crystal structure at RT. Both have a single octahedral Ln<sup>3+</sup> lattice site. This often results in complicated crystal growth due to phase transitions connected with the lowering of crystal symmetry during cooling.<sup>[127,195]</sup> Most of the investigated compositions contained La or Gd on Ln position and Cs at A position.<sup>[192,195,196]</sup> The best results were reported for Cs<sub>3</sub>GdBr<sub>6</sub>:Ce with LY of 47 000 ph MeV<sup>-1</sup> and ER of 4.0% (at 662 keV <sup>137</sup>Cs).<sup>[195]</sup> Full substitution with Ce at Ln position is possible, however, with inferior performance.<sup>[127,197]</sup> Lastly, Li<sub>3</sub>YCl<sub>6</sub>:Ce was suggested as a thermal neutron scintillator.<sup>[198]</sup>

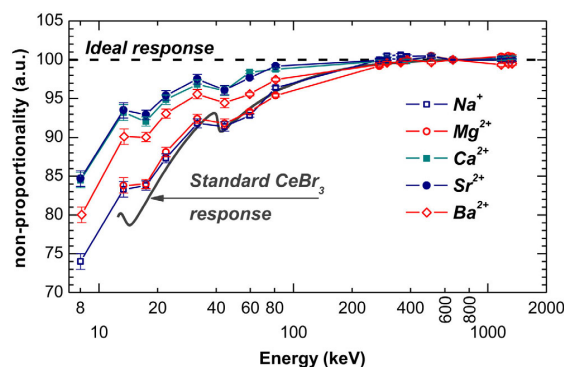


**Figure 6.** Measured nonproportionality characteristics of standard and codoped CeBr<sub>3</sub> samples. For all samples, the values are normalized to 100% at 662 keV. Reproduced with permission.<sup>[184]</sup> Copyright 2013, Elsevier.

#### 4.4. A<sub>2</sub>LnX<sub>5</sub>

All compounds of interest from the A<sub>2</sub>LnX<sub>5</sub> family crystallize in the orthorhombic crystal structure (*Pnma*, space group no. 62) with K<sub>2</sub>PrCl<sub>5</sub>-, Cs<sub>2</sub>DyCl<sub>5</sub>-, or Y<sub>2</sub>HfS<sub>5</sub>-type structure with a single Ln<sup>3+</sup> lattice site. Compositions with Tl on the A site exhibit the density up to 5.98 g cm<sup>-3</sup> and Z<sub>eff</sub> up to 79.<sup>[199]</sup> Therefore, Tl<sub>2</sub>LaCl<sub>5</sub>,<sup>[9,70,199–202]</sup> Tl<sub>2</sub>LaBr<sub>5</sub>,<sup>[199,202,203]</sup> Tl<sub>2</sub>GdCl<sub>5</sub>,<sup>[204,205]</sup> and Tl<sub>2</sub>GdBr<sub>5</sub><sup>[70]</sup> were most extensively investigated. Best samples reported in the literature exhibit LY up to 82 000 ph MeV<sup>-1</sup><sup>[201]</sup> and ER down to 2.8% (at 662 keV <sup>137</sup>Cs).<sup>[202]</sup> Crystals with complete Ce<sup>3+</sup> substitution on the Ln<sup>3+</sup> site exhibit inferior performance similar to A<sub>3</sub>LnX<sub>6</sub> compounds.<sup>[206]</sup>

#### 4.5. ALn<sub>2</sub>X<sub>7</sub>

Most of the compositions from the ALn<sub>2</sub>X<sub>7</sub> family crystallize in either KDy<sub>2</sub>Cl<sub>7</sub>-type monoclinic (*P2<sub>1</sub>/c*, space group no. 14) or RbDy<sub>2</sub>Cl<sub>7</sub>-type orthorhombic (*Pnma*, space group no. 62) crystal structure. Both have two Ln<sup>3+</sup> lattice sites. However, recently the crystal structure of CsCe<sub>2</sub>Cl<sub>7</sub> was derived from single-crystal diffraction having a new, previously unreported, monoclinic crystal structure.<sup>[207]</sup> Most of the reported crystals from the ALn<sub>2</sub>X<sub>7</sub> family have low quality due to complicated crystal growth<sup>[126,208–210]</sup> which results in worse scintillation performance. However, gadolinium-containing crystals were suggested as scintillators for both gamma and thermal neutron detection.<sup>[211]</sup>

### 5. Activation with ns<sup>2</sup> ions

The first member of the so-called heavy 6s<sup>2</sup> ion group, the Tl<sup>+</sup> ion, was used as the luminescence center in the very first single-crystal halide scintillator NaI:Tl in the late 1940s.<sup>[212]</sup> Two closely spaced <sup>3</sup>P<sub>0</sub> and <sup>3</sup>P<sub>1</sub> levels constitute its lowest excited state. Given the strong spin-orbit coupling, the <sup>3</sup>P<sub>1</sub> shows the decay times of the order of a few hundreds of nanoseconds which is faster compared with the 5*d*–4*f* transition of Eu<sup>2+</sup>. Furthermore, a considerably higher Stokes shift completely removes the reabsorption risk even in large scintillation elements. The Tl<sup>+</sup> has been recently adopted even as a cation in ternary iodides as mentioned above and the electronic band structures of InBa<sub>2</sub>I<sub>5</sub> or TlBa<sub>2</sub>I<sub>5</sub> were calculated showing noticeable contribution from In<sup>+</sup> and Tl<sup>+</sup> in the valence and conduction band edges.<sup>[213]</sup> Tl<sup>+</sup> and In<sup>+</sup> were also doped in CsBa<sub>2</sub>I<sub>5</sub><sup>[149]</sup> providing LY values of 40 000 and 35 000 ph MeV<sup>-1</sup>, respectively. Lower toxicity of indium is an advantage, but its weaker spin-orbit coupling results in 5–10 times slower luminescence and scintillation response compared with Tl<sup>+</sup> so that the dominant component in the decay is of the order of a few microseconds.

### 6. Self-Activated/Intrinsic Scintillators

#### 6.1. A<sub>2</sub>MX<sub>6</sub>

Many compositions with formula A<sub>2</sub>MX<sub>6</sub> where A stands for alkali metal (or thallium) and M stands for tetravalent cation

(mostly Hf and Zr) crystallize in the cubic  $K_2PtCl_6$ -type structure ( $Fm-3m$ , space group no. 225). The crystal structure often called “vacancy-ordered double perovskite” can be derived by doubling the  $ABX_3$  perovskite structure with one  $B^{2+}$  cation replaced by  $M^{4+}$  cation and the other by a vacancy, resulting in charge neutrality of the structure. Compositions with smaller alkali metal (i. e. Rb, K, or Na) on the A lattice site diverge from the cubic crystal structure and undergo distortion to the lower tetragonal or monoclinic symmetry.<sup>[214]</sup> Even though the luminescence of  $Cs_2HfCl_6$  was investigated by Ackerman already in 1984,<sup>[215]</sup> this material family did not attain much attention of the scintillation community until its rediscovery by Burger et al. in 2015.<sup>[8]</sup>

$Cs_2HfCl_6$  is prospective due to the combination of high  $Z_{eff}$ , high LY of 54 000 ph  $MeV^{-1}$ ,<sup>[8]</sup> and high proportionality resulting in excellent energy resolution of 3.3% (at 662 keV  $^{137}Cs$ )<sup>[8]</sup> in an undoped crystal with low hygroscopicity. The origin of intrinsic luminescence in  $Cs_2HfCl_6$  was ascribed to radiative recombination of excitons trapped on  $[HfCl_6]^{2-}$  octahedra.<sup>[72,216]</sup> The emission mechanism is schematically sketched in Figure 7.

These promising results motivated investigation of the properties of  $Cs_2HfCl_6$  using various methods including simultaneous thermogravimetric analysis,<sup>[217]</sup> electron paramagnetic resonance (EPR), and thermally stimulated luminescence (TSL).<sup>[72,73,218]</sup> Moreover, improvement of material purification and crystal growth conditions<sup>[121,219,220]</sup> resulted in improvement of the ER down to 2.8% (at 662 keV  $^{137}Cs$ ).<sup>[219]</sup> Furthermore, analogs of  $Cs_2HfCl_6$  were investigated including  $A_2MCl_6$ ,<sup>[221,222]</sup>  $Cs_2HfBr_xCl_{1-x}$ ,<sup>[45,223–225]</sup>  $A_2HfI_6$ ,<sup>[226–228]</sup>  $Tl_2MCl_6$ ,<sup>[199,229–232]</sup> and  $Tl_2HfBr_6$ .<sup>[199]</sup> All exhibit broadband emission with scintillation decay times in the microsecond range. The progress in the development of several scintillators with  $K_2PtCl_6$  structure was recently reported by Hawrami et al.<sup>[233]</sup> Substitution of chlorine with heavier halogens results in faster decay times due to stronger spin-orbit coupling<sup>[216]</sup> and higher LY due to a decrease in the bandgap. Moreover, a redshift of the self-trapped exciton (STE) emission can be utilized to match the spectral sensitivity of the avalanche photodiode<sup>[120,226]</sup> or region of low-transmission losses of silica optical fibers.<sup>[228]</sup> However, bromide and iodide analogs of  $Cs_2HfCl_6$  suffer from high hygroscopicity. For a review of the  $Cs_2HfCl_6$ -type scintillators, see the study by Nagorny.<sup>[234]</sup> First attempts of preparation of ceramic  $Cs_2HfCl_6$ <sup>[235,236]</sup> and  $Tl_2HfCl_6$ <sup>[236]</sup> showed very promising results.

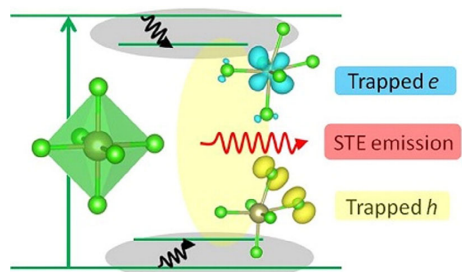


**Figure 7.** Schematics of luminescence mechanism in  $Cs_2HfCl_6$ . Reproduced with permission.<sup>[216]</sup> Copyright 2016, American Chemical Society.

Another advantage of scintillators from the  $A_2MX_6$  family is excellent pulse-shape discrimination of scintillation response to  $\alpha$  and  $\gamma$  radiation.<sup>[237,238]</sup> This makes  $Cs_2HfCl_6$  (and other scintillators from this family) prospective for the detection of fast neutrons in mixed neutron–gamma radiation fields. Moreover, the combination of  $\alpha/\gamma$  discrimination together with high Hf concentration allowed measurement of the rare  $\alpha$  decay time of  $^{174}Hf$  in the “source=detector” configuration.<sup>[239]</sup> However, such applications require the use of highly radiopure starting chemicals.<sup>[237]</sup>

Activation of the  $A_2MX_6$  matrix with  $Tl^+$ ,<sup>[240]</sup>  $Eu^{2+}$ ,<sup>[241]</sup> and  $Ce^{3+}$ <sup>[240,241]</sup> was unsuccessful so far, as well as doping with alkaline Earth metals.<sup>[242]</sup> However, doping on the  $Hf^{4+}$  site with either  $Zr^{4+}$ <sup>[243]</sup> or  $Te^{4+}$ <sup>[244]</sup> results in a redshift of the emission.

## 6.2. $Cs_3Cu_2I_5$ and $CsCu_2I_3$

Ternary cesium copper iodides have gained significant attention from the optoelectronic community due to their nontoxicity, air stability, and PLQY up to 91.2% for  $Cs_3Cu_2I_5$  single crystals.<sup>[10]</sup>  $Cs_3Cu_2I_5$  crystallizes in orthorhombic “0D perovskite” crystal structure ( $Pnma$ , space group no. 62) consisting of separated  $[Cu_2I_5]^{3-}$  units separated by  $Cs^+$  cations.<sup>[53]</sup> The first report of the bulk single-crystal  $Cs_3Cu_2I_5$  showed promising results with LY of 18 000 ph  $MeV^{-1}$  and ER of 7.7% (at 662 keV  $^{137}Cs$ ) for undoped crystal<sup>[74]</sup> and a significant improvement of scintillation performance after Tl doping. The sample doped with 1% of Tl exhibited LY of 51 000 ph  $MeV^{-1}$  and ER of 4.5% with an excellent proportionality.<sup>[74]</sup> Improvement in crystal quality increased LY up to 41 500 ph  $MeV^{-1}$ <sup>[53]</sup> and ER down to 3.6%<sup>[245]</sup> for an undoped crystal. Furthermore, Tl-doped crystals exhibit LY close to 100 000 ph  $MeV^{-1}$ <sup>[53]</sup> and ER below 3.5%.<sup>[53,246]</sup> This matrix also shows an extremely low afterglow of 0.015% (10 ms after excitation cut-off) for 0.1% Tl-doped samples.<sup>[246]</sup> Based on scintillation kinetics<sup>[74]</sup> and first-principle calculations,<sup>[53]</sup> the scintillation mechanism in  $Cs_3Cu_2I_5$  was not attributed to  $ns \rightarrow s^2$  radiative transition of  $Tl^+$ , but the recombination of a self-trapped hole with an electron trapped at the Tl impurity. The scintillation mechanism in Tl-doped  $Cs_3Cu_2I_5$  is schematically illustrated in Figure 8.

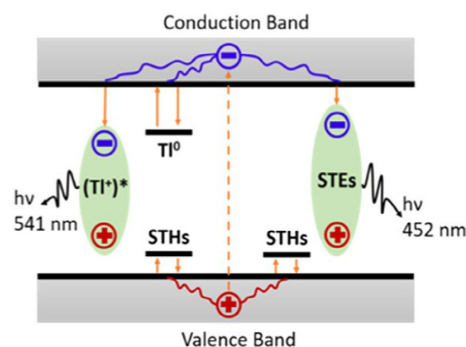


**Figure 8.** Schematic illustration of scintillation mechanism in Tl-doped  $Cs_3Cu_2I_5$ . Reproduced with permission.<sup>[74]</sup> Copyright 2020, American Chemical Society.

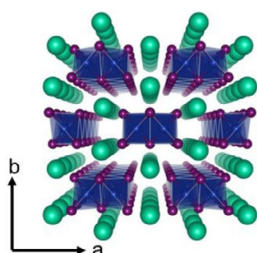


**Figure 9.** View of the  $\text{CsCu}_2\text{I}_3$  crystal structure along the  $c$ -axis. Reproduced with permission.<sup>[247]</sup> Copyright 2021, American Chemical Society.

$\text{CsCu}_2\text{I}_3$  crystallizes in orthorhombic “1D perovskite” crystal structure ( $Cmcm$ , space group no. 63) consisting of chains of  $[\text{Cu}_2\text{I}_6]^{4-}$  edge-sharing octahedra separated by rows of  $\text{Cs}^+$  cations.<sup>[247]</sup> **Figure 9** depicts a view of the crystal structure along the  $c$ -axis. Under X-ray excitation,  $\text{CsCu}_2\text{I}_3$  exhibits broadband emission peaking at 570 nm which was ascribed to localized exciton emission.<sup>[247]</sup> LY and ER at RT are inferior to that of  $\text{Cs}_3\text{Cu}_2\text{I}_5$ . However,  $\text{CsCu}_2\text{I}_3$  exhibits an extremely low afterglow at the level of 0.008% (10 ms after excitation cut-off).<sup>[247]</sup> Moreover, the temperature dependence of PL revealed the potential of  $\text{CsCu}_2\text{I}_3$  to achieve LY above 100 000 ph  $\text{MeV}^{-1}$  via exciton engineering.<sup>[247]</sup>

## 7. Cross-Luminescence Scintillators

Cross-luminescence (CL, also called “Auger-free luminescence” or “core-valence luminescence”) is radiative recombination of an electron from the valence band with a hole from the uppermost core band. It is observed mostly in halides containing heavier alkali metals (i.e., K, Rb, and Cs) or barium (see the review in another study<sup>[248]</sup>). A band structure of  $\text{BaF}_2$  with an indication of both the CL and STE emissions is schematically shown in **Figure 10**. CL is prospective for fast timing applications due to fast decay kinetics with decay time  $\approx 1$  ns. However, the position of CL emission in vacuum ultraviolet (VUV) complicates the practical application of CL scintillators. The recent development of UV-sensitive semiconductor photodetectors has renewed

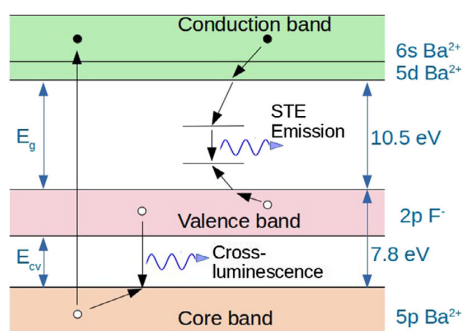


**Figure 10.** The band structure schematics of  $\text{BaF}_2$  showing CL and STE emission. Reproduced under terms of the CC-BY license.<sup>[355]</sup> Copyright 2020, The Authors. Published by Frontiers.

interest in CL scintillators. Using VUV-HD silicon photomultiplier (SiPM), a coincidence time resolution (CTR) of 51 ps was achieved for commercially available  $\text{BaF}_2$  crystal.<sup>[249]</sup> Currently, this is the lowest CTR value reported for the inorganic scintillator. Cross-luminescence can also be exploited for  $\alpha(n^0)$  and  $\gamma$  discrimination.<sup>[250]</sup>

An ideal cross-luminescence scintillator should exhibit the emission redshifted compared with  $\text{BaF}_2$  while keeping the fast scintillation kinetics and relatively high LY ( $\approx 1400$  ph  $\text{MeV}^{-1}$  for  $\text{BaF}_2$ <sup>[251]</sup>) without major slow components. The redshift of CL emission can be achieved by exploring cesium-based fluorides and chlorides. In the last decade, the research was focused on chloride materials, such as  $\text{CsBCl}_3$  ( $B = \text{Mg, Ca, Sr}$ ),<sup>[252–255]</sup>  $\text{Cs}_2\text{BaCl}_4$ ,<sup>[255,256]</sup>  $\text{Cs}_2\text{ZnCl}_4$ ,<sup>[257]</sup> and  $\text{Cs}_3\text{ZnCl}_5$ .<sup>[257]</sup> Preliminary measurements of time resolution of  $\text{CsCaCl}_3$  reported CTR of 148 ps<sup>[255]</sup> with the potential to surpass  $\text{BaF}_2$ . Only a few reports on CL in single-crystal fluorides can be found in the recent literature.<sup>[258,259]</sup>

## 8. Transparent Ceramics

Transparent ceramic scintillators were first introduced in the 1980s.<sup>[260,261]</sup> In the following years, the research was focused on oxide materials, mainly of the garnet structure. For more information about oxide ceramic scintillators, see the study by Nikl et al.<sup>[262]</sup> and references therein. The first attempt for preparation of the halide transparent ceramic scintillator was reported by Wisniewski<sup>[263]</sup> in 2007. They used hot pressing to produce uniformly shaped, millimeter-size translucent  $\text{LaBr}_3:\text{Ce}$  ceramics with an estimated LY of 42 000 ph  $\text{MeV}^{-1}$ .<sup>[263,264]</sup> In the last decade, development of translucent/transparent ceramics was reported for several halide scintillators, including  $\text{BaCl}_2$ ,<sup>[265]</sup>  $\text{Ba}_{1-x}\text{La}_x\text{Cl}_{2+x}$ ,<sup>[266]</sup>  $\text{SrI}_2:\text{Eu}$ ,<sup>[267]</sup>  $\text{Cs}_2\text{HfCl}_6$ ,<sup>[236,263]</sup> and  $\text{Tl}_2\text{HfCl}_6$ .<sup>[236]</sup>

## 9. Microstructured Halide Scintillators

Microstructured scintillators were developed for imaging screens to enable an increased X-ray stopping power with the help of increased thickness of scintillation element and simultaneously keeping high spatial resolution enabled by its light-guiding property. The columnar grown  $\text{CsI}:\text{Tl}$  became commercially successful<sup>[268–270]</sup> prepared by vacuum evaporation in the form of long (up to 1 mm) and thin (from few to several  $\mu\text{m}$  in diameter) densely packed needles, which are reasonably optically isolated. In practical applications, such a needle layer can be deposited directly on a semiconductor photodetector.<sup>[3]</sup> Radiographic panels of this kind were developed in the late 1980s and became widely used in routine radiographic imaging.<sup>[271]</sup>

Another approach in the scintillator element structure design appeared about a decade ago, namely, the so-called phase-separated scintillators, prepared from an eutectic melt by unidirectional solidification (using most frequently the Bridgman, CZ, or micro-pulling-down techniques).<sup>[272]</sup> Such a manufacturing technique enables the preparation of a monolithic element consisting of a crystal host with the embedded ordered thin rod-like second phase, as shown in **Figure 11**.

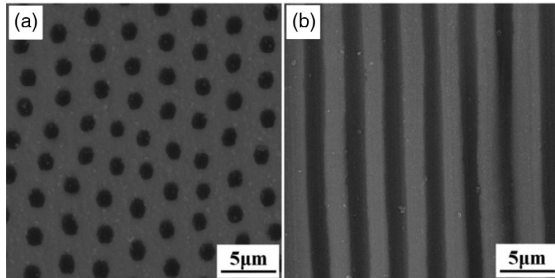
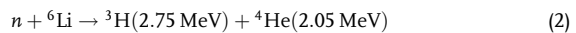


**Figure 11.** SEM images of the CsI–NaCl system with light and dark visual appearance, respectively. a) Top view and b) cross-sectional view. Reproduced with permission.<sup>[272]</sup> Copyright 2012, John Wiley and Sons.

Light-guiding property is achieved in the constituent of higher refraction index which usually works as a scintillator. In principle, both the host crystal and rod-like second phase can work in such a way, though light guidance within tiny rods is more efficient. In the study by Yasui et al.,<sup>[272]</sup> a couple of alkali halide compounds were used to demonstrate such a light-guiding property in scintillation mode and as the most advantageous eutectic composition the CsI(host)-NaI:Tl(scintillator) was found. It is worth noting that in this case, the higher refraction index is that of CsI, so that the generated scintillation light is guided out through the host constituent and not through the rod-like NaI:Tl scintillator phase. Scintillation characteristics of eutectic composition from this material family were reported later also in other studies,<sup>[87,273,274]</sup> focusing on a possibility to prepare larger optical elements for imaging devices; see an example of the grown Tl-doped CsI/CsCl/NaCl eutectic in **Figure 12**. In this case, the LY of the 12 mm h<sup>-1</sup>-pulled sample was about 16 000 ph MeV<sup>-1</sup>, that is, 27% of the CsI:Tl standard

single-crystal scintillator. The scintillation decay time value was measured to be 910 ns, the same as that of the CsI:Tl standard scintillator. The performed imaging test with  $\beta$  particles excitation and charged-coupled device (CCD) photodetectors provided a position resolution of 16  $\mu$ m FWHM.

Frequently, fluoride-based eutectic scintillators were reported based on the Eu<sup>2+</sup>-doped <sup>6</sup>LiF/CaF<sub>2</sub>,<sup>[275]</sup> or <sup>6</sup>LiF–SrF<sub>2</sub>,<sup>[276]</sup> Ce-doped LiF–SrF<sub>2</sub>,<sup>[277]</sup> or undoped LiF–SrF<sub>2</sub> and LiF–CaF<sub>2</sub><sup>[278]</sup> where the emission is due to the exciton in the alkali earth fluoride constituent. Eutectic composition of LiF host and scintillator phase based on another doped fluoride was reported for Eu<sup>2+</sup>-doped LiF/CaF<sub>2</sub>/LiBaF<sub>3</sub><sup>[279]</sup> and LiF/LiBaF<sub>3</sub><sup>[280]</sup> and Ce<sup>3+</sup>-doped fluorides LiF/LaF<sub>3</sub>,<sup>[280]</sup> LiF/LiLuF<sub>4</sub>,<sup>[281]</sup> and LiF/LiYF<sub>4</sub>.<sup>[282]</sup> From the point of view of efficient light guidance, the LiF/LaF<sub>3</sub> composition appears the most promising due to the largest difference of refractive indexes ( $n_{\text{LiF}} = 1.39$ ,  $n_{\text{LaF}_3} = 1.60$  at the emission peak of Ce<sup>3+</sup>), which enhances the total reflection in the rod-like LaF<sub>3</sub>:Ce scintillator. Given the LiF host, such materials were considered also for thermal neutron detection, especially in the case of <sup>6</sup>Li enrichment which provides a large energy deposit due to the reaction



As the smaller bandgap of scintillation phase may provide higher efficiency due to smaller energy required to create an electron–hole pair, apart from the reports dealing with chloride eutectic compositions, such as LiCl–BaCl<sub>2</sub>:Eu<sup>2+</sup>,<sup>[283]</sup> LiCl/Li<sub>2</sub>SrCl<sub>4</sub>:Eu<sup>2+</sup>, and<sup>[69]</sup> LiCl–CeCl<sub>3</sub>,<sup>[284]</sup> those based on bromides, such as Ce:LaBr<sub>3</sub>/AEBBr<sub>2</sub> (AE = Mg, Ca, Sr, Ba)<sup>[68]</sup> and LiBr/LaBr<sub>3</sub>:Ce,<sup>[285]</sup> or iodides as BaI<sub>2</sub>/LuI<sub>3</sub>:Ce<sup>[286]</sup> or Eu-doped LiSr<sub>3</sub>/LiI,<sup>[287]</sup> were published as well. The highest LY was reported in,<sup>[285]</sup> 74 000 ph per neutron, which is much superior to presently available commercial single-crystal scintillators for

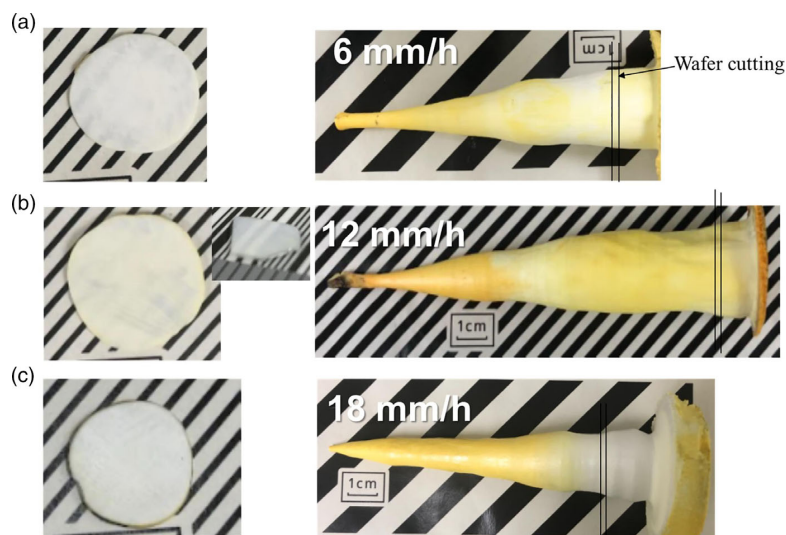


**Figure 12.** Photographs of the grown Tl-doped CsI/CsCl/NaCl eutectic (right) and the wafers cut in the transverse cross section (left) for the pulling rate of a) 6, b) 12, and c) 18 mm h<sup>-1</sup>. Reproduced with permission.<sup>[87]</sup> Copyright 2021, Elsevier.

thermal neutron detection. A practical drawback of most of these materials is, however, their hygroscopicity so that the hermetic sealing of the eutectic element becomes necessary.

## 10. Halide Perovskite NCs

### 10.1. Hybrid Perovskites

Increased interest in research of halide perovskites first focused on the family of organic–inorganic, or so-called hybrid, perovskites, where the cuboctahedrally coordinated A site of the  $ABX_3$  perovskite formula is occupied by organic cations, such as  $CH_3NH_3$  (methylammonium: MA) and  $NH_2CH=NH^{2+}$  (formamidinium: FA). B cations, octahedrally coordinated by X anions, are metal atoms, typically  $Pb^{2+}$  or  $Sn^{2+}$ , and X anions are usually Cl, Br, or I. Hybrid perovskites became drivers of alternative photovoltaic technology in the past decades. In the early work,<sup>[288]</sup> MAPbBr<sub>3</sub> and MAPbI<sub>3</sub> were used as light absorbers in photovoltaic devices. Since then, the bulk and nanocrystalline hybrid perovskites were mainly investigated in the solar cell applications (see, e.g., a recent review<sup>[289]</sup>). The certified efficiency of perovskite solar cells has increased drastically to over 25% and can now compete in this respect with Si technology.<sup>[290]</sup>

Recently, hybrid perovskites in nanocrystalline form were investigated as potentially interesting candidates also for scintillator applications. High LY alpha particle scintillators based on hybrid perovskite MAPbBr<sub>3</sub> NCs (NCs) with an ultrafast response time at low temperatures are reported.<sup>[291]</sup> The LY of the hybrid perovskite MAPbBr<sub>3</sub> increases with decreasing temperature and appears much higher when compared with that of the commercial (Lu,Y)<sub>2</sub>SiO<sub>5</sub>:Ce (LYSO:Ce)-based scintillators at around 150 K as well as CsI-based scintillators at around 50 K. In addition, it also showed an ultrafast alpha response with the fastest decay component of 0.1 ns at 77 K. The measurement of the pulse height spectra showed that MAPbBr<sub>3</sub> exhibits an ability to detect alpha particles comparable with that of the commercial scintillators.

FAPbBr<sub>3</sub> colloidal NCs were investigated for fast neutron imaging through the detection of recoil protons generated by neutron scattering.<sup>[292]</sup> A variety of NCs were screened for their LY and spatial resolution under fast neutron irradiation, with FAPbBr<sub>3</sub> providing the highest LY. Concentration and thickness-dependent measurements reveal that self-absorption and low concentrations are the primary limiting factors in these scintillators, providing design principles to foster the development of next-generation fast neutron detectors based on colloidal semiconductor NCs.

### 10.2. All-Inorganic Halide Perovskites

In all-inorganic halide perovskites, the A site of the  $ABX_3$  formula is occupied by a monovalent  $Cs^+$  cation. Colloidal NCs represent highly promising types of semiconductors for a variety of applications due to their narrow band photoluminescence (PL), tunable from ultraviolet to infrared spectral range, by simply manipulating the NC size and halide composition. High quantum efficiency and (ultra) fast decay times became attractive features also for manufacturing a new generation of scintillation

detector systems. A body of associated work can be found in recent reviews, those mentioned in the Introduction or also other studies.<sup>[293,294]</sup> In the following we focus on some of the most recent works.

The most critical issue for scintillator performance can be carrier trapping. The study<sup>[295]</sup> shows CsPbBr<sub>3</sub> NCs as superior candidates for scintillating materials compared with higher-dimensional analogs. CsPbBr<sub>3</sub> with increasing dimensionality, namely, nanocubes, nanowires, nanosheets, and bulk crystals, was comprehensively studied to shed light on trapping and detrapping mechanisms to and from shallow and deep traps. The study involved radioluminescence and PL measurements together with thermally stimulated luminescence and afterglow experiments. All systems show detrapping physics related to shallow localized states due to surface defects. However, unlike in NCs, in higher-dimensional analogs, the suppression of defects needs to be operated on both the surface and volume levels.

Target applications of inorganic halide perovskites in the scintillation detection systems include X-ray imaging (see some works mentioned in Subsection 10.4. Nanocomposites), fast neutron imaging, and fast timing applications.

Successful fast neutron imaging scintillator requires a compelling and rare combination of high PLQY, high concentrations of NCs, and high Stokes shifts with low self-absorption. Such a combination was only recently found in colloidal NC system of  $Mn^{2+}$ :CsPb(Br,Cl)<sub>3</sub>. A new synthesis based on zwitterionic ASC18 ligands yielded NCs which are colloiddally stable to high concentrations while maintaining excellent optical quality. Fast neutron imaging experiments showed that these dense ASC18-capped NCs achieved light yields over 8 times greater than those of their oleyl-capped counterparts. Furthermore, thickness and concentration-dependent measurements under fast neutron irradiation showed the lack of self-absorption in this doped system, with essentially linear concentration dependence and drastically enhanced scalability with greater than 91.9% of the expected LY achieved for a tenfold increase in thickness.<sup>[296]</sup>

Fast timing applications, in particular those in medical imaging (time-of-flight-positron emission tomography [TOF-PET]) and high-energy physics, put challenging requirements especially on the timing resolution of scintillating material. A possible way to overcome the limits of standard scintillators so far commonly used is based on the metascintillator concept,<sup>[297]</sup> combining and optimizing several functionalities in the same scintillator heterostructure. In such heterostructures, the semiconductor NCs with ultrafast decay times, such as lead halide perovskites, can serve as efficient time taggers.

Three different perovskite NCs, CsPbBr<sub>3</sub>, FAPbBr<sub>3</sub>, and CsPbI<sub>3</sub>, were investigated in the study by Maddalena.<sup>[298]</sup> Temperature-dependent RL measurements revealed that all NCs exhibit intense emission at cryogenic temperatures. CsPbBr<sub>3</sub> NCs exhibit negative temperature quenching (increasing emission with increasing temperature), leading to a high RL emission even at RT, with a deterministic LY of  $24\,000 \pm 2100$  ph MeV<sup>-1</sup>. On the other hand, FAPbBr<sub>3</sub> and CsPbI<sub>3</sub> NCs exhibit thermal quenching, leading to a lower RL emission at RT. The materials also exhibit very small afterglow with no traps. Investigated NCs display a fast RL decay time, with the average decay times below 6 ns for CsPbBr<sub>3</sub> and CsPbI<sub>3</sub> NCs

and below 20 ns for FAPbBr<sub>3</sub> NCs, faster than those of previous CdSe/ZnS NCs,<sup>[299]</sup> cadmium telluride (CdTe) NCs,<sup>[300]</sup> and commercial scintillators that are currently used for fast-timing applications.

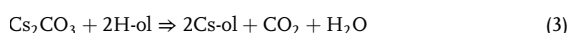
In the study by Kang et al.,<sup>[301]</sup> the authors study the time-resolved RL response of CsPbBr<sub>3</sub> QDs in their clustered state induced by  $\alpha$  particles. Based on the statistical analysis of timing characteristics, they assessed the potential of using perovskite nanomaterials in timing applications performing a comparative measurement with a CsI(Tl) scintillator. The RL yield and detection efficiency were estimated to be 2.95 ph keV<sup>-1</sup> and 29.2%, respectively, referring to the mean cluster thickness of 5 QD layers.

Lead halide perovskite NCs with 3D structure have direct bandgap<sup>[302]</sup> featuring one main PL peak.<sup>[18]</sup> Due to toxicity of Pb element and poor stability of lead halide perovskite NCs in air, a great deal of effort was devoted to develop lead-free alternatives with improved stability. Lead-free variants based on Bi<sup>3+</sup>, Sb<sup>3+</sup>, or Sn<sup>2+</sup> and lead-free double perovskites, such as Cs<sub>2</sub>AgBiBr<sub>6</sub> or Cs<sub>2</sub>AgInCl<sub>6</sub>, have attracted research attention. Interestingly, these reported lead-free perovskite NCs generally show an indirect-bandgap character. Consequently, the coexistence of direct and indirect transitions in some lead-free perovskite NCs could potentially induce the dual-color emission. For more details on lead-free perovskite NCs see, e.g., the recent review.<sup>[303]</sup>

### 10.3. Synthesis and Upscaling

The first synthesis that was introduced specifically for the colloidal CsPbX<sub>3</sub> NCs was hot injection.<sup>[18]</sup> This method is based on the precipitation of degassed precursors in an inert atmosphere at high temperatures (150–200 °C). This allows for good control of the reaction conditions and therefore good reproducibility. This method has been readily adapted for other shapes of NCs.<sup>[304–307]</sup>

First, cesium precursor (cesium oleate, Cs-ol) is synthesized. Degassed oleic acid is mixed with cesium carbonate in degassed 1-octadecene and the mixture is heated to 150 °C. Cs-ol is formed according to reaction (3) (-ol refers to the deprotonated form of oleic acid CH<sub>3</sub>(CH<sub>2</sub>)<sub>7</sub>CH = CH(CH<sub>2</sub>)<sub>7</sub>COO<sup>-</sup>).<sup>[308]</sup>



Next, degassed oleic acid, oleylamine, and lead halide are mixed in degassed 1-octadecene and the temperature is raised to 150–200 °C, depending on the desired size of NCs. Preheated (100 °C) Cs-ol is quickly injected and after a few seconds, the reaction is quenched in an ice-water bath (see Figure 13). The formed CsPbX<sub>3</sub> NCs are separated by centrifugation and dispersed in a nonpolar solvent, typically hexane. Formation of perovskite follows the salt metathesis reaction (4). However, other reaction mechanisms with various byproducts were suggested; see recently published Perspective for more details.<sup>[308]</sup>

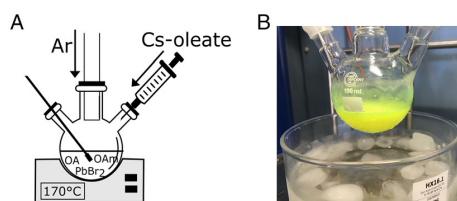
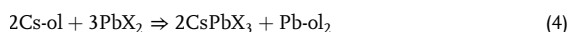
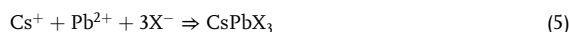


**Figure 13.** A) Schematic representation of the hot injection process. Reproduced under terms of the CC-BY license.<sup>[350]</sup> Copyright 2018, The Authors. Published by MDPI. B) Photograph of the as-synthesized CsPbBr<sub>3</sub> NCs after cooling in the ice-water bath.

Usually, the Cs-ol precipitates from 1-octadecene solution at RT and hence the preheating step before injection. A study by Lu et al.<sup>[309]</sup> points out that the reason behind this lies in strong permanent dipole of the Cs-ol molecule that significantly reduces its solubility in nonpolar solvents. To shield the polar Cs-ol molecule from the nonpolar solvent, they suggest using the ideal molar ratio 5 : 1 (oleic acid : Cs<sup>+</sup>) in Cs-ol synthesis that leads to the formation of reverse micelle, Cs<sup>+</sup> ion, capped by oleate molecules. Using at least this molar ratio during the synthesis, the Cs-ol no longer precipitates at RT from the 1-octadecene solution, which allows for better reproducibility of the subsequent hot injection synthesis.

Another widely used synthesis is the so-called room-temperature precipitation (RTP) method. This method was introduced for CsPbX<sub>3</sub> NCs shortly after the introduction of the hot injection synthesis.<sup>[310]</sup> However, a similar method was first introduced for CH<sub>3</sub>NH<sub>3</sub>PbX<sub>3</sub> in 2015 already, by that time called ligand-assisted reprecipitation (LARP) technique.<sup>[311]</sup> So by the time of adaptation of this protocol to CsPbX<sub>3</sub> NCs, it has already been an established method for hybrid organic–inorganic perovskites preparation.<sup>[312–316]</sup>

The method is rather simple in its principle. All the precursor ions are dissolved in the polar solvent (CsX and PbX<sub>2</sub> in dimethylformamide or dimethylsulfoxide) together with oleic acid and oleylamine. This solution is then swiftly added to a nonpolar solvent in which the polar solvent is soluble (e.g., toluene) and by this step, rapid precipitation of the product is induced (5).<sup>[310]</sup>



This method was also adapted for preparation of other NC shapes.<sup>[302,317–319]</sup> The example of adaptation to prepare nanoplatelets is schematically shown in Figure 14.

Other synthetic methods were developed for CsPbX<sub>3</sub> NCs including ultrasonic irradiation,<sup>[320–322]</sup> adaptation of classical heat-up method,<sup>[323–325]</sup> or solvothermal synthesis.<sup>[326,327]</sup>

The main idea behind many of the published alternative protocols was to enable scaling-up of the CsPbX<sub>3</sub> NC synthesis, which is not feasible for the original hot injection process. Even though hot injection yields NCs of better quality,<sup>[328,329]</sup> RTP has been identified as the viable option for the production scale-up.<sup>[330]</sup> Several studies reported successful scale-up of their protocols to a gram level.<sup>[323,331,332]</sup> However, this amount is still far from commercial production. It is also worth mentioning that



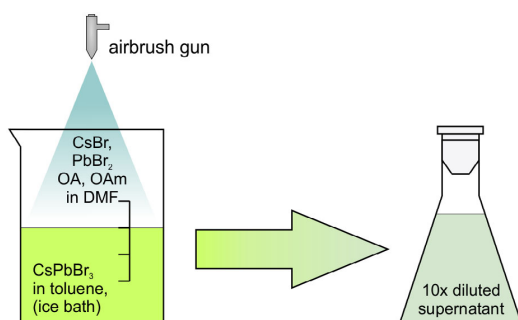


**Figure 14.** Schematic representation of RTP procedure adapted for nanoplatelets preparation using an airbrush gun. Reproduced under terms of the CC-BY license.<sup>[302]</sup> Copyright 2018, The Authors. Published by AIP Publishing.

some recent studies raised issues with reproducibility of the RTP synthesis; small variations of the synthetic protocol can lead to significant changes in optical properties and even compositional changes.<sup>[329,333]</sup>

#### 10.4. Nanocomposites

The applicability of lead halide perovskites is significantly limited due to their poor chemical stability against air moisture and oxygen.<sup>[334]</sup> Recent reviews explore their stability in detail, including proposed strategies to solve this by adjusting reaction conditions, changing composition, or surface passivation.<sup>[42,289]</sup> However, for application in scintillation detectors, immobilization of the NCs in a solid monolith matrix is needed. Some recent reviews discuss progress on such matrices as well<sup>[335,336]</sup> but with different target applications in mind. Their results are readily applicable in the field of materials for scintillation detectors and the reader is encouraged to get familiar with them.

##### 10.4.1. Plastic Matrix

The easiest way to incorporate perovskite QDs in a solid matrix is to mix them with a kind of plastic. The most basic method is to dissolve a polystyrene in a toluene, mix it with CsPbX<sub>3</sub> colloidal solution in toluene, and leave it to evaporate. It has been shown that in this way, a nanocomposite can be fabricated using CsPbBr<sub>3</sub> nanoplatelets with blue emission (i.e., with strong quantum confinement effect) that, while properly stored in a cool, dark place, can maintain its blue emission.<sup>[302]</sup> However, this preliminary study showed only a weak radioluminescence response, as shown in **Figure 15**.

More recently, a similar approach was exploited to prepare CsPbBr<sub>3</sub> nanocomposite in a polymethylmethacrylate (PMMA) matrix.<sup>[337]</sup> PMMA was dissolved in CHCl<sub>3</sub> and the CsPbBr<sub>3</sub> toluene solution was added into the mixture. However, they controlled the evaporation/drying time to  $\approx 22$  h to avoid cracks and bubbles that can occur upon fast evaporation in a thick layer. They also added a perylene dyad wavelength shifter into the mixture to suppress severe reabsorption caused by a small Stokes shift that is typical for semiconductor NCs. They demonstrate

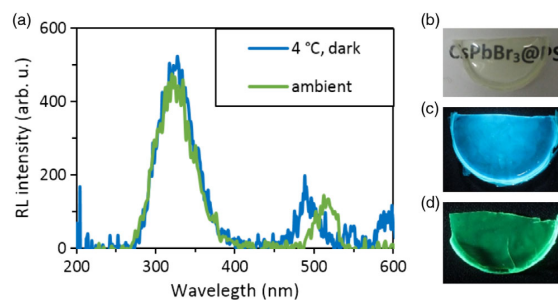


**Figure 15.** a) Radioluminescence of CsPbBr<sub>3</sub>-polystyrene nanocomposite stored in a refrigerator (blue line) and under ambient conditions (green line), emission peaking at 320 nm is from polystyrene, emission around 500 nm is from CsPbBr<sub>3</sub> NCs. b) Photograph of the nanocomposite in daylight; c,d) Photographs of the nanocomposite stored in a refrigerator and under ambient conditions, respectively, under UV illumination. Reproduced under terms of the CC-BY license.<sup>[302]</sup> Copyright 2018, The Authors. Published by AIP Publishing.

radioluminescence intensities comparable with commercial Bi<sub>4</sub>Ge<sub>3</sub>O<sub>12</sub> (BGO) crystal, thanks to essentially no loss of sensitization due to perfect spectral overlap of CsPbBr<sub>3</sub> emission spectrum with perylene dyad absorption. Their nanocomposite shows good long-term stability (no degradation after 6 months of storage in air) and radiation hardness (>85% of radioluminescence intensity is retained after irradiation by 800 Gy of X-rays).

Another approach is to mix the colloidal solution with a monomer and then induce polymerization. This approach is somewhat risky, because the radicals generated during the polymerization process may damage and/or strip away the surface ligands, that are already highly dynamically bound to the NC surface.<sup>[338]</sup>

This approach was exploited in its most simple and effective way by Chhangani.<sup>[339]</sup> The authors prepared CsPbBr<sub>3</sub> NCs directly in the methyl methacrylate (MMA) monomer by the modified RTP method and this solution was directly polymerized by gamma irradiation without any catalysts. However, some degree of aggregation occurred in MMA already. NCs with wide size distribution centered at 43 nm were prepared, that resulted in redshift of PL compared with other NCs prepared by the similar method. After polymerization, the emission is slightly more redshifted, and the peak is widened and less intense, suggesting some degree of degradation, but a more detailed explanation of this phenomenon was not in the scope of this study. RT scintillation response of CsPbBr<sub>3</sub> NCs toward alpha particles was demonstrated for this nanocomposite.

However, a similar nanocomposite based on polybutylmethacrylate (PBMA) was very successfully prepared by polymerization, enabled by including a ligand exchange step. In the study by Nie et al.,<sup>[340]</sup> CsPbBr<sub>3</sub> NCs were treated with BMEP (bis(2-(methacryloyloxy)ethyl) phosphate) ligand that has a methacrylate tail, that can polymerize with butyl methacrylate. This ensured high transmittance of the prepared nanocomposite (i.e., the NCs were well dispersed in the matrix). The stability was tested by immersion in water for 7 days during which no decrease in PL intensity was observed. The collected X-ray image of resistor with good spatial resolution showed a potential of CsPbBr<sub>3</sub>/PBMA nanocomposites for application in X-ray imaging.

#### 10.4.2. Glass Ceramics

Incorporation of CsPbX<sub>3</sub> NCs into a glass matrix has attracted considerable attention recently, because it promises superior stability compared with the plastic matrices.<sup>[341–346]</sup> The fabrication technique is a conventional melt-quenching process. To crystallize CsPbX<sub>3</sub> NCs in the precursor glass, several hours of heat treatment are required, ranging from 340 °C for 15 h<sup>[343]</sup> to 550 °C for 4–18 h.<sup>[346]</sup>

A basic example of such nanocomposites was studied in the work by Wang et al.<sup>[341]</sup> The authors annealed borate precursor glass at 470 and 520 °C for just 1 h. They demonstrated that higher temperature led to an opaque sample due to too large NCs causing significant light scattering. On the other hand, nanocomposites treated at 470 °C had very weak radioluminescence intensity and both samples had immeasurable light yield under gamma rays. They prepared nanocomposites based on CsPbBr<sub>3</sub> and CsPb(Cl,Br)<sub>3</sub> demonstrated faster decay times with increasing Cl content, but even lower luminescence intensities. On the other hand, they demonstrated good stability of such glass ceramics. X-ray irradiation caused progressively darker spots with increasing power input (up to 12 W) with progressively lower luminescence intensity under UV illumination. However, this radiation damage was reversible by annealing at temperatures above glass transition temperature (350 °C) for 2 h, showing that this material is reusable even after high-power X-ray exposure. The authors also demonstrated good stability against heating-cooling cycle (25–300 °C).

More recent studies clearly turned their attention to improved properties by RE elements (RE) doping, for example, Eu<sup>3+</sup>,<sup>[342,343]</sup> Ce<sup>3+</sup>,<sup>[346]</sup> and Lu<sup>3+</sup>.<sup>[345]</sup> Overall, RE doping caused significant improvement of transmittance that was accompanied by less light scattering in the sample, which is important to achieve high-quality X-ray imaging. RE ions in precursor glass probably serve as nucleating agents that promote rapid growth and precipitation of CsPbX<sub>3</sub>, thus preparing more uniformly distributed, smaller crystals.<sup>[342,344]</sup> A similar effect was achieved by introducing AgCl into the precursor glass.<sup>[343]</sup>

Also, the radioluminescence performance has been significantly improved by RE doping. Not only the emission from CsPbX<sub>3</sub> was enhanced,<sup>[346]</sup> but in case of Eu<sup>3+</sup> doping, strong emission from dopant emerged to accompany the enhanced CsPbX<sub>3</sub> emission, that caused larger Stokes shift in such a material, effectively suppressing self-absorption.<sup>[342,344]</sup>

Improved stability against various conditions was successfully tested, for example, against humidity,<sup>[342,344,346]</sup> heat-cooling cycles,<sup>[343]</sup> and X-ray exposure.<sup>[344]</sup> Exposing the material to high radiation doses (for 120 h by dose rate of 8 mGy<sub>air</sub> s<sup>-1</sup>) caused the radiation damage, but it was reversible by thermal annealing at 300 °C for 3 h.<sup>[345]</sup> Overall, this glass ceramics based on CsPbX<sub>3</sub> NCs was proven very promising for scintillation application. High-quality X-ray images were achieved<sup>[342,344,345]</sup> with spatial resolution as high as ≈15–17 lp mm<sup>-1</sup>.<sup>[342,345]</sup>

To further improve transmittance and radioluminescent properties, the use of tellurite glass was proposed.<sup>[343]</sup> Tellurite glass is beneficial thanks to its larger density (>5.0 g cm<sup>-3</sup>) that results in better stopping power. Moreover, its refractive index is large (>2.0), leading to smaller mismatch with CsPbX<sub>3</sub> NCs, thus

significantly improving transparency of the resulting nanocomposite.

#### 10.4.3. Polycrystalline Thin Films

Lead halide perovskite NCs have been selected as potential candidates for ultrafast detector development for TOF-PET and high-energy physics.<sup>[347]</sup> The proposed strategy is to fabricate a sandwich-like structure combining layers of a single-crystal scintillator and semiconductor NCs, as shown in **Figure 16**. The bulk scintillator (e. g. LYSO:Ce, BGO, or Gd<sub>3</sub>(Ga,Al)<sub>5</sub>O<sub>12</sub>:Ce–GGAG:Ce) possesses high stopping power and energy resolution, while NCs (e. g. CsPbX<sub>3</sub> or CdSe) have ultrafast decay times. A combination of such materials results in improved coincidence time resolution (CTR) that ultimately leads to better spatial resolution of TOF-PET detectors.<sup>[347]</sup> This concept was already tested for CdSe nanoplatelets and LYSO:Ce pixel.<sup>[348]</sup>

The first preliminary study following this concept was fabricating CsPbBr<sub>3</sub> thin films on LYSO:Ce bulk scintillator wafer.<sup>[349]</sup> CsPbBr<sub>3</sub> NCs were prepared by RTP method and then drop cast on the LYSO:Ce wafer. Enhanced CsPbBr<sub>3</sub> radioluminescence was observed in the steady-state radioluminescence spectrum and fast decay components of CsPbBr<sub>3</sub> NCs were preserved in both photo- and radioluminescence decays. However, the scintillation decay measurement had rather a poor dynamic range, suggesting poor scintillation light output of such samples. The reason for such performance probably lies in significant contamination by the Cs<sub>4</sub>PbBr<sub>6</sub> phase that was later found to be detrimental for the scintillation light output of CsPbBr<sub>3</sub> NCs.<sup>[329]</sup>

Recently, CsPbBr<sub>3</sub> thin films were prepared on GGAG:Ce scintillating wafer.<sup>[350]</sup> The NCs prepared by the hot injection method featured pure CsPbBr<sub>3</sub> phase (no presence of Cs<sub>4</sub>PbBr<sub>6</sub> phase) and thin films were fabricated using a spin-coating method. A synergic effect was demonstrated; both CsPbBr<sub>3</sub> and GGAG:Ce radioluminescence emissions were enhanced in the steady-state radioluminescence spectra, the former probably by absorption and subsequent reemission of GGAG:Ce emission by CsPbBr<sub>3</sub> layer and the latter by light-guiding effect of cracks in the CsPbBr<sub>3</sub> layer. This enhancement was also observed in the subnanosecond time gate, suggesting the applicability of such composites in future fast timing detectors.

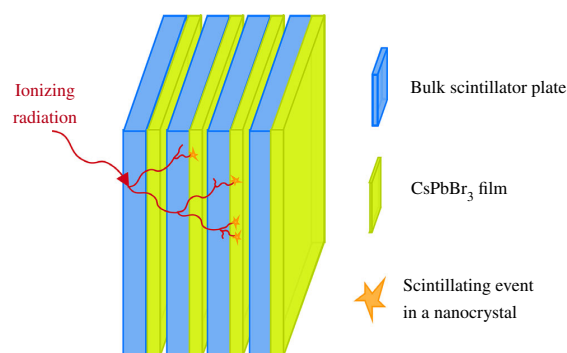


**Figure 16.** Schematic representation of the proposed sandwich pixel for ultrafast detector system.

However, such unprotected thin films suffer from poor stability. To improve thin-film stability, solution-protected annealing strategy was successfully implemented.<sup>[351]</sup> After purification of hot injection-prepared NCs, the colloidal solution returned to the mixture of 1-octadecene, oleic acid, and oleylamine and NCs were treated at 80 °C. Obtained NCs had better crystallinity, a well-passivated surface, and showed improved luminescence properties and stability toward the heating-cooling cycle, air, UV, electron, and X-Ray irradiation. X-ray imaging capability of a thin film fabricated using such treated NCs was also demonstrated.

Similarly, as for bulk monoliths of glass or plastic, encapsulation in matrices has been explored for enhancing stability of thin films as well. Recently, CsPbBr<sub>3</sub> NCs embedded in Al<sub>2</sub>O<sub>3</sub> arrays have been shown to have significantly improved stability compared with conventional dense nanocrystalline thin films and X-ray imaging capability with superior resolution of 250 lp mm<sup>-1</sup>.<sup>[352]</sup> The pore diameter was 300 nm, with 20 μm pore depth. CsPbBr<sub>3</sub> NCs were prepared beforehand by the hot injection method and then incorporated into Al<sub>2</sub>O<sub>3</sub> arrays by negative pressure filling, forming a micropillar structure. These micropillars serve as optical waveguides that significantly improve spatial resolution compared with the standard thin film of the same thickness (20 μm).

Another approach was explored by Zhao et al.,<sup>[353]</sup> who fabricated perovskite-based flexible detectors by incorporating MAPb(I<sub>0.9</sub>Cl<sub>0.1</sub>)<sub>3</sub> into a 100 μm-thick porous nylon membrane. They prepared ultraconcentrated saturated MAPbI<sub>3</sub> solutions (2.2 mol dm<sup>-3</sup>) in a mixture of 2-methoxyethanol and methylammonium chloride. This solution was repeatedly infiltrated into the membrane pores by negative pressure filling and subsequent annealing at 150 °C for 2 h. This led to a fully filled membrane by interconnected perovskite crystals allowing efficient charge transport and providing high stopping power of the composite. Flexible scintillation screen with resolution of 3.5 lp mm<sup>-1</sup> was achieved and its applicability in industrial X-ray imaging and defect detection was demonstrated.

## 11. Conclusion

We gave an extensive overview of the R&D of halide scintillators in the last decade going from the bulk single crystals through microstructured systems to scintillating NCs. In bulk single crystals, the multicomponent compositions are explored to achieve optimal performance and create an application-specific scintillator. Moreover, codoping is used to improve the performance of both classical and recent innovative scintillators. Ceramic technology has been also applied for several material compositions to create transparent monoliths. In microstructured scintillators, light guiding is exploited to significantly improve 2D resolution in X-ray imaging techniques. Complex eutectic compositions are explored to maximize the difference in refraction index and to enable the detection of both γ (X-ray) and neutrons. In lead halide perovskite NCs, the synthesis routes are being optimized and NC embedding in various matrices is used to increase their stability. Moreover, ensembles of NC-based materials with classical scintillators (so-called metascintillators) possess both high stopping power and light output of classical scintillator and ultrafast

emission of NCs. Research in all the above-mentioned fields achieved significant progress in the last decade and several materials emerged as candidates for commercialization. With new applications requiring high-performance scintillators with tailored parameters, modern halide scintillators could play an increasing role in the future scintillation market.

## Supporting Information

Supporting Information is available from the Wiley Online Library or from the author.

## Acknowledgements

The authors would like to dedicate this article to a colleague and a long-term senior researcher of the Institute of Physics of the Czech Academy of Sciences Dr. Karel Nitsch. He significantly contributed to the research of dielectric materials for optical applications (based on e.g., halides, oxides, and phosphate glasses), development of crystal growth technology, and education and popularization of the field in the crystal growth community. He was a leading coordinator and founder of the Czechoslovak Association for Crystal Growth in 1990 and served as its chairman until 2012. Further, he periodically organized domestic conferences and seminars and contributed into international journals and periodicals. Financial support of the Czech Science Foundation, grant number GA20-06374S, is acknowledged.

## Conflict of Interest

The authors declare no conflict of interest.

## Keywords

halides, nanocrystals, scintillator, single crystals

Received: January 13, 2022

Revised: March 18, 2022

Published online:

- [1] M. Ishii, M. Kobayashi, *Prog. Cryst. Growth Charact. Mater.* **1992**, *23*, 245.
- [2] M. Nikl, *Phys. Status Solidi A* **2000**, *178*, 595.
- [3] C. W. E. van Eijk, *Phys. Med. Biol.* **2002**, *47*, R85.
- [4] *Inorganic Scintillators for Detector Systems: Physical Principles and Crystal Engineering* (Eds: P. Lecoq, A. Annenkov, A. Gektin, M. Korzhik, C. Pedrini), Springer, Berlin, Heidelberg **2006**, pp. 81–122.
- [5] M. Nikl, A. Yoshikawa, *Adv. Opt. Mater.* **2015**, *3*, 463.
- [6] P. Dorenbos, *Opt. Mater.: X* **2019**, *1*, 100021.
- [7] K. W. Krämer, P. Dorenbos, H. U. Güdel, C. W. E. van Eijk, *J. Mater. Chem.* **2006**, *16*, 2773.
- [8] A. Burger, E. Rowe, M. Groza, K. Morales Figueroa, N. J. Cherepy, P. R. Beck, S. Hunter, S. A. Payne, *Appl. Phys. Lett.* **2015**, *107*, 143505.
- [9] H. J. Kim, G. Rooh, S. Kim, *J. Lumin.* **2017**, *186*, 219.
- [10] T. Jun, K. Sim, S. Iimura, M. Sasase, H. Kamioka, J. Kim, H. Hosono, *Adv. Mater.* **2018**, *30*, 1804547.

- [11] M. Nikl, E. Mihokova, K. Nitsch, K. Polak, M. Rodova, M. Dusek, G. Pazzi, P. Fabeni, L. Salvini, M. Gurioli, *Chem. Phys. Lett.* **1994**, *220*, 14.
- [12] K. Nitsch, V. Hamplová, M. Nikl, K. Polák, M. Rodová, *Chem. Phys. Lett.* **1996**, *258*, 518.
- [13] M. Nikl, K. Nitsch, K. Polak, G. P. Pazzi, P. Fabeni, D. S. Citrin, M. Gurioli, *Phys. Rev. B* **1995**, *51*, 5192.
- [14] M. Nikl, K. Nitsch, E. Mihoková, K. Polák, P. Fabeni, G. P. Pazzi, M. Gurioli, S. Santucci, R. Phani, A. Scacco, F. Somma, *Physica E* **1999**, *4*, 323.
- [15] W.-J. Yin, T. Shi, Y. Yan, *Appl. Phys. Lett.* **2014**, *104*, 063903.
- [16] A. Miyata, A. Mitioglu, P. Plochocka, O. Portugall, J. T.-W. Wang, S. D. Stranks, H. J. Snaith, R. J. Nicholas, *Nat. Phys.* **2015**, *11*, 582.
- [17] L. C. Schmidt, A. Pertegás, S. González-Carrero, O. Malinkiewicz, S. Agouram, G. Mínguez Espallargas, H. J. Bolink, R. E. Galian, J. Pérez-Prieto, *J. Am. Chem. Soc.* **2014**, *136*, 850.
- [18] L. Protesescu, S. Yakunin, M. I. Bodnarchuk, F. Krieg, R. Caputo, C. H. Hendon, R. X. Yang, A. Walsh, M. V. Kovalenko, *Nano Lett.* **2015**, *15*, 3692.
- [19] M. Kulbak, S. Gupta, N. Kedem, I. Levine, T. Bendikov, G. Hodes, D. Cahen, *J. Phys. Chem. Lett.* **2016**, *7*, 167.
- [20] A. Swarnkar, A. R. Marshall, E. M. Sanehira, B. D. Chernomordik, D. T. Moore, J. A. Christians, T. Chakrabarti, J. M. Luther, *Science* **2016**, *354*, 92.
- [21] R. Wang, M. Mujahid, Y. Duan, Z.-K. Wang, J. Xue, Y. Yang, *Adv. Funct. Mater.* **2019**, *29*, 1808843.
- [22] J. Zhang, G. Hodes, Z. Jin, S. (Frank) Liu, *Angew. Chem., Int. Ed.* **2019**, *58*, 15596.
- [23] M. Liu, H. Pasanen, H. Ali-Löyty, A. Hiltunen, K. Lahtonen, S. Qudsia, J.-H. Småt, M. Valden, N. V. Tkachenko, P. Vivo, *Angew. Chem., Int. Ed.* **2020**, *59*, 22117.
- [24] P. Ramasamy, D.-H. Lim, B. Kim, S.-H. Lee, M.-S. Lee, J.-S. Lee, *Chem. Commun.* **2016**, *52*, 2067.
- [25] I. M. Asuo, P. Fourmont, I. Ka, D. Gedamu, S. Bouzidi, A. Pignolet, R. Nechache, S. G. Cloutier, *Small* **2019**, *15*, e1804150.
- [26] J. Miao, F. Zhang, *J. Mater. Chem. C* **2019**, *7*, 1741.
- [27] J. Song, J. Li, X. Li, L. Xu, Y. Dong, H. Zeng, *Adv. Mater.* **2015**, *27*, 7162.
- [28] Y. H. Song, J. S. Yoo, B. K. Kang, S. H. Choi, E. K. Ji, H. S. Jung, D. H. Yoon, *Nanoscale* **2016**, *8*, 19523.
- [29] L. N. Quan, F. P. García de Arquer, R. P. Sabatini, E. H. Sargent, *Adv. Mater.* **2018**, *30*, 1801996.
- [30] N. Mondal, A. De, A. Samanta, *ACS Energy Lett.* **2019**, *4*, 32.
- [31] Y. Wei, Z. Cheng, J. Lin, *Chem. Soc. Rev.* **2019**, *48*, 310.
- [32] T. Xuan, J. Huang, H. Liu, S. Lou, L. Cao, W. Gan, R.-S. Liu, J. Wang, *Chem. Mater.* **2019**, *31*, 1042.
- [33] A. Swarnkar, R. Chulliyil, V. K. Ravi, M. Irfanullah, A. Chowdhury, A. Nag, *Angew. Chem., Int. Ed.* **2015**, *54*, 15424.
- [34] M. Liu, G. Zhong, Y. Yin, J. Miao, K. Li, C. Wang, X. Xu, C. Shen, H. Meng, *Adv. Sci.* **2017**, *4*, 1700335.
- [35] B. Liu, B. Liu, J. Li, J. Li, J. Li, G. Duan, M. Ji, Y. Lu, T. Yan, B. Cao, Z. Liu, Z. Liu, *Opt. Express* **2020**, *28*, 10714.
- [36] W. Lin, Q. Nie, X.-F. Jiang, X. Jiang, K. Wang, L. Shui, S. Priya, G. Zhou, X. Hu, *Front. Chem.* **2020**, *8*, 574.
- [37] Y. Wang, X. Li, J. Song, L. Xiao, H. Zeng, H. Sun, *Adv. Mater.* **2015**, *27*, 7101.
- [38] Y. Jia, R. A. Kerner, A. J. Grede, B. P. Rand, N. C. Giebink, *Nat. Photonics* **2017**, *11*, 784.
- [39] T. J. S. Evans, A. Schlaus, Y. Fu, X. Zhong, T. L. Atallah, M. S. Spencer, L. E. Brus, S. Jin, X.-Y. Zhu, *Adv. Opt. Mater.* **2018**, *6*, 1700982.
- [40] L.-J. Xu, M. Worku, Q. He, B. Ma, *MRS Bull.* **2020**, *45*, 458.
- [41] O. D. I. Moseley, T. A. S. Doherty, R. Parmee, M. Anaya, S. D. Stranks, *J. Mater. Chem. C* **2021**, *9*, 11588.
- [42] S. Sarkar, *Phys. Status Solidi A* **2021**, *218*, 2100185.
- [43] H. Yang, H. Li, R. Yuan, J. Chen, J. Zhao, S. Wang, Y. Liu, Q. Li, Z. Zhang, *J. Mater. Chem. C* **2021**, *9*, 7905.
- [44] M. Zhuravleva, L. Stand, H. Wei, C. Hobbs, L. A. Boatner, J. O. Ramey, K. Shah, A. Burger, E. Rowe, P. Bhattacharya, E. Tupitsyn, C. L. Melcher, in *2013 IEEE Nuclear Science Symp. and Medical Imaging Conf. (Nss/Mic)*, IEEE, New York, **2013**.
- [45] S. Lam, C. Guguschev, A. Burger, M. Hackett, S. Motakef, *J. Cryst. Growth* **2018**, *483*, 121.
- [46] F. Rosenberger, *Ultrapurity; Methods and Techniques* (Eds: M. Zief, R. Speights), M. Dekker, New York **1972**, pp. 3–69.
- [47] K. Nitsch, A. Cihlák, Z. Málková, M. Rodová, M. Vaněček, *J. Cryst. Growth* **1993**, *131*, 612.
- [48] M. Lébl, J. Trnka, *Z. Physik* **1965**, *186*, 128.
- [49] S. Sakuragi, *Am. J. Chem. Eng.* **2021**, *9*, 25.
- [50] E. Brown, E. Kumi-Barimah, U. Hömmerich, A. G. Bluiett, S. B. Trivedi, *J. Cryst. Growth* **2014**, *393*, 159.
- [51] R. Hofstadter, *Europium Activated Strontium Iodide Scintillators*, U.S. Pat. 3,373,279 2, United States Patent Office, **1968**.
- [52] U. N. Roy, Y. Cui, M. Guo, M. Groza, A. Burger, G. J. Wagner, T. J. Carrig, S. A. Payne, *J. Cryst. Growth* **2003**, *258*, 331.
- [53] L. Stand, D. Rutstrom, M. Koschan, M.-H. Du, C. Melcher, U. Shirwadkar, J. Glodo, E. Van Loef, K. Shah, M. Zhuravleva, *Nucl. Instrum. Methods Phys. Res., Sect. A* **2021**, *991*, 164963.
- [54] W. G. Pfann, *Trans. Am. Inst. Min. Metall. Eng.* **1952**, *194*, 747.
- [55] A. C. Lindsey, M. Zhuravleva, L. Stand, Y. Wu, C. L. Melcher, *Opt. Mater.* **2015**, *48*, 1.
- [56] I. K. Jones, U. Hömmerich, E. Brown, S. B. Trivedi, *Solid State Lasers XXIII: Technology and Devices*, SPIE Bellingham, Washington, **2014**, pp. 302–307.
- [57] H. Kanzaki, S. Sakuragi, *J. Phys. Soc. Jpn.* **1969**, *27*, 109.
- [58] P. W. Bridgman, *Proc. Am. Acad. Arts Sci.* **1925**, *60*, 385.
- [59] D. C. Stockbarger, *Rev. Sci. Instrum.* **1936**, *7*, 133.
- [60] A. C. Lindsey, Y. Wu, M. Zhuravleva, M. Loyd, M. Koschan, C. L. Melcher, *J. Cryst. Growth* **2017**, *470*, 20.
- [61] M. Loyd, A. Lindsey, Y. Wu, L. Stand, M. Folsom, D. Rutstrom, M. Koschan, C. L. Melcher, M. Zhuravleva, *Nucl. Instrum. Methods Phys. Res., Sect. A* **2019**, *914*, 8.
- [62] S. Eichler, T. Bünger, M. Butter, R. Rühmann, M. Scheffer-Czygan, *US9368585B2*, **2016**.
- [63] B. Ferrand, Y. Grange, EP0130865A1, **1985**.
- [64] R. Hofstadter, *Phys. Rev.* **1949**, *75*, 796.
- [65] L. A. Boatner, J. O. Ramey, J. A. Kolopus, R. Hawrami, W. M. Higgins, E. van Loef, J. Glodo, K. S. Shah, E. Rowe, P. Bhattacharya, E. Tupitsyn, M. Groza, A. Burger, N. J. Cherepy, S. A. Payne, *J. Cryst. Growth* **2013**, *379*, 63.
- [66] Y. Wu, Q. Li, D. J. Rutstrom, I. Greeley, L. Stand, M. Loyd, M. Koschan, C. L. Melcher, *Nucl. Instrum. Methods Phys. Res., Sect. A* **2020**, *954*, 161242.
- [67] E. V. D. van Loef, P. Dorenbos, C. W. E. van Eijk, K. Krämer, H. U. Güdel, *Appl. Phys. Lett.* **2001**, *79*, 1573.
- [68] K. J. Kim, Y. Furuya, K. Kamada, R. Murakami, V. V. Kochurikhin, M. Yoshino, H. Chiba, S. Kurosawa, A. Yamaji, Y. Shoji, S. Toyoda, H. Sato, Y. Yokota, Y. Ohashi, A. Yoshikawa, *Crystals* **2020**, *10*, 584.
- [69] N. Kutsuzawa, Y. Takizawa, K. Kamada, M. Yoshino, K. J. Kim, R. Murakami, Y. Shoji, V. V. Kochurikhin, A. Yoshikawa, *J. Cryst. Growth* **2021**, *576*, 126373.
- [70] R. Hawrami, E. Ariesanti, A. Burger, H. Parkhe, *Opt. Mater.* **2021**, *121*, 111495.
- [71] L. Stand, M. Zhuravleva, J. Johnson, M. Koschan, E. Lukosi, C. L. Melcher, *Nucl. Instrum. Methods Phys. Res., Sect. A* **2020**, *962*, 163700.

- [72] R. Král, V. Babin, E. Mihóková, M. Buryi, V. V. Laguta, K. Nitsch, M. Nikl, *J. Phys. Chem. C* **2017**, 121, 12375.
- [73] M. Buryi, R. Král, V. Babin, J. Páterek, V. Vaněček, P. Veverka, M. Kohoutková, V. Laguta, M. Fasoli, I. Villa, F. Cova, A. Vedda, M. Nikl, *J. Phys. Chem. C* **2019**, 123, 19402.
- [74] D. Yuan, *ACS Appl. Mater. Interfaces* **2020**, 12, 38333.
- [75] E. D. Bourret-Courchesne, G. Bizarri, R. Borade, Z. Yan, S. M. Hanrahan, G. Gundiah, A. Chaudhry, A. Canning, S. E. Derenzo, *Nucl. Instrum. Methods Phys. Res., Sect. A* **2009**, 612, 138.
- [76] G. Bizarri, E. D. Bourret-Courchesne, Z. Yan, S. E. Derenzo, *IEEE Trans. Nucl. Sci.* **2011**, 58, 3403.
- [77] J. Czochralski, *Z. Phys. Chem.* **1918**, 92U, 219.
- [78] K. H. J. C. Marshall, R. Wickham, *J. Sci. Instrum.* **1958**, 35, 121.
- [79] H. Scheel, *Crystal Growth Technology*, J. Wiley, Chichester, West Sussex New York **2003**.
- [80] J. Kvapil, J. Kvapil, B. Manek, B. Perner, R. Aufrata, P. Schauer, *J. Cryst. Growth* **1981**, 52, 542.
- [81] A. Yoshikawa, K. Kamada, S. Kurosawa, Y. Shoji, Y. Yokota, V. I. Chani, M. Nikl, *J. Lumin.* **2016**, 169, 387.
- [82] P. E. Tomaszewski, *J. Cryst. Growth* **2002**, 236, 1.
- [83] G. Teal, J. Little, *Phys. Rev.* **1950**, 78, 647.
- [84] W. Bond, W. Mason, H. Mckimmin, K. Olsen, G. Teal, *Phys. Rev.* **1950**, 78, 176.
- [85] Z. Yan, T. Shalapska, E. D. Bourret, *J. Cryst. Growth* **2016**, 435, 42.
- [86] J. Tonn, A. N. Danilewsky, A. Croell, M. Matuchova, J. Maixner, *J. Cryst. Growth* **2011**, 318, 558.
- [87] Y. Takizawa, K. Kamada, N. Kutsuzawa, M. Yoshino, S. Yamamoto, K. Jin Kim, R. Murakami, V. V. Kochurikhin, A. Yoshikawa, *J. Cryst. Growth* **2021**, 572, 126266.
- [88] G. Rooh, H. J. Kim, S. Kim, *Key Eng. Mater.* **2010**, 442, 275.
- [89] E. Galenin, O. Sidletskiy, C. Dujardin, A. Gektin, *IEEE Trans. Nucl. Sci.* **2018**, 65, 2174.
- [90] S. Kyropoulos, *Z. Anorg. Allg. Chem.* **1926**, 154, 308.
- [91] A. Novoselov, *J. Cryst. Growth* **2022**, 578, 126431.
- [92] T. Asahi, T. Yabe, K. Sato, *J. Electron. Mater.* **2004**, 33, 651.
- [93] J. B. Levine, R. Burks, J. Ciraldo, M. Montgomery, A. Novoselov, S. Podlozhenov, *Window and Dome Technologies and Materials XIII*, SPIE Bellingham, Washington, **2013**, pp. 80–85.
- [94] A. Menzies, *Proc. Phys. Soc., London, Sect. B* **1952**, 65, 576.
- [95] A. Levaldi, G. Spinolo, *Nuovo Cimento* **1962**, 26, 1153.
- [96] V. Taranyuk, A. Gektin, N. Shiran, V. Shlyakhturov, S. Gridin, I. Boiaryntseva, D. Sofronov, *J. Cryst. Growth* **2013**, 380, 205.
- [97] H. E. Labelle, A. I. Mlavsky, *Nature* **1967**, 216, 574.
- [98] A. V. Stepanov, *Soviet Phys.-Tech. Phys.* **1959**, 4, 339.
- [99] H. E. LaBelle, *J. Cryst. Growth* **1980**, 50, 8.
- [100] C. B. Finch, G. W. Clark, O. C. Kopp, *J. Cryst. Growth* **1975**, 29, 269.
- [101] Q. Yao, L. Liu, W. Dong, H. Wen, Q. Wang, J. Li, J. Wang, *Opt. Mater. Express* **2019**, 9, 4742.
- [102] G. I. Rogalski, V. I. Vettegren, V. V. Peller, V. A. Ryzhov, E. Hartmann, *J. Cryst. Growth* **1987**, 82, 162.
- [103] G. Calvert, C. Gugushev, A. Burger, M. Groza, J. J. Derby, R. S. Feigelson, *J. Cryst. Growth* **2016**, 455, 143.
- [104] G. Calvert, S. Swider, F. Ruta, G. Rossman, R. S. Feigelson, *J. Cryst. Growth* **2018**, 498, 263.
- [105] A. Datta, P. Becla, C. Gugushev, S. Motakef, *J. Cryst. Growth* **2018**, 483, 211.
- [106] C. Gugushev, G. Calvert, S. Podowitz, A. Vailionis, A. Yeckel, R. S. Feigelson, *J. Cryst. Growth* **2014**, 404, 231.
- [107] A. Yeckel, R. S. Feigelson, J. J. Derby, in (Eds: M. Fiederle, A. Burger, L. Franks, R.B. James), *Hard X-Ray, Gamma-Ray, and Neutron Detector Physics XV*, SPIE, San Diego, CA, **2013**, p. 88520V.
- [108] D.-H. Yoon, I. Yonenaga, T. Fukuda, N. Ohnishi, *J. Cryst. Growth* **1994**, 142, 339.
- [109] S. Uda, J. Kon, K. Shimamura, T. Fukuda, *J. Cryst. Growth* **1996**, 167, 64.
- [110] B. M. Epelbaum, K. Inaba, S. Uda, T. Fukuda, *J. Cryst. Growth* **1997**, 178, 426.
- [111] Y. M. Yu, V. I. Chani, K. Shimamura, T. Fukuda, *J. Cryst. Growth* **1997**, 171, 463.
- [112] A. Yoshikawa, B. M. Epelbaum, K. Hasegawa, S. D. Durbin, T. Fukuda, *J. Cryst. Growth* **1999**, 205, 305.
- [113] A. M. E. Santo, B. M. Epelbaum, S. P. Morato, N. D. Vieira, S. L. Baldochi, *J. Cryst. Growth* **2004**, 270, 121.
- [114] K. Oikawa, R. Saito, K. Anzai, H. Ishikawa, Y. Sutou, T. Otori, A. Yoshikawa, V. A. Chernenko, S. Besseghini, A. Gambardella, R. Kainuma, K. Ishida, *Mater. Trans.* **2009**, 50, 934.
- [115] Y. Yokota, T. Yanagida, Y. Fujimoto, M. Nikl, A. Yoshikawa, *Radiat. Meas.* **2010**, 45, 472.
- [116] Y. Yokota, K. Nishimoto, S. Kurosawa, D. Totsuka, A. Yoshikawa, *J. Cryst. Growth* **2013**, 375, 49.
- [117] Y. Yokota, N. Kawaguchi, K. Fukuda, T. Yanagida, A. Yoshikawa, M. Nikl, *J. Cryst. Growth* **2011**, 318, 908.
- [118] R. Kral, K. Nitsch, V. Babin, J. Sulc, H. Jelinkova, Y. Yokota, A. Yoshikawa, M. Nikl, *Opt. Mater.* **2013**, 36, 214.
- [119] Y. Yokota, S. Kurosawa, Y. Shoji, Y. Ohashi, K. Kamada, A. Yoshikawa, *Opt. Mater.* **2017**, 65, 46.
- [120] S. Kurosawa, S. Kodama, Y. Yokota, T. Horiai, A. Yamaji, Y. Shoji, R. Král, J. Pejchal, Y. Ohashi, K. Kamada, M. Nikl, A. Yoshikawa, *J. Instrum.* **2017**, 12, C02042.
- [121] V. Vanecek, R. Kral, J. Páterek, V. Babin, V. Jary, J. Hybler, S. Kodama, S. Kurosawa, Y. Yokota, A. Yoshikawa, M. Nikl, *J. Cryst. Growth* **2020**, 533, 125479.
- [122] P. Rudolph, *Prog. Cryst. Growth Charact. Mater.* **1994**, 29, 275.
- [123] W. Gault, E. Monberg, J. Clemans, *J. Cryst. Growth* **1986**, 74, 491.
- [124] A. Tanaka, Y. Masa, S. Seto, T. Kawasaki, *J. Cryst. Growth* **1989**, 94, 166.
- [125] K. Lay, D. Nichols, S. Mcdevitt, B. Dean, C. Johnson, *J. Cryst. Growth* **1988**, 86, 118.
- [126] M. Zhuravleva, K. Yang, A. Green, C. L. Melcher, *J. Cryst. Growth* **2011**, 318, 796.
- [127] K. Yang, M. Zhuravleva, C. L. Melcher, *J. Cryst. Growth* **2011**, 318, 833.
- [128] S. G. Singh, D. G. Desai, A. K. Singh, M. Tyagi, S. Sen, A. K. Sinha, S. C. Gadkari, S. K. Gupta, *J. Cryst. Growth* **2012**, 351, 88.
- [129] M. Perez y Jorba, R. Collongues, *Compt. Rend.* **1963**, 257.
- [130] V. V. Osiko, M. A. Borik, E. E. Lomonova, *Springer Handbook of Crystal Growth* (Eds: G. Dhanaraj, K. Byrappa, V. Prasad, M. Dudley), Springer, Berlin, Heidelberg **2010**433477.
- [131] A. Christensen, *J. Cryst. Growth* **1983**, 62, 320.
- [132] D. Oliver, G. Brower, F. Horn, *J. Cryst. Growth* **1972**, 12, 125.
- [133] T. Cizek, *J. Electrochem. Soc.* **1985**, 132, 963.
- [134] M. Agarkov, M. Borik, G. Eliseeva, A. Kulebyakin, E. Lomonova, F. Milovich, V. Myzina, Y. Parkhomenko, E. Skryleva, N. Tabachkova, *Crystals* **2020**, 10, 49.
- [135] V. Taranyuk, A. Gektin, I. Kisel, A. Kolesnikov, *J. Cryst. Growth* **2012**, 360, 95.
- [136] V. I. Taranyuk, A. V. Gektin, A. V. Kolesnikov, *Cryst. Res. Technol.* **2014**, 49, 789.
- [137] P. Dorenbos, *J. Phys.: Condens. Matter* **2003**, 15, 575.
- [138] M. Suta, W. Umland, C. Daul, C. Wickleder, *Phys. Chem. Chem. Phys.* **2016**, 18, 13196.
- [139] M. Suta, T. Senden, J. Olchowka, M. Adlung, A. Meijerink, C. Wickleder, *Phys. Chem. Chem. Phys.* **2017**, 19, 7188.
- [140] M. Suta, C. Wickleder, *Adv. Funct. Mater.* **2017**, 27, 1602783.

- [141] W. Wolszczak, K. W. Krämer, P. Dorenbos, *J. Lumin.* **2020**, 222, 117101.
- [142] R. Shannon, *Acta Crystallogr., Sect. A* **1976**, 32, 751.
- [143] A. Smerechuk, E. Galenin, V. Nesterkina, O. Sidletskiy, C. Dujardin, *J. Cryst. Growth* **2019**, 521, 41.
- [144] P. A. Rodnyi, P. Dorenbos, C. W. E. van Eijk, *Phys. Status Solidi B* **1995**, 187, 15.
- [145] C. M. Fang, K. Biswas, *Phys. Rev. Appl.* **2015**, 4, 014012.
- [146] M. S. Alekhin, D. A. Biner, K. W. Krämer, P. Dorenbos, *J. Lumin.* **2014**, 145, 723.
- [147] W. Wolszczak, K. W. Krämer, P. Dorenbos, *Phys. Status Solidi RRL* **2019**, 13, 1900158.
- [148] R. Borade, E. Bourret-Courchesne, S. Derenzo, *Nucl. Instrum. Methods Phys. Res., Sect. A* **2011**, 652, 260.
- [149] M. Gascón, E. C. Samulon, G. Gundiah, Z. Yan, I. V. Khodyuk, S. E. Derenzo, G. A. Bizarri, E. D. Bourret-Courchesne, *J. Lumin.* **2014**, 156, 63.
- [150] L. Stand, M. Zhuravleva, A. Lindsey, C. L. Melcher, *Nucl. Instrum. Methods Phys. Res., Sect. A* **2015**, 780, 40.
- [151] L. Stand, M. Zhuravleva, H. Wei, C. L. Melcher, *Opt. Mater.* **2015**, 46, 59.
- [152] L. Stand, M. Zhuravleva, G. Camarda, A. Lindsey, J. Johnson, C. Hobbs, C. L. Melcher, *J. Cryst. Growth* **2016**, 439, 93.
- [153] L. Stand, M. Zhuravleva, J. Johnson, M. Koschan, Y. Wu, S. Donnal, K. Vaigneur, E. Lukosi, C. L. Melcher, *J. Cryst. Growth* **2018**, 483, 301.
- [154] M. Rust, C. Melcher, E. Lukosi, *Nucl. Instrum. Methods Phys. Res., Sect. A* **2016**, 833, 33.
- [155] E. Lukosi, M. Rust, L. Stand, C. L. Melcher, *Nucl. Instrum. Methods Phys. Res., Sect. A* **2019**, 938, 36.
- [156] L. Stand, M. Zhuravleva, J. Johnson, M. Koschan, M. Loyd, Y. Wu, E. Lukosi, C. L. Melcher, *J. Cryst. Growth* **2019**, 526, 125213.
- [157] L. Stand, M. Zhuravleva, J. Johnson, M. Koschan, E. Lukosi, C. L. Melcher, *Opt. Mater.* **2017**, 73, 408.
- [158] L. Stand, M. Zhuravleva, B. Chakoumakos, J. Johnson, A. Lindsey, C. L. Melcher, *J. Lumin.* **2016**, 169, 301.
- [159] M. Arai, K. Takahashi, Y. Fujimoto, M. Koshimizu, T. Yanagida, K. Asai, *J. Mater. Sci: Mater Electron* **2020**, 31, 14767.
- [160] G. Rooh, A. Khan, H. J. Kim, H. Park, S. Kim, *Opt. Mater.* **2017**, 73, 523.
- [161] H. J. Kim, G. Rooh, A. Khan, H. Park, S. Kim, *Opt. Mater.* **2018**, 82, 7.
- [162] R. Hawrami, E. Ariesanti, V. Buliga, A. Burger, *Opt. Mater.* **2020**, 100, 109624.
- [163] L. Soundara Pandian, M. Loyd, M.-H. Du, E. van Loef, G. Ciampi, L. Stand, M. Zhuravleva, M. Koschan, J. Glodo, C. Melcher, K. Shah, *Nucl. Instrum. Methods Phys. Res., Sect. A* **2021**, 988, 164876.
- [164] K. Yang, M. Zhuravleva, C. L. Melcher, *Phys. Status Solidi RRL* **2011**, 5, 43.
- [165] Y. Wu, S. S. Gokhale, A. C. Lindsey, M. Zhuravleva, L. Stand, J. A. Johnson, M. Loyd, M. Koschan, C. L. Melcher, *Cryst. Growth Des.* **2016**, 16, 7186.
- [166] Y. Wu, M. Zhuravleva, A. C. Lindsey, M. Koschan, C. L. Melcher, *Nucl. Instrum. Methods Phys. Res., Sect. A* **2016**, 820, 132.
- [167] Y. Wu, Q. Li, B. C. Chakoumakos, M. Zhuravleva, A. C. Lindsey, J. A. Johnson, L. Stand, M. Koschan, C. L. Melcher, *Adv. Opt. Mater.* **2016**, 4, 1518.
- [168] Y. Wu, Q. Li, S. Jones, C. Dun, S. Hu, M. Zhuravleva, A. C. Lindsey, L. Stand, M. Loyd, M. Koschan, J. Auxier, H. L. Hall, C. L. Melcher, *Phys. Rev. Applied* **2017**, 8, 034011.
- [169] Y. Wu, Q. Li, D. J. Rutstrom, M. Zhuravleva, M. Loyd, L. Stand, M. Koschan, C. L. Melcher, *Phys. Status Solidi RRL* **2018**, 12, 1700403.
- [170] K. Mizoi, M. Arai, Y. Fujimoto, D. Nakauchi, M. Koshimizu, T. Yanagida, K. Asai, *J. Lumin.* **2020**, 227, 117521.
- [171] L. Stand, M. Zhuravleva, B. Chakoumakos, J. Johnson, M. Loyd, Y. Wu, M. Koschan, C. L. Melcher, *J. Cryst. Growth* **2018**, 486, 162.
- [172] J. A. Johnson, M. Zhuravleva, L. Stand, B. C. Chakoumakos, Y. Wu, I. Greeley, D. Rutstrom, M. Koschan, C. L. Melcher, *Cryst. Growth Des.* **2018**, 18, 5220.
- [173] D. Rutstrom, L. Stand, B. Dryzhakov, M. Koschan, C. L. Melcher, M. Zhuravleva, *Opt. Mater.* **2020**, 110, 110536.
- [174] Y. Wu, D. Han, B. C. Chakoumakos, H. Shi, S. Chen, M.-H. Du, I. Greeley, M. Loyd, D. J. Rutstrom, L. Stand, M. Koschan, C. L. Melcher, *J. Mater. Chem. C* **2018**, 6, 6647.
- [175] S. Wang, D. J. Rutstrom, L. Stand, M. Koschan, C. L. Melcher, Y. Wu, *IEEE Trans. Nucl. Sci.* **2020**, 67, 876.
- [176] S. E. Swider, S. Lam, A. Datta, *IEEE Trans. Nucl. Sci.* **2016**, 63, 2830.
- [177] Y. Wu, L. A. Boatner, A. C. Lindsey, M. Zhuravleva, S. Jones, J. D. Auxier, H. L. Hall, C. L. Melcher, *Cryst. Growth Des.* **2015**, 15, 3929.
- [178] A. Yoshikawa, Y. Shoji, Y. Yokota, S. Kurosawa, S. Hayasaka, V. I. Chani, T. Ito, K. Kamada, Y. Ohashi, V. Kochurikhin, *J. Cryst. Growth* **2016**, 452, 73.
- [179] B. W. Sturm, N. J. Cherepy, O. B. Drury, P. A. Thelin, S. E. Fisher, S. A. Payne, A. Burger, L. A. Boatner, J. O. Ramey, K. S. Shah, R. Hawrami, *Nucl. Instrum. Methods Phys. Res., Sect. A* **2011**, 652, 242.
- [180] E. Rowe, P. Bhattacharya, E. Tupitsyn, M. Groza, A. Burger, N. J. Cherepy, S. A. Payne, B. W. Sturm, C. Pédrini, *IEEE Trans. Nucl. Sci.* **2013**, 60, 1057.
- [181] A. M. Srivastava, U. Happek, P. Schmidt, *Opt. Mater.* **2008**, 31, 213.
- [182] M. S. Alekhin, J. T. M. de Haas, I. V. Khodyuk, K. W. Krämer, P. R. Menge, V. Ouspenski, P. Dorenbos, *Appl. Phys. Lett.* **2013**, 102, 161915.
- [183] P. Guss, M. E. Foster, B. M. Wong, F. Patrick Doty, K. Shah, M. R. Squillante, U. Shirwadkar, R. Hawrami, J. Tower, D. Yuan, *J. Appl. Phys.* **2014**, 115, 034908.
- [184] F. G. A. Quarati, M. S. Alekhin, K. W. Krämer, P. Dorenbos, *Nucl. Instrum. Methods Phys. Res., Sect. A* **2014**, 735, 655.
- [185] R. H. P. Awater, K. W. Krämer, P. Dorenbos, *IEEE Trans. Nucl. Sci.* **2015**, 62, 2343.
- [186] H. Wei, V. Martin, A. Lindsey, M. Zhuravleva, C. L. Melcher, *J. Lumin.* **2014**, 156, 175.
- [187] M. Loyd, L. Stand, D. Rutstrom, Y. Wu, J. Glodo, K. Shah, M. Koschan, C. L. Melcher, M. Zhuravleva, *J. Cryst. Growth* **2020**, 537, 125365.
- [188] R. Hawrami, E. Ariesanti, A. Burger, *J. Cryst. Growth* **2021**, 565, 126150.
- [189] R. Hawrami, E. Ariesanti, L. Soundara-Pandian, J. Glodo, K. S. Shah, *IEEE Trans. Nucl. Sci.* **2016**, 63, 2838.
- [190] H. Wei, L. Stand, M. Zhuravleva, F. Meng, V. Martin, C. L. Melcher, *Opt. Mater.* **2014**, 38, 154.
- [191] H. Wei, *Phys. Rev. Appl.* **2016**, 5, 024008.
- [192] G. Gundiah, K. Brennan, Z. Yan, E. C. Samulon, G. Wu, G. A. Bizarri, S. E. Derenzo, E. D. Bourret-Courchesne, *J. Lumin.* **2014**, 149, 374.
- [193] G. Rooh, H. J. Kim, S. Kim, S. Khan, *Nucl. Instrum. Methods Phys. Res., Sect. A* **2016**, 832, 187.
- [194] M.-H. Du, K. Biswas, *J. Lumin.* **2013**, 143, 710.
- [195] E. C. Samulon, G. Gundiah, M. Gascón, I. V. Khodyuk, S. E. Derenzo, G. A. Bizarri, E. D. Bourret-Courchesne, *J. Lumin.* **2014**, 153, 64.
- [196] H. Wei, M. Zhuravleva, M. Tyagi, C. L. Melcher, *IEEE Trans. Nucl. Sci.* **2014**, 61, 390.
- [197] M. Zhuravleva, K. Yang, H. Rothfuss, C. L. Melcher, in *IEEE Nuclear Science Symposium Medical Imaging Conf.*, IEEE, New Jersey, **2010**, pp. 1296–1299.
- [198] P. Putaj, J. T. M. de Haas, K. W. Kramer, P. Dorenbos, *IEEE Trans. Nucl. Sci.* **2010**, 57, 1675.

- [199] E. V. van Loef, G. Ciampi, U. Shirwadkar, L. Soundara Pandian, K. S. Shah, *J. Cryst. Growth* **2020**, 532, 125438.
- [200] R. Hawrami, E. Ariesanti, H. Wei, J. Finkelstein, J. Glodo, K. S. Shah, *Nucl. Instrum. Methods Phys. Res., Sect. A* **2017**, 869, 107.
- [201] A. Khan, P. Q. Vuong, G. Rooh, H. J. Kim, S. Kim, *J. Alloys Compd.* **2020**, 827, 154366.
- [202] U. Shirwadkar, M. Loyd, M.-H. Du, E. van Loef, G. Ciampi, L. Soundara Pandian, L. Stand, M. Koschan, M. Zhuravleva, C. Melcher, K. Shah, *Nucl. Instrum. Methods Phys. Res., Sect. A* **2020**, 962, 163684.
- [203] H. J. Kim, G. Rooh, A. Khan, S. Kim, *Nucl. Instrum. Methods Phys. Res., Sect. A* **2017**, 849, 72.
- [204] A. Khan, G. Rooh, H. J. Kim, S. Kim, *J. Alloys Compd.* **2018**, 741, 878.
- [205] A. Khan, G. Rooh, H. J. Kim, S. Kim, *IEEE Trans. Nucl. Sci.* **2018**, 65, 2152.
- [206] E. Rowe, E. Tupitsyn, P. Bhattacharya, L. Matei, M. Groza, V. Buliga, G. Atkinson, A. Burger, *J. Cryst. Growth* **2014**, 393, 156.
- [207] M. Zhuravleva, A. Lindsey, B. C. Chakoumakos, R. Custelcean, F. Meilleur, R. W. Hughes, W. M. Kriven, C. L. Melcher, *J. Solid State Chem.* **2015**, 227, 142.
- [208] Y. Wu, H. Shi, B. C. Chakoumakos, M. Zhuravleva, M.-H. Du, C. L. Melcher, *J. Mater. Chem. C* **2015**, 3, 11366.
- [209] A. C. Lindsey, M. Zhuravleva, C. L. Melcher, in *2013 IEEE Nuclear Science Symp. and Medical Imaging Conf. (2013 NSS/MIC)*, IEEE, New Jersey, **2013**, pp. 1–5.
- [210] E. van Loef, U. Shirwadkar, L. S. Pandian, G. Ciampi, L. Stand, M.-H. Du, M. Koschan, M. Loyd, M. Zhuravleva, C. Melcher, K. Shah, *Nucl. Instrum. Methods Phys. Res., Sect. A* **2021**, 995, 165047.
- [211] K. Yang, M. Zhuravleva, H. Rothfuss, C. L. Melcher, in *IEEE Nuclear Science Symposium Medical Imaging Conf.*, IEEE, New Jersey, **2010**, pp. 1300–1303.
- [212] R. Hofstadter, *Phys. Rev.* **1948**, 74, 100.
- [213] B. Kang, C. M. Fang, K. Biswas, *J. Phys. D: Appl. Phys.* **2016**, 49, 395103.
- [214] E. A. Kravchenko, V. G. Morgunov, Z. B. Mukhametshina, V. V. Chibrikov, G. A. Yagodin, *Z. Naturforsch., A* **1986**, 41, 294.
- [215] J. F. Ackerman, *Mater. Res. Bull.* **1984**, 19, 783.
- [216] B. Kang, K. Biswas, *J. Phys. Chem. C* **2016**, 120, 12187.
- [217] R. Král, P. Zemenová, V. Vaněček, A. Bystřický, M. Kohoutková, V. Jarý, S. Kodama, S. Kurosawa, Y. Yokota, A. Yoshikawa, M. Nikl, *J. Therm. Anal. Calorim.* **2020**, 141, 1101.
- [218] M. Buryi, V. Babin, R. A. M. Ligthart, S. S. Nagorny, V. B. Mikhailik, V. Vaněček, L. P. Prochazková, R. Kandel, V. V. Nahorna, P. Wang, *J. Mater. Chem. C* **2021**, 9, 2955.
- [219] E. Ariesanti, R. Hawrami, A. Burger, S. Motakef, *J. Lumin.* **2020**, 217, 116784.
- [220] C. Delzer, M. Zhuravleva, L. Stand, C. Melcher, N. Cherepy, S. Payne, R. Sanner, J. P. Hayward, *J. Cryst. Growth* **2020**, 531, 125336.
- [221] K. Saeki, Y. Wakai, Y. Fujimoto, M. Koshimizu, T. Yanagida, D. Nakauchi, K. Asai, *Jpn. J. Appl. Phys.* **2016**, 55, 110311.
- [222] K. Saeki, Y. Fujimoto, M. Koshimizu, T. Yanagida, K. Asai, *Appl. Phys. Express* **2016**, 9, 042602.
- [223] E. Rowe, W. B. Goodwin, P. Bhattacharya, G. Cooper, N. Schley, M. Groza, N. J. Cherepy, S. A. Payne, A. Burger, *J. Cryst. Growth* **2019**, 509, 124.
- [224] R. Hawrami, E. Ariesanti, V. Buliga, L. Matei, S. Motakef, A. Burger, *J. Cryst. Growth* **2020**, 533, 125473.
- [225] S. Kodama, S. Kurosawa, K. Fujii, T. Murakami, M. Yashima, J. Pejchal, R. Král, M. Nikl, A. Yamaji, M. Yoshino, S. Toyoda, H. Sato, Y. Ohashi, K. Kamada, Y. Yokota, A. Yoshikawa, *Opt. Mater.* **2020**, 106, 109942.
- [226] S. Kodama, S. Kurosawa, M. Ohno, A. Yamaji, M. Yoshino, J. Pejchal, R. Král, Y. Ohashi, K. Kamada, Y. Yokota, M. Nikl, A. Yoshikawa, *Radiat. Meas.* **2019**, 124, 54.
- [227] S. Kodama, S. Kurosawa, Y. Morishita, H. Usami, T. Torii, M. Hayashi, M. Sasano, T. Azuma, H. Tanaka, V. Kochurikhin, J. Pejchal, R. Kral, M. Yoshino, A. Yamaji, S. Toyoda, H. Sato, Y. Ohashi, Y. Yokota, K. Kamada, M. Nikl, A. Yoshikawa, *IEEE Trans. Nucl. Sci.* **2020**, 67, 1055.
- [228] S. Kodama, S. Kurosawa, M. Ohno, Y. Morishita, H. Usami, M. Hayashi, M. Sasano, T. Azuma, H. Tanaka, V. Kochurikhin, A. Yamaji, M. Yoshino, S. Toyoda, H. Sato, Y. Ohashi, K. Kamada, Y. Yokota, A. Yoshikawa, T. Torii, *Appl. Phys. Express* **2020**, 13, 047002.
- [229] R. Hawrami, E. Ariesanti, V. Buliga, A. Burger, S. Lam, S. Motakef, *J. Cryst. Growth* **2020**, 531, 125316.
- [230] P. Q. Vuong, M. Tyagi, S. H. Kim, H. J. Kim, *CrystEngComm* **2019**, 21, 5898.
- [231] Q. V. Phan, H. J. Kim, G. Rooh, S. H. Kim, *J. Alloys Compd.* **2018**, 766, 326.
- [232] P. Bhattacharya, C. Brown, C. Sosa, M. Wart, S. Miller, C. Brecher, V. V. Nagarkar, *IEEE Trans. Nucl. Sci.* **2020**, 67, 1032.
- [233] R. Hawrami, E. Ariesanti, V. Buliga, S. Motakef, A. Burger, *IEEE Trans. Nucl. Sci.* **2020**, 67, 1020.
- [234] S. Nagorny, *Physics* **2021**, 3, 320.
- [235] A. Hunsaker, W. B. Goodwin, E. Rowe, C. Wheeler, L. Matei, V. Buliga, A. Burger, *Cryst. Res. Technol.* **2021**, 56, 2000166.
- [236] R. Hawrami, E. Ariesanti, A. Burger, H. Parkhe, *Opt. Mater.* **2021**, 119, 111307.
- [237] C. Cardenas, A. Burger, B. Goodwin, M. Groza, M. Laubenstein, S. Nagorny, E. Rowe, *Nucl. Instrum. Methods Phys. Res., Sect. A* **2017**, 869, 63.
- [238] P. Q. Vuong, H. Kim, H. Park, G. Rooh, S. Kim, *Radiat. Meas.* **2019**, 123, 83.
- [239] V. Caracciolo, S. S. Nagorny, P. Belli, R. Bernabei, F. Cappella, R. Cerulli, A. Incicchitti, M. Laubenstein, V. Merlo, S. Nisi, P. Wang, *Nucl. Phys. A* **2020**, 1002, 121941.
- [240] K. Saeki, Y. Fujimoto, M. Koshimizu, D. Nakauchi, H. Tanaka, T. Yanagida, K. Asai, *Jpn. J. Appl. Phys.* **2017**, 56, 020307.
- [241] S. Kodama, S. Kurosawa, A. Yamaji, J. Pejchal, R. Král, Y. Ohashi, K. Kamada, Y. Yokota, M. Nikl, A. Yoshikawa, *J. Cryst. Growth* **2018**, 492, 1.
- [242] S. Kodama, S. Kurosawa, J. Pejchal, R. Král, A. Yamaji, Y. Ohashi, Y. Yokota, K. Kamada, M. Nikl, A. Yoshikawa, *IEEE Trans. Nucl. Sci.* **2018**, 65, 2169.
- [243] V. Vaněček, J. Páterek, R. Král, M. Buryi, V. Babin, K. Zloužeová, S. Kodama, S. Kurosawa, Y. Yokota, A. Yoshikawa, M. Nikl, *J. Cryst. Growth* **2021**, 573, 126307.
- [244] Y. Fujimoto, K. Saeki, D. Nakauchi, H. Fukada, T. Yanagida, H. Kawamoto, M. Koshimizu, K. Asai, *Mater. Res. Bull.* **2018**, 105, 291.
- [245] S. Cheng, A. Beitlerova, R. Kucerkova, M. Nikl, G. Ren, Y. Wu, *Phys. Status Solidi RRL* **2020**, 14, 2000374.
- [246] S. Cheng, M. Nikl, A. Beitlerova, R. Kucerkova, X. Du, G. Niu, Y. Jia, J. Tang, G. Ren, Y. Wu, *Adv. Opt. Mater.* **2021**, 9, 2100460.
- [247] S. Cheng, A. Beitlerova, R. Kucerkova, E. Mihokova, M. Nikl, Z. Zhou, G. Ren, Y. Wu, *ACS Appl. Mater. Interfaces* **2021**, 13, 12198.
- [248] C. W. E. van Eijk, *J. Lumin.* **1994**, 60–61, 936.
- [249] S. Gundacker, R. H. Pots, A. Nepomnyashchikh, E. Radzhabov, R. Shendrik, S. Omelkov, M. Kirm, F. Acerbi, M. Capasso, G. Paternoster, A. Mazzi, A. Gola, J. Chen, E. Auffray, *Phys. Med. Biol.* **2021**, 66, 114002.
- [250] F. Ferrulli, M. Caresana, F. Cova, S. Gundacker, N. Kratochwil, R. Pots, M. Silari, A. Vedda, I. Veronese, G. Zorloni, *Sens. Actuators, A* **2021**, 332, 113151.

- [251] P. Dorenbos, J. T. M. de Haas, R. Visser, C. W. E. van Eijk, R. W. Hollander, *IEEE Trans. Nucl. Sci.* **1993**, *40*, 424.
- [252] M. Koshimizu, N. Yahaba, R. Haruki, F. Nishikido, S. Kishimoto, K. Asai, *Opt. Mater.* **2014**, *36*, 1930.
- [253] K. Takahashi, M. Koshimizu, Y. Fujimoto, T. Yanagida, K. Asai, *J. Ceram. Soc. Jpn.* **2018**, *126*, 755.
- [254] K. Takahashi, M. Koshimizu, Y. Fujimoto, T. Yanagida, K. Asai, *Nucl. Instrum. Methods Phys. Res., Sect. A* **2020**, *954*, 161842.
- [255] V. Vaněček, J. Pátek, R. Král, R. Kučerková, V. Babin, J. Rohlíček, R. Cala', N. Kratochvíl, E. Auffray, M. Nikl, *Opt. Mater.: X* **2021**, *12*, 100103.
- [256] K. Takahashi, M. Arai, M. Koshimizu, Y. Fujimoto, T. Yanagida, K. Asai, *Jpn. J. Appl. Phys.* **2020**, *59*, 032003.
- [257] K. Takahashi, M. Arai, M. Koshimizu, Y. Fujimoto, T. Yanagida, K. Asai, *Jpn. J. Appl. Phys.* **2020**, *59*, 072002.
- [258] M. Cadatal-Raduban, A. Yoshikawa, L. V. Mui, M. H. Pham, T. Shimizu, N. Sarukura, T. Togashi, K. Yamanoi, *Jpn. J. Appl. Phys.* **2020**, *59*, 052005.
- [259] M. Cadatal-Raduban, K. Yamanoi, A. Yoshikawa, Y. Yokota, T. Shimizu, N. Sarukura, T. Togashi, A. Kondo, M. V. Luong, *J. Chem. Phys.* **2021**, *154*, 124707.
- [260] D. A. Cusano, F. F. Holub, S. Prochazka, May **1982** [http://inis.iaea.org/search/search.aspx?orig\\_q=RN:14762119](http://inis.iaea.org/search/search.aspx?orig_q=RN:14762119).
- [261] F. A. DiBianca, D. A. Cusano, J.-P. J. Georges, C. D. Greskovich, Rare earth ceramic scintillator. United States: N. p., **1985** <https://www.osti.gov/biblio/6393414>.
- [262] M. Nikl, T. Yanagida, H. Yagi, T. Yanagitani, E. Mihokova, A. Yoshikawa, *Recent Advances in Ceramic Materials Research* (Eds: J.J. Roa Rovira, M.S. Rubi), Nova Publishers, Hauppauge, New York **2013**, pp. 127–176.
- [263] D. J. Wisniewski, L. A. Boatner, J. S. Neal, G. E. Jellison, J. O. Ramey, A. North, M. Wisniewska, A. Lempicki, C. Brecher, J. Glodo, *Hard X-Ray and Gamma-Ray Detector Physics IX*, SPIE Bellingham, Washington, **2007**, pp. 308–319.
- [264] D. J. Wisniewski, L. A. Boatner, J. S. Neal, G. E. Jellison, J. O. Ramey, A. North, M. Wisniewska, A. E. Payzant, J. Y. Howe, A. Lempicki, C. Brecher, J. Glodo, *IEEE Trans. Nucl. Sci.* **2008**, *55*, 1501.
- [265] W. T. Shoulders, R. M. Gaume, *J. Alloys Compd.* **2017**, *705*, 517.
- [266] A. Edgar, M. Bartle, S. G. Raymond, G. V. M. Williams, C. Varoy, *IEEE Trans. Nucl. Sci.* **2008**, *55*, 1160.
- [267] S. R. Podowitz, R. M. Gaumé, W. T. Hong, A. Laouar, R. S. Feigelson, *IEEE Trans. Nucl. Sci.* **2010**, *57*, 3827.
- [268] K. Oba, M. Ito, M. Yamaguchi, M. Tanaka, *Advances in Electronics and Electron Physics* (Ed: B.L. Morgan), Academic Press INC. San Diego, **1988**, pp. 247–255.
- [269] C. M. Castelli, N. M. Allinson, K. J. Moon, D. L. Watson, *Nucl. Instrum. Methods Phys. Res., Sect. A* **1994**, *348*, 649.
- [270] V. V. Nagarkar, T. K. Gupta, S. R. Miller, Y. Klugerman, M. R. Squillante, G. Entine, *IEEE Trans. Nucl. Sci.* **1998**, *45*, 492.
- [271] J.-P. Moy, *Nucl. Instrum. Methods Phys. Res., Sect. A* **2000**, *442*, 26.
- [272] N. Yasui, Y. Ohashi, T. Kobayashi, T. Den, *Adv. Mater.* **2012**, *24*, 5464.
- [273] N. Yasui, T. Kobayashi, Y. Ohashi, T. Den, *J. Cryst. Growth* **2014**, *399*, 7.
- [274] Y. Takizawa, K. Kamada, M. Yoshino, A. Yamaji, S. Kurosawa, Y. Yokota, H. Sato, S. Toyoda, Y. Ohashi, T. Hanada, V. V. Kochurikhin, A. Yoshikawa, *Jpn. J. Appl. Phys.* **2020**, *60*, SBBK01.
- [275] N. Kawaguchi, K. Fukuda, T. Yanagida, Y. Fujimoto, Y. Yokota, T. Suyama, K. Watanabe, A. Yamazaki, A. Yoshikawa, *Nucl. Instrum. Methods Phys. Res., Sect. A* **2011**, *652*, 209.
- [276] T. Yanagida, K. Fukuda, Y. Fujimoto, N. Kawaguchi, S. Kurosawa, A. Yamazaki, K. Watanabe, Y. Futami, Y. Yokota, J. Pejchal, A. Yoshikawa, A. Uritani, T. Iguchi, *Opt. Mater.* **2012**, *34*, 868.
- [277] T. Yanagida, Y. Fujimoto, K. Fukuda, N. Kawaguchi, K. Watanabe, A. Yamazaki, A. Uritani, V. Chani, *Opt. Mater.* **2013**, *35*, 1449.
- [278] T. Yanagida, N. Kawaguchi, Y. Fujimoto, K. Fukuda, K. Watanabe, A. Yamazaki, A. Uritani, *J. Lumin.* **2013**, *144*, 212.
- [279] K. Hishinuma, K. Kamada, S. Kurosawa, A. Yamaji, J. Pejchal, Y. Yokota, Y. Ohashi, A. Yoshikawa, *Jpn. J. Appl. Phys.* **2015**, *54*, 04DH04.
- [280] S. Kurosawa, A. Yamaji, J. Pejchal, Y. Yokota, Y. Ohashi, K. Kamada, A. Yoshikawa, *J. Mater. Sci.* **2017**, *52*, 5531.
- [281] Y. Yokota, S. Kurosawa, K. Nishimoto, V. Chani, A. Yoshikawa, *J. Eur. Ceram. Soc.* **2014**, *34*, 2095.
- [282] K. Nishimoto, Y. Yokota, S. Kurosawa, Y. Fujimoto, N. Kawaguchi, K. Fukuda, A. Yoshikawa, *J. Eur. Ceram. Soc.* **2014**, *34*, 2117.
- [283] Y. Wu, E. D. Lukosi, M. Zhuravleva, A. C. Lindsey, C. L. Melcher, *Nucl. Instrum. Methods Phys. Res., Sect. A* **2015**, *797*, 319.
- [284] S. Cheng, R. E. Hunneke, M. Tian, E. Lukosi, M. Zhuravleva, C. L. Melcher, Y. Wu, *CrystEngComm* **2020**, *22*, 3269.
- [285] Y. Takizawa, K. Kamada, M. Yoshino, K. J. Kim, A. Yamaji, S. Kurosawa, Y. Yokota, H. Sato, S. Toyoda, Y. Ohashi, T. Hanada, V. V. Kochurikhin, A. Yoshikawa, *Nucl. Instrum. Methods Phys. Res., Sect. A* **2022**, *1028*, 166384.
- [286] K. Origuchi, Y. Yokota, R. Kral, M. Yoshino, A. Yamaji, S. Toyoda, H. Sato, Y. Ohashi, S. Kurosawa, K. Kamada, A. Yoshikawa, *J. Cryst. Growth* **2020**, *536*, 125573.
- [287] K. Kamada, H. Chiba, M. Yoshino, A. Yamaji, Y. Shoji, S. Kurosawa, Y. Yokota, Y. Ohashi, A. Yoshikawa, *Opt. Mater.* **2017**, *68*, 70.
- [288] A. Kojima, K. Teshima, Y. Shirai, T. Miyasaka, *J. Am. Chem. Soc.* **2009**, *131*, 6050.
- [289] W. Xiang, S. (Frank) Liu, W. Tress, *Energy Environ. Sci.* **2021**, *14*, 2090.
- [290] L. Schmidt-Mende, V. Dyakonov, S. Olthof, F. Ünlü, K. M. T. Lê, S. Mathur, A. D. Karabanov, D. C. Lupascu, L. M. Herz, A. Hinderhofer, F. Schreiber, A. Chernikov, D. A. Egger, O. Shargaieva, C. Cocchi, E. Unger, M. Saliba, M. M. Bryanvand, M. Kroll, F. Nehm, K. Leo, A. Redinger, J. Höcker, T. Kirchartz, J. Warby, E. Gutierrez-Partida, D. Neher, M. Stollerfoht, U. Würfel, M. Unmüßig, et al., *APL Materials* **2021**, *9*, 109202.
- [291] V. B. Mykhaylyk, H. Kraus, M. Saliba, *Mater. Horiz.* **2019**, *6*, 1740.
- [292] K. M. McCall, K. Sakhatskiy, E. Lehmann, B. Walfort, A. S. Losko, F. Montanarella, M. I. Bodnarchuk, F. Krieg, Y. Kelestemur, D. Mannes, Y. Shynkarenko, S. Yakunin, M. V. Kovalenko, *ACS Nano* **2020**, *14*, 14686.
- [293] F. Maddalena, L. Tjahjana, A. Xie, S. Zeng, H. Wang, P. Coquet, W. Drozdowski, C. Dujardin, C. Dang, M. D. Birowosuto, *Crystals* **2019**, *9*, 88.
- [294] V. S. Shevelev, A. V. Ishchenko, A. S. Vanetsev, V. Nagirnyi, S. I. Omelkov, *J. Lumin.* **2022**, *242*, 118534.
- [295] C. Rodà, M. Fasoli, M. L. Zaffalon, F. Cova, V. Pinchetti, J. Shamsi, A. L. Abdelhady, M. Imran, F. Meinardi, L. Manna, A. Vedda, S. Brovelli, *Adv. Funct. Mater.* **2021**, *31*, 2104879.
- [296] F. Montanarella, K. M. McCall, K. Sakhatskiy, S. Yakunin, P. Trtik, C. Bernasconi, I. Cherniukh, D. Mannes, M. I. Bodnarchuk, M. Strobl, B. Walfort, M. V. Kovalenko, *ACS Energy Lett.* **2021**, *6*, 4365.
- [297] P. Lecoq, *IEEE Trans. Radiat. Plasma Med. Sci.* **2017**, *1*, 473.
- [298] F. Maddalena, A. Xie, X. Y. Chin, R. Begum, M. E. Witkowski, M. Makowski, B. Mahler, W. Drozdowski, S. V. Springham, R. S. Rawat, N. Mathews, C. Dujardin, M. D. Birowosuto, C. Dang, *J. Phys. Chem. C* **2021**, *125*, 14082.
- [299] M. Hunyadi, C. Buga, L. Csige, A. Csík, *Mater. Lett.* **2021**, *289*, 129398.
- [300] S. E. Létant, T.-F. Wang, *Nano Lett.* **2006**, *6*, 2877.



- [301] Z. Kang, Y. Zhang, H. Menkara, B. K. Wagner, C. J. Summers, W. Lawrence, V. Nagarkar, *Appl. Phys. Lett.* **2011**, *98*, 181914.
- [302] K. Tomanová, V. Čuba, M. G. Brik, E. Mihóková, R. Martínez Turtos, P. Lecoq, E. Auffray, M. Nikl, *APL Mater.* **2019**, *7*, 011104.
- [303] F. Cao, X. Xu, D. Yu, H. Zeng, *Nanophotonics* **2020**, *10*, 2221.
- [304] M. Imran, F. Di Stasio, Z. Dang, C. Canale, A. H. Khan, J. Shamsi, R. Brescia, M. Prato, L. Manna, *Chem. Mater.* **2016**, *28*, 6450.
- [305] Z. Liang, S. Zhao, Z. Xu, B. Qiao, P. Song, D. Gao, X. Xu, *ACS Appl. Mater. Interfaces* **2016**, *8*, 28824.
- [306] A. Pan, B. He, X. Fan, Z. Liu, J. J. Urban, A. P. Alivisatos, L. He, Y. Liu, *ACS Nano* **2016**, *10*, 7943.
- [307] V. K. Ravi, A. Swarnkar, R. Chakraborty, A. Nag, *Nanotechnology* **2016**, *27*, 325708.
- [308] Y. Zhang, T. D. Siegler, C. J. Thomas, M. K. Abney, T. Shah, A. De Gorostiza, R. M. Greene, B. A. Korgel, *Chem. Mater.* **2020**, *32*, 5410.
- [309] C. Lu, M. W. Wright, X. Ma, H. Li, D. S. Itanze, J. A. Carter, C. A. Hewitt, G. L. Donati, D. L. Carroll, P. M. Lundin, S. M. Geyer, *Chem. Mater.* **2019**, *31*, 62.
- [310] X. Li, Y. Wu, S. Zhang, B. Cai, Y. Gu, J. Song, H. Zeng, *Adv. Funct. Mater.* **2016**, *26*, 2435.
- [311] F. Zhang, H. Zhong, C. Chen, X. Wu, X. Hu, H. Huang, J. Han, B. Zou, Y. Dong, *ACS Nano* **2015**, *9*, 4533.
- [312] H. Huang, F. Zhao, L. Liu, F. Zhang, X. Wu, L. Shi, B. Zou, Q. Pei, H. Zhong, *ACS Appl. Mater. Interfaces* **2015**, *7*, 28128.
- [313] H. Huang, A. S. Susha, S. V. Kershaw, T. F. Hung, A. L. Rogach, *Adv. Sci.* **2015**, *2*, 1500194.
- [314] F. Zhu, L. Men, Y. Guo, Q. Zhu, U. Bhattacharjee, P. M. Goodwin, J. W. Petrich, E. A. Smith, J. Vela, *ACS Nano* **2015**, *9*, 2948.
- [315] S. Gonzalez-Carrero, L. Francés-Soriano, M. González-Béjar, S. Agouram, R. E. Galian, J. Pérez-Prieto, *Small* **2016**, *12*, 5245.
- [316] M. Mittal, A. Jana, S. Sarkar, P. Mahadevan, S. Sapra, *J. Phys. Chem. Lett.* **2016**, *7*, 3270.
- [317] S. Seth, A. Samanta, *Sci. Rep.* **2016**, *6*, 37693.
- [318] X. Li, F. Cao, D. Yu, J. Chen, Z. Sun, Y. Shen, Y. Zhu, L. Wang, Y. Wei, Y. Wu, H. Zeng, *Small* **2017**, *13*, 1603996.
- [319] S. Sun, D. Yuan, Y. Xu, A. Wang, Z. Deng, *ACS Nano* **2016**, *10*, 3648.
- [320] D. Myung Jang, D. Hwan Kim, K. Park, J. Park, J. Woon Lee, J. Kyu Song, *J. Mater. Chem. C* **2016**, *4*, 10625.
- [321] Y. Tong, E. Bladt, M. F. Aygüler, A. Manzi, K. Z. Milowska, V. A. Hintermayr, P. Docampo, S. Bals, A. S. Urban, L. Polavarapu, J. Feldmann, *Angew. Chem., Int. Ed.* **2016**, *55*, 13887.
- [322] L. Rao, X. Ding, X. Du, G. Liang, Y. Tang, K. Tang, J. Z. Zhang, *Beilstein J. Nanotechnol.* **2019**, *10*, 666.
- [323] X. Chen, L. Peng, K. Huang, Z. Shi, R. Xie, W. Yang, *Nano Res.* **2016**, *9*, 1994.
- [324] E. Acheampong Tsiwah, Y. Ding, Z. Li, Z. Zhao, M. Wang, C. Hu, X. Liu, C. Sun, X. Zhao, Y. Xie, *CrystEngComm* **2017**, *19*, 7041.
- [325] S. Ye, M. Yu, M. Zhao, J. Song, J. Qu, *J. Alloys Compd.* **2018**, *730*, 62.
- [326] M. Chen, Y. Zou, L. Wu, Q. Pan, D. Yang, H. Hu, Y. Tan, Q. Zhong, Y. Xu, H. Liu, B. Sun, Q. Zhang, *Adv. Funct. Mater.* **2017**, *27*, 1701121.
- [327] X. Chen, D. Chen, J. Li, G. Fang, H. Sheng, J. Zhong, *Dalton Trans.* **2018**, *47*, 5670.
- [328] B. Clasen Hames, R. Sánchez, A. Fakharuddin, I. Mora-Seró, *ChemPlusChem* **2018**, *83*, 294.
- [329] K. Děcká, A. Suchá, J. Král, I. Jakubec, M. Nikl, V. Jarý, V. Babin, E. Mihóková, V. Čuba, *Nanomaterials* **2021**, *11*, 1935.
- [330] A. A. M. Brown, B. Damodaran, L. Jiang, J. N. Tey, S. H. Pu, N. Mathews, S. G. Mhaisalkar, *Adv. Mater.* **2020**, *10*, 2001349.
- [331] S. Wei, Y. Yang, X. Kang, L. Wang, L. Huang, D. Pan, *Chem. Commun.* **2016**, *52*, 7265.
- [332] J. Guo, S. Ye, J. Song, J. Qu, *J. Nanopart. Res.* **2020**, *22*, 153.
- [333] B. McKenna, A. Shivkumar, B. Charles, R. C. Evans, *Nanoscale* **2020**, *12*, 11694.
- [334] Z. Zhu, Q. Sun, Z. Zhang, J. Dai, G. Xing, S. Li, X. Huang, W. Huang, *J. Mater. Chem. C* **2018**, *6*, 10121.
- [335] G. K. Grandhi, K. Mokurala, J. H. Han, H. B. Cho, J. Y. Han, W. B. Im, *ECS J. Solid State Sci. Technol.* **2021**, *10*, 106001.
- [336] S. Liang, M. Zhang, G. M. Biesold, W. Choi, Y. He, Z. Li, D. Shen, Z. Lin, *Adv. Mater.* **2021**, *33*, 2005888.
- [337] M. Gandini, I. Villa, M. Beretta, C. Gotti, M. Imran, F. Carulli, E. Fantuzzi, M. Sassi, M. Zaffalon, C. Brofferio, L. Manna, L. Beverina, A. Vedda, M. Fasoli, L. Gironi, S. Brovelli, *Nat. Nanotechnol.* **2020**, *15*, 462.
- [338] J. De Roo, M. Ibáñez, P. Geiregat, G. Nedelcu, W. Walravens, J. Maes, J. C. Martins, I. Van Driessche, M. V. Kovalenko, Z. Hens, *ACS Nano* **2016**, *10*, 2071.
- [339] S. Chhangani, M. Kumar, R. M. Sahani, A. Bera, A. Pandya, *Mater. Today: Proc.* **2022**, *48*, 1028.
- [340] J. Nie, C. Li, S. Zhou, J. Huang, X. Ouyang, Q. Xu, *ACS Appl. Mater. Interfaces* **2021**, *13*, 54348.
- [341] C. Wang, H. Lin, Z. Zhang, Z. Qiu, H. Yang, Y. Cheng, J. Xu, X. Xiang, L. Zhang, Y. Wang, *J. Eur. Ceram. Soc.* **2020**, *40*, 2234.
- [342] W. Ma, T. Jiang, Z. Yang, H. Zhang, Y. Su, Z. Chen, X. Chen, Y. Ma, W. Zhu, X. Yu, H. Zhu, J. Qiu, X. Liu, X. Xu, Y. (Michael) Yang, *Adv. Sci.* **2021**, *8*, 2003728.
- [343] L. Niu, S. Wang, Z. Sui, Y. Song, L. Zhao, L. Liu, J. Ren, J. Ren, J. Zhang, J. Zhang, *Opt. Lett., OL* **2021**, *46*, 3448.
- [344] Y. Tong, Q. Wang, H. Yang, X. Liu, E. Mei, X. Liang, X. Liang, Z. Zhang, Z. Zhang, W. Xiang, *Photon. Res., PRJ* **2021**, *9*, 2369.
- [345] H. Zhang, Z. Yang, M. Zhou, L. Zhao, T. Jiang, H. Yang, X. Yu, J. Qiu, Y. (Michael) Yang, X. Xu, *Adv. Mater.* **2021**, *33*, 2102529.
- [346] M. L. Su, Q. Zhang, Y. J. Gao, D. X. Wang, C. Chen, W. Wei, *J. Lumin.* **2022**, *242*, 118553.
- [347] P. Lecoq, C. Morel, J. O. Prior, D. Visvikis, S. Gundacker, E. Auffray, P. Križan, R. M. Turtos, D. Thers, E. Charbon, J. Varela, C. de La Taille, A. Rivetti, D. Breton, J.-F. Pratte, J. Nuyts, S. Surti, S. Vandenberghe, P. Marsden, K. Parodi, J. M. Benlloch, M. Benoit, *Phys. Med. Biol.* **2020**, *65*, 21RM01.
- [348] R. M. Turtos, S. Gundacker, S. Omelkov, B. Mahler, A. H. Khan, J. Saaring, Z. Meng, A. Vasil'ev, C. Dujardin, M. Kirm, I. Moreels, E. Auffray, P. Lecoq, *npj 2D Mater Appl* **2019**, *3*, 1.
- [349] K. Tomanová, A. Suchá, E. Mihóková, L. Procházková, I. Jakubec, R. M. Turtos, S. Gundacker, E. Auffray, V. Čuba, *IEEE Trans. Nucl. Sci.* **2020**, *67*, 933.
- [350] K. Děcká, J. Král, F. Hájek, P. Průša, V. Babin, E. Mihóková, V. Čuba, *Nanomaterials* **2022**, *12*, 14.
- [351] L. Yang, H. Zhang, M. Zhou, L. Zhao, W. Chen, T. Wang, X. Yu, D. Zhou, J. Qiu, X. Xu, *J. Phys. Chem. Lett.* **2020**, *11*, 9203.
- [352] H. Li, H. Yang, R. Yuan, Z. Sun, Y. Yang, J. Zhao, Q. Li, Z. Zhang, *Adv. Opt. Mater.* **2021**, *9*, 2101297.
- [353] J. Zhao, L. Zhao, Y. Deng, X. Xiao, Z. Ni, S. Xu, J. Huang, *Nat. Photonics* **2020**, *14*, 612.
- [354] P. Dorenbos, E. V. D. van Loef, A. P. Vink, E. van der Kolk, C. W. E. van Eijk, K. W. Krämer, H. U. Güdel, W. M. Higgins, K. S. Shah, *J. Lumin.* **2006**, *117*, 147.
- [355] R. H. Pots, E. Auffray, S. Gundacker, *Front. Phys.* **2020**, *8*, 482.



**Eva Mihóková** is a senior scientist at FZU Institute of Physics, Czech Academy of Sciences, and also an associate professor at the Czech Technical University in Prague. She obtained her Ph.D. (1996) in the solid-state physics in the Institute of Physics, Academy of Sciences of the Czech Republic. Her research includes study of decay kinetics of heavy  $ns^2$  ions and rare earth ions in oxides and halides, luminescence and scintillation mechanisms, quantum confinement effects in the foreign aggregated phases in selected halide matrices, development of nanocomposites for fast timing detection systems, and biomedical applications.



**Václav Čuba** is an associate professor at the Czech Technical University in Prague. He obtained his Ph.D. (2003) in nuclear chemistry at the Faculty of Nuclear Sciences and Physical Engineering. He has been focused on research in applied radiation chemistry and processing, photochemistry, materials chemistry, and nanotechnology and he leads a subgroup focused on synthesis of scintillating NCs and nanomaterials for a wide array of applications.



**Martin Nikl** graduated in 1981 from the Faculty of Nuclear Science and Physical Engineering, Czech Technical University, and obtained his Ph.D. in 1986 at the Institute of Physics, CAS. He became an associated and full professor at Czech Technical University in 2015 and 2021, respectively. His research interests include luminescence and scintillation mechanisms in wide-bandgap solids, energy-transfer processes, and the role of material defects in them. He currently serves as the department head at the Institute of Physics, Academy of Sciences of the Czech Republic.

# Trapping and Recombination Centers in Cesium Hafnium Chloride Single Crystals: EPR and TSL Study

M. Buryi,<sup>†</sup> R. Král,<sup>†</sup> V. Babin,<sup>†</sup> J. Páterek,<sup>†,‡</sup> V. Vaněček,<sup>†,‡</sup> P. Veverka,<sup>†</sup> M. Kohoutková,<sup>§</sup> V. Laguta,<sup>†</sup> M. Fasoli,<sup>||</sup> I. Villa,<sup>||</sup> F. Cova,<sup>||</sup> A. Vedda,<sup>||</sup> and M. Nikl<sup>\*,†,§</sup>

<sup>†</sup>Institute of Physics of the Czech Academy of Science, Cukrovarnická 10/112, 16200 Prague, Czech Republic

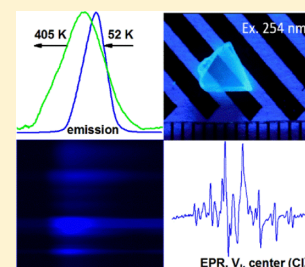
<sup>‡</sup>Czech Technical University in Prague, Břehová 7, 115 19 Prague, Czech Republic

<sup>§</sup>University of Chemistry and Technology, Prague, Technická 5, 166 28 Prague, Czech Republic

<sup>||</sup>Department of Materials Science, University of Milano-Bicocca, Via Cozzi 55, 20125 Milano, Italy

## Supporting Information

**ABSTRACT:** Charge trapping phenomena and recombination centers were studied in three Cs<sub>2</sub>HfCl<sub>6</sub> single crystals of slightly different stoichiometry grown by the vertical Bridgeman method. Electron paramagnetic resonance (EPR) spectra measured both before and after X-ray irradiation show creation of two distinct V<sub>k</sub> centers. One of them was V<sub>k</sub>(a) already known from a recent work by “R. Král, V. Babin, E. Mihoková, M. Buryi, V. V. Laguta, K. Nitsch, and M. Nikl, Luminescence and Charge Trapping in Cs<sub>2</sub>HfCl<sub>6</sub> Single Crystals: Optical and Magnetic Resonance Spectroscopy Study, *J. Phys. Chem. C* 121, 12375–12382 (2017)”. Its quantity was different in each of the samples studied; the smallest, however, was in the one with the best stoichiometry. The second V<sub>k</sub> center presently observed has never been described before. Its existence at an almost undetectable level was observed only in two of the three crystals. Thermally stimulated luminescence (TSL) spectra measured in the three samples were evidently composed of at least 2–3 strongly overlapped components within the 10–500 K temperature range. This suggested the existence of several recombination centers activated by the depletion of specific charge carrier traps. The corresponding TSL glow curves composed of seven complex peaks demonstrated significant decrease of the peaks amplitude in the sample with the best stoichiometry. Along with decreased radioluminescence amplitude, the combined EPR and TSL study allowed us to assume the reduction of both the recombination and trap center concentration with the increased crystal quality.



## 1. INTRODUCTION

Cesium hafnium chloride, Cs<sub>2</sub>HfCl<sub>6</sub> (CHC), single crystals have been reported in scientific literature several times since 1970s, initially serving as hosts for, for example, molybdenum and tungsten ions studied by the electron paramagnetic resonance (EPR) technique.<sup>1,2</sup> Later, optical properties of the activating ions, namely, Mo<sup>3+</sup>, Re<sup>4+</sup>, Ir<sup>4+</sup>, and Os<sup>4+</sup> were studied.<sup>3–5</sup> Since the introduction of NaI:Tl in 1948 (ref 6), there is a demanding ongoing search for a better scintillator. A variety of optical materials was tested to obtain the one providing the fastest and most efficient transformation of incident high-energy radiation into easily detectable light. The following commonly known factors are of particular importance: high effective atomic number, high density, ruggedness, and radiation resistance. CHC single crystals have become attractive as the scintillator material relatively recently, when their excellent scintillation properties were reported.<sup>7,8</sup> The undisputed advantages of CHC in contrast to well-known LaCl(Br)<sub>3</sub>:Ce<sup>3+</sup>, CeBr<sub>3</sub>, SrI<sub>2</sub>:Eu<sup>2+</sup>, or CsBa<sub>2</sub>I<sub>3</sub>:Eu<sup>2+</sup> (refs<sup>9–16</sup>) are considerably low hygroscopicity (refs 7 and 8) and an efficient intrinsic emission center. The former allows to grow large-volume crystals operating at room temperature. The latter completely removes the problem of activator ion

solubility and homogeneous distribution inside the host. The light yield of CHC was reported to be 37 000–54 000 photons/MeV.<sup>7,8,17</sup> The scintillation intensity exhibited a monotonic increase with temperature without any significant changes in the scintillation decay explained by the three-state model.<sup>18</sup> Under excitation, the holes and electrons become self-trapped, producing V<sub>k</sub> centers and self-trapped electrons in the HfCl<sub>6</sub><sup>2-</sup> octahedra [self-trapped excitons (STE)] with the d orbitals of Hf and p orbitals of Cl predominantly creating the conduction and valence bands, respectively.<sup>19–21</sup> Emission spectra measured in the material are mainly composed of two broad overlapping bands. One band peaking at 375 nm (3.31 eV) is supposedly produced by STE at the HfCl<sub>6</sub><sup>2-</sup> octahedra. The other band at 435 nm (2.85 eV) is attributed to Zr impurity.<sup>8</sup> The self-trapping of charge carriers has also been theoretically predicted earlier for several STEs emitting at 2.96, 3.06, and 4.97 eV.<sup>21</sup>

Scintillation performance can easily be affected by the presence of lattice and impurity-associated defects.<sup>22</sup> Their

Received: June 17, 2019

Revised: July 19, 2019

Published: July 23, 2019

own energy states within the bandgap can lead to processes biasing the energy transfer toward luminescence centers, such as non-radiative recombination of charge carriers at the lattice defects. Consequently, the luminescence response is degraded and the afterglow can increase. Therefore, the knowledge of the defect type, its charge state, local structure, and thermal stability are of great importance in order to proceed with further material improvement. The existence of two different  $V_k$  centers, one of which is created by the self-trapping of a hole at two regular chlorines forming the  $\text{Cl}_2^-$  molecular ion in the  $\text{Cs}_2\text{HfCl}_6$ , has recently been confirmed by the EPR technique.<sup>23</sup> To the best of our knowledge it is, so far, the only work reporting EPR investigations in the material and in the single type of samples. In addition, no work dedicated to thermally stimulated luminescence (TSL) study in this type of material is available in the literature. The influence of the material stoichiometry on both the irradiation-induced defects, their types as well as quantity, and emission centers in general is not known till now. Therefore, the aim of the present research is to shed light on this problem by using correlated EPR, TSL, and radioluminescence (RL) techniques. The results should provide extended information about the irradiation-induced defects and their role in luminescence processes including their dependence on different stoichiometry of the CHC crystals.

## 2. EXPERIMENTAL DETAILS

The  $\text{Cs}_2\text{HfCl}_6$  material was synthesized by direct reaction of starting cesium chloride ( $\text{CsCl}$ ) and hafnium chloride ( $\text{HfCl}_4$ ) mixed together in the stoichiometric ratio 2:1. Two technological approaches were tested using open and closed systems. In the open system, the  $\text{Cs}_2\text{HfCl}_6$  material was purified with gaseous mixture of halogenation agents followed by zone refining as described in refs.<sup>24–26</sup> In contrast, in the closed system, the starting  $\text{CsCl}$  and  $\text{HfCl}_4$  were purified separately using the same refinement techniques and afterwards sealed in the required stoichiometric ratio in a quartz ampule under vacuum. The  $\text{Cs}_2\text{HfCl}_6$  single crystals were grown in sealed quartz ampules by the unseeded vertical Bridgman method with the pulling rate of ca. 0.5 mm/h and temperature gradient of 40 K/cm under the atmosphere of halogenation agents and vacuum for the open and closed systems, respectively. Specimens for further optical, TSL, and EPR characterizations were cleaved from the as-grown crystals along the (111) plane as platelets with both facets were mirror polished. All procedures including weighing, handling, or manufacturing were performed in the atmosphere-controlled glovebox unit with the contents of  $\text{H}_2\text{O}$  and  $\text{O}_2$  below 1 ppm.

The phase composition of the powder samples prepared in the open system was evaluated by the X-ray diffraction (XRD) analysis at room temperature using powder X-ray Bruker D8 ADVANCE diffractometer with a scintillation detector under  $\text{Cu K}\alpha$  irradiation in the angular range  $10\text{--}100^\circ 2\theta$  and step  $0.04^\circ$ . Diffraction patterns were analyzed by the Rietveld method in the FullProf program. The powder XRD patterns of the samples obtained in the closed system were determined using powder diffractometer PANalytical X'Pert<sup>3</sup> with the  $\text{Cu K}\alpha$  radiation ( $\lambda = 1.5418 \text{ \AA}$ ,  $U = 40 \text{ kV}$ ,  $I = 30 \text{ mA}$ ) in the angular range  $5\text{--}100^\circ 2\theta$ , step size of  $0.04^\circ$ , and counting time of  $115 \text{ s step}^{-1}$ . The XRD patterns were evaluated using the commercial software PANalytical X'Pert HighScore Plus 3.0e.

TSL experiments were performed by different apparatus and conditions. Wavelength-resolved TSL experiments were carried out in the  $10\text{--}320 \text{ K}$  temperature range with a  $0.1 \text{ K/s}$  heating rate. Samples were X-ray irradiated at  $10 \text{ K}$ . The excitation source was a Philips 2274 X-ray tube with a tungsten target operating at  $20\text{--}32 \text{ kV}$  and  $10\text{--}30 \text{ mA}$  current. The TSL equipment (apparatus 1) consisted of a custom-made spectrometer measuring the TSL intensity as a function of temperature and wavelength simultaneously. The detection system was a TRIAX 180 Jobin-Yvon monochromator coupled to Jobin-Yvon Spectrum One 3000 charge-coupled device detector with the  $190\text{--}1100 \text{ nm}$  operating range and with the spectral resolution of about  $5 \text{ nm}$ . The obtained TSL emission spectra were corrected for the spectral efficiency of the detector. Using apparatus 2, the sample was irradiated by a Seifert X-ray tube with a tungsten target, operated at  $40 \text{ kV}$ . All measurements were performed in the temperature range  $77\text{--}700 \text{ K}$  with a Janis nitrogen cryostat. The TSL signal was detected with two branches simultaneously: spectrally resolved, detected by the spectrometer Ocean Optics QE65000 equipped with a CCD sensor ( $200\text{--}1000 \text{ nm}$  wavelength range) and unresolved one, detected by a TBX-04 PMT (IBH). In apparatus 3, a custom-made 5000 M HORIBA Jobin Yvon setup was used. The sample was selectively photo-irradiated by deuterium lamp (Heraeus) through excitation monochromator (Horiba) and spectrally unresolved TSL signal was detected by TBX-04 PMT. In this setup, the closed-cycle refrigerator (Janis), operating in  $10\text{--}500 \text{ K}$  temperature range, was used. Heating rate in apparatuses 2 and 3 was  $0.1 \text{ K/s}$ .

EPR experiments were carried out in the X-band ( $9.5 \text{ GHz}$ ) using a commercial Bruker X/Q-band E580 FT/CW ELEXSYS spectrometer in the  $20\text{--}296 \text{ K}$  temperature range in an Oxford Instruments ESR900 continuous flow cryostat. To irradiate the samples at liquid nitrogen temperature, an ISO-DEBYEFLEX 3003 highly stabilized X-ray equipment for structure analysis (tungsten X-ray tube,  $55 \text{ kV}$ ,  $30 \text{ mA}$ ) was used. The simulations of all EPR spectra and corresponding angular dependencies have been supplied by the EasySpin toolbox 5.1.12 program.<sup>27</sup>

## 3. RESULTS AND DISCUSSION

Three  $\text{Cs}_2\text{HfCl}_6$  single crystals were grown from materials prepared by the two approaches described in the [Experimental details](#) section. They are displayed in [Figure 1](#). For subsequent characterizations, the crystals and their specimens are further designated as CHC1 for the open and CHC2,3 for the closed systems.

The cylindrical shape of the as-grown  $\text{Cs}_2\text{HfCl}_6$  crystals was determined by the inner dimensions of the ampule reaching values of  $12 \text{ mm}$  in diameter and  $40\text{--}55 \text{ mm}$  in length depending on the starting charge of the material.

In the CHC1 crystals, several secondary grains in the tip of the ampule were observed, affecting the final quality of the grown ingot. Nevertheless, homogeneous grains of various sizes from  $5$  to  $15 \text{ mm}$  in the cylindrical part could be obtained. The biggest issue was the stoichiometry change along the crystal axis reaching the content of  $97 \text{ mol } \%$  of the  $\text{Cs}_2\text{HfCl}_6$  phase at the start of the crystal and only  $22 \text{ mol } \%$  at the end. In contrast, higher uniformity was achieved in the CHC2 crystal, with  $100$  and  $93 \text{ mol } \%$  of the  $\text{Cs}_2\text{HfCl}_6$  phase content along its axis. The CHC3 crystal possessed an excellent uniformity, being  $100 \text{ mol } \%$  of the  $\text{Cs}_2\text{HfCl}_6$  phase

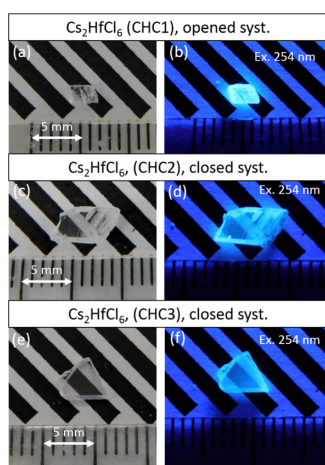


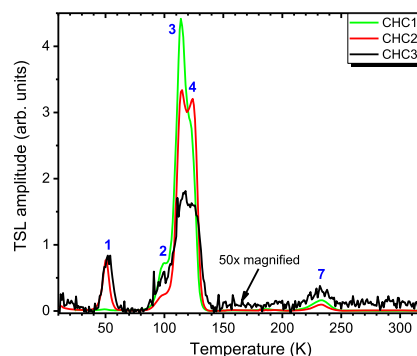
**Figure 1.** Polished samples of  $\text{Cs}_2\text{HfCl}_6$  were prepared from CHC1 (a), CHC2 (c), and CHC3 (e) crystals and displayed under UV excitation at 254 nm (b,d,f), respectively.

over the whole ingot. It means that the samples cut from CHC3 crystal consisted of 100%  $\text{Cs}_2\text{HfCl}_6$  crystal phase; in CHC2, it was about 100% (93–100%), whereas sample CHC1 consisted of 97% or less  $\text{Cs}_2\text{HfCl}_6$  phase. The other phase identified in the crystals was  $\text{CsCl}$ ; no other phase was present. Samples for subsequent characterizations were selected from the start of the obtained ingots with the highest  $\text{Cs}_2\text{HfCl}_6$  phase content. The size of the specimens cleaved and polished from the as-grown crystals was approximately  $2 \times 2 \times 1 \text{ mm}^3$ . The detailed information about the structural and physical

properties and crystal stoichiometry will be discussed in another work under preparation.

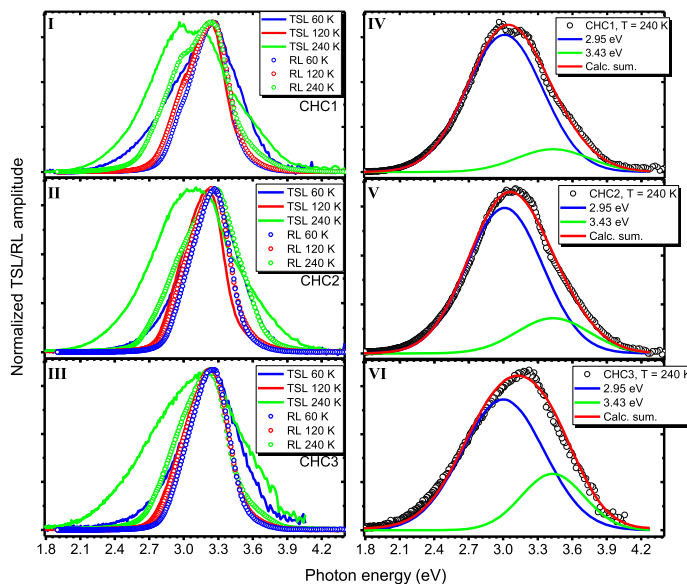
**3.1. TSL and RL Characterization.** Spectrally resolved TSL and RL experiments were carried out for all  $\text{Cs}_2\text{HfCl}_6$  samples using the apparatus 1. Corresponding emission spectra are shown in Figure 2.

In Figure 2I–III, the TSL and RL spectra are shown for temperatures chosen approximately  $\pm 10 \text{ K}$  aside from the observed TSL peaks in the glow curves reported in Figure 3.



**Figure 3.** TSL glow curves measured in three  $\text{Cs}_2\text{HfCl}_6$  samples indicated in the legend. The TSL signal in the CHC3 sample was 50 times magnified. Only the observed peaks were numbered in accordance with the peaks numbering used in Figure 4II and throughout the text below.

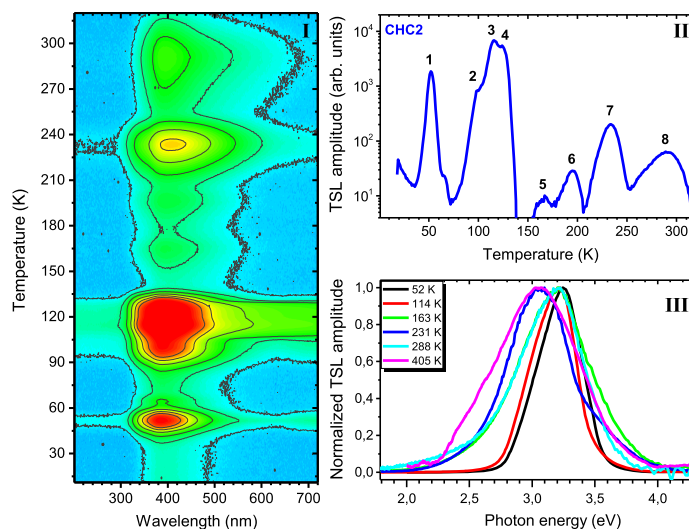
One can immediately see a drastic discrepancy between the TSL and RL spectra in all samples. Note that the spectral line shapes are approximately the same moving from sample to



**Figure 2.** TSL and RL emission spectra measured in the three  $\text{Cs}_2\text{HfCl}_6$  samples, CHC1–3 at different temperatures indicated in the legends (I–III). The irradiation doses in the TSL measurements were the same in all samples, whereas in RL, they are approximately 14–20 times different in the CHC1,2 and CHC3, lower in the former, regulated by exposure times of 3, 2, and 40 s, respectively. The 240 K TSL spectrum in each sample was decomposed into two Gaussian components with the energy maxima listed in the legends (IV–VI).

**Table 1.** Spectral Parameters of Fits (Spectral Components) Shown in Figure 2, Including TSL Emission Maxima  $E_{1,2}$ ,  $\text{fwhm}_{1,2}$ , and Amplitude  $A_{1,2}$ 

sample	$E_1$ (eV)	$\text{fwhm}_1$ (eV)	$A_1$ (a.u.)	$E_2$ (eV)	$\text{fwhm}_2$ (eV)	$A_2$ (a.u.)
CHC1		$0.78 \pm 0.07$	$0.76 \pm 0.05$		$0.74 \pm 0.07$	$0.13 \pm 0.02$
CHC2	$2.95 \pm 0.07$	$0.78 \pm 0.07$	$0.74 \pm 0.05$	$3.43 \pm 0.05$	$0.74 \pm 0.07$	$0.17 \pm 0.02$
CHC3		$0.84 \pm 0.07$	$0.73 \pm 0.05$		$0.64 \pm 0.07$	$0.24 \pm 0.02$

**Figure 4.** (I) Contour plot of a wavelength resolved TSL measurement performed in  $\text{Cs}_2\text{HfCl}_6$  (CHC2 sample) after X-ray irradiation at 10 K. A 0.1 K/s heating rate was adopted. (II) TSL glow curve obtained after integration of the wavelength-resolved measurements in the 1.77–4.96 eV range. The peaks are numbered (1–8). (III) Emission spectra of the TSL signal at selected temperatures shown in the legend. The 405 K spectrum was measured in the high-temperature (above room temperature) TSL measurements using apparatus 2.

sample. Obviously, the TSL and RL spectra are composed of several, at least two, strongly overlapping bands as it is shown as an example for the 240 K TSL spectrum in each CHC1–3 sample (Figure 2IV–VI) by decomposition on the single Gaussian component given by the standard expression:

$$G(E) = (A_{1,2} / (\text{FWHM}_{1,2} \sqrt{\pi/4 \ln 2})) \exp\left(-4 \ln 2 \frac{(E - E_{1,2})^2}{\text{FWHM}_{1,2}^2}\right)$$

using numerical fit of the experimental data. The parameters used for the fit are listed in Table 1. One can immediately see (Figure 2IV–VI) that the composition of the spectra is the same in each sample. The intensity distribution of two single components is, however, different.

This property is supposedly due to the existence of at least two emission centers, discussed in detail below. The complete discussion of the Gaussians evolution with temperature is given in subsection 3.1.1 for the CHC2 sample, taken as an example.

The TSL bands experience dramatic changes with temperature in the whole energy region, whereas those of RL exhibit less pronounced differences almost exclusively at the  $\sim 3$  eV edge. Remarkably, the RL emission was more than one order of magnitude weaker in the CHC3 sample compared to those in CHC1,2. The sample area exposed to irradiation was approximately the same in all experiments.

TSL glow curves (one for each sample) were obtained by integration of the TSL spectra (some of them are discussed above) within the 1.77–4.96 eV range for two different (10 times) X-ray irradiation doses, X1 (Figure 3) and X2 (not shown),  $X1 < X2$ , regulated by the exposure time. It is seen that those measured in the CHC1, CHC2 samples after the

dose, X1 are almost the same when considering the complex 2–4 and 7 peaks. The peak 1 in the CHC1 glow curve is negligibly weak, almost at the level of background noise. Even the higher irradiation dose, X2 did not significantly change its amplitude. In case of the CHC3 sample, the peak 1 is approximately 50 times weaker than that in CHC2 (Figure 3), thereby manifesting the same features independent of the sample stoichiometry. The position of this peak is independent of the irradiation dose, therefore, the recombination kinetics in this case was supposed to be that of the first order.<sup>28</sup> The peak 7 is present in all samples showing about the same properties as peak 1. The large difference is observed in the 2–4 peak complex. It can be seen that this composite peak is about 100 times weaker in CHC3 than those in CHC1,2 (Figure 3). The drop of the TSL glow curve amplitude in the most stoichiometric CHC3 sample might be connected with the reduced number of trapping centers in the host. However, the lower RL signal observed may also point to reduction of the initially high content of emission (recombination) centers (CHC1,2 samples). Therefore, better stoichiometry of the CHC3 sample should result in both suppression of traps and reduction of emission centers, not only those defect-related but also intrinsic (exciton luminescence) because the RL and TSL spectra in all samples feature similar multicomponent structure including similar intensity distribution of single components (Figure 2).<sup>23</sup>

As the CHC2 sample exhibited almost the same TSL and RL properties as CHC1, moreover, the pronounced amplitude of the peak 1 was registered (Figure 3), it was chosen for more

detailed study of the phenomena discussed above. The corresponding contour plot, TSL glow curve, and emission spectra are shown in Figure 4. The contour plot, panel I of Figure 4, features six clearly visible TSL structures with a broad and composite emission at about 400 nm. The signals above 700 nm can be assigned to the second order of the main emission.

The glow curve and TSL emission spectra at selected temperatures are reported in panel II and III of Figure 4, respectively. Several sharp TSL peaks are evidenced, whose emission spectrum is varying in shape. As it was mentioned above, at least two components can be determined in the spectra. The emission peaking at about 3.3 eV dominates the TSL spectrum at the lowest temperatures, together with a lower energy shoulder that becomes more evident with the temperature increasing.

The TSL was measured in the CHC2 sample in two ways: spectrally resolved, using X-rays as an excitation source at apparatus 2 and spectrally unresolved, with a deuterium lamp as the selective excitation source. In this experiment, the TSL glow curves were obtained after irradiation of the sample by the 6.5 and 4.59 eV energies (190 and 270 nm excitation wavelengths, respectively). The resulting glow curves are shown in Figure 5.

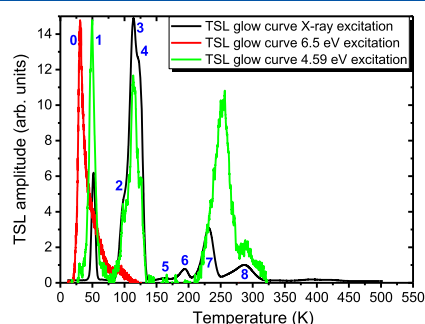


**Figure 5.** TSL glow curves measured in the CHC2 sample: spectrally resolved, constructed from the TSL spectra integrated within 1.24–4 eV after the X-ray irradiation; spectrally unresolved, using a deuterium lamp with the 6.5 and 4.59 eV excitation energies as an irradiation source. “1–8” numbers correspond to the peaks described in Figure 4II, whereas “0” is the newly observed peak.

As one can see, different excitation energies result in more or less the same glow curves, at least the strongest peaks in case of the X-ray and 4.59 eV excitations. However, the intensity distribution between the 1–4 and 5–8 peaks is considerably different. The 6.5 eV excitation is responsible for only two visible peaks, the newly observed 0 and partly 1, but to a very small extent. One can expect thus that the 4.59 eV excitation allows trapping processes connected with a different emission center than that in the case of the 6.5 eV excitation surpassing the crystal bandgap ( $\sim 6.3$  eV).<sup>23</sup> It is known that there are two kinds of main emission centers of exciton origin, related to Hf: the intrinsic self-trapped exciton and that affected by the presence of Zr.<sup>8,17,21</sup> The zirconium ion is a natural impurity inside the material because  $\text{Cs}_2\text{ZrCl}_6$  is isostructural with the  $\text{Cs}_2\text{HfCl}_6$ .<sup>29,30</sup>

**3.1.1. Discussion of the Temperature Evolution of the TSL Spectra.** To get a deep insight into the recombination phenomena during the TSL processes, the TSL spectra

obtained in the CHC2 sample by spectrally resolved TSL, apparatus 1 (10–320 K) and 2 (77–450 K, only the spectrum at 405 K was taken into account) were analyzed. They are presented in Figure S1 in the Supporting Information for the selected temperatures which correspond to the 1–8 peaks approximate maxima (Figures 4II and 5): 52, 100, 114, 122, 163, 194, 231, and 288, respectively. As one can see, the spectra manifest a complex, not a single Gaussian shape similarly to those discussed above, shown in Figure 2IV–VI, especially when moving along the temperature scale toward higher temperatures. A broadening of the spectrum occurs at 163 K, which is expected with increasing temperature. Because of their complex structure, the spectra have been decomposed into two-three Gaussian components centered at  $2.95 \pm 0.07$ ,  $3.22 \pm 0.04$ , and  $3.43 \pm 0.05$  eV (see also Table 1). The fits (sum of the components) and separate contributions are shown in each plot in Figure S1 in the Supporting Information. The parameters of the fit for each component are listed in Table S1 in the Supporting Information, including the energy of emission maximum, full width at half maximum (FWHM), and area under the curve. Remarkably, the spectra are almost the same from 52 to 100 K. They feature two Gaussian components (see details in Table S1 in the Supporting Information). The third one appears only at approximately 114 K being distinguishable until 231 K. At 288 K, only two Gaussians can be recognized again but about two times broader than those at 52–100 K (Figure S1, Table S1 in the Supporting Information). Note that the exciton emission in zinc oxide exhibits similar tendency of band broadening.<sup>31</sup> On the other hand, the presence of several strongly overlapping narrower bands forming these broad bands cannot be excluded. The temperature dependencies of the emission maxima, FWHM, and area of a single band are shown in Figure S2 in the Supporting Information. On the basis of the obtained results, one can conclude that there are indeed several emission mechanisms activated during the sample heating or cooling. Depletion of some specific trap(s) should be connected with those mechanisms, to a larger extent above approximately 120 K, as it has already been discussed previously for different light excitations (Figure 5). As the intrinsic Hf-related excitonic emission (broad band) is peaking at approximately 3.31 eV, the  $3.22 \pm 0.04$  eV band (Table S1, Figures S1 and S2 in the Supporting Information) may probably be related to this type of emission center.<sup>23</sup> The other distinguished band (Table S1, Figures S1 and S2 in the Supporting Information) peaking at  $2.95 \pm 0.07$  eV was attributed to the Zr-related emission (broad band) having the maximum at about 2.85 eV.<sup>23</sup> The single band at 3.43 eV is, presumably, also a defect-related emission; however, based on experimental data presented, it was hard to make the assumption about its origin.

**3.1.2. Trap Depths and Frequency Factors Determination.** Two TSL glow curves were measured by apparatus 2 applying 100 times different X-ray irradiation doses—governed by the exposure time of 1 (shown in Figure 6) and 100 min—to determine the order of recombination kinetics (both shown in Figure S3 in the Supporting Information). The 2–8 peaks in Figure 6 do not change their positions, regardless of the irradiation dose (Figure S3 in the Supporting Information), therefore, the first order kinetics was expected.<sup>28</sup> To derive corresponding trap depths and frequency factors, the initial rise technique was used after the partial cleaning (PC) procedure was carried out for the broad and/or strongly overlapped 1–4 and 6–8 peaks (Figure 4II).<sup>28</sup> The PC of the 6–8 peaks was

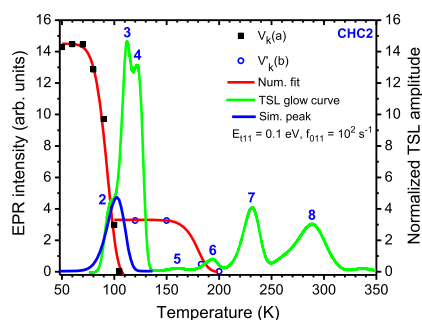


**Figure 6.** Experimental  $V_k(a)$  and  $V_k(b)$  EPR signals decay curves (dots) measured in the CHC2 sample fitted with the calculated ones (red solid lines) shown together with the TSL glow curve. Numbers 2–8 stand for the peak numbers. One glow peak has been simulated (sim. peak) using  $E_{t11} = 0.1$  eV,  $f_{011} = 10^2$  s $^{-1}$  for the trap depth and frequency factor.

carried out after X-ray irradiation dose 4 times higher compared to that used for 1–4 peaks. Corresponding Arrhenius plots are shown in Figure 7 along with the exponential fits of initial rise only for the 1, 4, 7, and 8 peaks (Figure 4II).

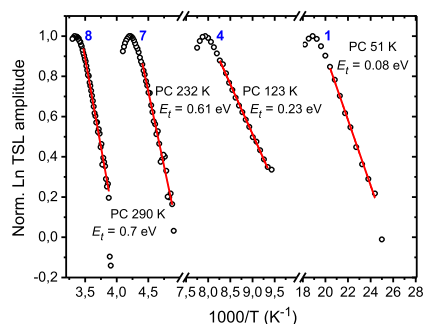


**Figure 7.** Arrhenius plots of the TSL glow curve peaks (1, 4, 7, 8) obtained in the CHC2 sample after PC procedure shown along with fits of initial rise. Stop temperatures of the performed PC as well as the determined trap depths are indicated.

The obtained trap depths ( $E_t$ ) together with frequency factors ( $f_0$ ) calculated using the expression,  $f_0 = \beta E_t / k_B T_{max}^2 \exp(E_t / k_B T_{max})$  ( $\beta = 0.1$  K/s is the heating rate) for the certain  $T_{max}$ , the single peak maximum, are listed in Table 2.

The analysis was carried out only for the 1, 4, 7, and 8 peaks because the others are either overlapping too strongly (2 and 3) or too weak (5 and 6) to give reliable results.

**Table 2. Trap Depths and Frequency Factors<sup>a</sup>**

peak number	$T_{stop}$ , K	$T_{max}$ , K	$E_t$ , eV	$f_0$ , s $^{-1}$
1	51	52	$0.08 \pm 0.03$	$\sim 10^6$
4	123	126	$0.23 \pm 0.03$	$\sim 10^7$
7	232	238	$0.61 \pm 0.06$	$\sim 10^{11}$
8	290	297	$0.7 \pm 0.06$	$\sim 10^{10}$

<sup>a</sup>The peak maxima temperatures are given for the separated peaks after the PC procedure

### 3.2. EPR Characterization of the CHC2,3 Samples.

In this article, the EPR study is mainly focused on the CHC2 and CHC3 samples. The obtained results are compared with CHC1 reported previously in ref 23. EPR spectra of CHC2 do not reveal any meaningful signals before X-ray irradiation. After being exposed to the beam, new resonances appeared. They are presented in Figure 8.

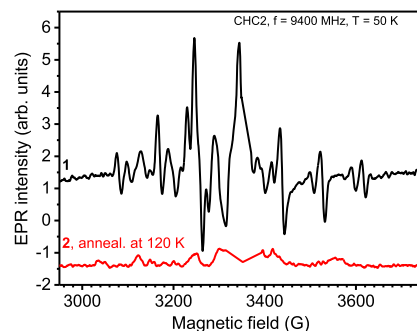


**Figure 8.** EPR spectra measured in CHC2 sample at the B||[110] orientation of an external magnetic field. The spectrum 1 appeared immediately after the X-ray irradiation, whereas the signal 2 becomes visible after annealing for 4 min at 120 K. The spectra have been measured at 50 K.

The  $g$  factors of the spectra centers of gravity at the chosen B||[110] orientation of the external magnetic field with respect to the crystal direction were 2.003 for signal 1 and 2.030 for signal 2, both larger than 2.0023, which is the free electron value. This suggests a half-filled outer shell, the so-called hole-like mechanism of the paramagnetic center (hole trapping, see e.g., ref 33).<sup>32</sup> The spectra are multicomponent with very specific distribution of the single resonance positions (and intensity) over the magnetic field region studied. Moreover, all of them show the same temperature dependence pointing to the hyperfine structure (HFS). Referring to the composition of the  $\text{Cs}_2\text{HfCl}_6$  material, one may expect that the discovered EPR signals (Figure 8) are due to the  $V_k$  centers, the two chlorine anions sharing a trapped hole ( $\text{Cl}_2^-$  molecular ions). The observed HFS in this case should come from  $^{35,37}\text{Cl}$  nuclei. Note that the  $V_k$  centers with very similar spectral features have been explored earlier in alkali halides.<sup>34</sup> Moreover, the two different types of  $V_k$  centers,  $V_k(a)$  and  $V_k(b)$ , have recently been reported also in the  $\text{Cs}_2\text{HfCl}_6$  itself.<sup>23</sup> Remarkably, the  $V_k(a)$  EPR spectrum resembles in detail the spectrum 1 in Figure 8 at the same orientation of the external magnetic field. To verify a connection between the two spectra, the experimental spectrum 1 has been approximated by that calculated using the following spin-Hamiltonian

$$\hat{H} = \beta_e \hat{S}_z g B + \sum_{i=1}^2 \hat{S}_z A_{zi} (^{35,37}\text{Cl}) \hat{I}_{zi} (^{35,37}\text{Cl}) \quad (1)$$

where  $\beta_e$  is the Bohr magneton,  $\hat{S}_z$  is the  $z$ -component of an electron spin operator, and  $B$  is a magnetic field along the  $z$  axis. For the present case, the [110] crystal direction is considered as  $z$  (Figure 8).  $A_{zi} (^{35,37}\text{Cl})$  are hyperfine (HF) constants of the  $^{35,37}\text{Cl}$  nuclei in any of three possible combinations in the created chlorine molecular ion:  $^{35}\text{Cl}-^{35}\text{Cl}$ ,  $^{37}\text{Cl}-^{37}\text{Cl}$ , and  $^{35}\text{Cl}-^{37}\text{Cl}$ .  $\hat{I}_{zi} (^{35,37}\text{Cl})$  are  $z$



components of nuclear spin operators of the  $^{35}\text{Cl}$  ( $I = 3/2$ , total abundance  $\sim 76\%$ ) and  $^{37}\text{Cl}$  ( $I = 3/2$ ,  $\sim 24\%$  abundance) isotopes. The parameters of the simulation were:  $g = 2.003$ ,  $A_{z1}(^{35}\text{Cl}) = A_{z2}(^{35}\text{Cl}) = 255$  MHz, the same as that reported for the  $V_k(a)$  center in the  $\text{Cs}_2\text{HfCl}_6$  along the  $[110]$  direction.<sup>23</sup> Both the experimental and the calculated spectra are shown in Figure 9.

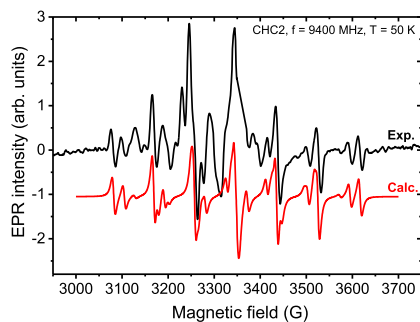


**Figure 9.** Experimental spectrum 1 (CHC2 sample) after exposure to X-rays along the  $\text{B}||[110]$  orientation shown together with the calculated one assuming only the  $\text{Cl}_2^-$  molecular ion with the  $z$  axis parallel to the  $[110]$  crystal direction.

The CHC  $Fm\bar{3}m$  simple cubic structure (ref 35) allows several magnetically inequivalent positions (possess the same local symmetry and crystal field strength but their local surroundings are differently posed with respect to one another and crystal axes) for a paramagnetic particle.<sup>36</sup> Only one position of that kind was taken into account for the spectrum simulation (Figure 9) with the  $z$  axis parallel to the  $[110]$  crystal direction similarly to  $V_k(a)$  in ref 23. It can be seen in Figure 9 that the calculated spectrum manifests in almost perfect agreement with the experimental one corroborating anticipated correlation. The angular dependence of its resonance fields in the  $(111)$  plane (see Figure S4 in the Supporting Information) was approximated by the calculated one using the expression in eq 2 as well. The determined signal 1 spin-Hamiltonian parameters are listed in Table 3 along with those obtained for  $V_k(a)$  and  $V_k(b)$  in ref 23 for the CHC1 sample.

One can easily see that the signal 1 and  $V_k(a)$  center parameters are the same. Seemingly, signal 1 (Figures 8 and 9) in the CHC2, as well as in the CHC1 sample is produced by the  $V_k(a)$  center.<sup>23</sup> The EPR spectrum measured in the CHC3 sample (see Figure 10) was at least several times weaker than that in CHC2 exhibiting supposedly only faint traces of signal 1. The EPR spectra were measured after the sample annealing at 100 K when obvious decrease in intensity of the initial spectrum had been observed. This correlates well with the thermal stability of the  $V_k(a)$  center (does not withstand annealing at  $\sim 100$  K) discussed in detail in subsection 3.3

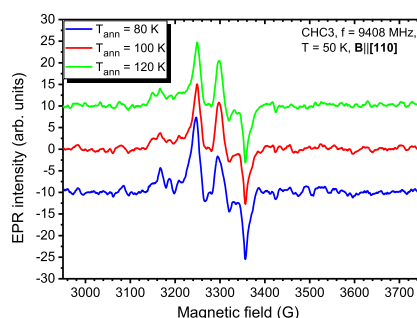


**Figure 10.** EPR spectra measured in CHC3 sample at the  $\text{B}||[110]$  orientation of an external magnetic field. An error of the orientation is expected to be not larger than  $\pm 5^\circ$  in the  $(111)$  plane because the angular dependence of the spectrum is not sharp. Two overlapped signals similar to 1, 2 in Figure 8 can be guessed. The presence of signal 1 appears as the change in the spectrum after annealing at 100 K; its intensity is getting weaker. The signal 2 is still visible even after 120 K annealing.

below (see also ref 23). Therefore, formation of this kind of  $V_k$  centers being observed in three differently synthesized samples is expected to be an intrinsic property of the material, in general, independent of its stoichiometry. The spectrum that remained after annealing at 100 K was supposed to be produced by the  $V_k(b)$  center because it disappears after annealing at  $\sim 200$  K as well as that of  $V_k(b)$  (see subsection 3.3 below for details). The intensity of the signal was insufficient to perform rigorous analysis.

The spectrum 2 in Figure 8 was measured at  $T = 50$  K. Its major features (HFS, similar to signal 1) are scarcely discernible, and the signal is saturated.<sup>32</sup> In order to carry out more or less qualitative analysis, the spectrum intensity needs to be increased. The only option was to decrease the temperature down to 20 K; however, this made the signal even more saturated (see Figure 11). Nevertheless, the HF structure became sufficiently visible to roughly approximate the spectrum (similarly to signal 1) by the one calculated using the spin-Hamiltonian in eq 1. The effective spin-Hamiltonian parameters,  $g$ ,  $A_1(^{35}\text{Cl})$ , and  $A_2(^{35}\text{Cl})$  are listed in Table 3. The origin of signal 2 is thus expected to be some kind of  $V_k$  center as well. The obtained HF constants differ from those obtained for  $V_k(a)$  above. Moreover, as  $A_{z1}(^{35}\text{Cl}) > A_{z2}(^{35}\text{Cl})$  (see Table 3), the chlorine nuclei in the  $\text{Cl}_2^-$  molecular ion are inequivalent. The charge density should experience inhomogeneous distribution in two  $\text{Cl}^-$  forming the molecular ion, most probably due to the so-called bending bond.<sup>34</sup> Despite very low temperature, the signal 2 is still too weak and saturated to provide a possibility of complete analysis like that for the  $V_k(a)$  center. Therefore, the model of the corresponding center remains rather obscure. It can be the molecular ion formed by two regular chlorine ions perturbed by a vacancy or one of the chlorine ions is interstitial (H center, see ref 37).<sup>34</sup> Signal 2 is

**Table 3.** Spin-Hamiltonian Parameters of Observed  $V_k$  Centers in CHC2 along with the Parameters Obtained in CHC1<sup>23</sup>

center	$g_z$	$g_{\perp}$	$A_z(^{35}\text{Cl}), 10^{-4} \text{ cm}^{-1}$	$A_{\perp}(^{35}\text{Cl}), 10^{-4} \text{ cm}^{-1}$	$z$ principal axis	thermal stability (K)
$V_k(a)$ in CHC2 (signal 1)	2.003(3)	2.046(3)	85(2)	10(1)	$[110]$	$\sim 60$
$V_k(b)$ in CHC2 (signal 2)	$g = 2.03(2)$		$A_1 = 90(2), A_2 = 77(2)$			$\sim 150$
$V_k(a)$ , ref 23	2.003	2.046	85	10	$[110]$	$\sim 55$
$V_k(b)$ , ref 23	2.000	2.0320	100	18	$[100]$	$\sim 200$

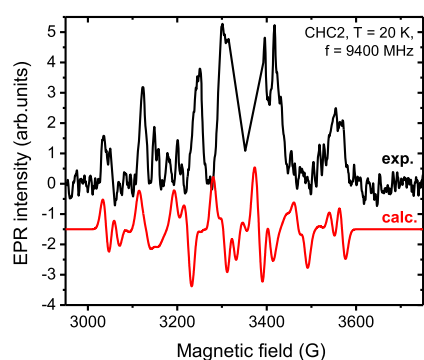


**Figure 11.** Experimental spectrum 2 (CHC2 sample) along B||[110] after annealing at 120 K shown together with the calculated one assuming only one type of the  $\text{Cl}_2^-$  molecular ion magnetically inequivalent position. Note that the spectrum 2 also had very low EPR signal peak-to-peak intensity as compared to the spectrum 1 ( $V_k(a)$  center), approximately 10 times, see Figure 8, whereas  $V_k(a)$  and  $V_k(b)$  spectra have the peak-to-peak intensity of the same order of magnitude.<sup>23</sup> It is also worth noting that this EPR signal (Figure 8) was already strongly saturated at 50 K and much more at 20 K (Figure 11), whereas the  $V_k(b)$  one showed no sign of saturation even at 18 K. To preserve the analogy with the CHC1 sample, the source of signal 2 was designated as  $V_k(b)$ .<sup>23</sup> On the basis of the analysis done, it can be concluded that the stoichiometry plays a significant role in different defects formation in the CHC crystals, while the self-trapping processes are always present similarly to lead chloride and lead molybdate.<sup>38,39</sup> It cannot be excluded also that the decreased concentration of the  $V_k$  centers is connected with the reduction of unexpected impurities content. It is well known that, for example, Zr contributes to  $V_k$  centers creation in halides. This will be studied in detail in the new upcoming work, which will be published elsewhere.

not consistent with that of  $V_k(b)$  reported earlier (its parameters are shown in Table 3 as well).<sup>23</sup> The latter features homogeneous charge density of a paramagnetic electron in the  $\text{Cl}_2^-$  molecular ion (HF constants are the same for both chlorine nuclei). Besides, signal 2 is much less thermally stable than that of  $V_k(b)$  (compare 150 and 200 K in ref 23, Table 3, respectively).

**3.3. Thermal Stability of the EPR Active Centers in Correlation with TSL.** To study thermal stability of the  $V_k(a)$  and  $V_k(b)$  centers and possibly correlate it with the TSL peaks, the well-known pulse annealing method was applied (see e.g., ref 40). EPR spectra were always measured at  $T = 50$  K, while from cycle to cycle, the annealing temperature had been increased until the signals disappeared completely. The annealing time of 4 min was chosen to reach good thermalization of the sample. The obtained decay curves are shown in Figure 6 together with measured TSL glow curves. As the first order recombination kinetics was proven in Section 3.1, the EPR decay curves were expected to follow it as well. To determine the trap depths and frequency factors, they have been fitted using the following recursive expression<sup>41</sup>

$$I_{i+1} = I_i \exp\left(-f_0 t \exp\left(-\frac{E_i}{k_B T_i}\right)\right) \quad (2)$$

where  $I_i$  is the EPR intensity prior to the  $i$ -th cycle of annealing at the chosen temperature,  $T_i$  for  $t = 4$  minutes. The trap depths,  $E_{i1} = 0.11 \pm 0.03$  eV and  $E_{i2} = 0.30 \pm 0.03$  eV, and frequency factors,  $f_{01} \approx 10^{2-3} \text{ s}^{-1}$  and  $f_{02} \approx 10^6 \text{ s}^{-1}$ , were

determined for the  $V_k(a)$  and  $V_k(b)$  centers, respectively. It was useful to make an effort to find if correspondence between some of the peaks 2–4 and the  $V_k(a)$  EPR signal thermal decay indeed exists, taking into account their overlap (Figure 6). With this aim, a TSL glow peak was simulated, assuming the first order kinetics governed by the expression<sup>28</sup>

$$I(T) = n_0 f_0 \exp\left(-\frac{E_t}{k_B T}\right) \exp\left(-\left(\frac{f_0}{\beta}\right) \int_{T_0}^T \exp\left(-\frac{E_t}{k_B T}\right) dT\right) \quad (3)$$

where  $\beta = 0.1 \text{ K/s}$  is the heating rate used in the TSL experiments, in particular, to obtain the glow curves shown in Figure 6,  $n_0$  (taken  $2 \times 10^{11} \text{ m}^{-3}$ ) and  $T_0$  are the starting concentration of traps and initial temperature. The following parameters have been used:  $E_{t11} = 0.1 \text{ eV}$ ,  $f_{011} \approx 10^2 \text{ s}^{-1}$ . They were derived from  $E_{t1} = 0.11 \text{ eV}$  and  $f_{01} \approx 10^{2-3} \text{ s}^{-1}$  obtained from the  $V_k(a)$  EPR signal thermal decay curve fitting (Figure 6). It is shown in Figure 6 as well, demonstrating indeed strong superimposition on peak 2 at about 100 K, where the PC procedure with the subsequently applied initial rise technique did not give trustful result, as it was mentioned in the previous section. This provides a clear evidence for the  $V_k(a)$  center EPR signal decay to be correlated with peak 2. Remarkably, the TSL glow curves measured in the CHC1-3 samples exhibit the same number of peaks and their constant positions (Figures 3, 4II, and 5). By contrast, the  $V_k(b)$  center observed in the CHC2 sample (Figures 8 and 11) is of different origin than that of  $V_k(b)$  in CHC1.<sup>23</sup> Additionally, both demonstrate different thermal stability, surviving below 150 and 200 K, respectively.<sup>23</sup> The  $E_{t3} = 0.43 \pm 0.03 \text{ eV}$  trap depth and  $f_{03} \approx 10^5 \text{ s}^{-1}$  frequency factor were also determined presently for the  $V_k(b)$  center in the CHC1 sample using pulse annealing technique as well (see Figure S5 in the Supporting Information). Comparing the kinetic parameters determined for the  $V_k(b)$  and  $V_k(a)$  centers with the ones listed in Table 2, one can find no correspondence with the TSL peaks introduced there. Note also that the peak 8 (Figures 4II and 5) is completely absent in the CHC1 TSL glow curve (Figure S5 in the Supporting Information). One may conclude then that the emission produced in TSL processes is due to recombination of detrapped electrons. To support this suggestion, we considered the results reported in for another halide,  $\text{LaBr}_3:\text{Ce}$ .<sup>42</sup> There, the TSL emission from  $\text{Ce}^{3+}$ , commonly known as the recombination center for electrons, was observed together with the self-trapped electron emission. Moreover, both emissions give approximately the same shape of the TSL glow curve. This proves the STE to be the recombination center for electrons as well. Similarly, the  $V_k(a)$  center is thus supposed to be a part of the  $\text{Hf}^{3+}-\text{Cl}_2^-$  self-trapped exciton (here, the  $\text{Hf}^{3+}$  serves as an electron trap) and, probably, peak 2 in the TSL glow curve (Figures 4II and 5) is due to its disintegration. Low trap depth,  $E_{t1} = 0.11 \text{ eV}$  suggests that the  $\text{Cl}_2^-$  hole trap is shallow. The  $\text{Hf}^{3+}$  ion is, most probably, invisible in EPR, as it has been discussed in ref 23. The simultaneously trapped electron and hole, both shallow, were reported in, for example,  $\text{ZnMoO}_4$ .<sup>43,44</sup> In favor of this suggestion, the theoretical calculations done recently, in ref 21, report creation of the self-trapped electrons and holes in the material. The  $V_k(b)$  center should be the usual hole trapping center.

#### 4. CONCLUSIONS

EPR and TSL methods have been combined to study the mechanism of charge trapping and its nature in  $\text{Cs}_2\text{HfCl}_6$  single crystals. Two different EPR signals of  $V_k$  centers ( $\text{Cl}_2^-$  molecular ions,  $V_k(\text{a})$  and  $V_k'(\text{b})$ ) were detected in the CHC2,3 samples. As the  $V_k(\text{a})$  center has recently been reported in the CHC1 sample, see ref 23, and was observed in the CHC2,3 samples as well, the creation of such kinds of defects is supposed to be the intrinsic property of the CHC material. The  $V_k'(\text{b})$  center detected along with  $V_k(\text{a})$  in CHC2,3 recently is different from the  $V_k(\text{b})$  center reported in CHC1. The latter features uniform charge distribution of a paramagnetic electron in the molecular ion. By contrast,  $V_k'(\text{b})$  is characterized by inhomogeneous charge density distribution in the molecular ion, probably, due to either bending of the Cl–Cl pseudo-bond because of some imperfection nearby or one of the  $\text{Cl}^-$  ions being interstitial. Besides, the thermal stability of the  $V_k'(\text{b})$  center is much lower (approximately up to 150 K) than that of  $V_k(\text{b})$  (200 K), with respect to ref 23. It also has very low EPR signal peak-to-peak intensity strongly saturated already at 50 K, whereas  $V_k(\text{b})$  shows no sign of saturation even at 18 K. Consequently, the detailed analysis of the  $V_k'(\text{b})$  center was not feasible except for rough approximation of its stability. The  $V_k(\text{a})$  and  $V_k'(\text{b})$  trap depths,  $E_{t1} = 0.11 \pm 0.03$  eV and  $E_{t2} = 0.30 \pm 0.03$  eV, and frequency factors,  $f_{01} \approx 10^{2-3} \text{ s}^{-1}$  and  $f_{02} \approx 10^6 \text{ s}^{-1}$ , respectively, were determined from the fit of the EPR signal decay curves. For the  $V_k(\text{b})$ , the following parameters were obtained:  $E_{t3} = 0.43 \pm 0.03$  eV and  $f_{03} \approx 10^5 \text{ s}^{-1}$  in a similar way. Therefore, one can infer that the charge carrier trapping processes strongly depend on the CHC stoichiometry.

TSL spectra were very complex, featuring a multicomponent structure within the 10–500 K temperature range. They could be decomposed to up to 2–3 single contributions. Their temperature evolution enabled to distinguish at least two main luminescence mechanisms attributed to Hf and Zr impurity-based emissions. The glow curves manifested eight peaks at approximately 52, 100, 114, 122, 163, 194, 231, and 288 K. They exhibit first-order recombination kinetics. PC with subsequent application of the initial rise method provided reliable results only for four of them. In particular, the trap depths and frequency factors could be determined only for the broad 52, 122, 231, and 288 K peaks. Using the trap depth and frequency factor of the  $V_k(\text{a})$  center obtained above, the corresponding TSL peak was simulated. It correlates well with the measured 114 K peak. However, comparison with results of the TSL study in cerium-doped lanthanum halides suggests that TSL peaks measured in the present work are due to recombination of trapped electrons.<sup>42</sup> Therefore, the  $V_k(\text{a})$  center (hole-like) was expected to be a part of the self-trapped exciton of the  $\text{Hf}^{3+}-\text{Cl}_2^-$  form. The  $V_k'(\text{b})$  center is anticipated to be the usual hole-trapping center because its disintegration could not be trustfully correlated with any of the studied peaks existing in all three samples. Furthermore, based on RL, TSL, and EPR measurements, we conclude that better stoichiometry leads to simultaneous reduction of the number of both the emission (recombination) centers (Hf- and Zr-based, e.g. ref 23) as well as the trapping centers.

#### ■ ASSOCIATED CONTENT

##### Supporting Information

The Supporting Information is available free of charge on the ACS Publications website at DOI: 10.1021/acs.jpcc.9b05760.

TSL spectra measured in CHC2 sample at different temperatures near the TSL peaks maxima, spectral parameters of their fits; evolution of the emission maxima, integral intensities, and FWHM of single components in the TSL spectra, TSL glow curves, angular dependencies of the resonance magnetic field of signal 1 (CHC2 sample), EPR spectra measured in CHC3 sample, and experimental  $V_k(\text{b})$  center EPR decay curve measured in CHC1 sample (PDF)

#### ■ AUTHOR INFORMATION

##### Corresponding Author

\*E-mail: [nikl@fzu.cz](mailto:nikl@fzu.cz). Phone: +420220318445.

##### ORCID

R. Král: 0000-0002-4519-6030

M. Nikl: 0000-0002-2378-208X

##### Notes

The authors declare no competing financial interest.

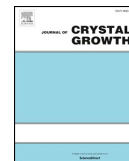
#### ■ ACKNOWLEDGMENTS

The authors gratefully acknowledge the financial support of the Ministry of Education, Youth and Sports of Czech Republic under projects LO1409 and CZ.02.1.01/0.0/0.0/16\_013/0001406 and the Czech Science Foundation project no. 18-17555Y.

#### ■ REFERENCES

- (1) Maniv, S.; Low, W.; Gabay, A. EPR Sites of Molybdenum Ions in Single Crystals of  $\text{Cs}_2\text{HfCl}_6$  and  $\text{Cs}_2\text{ZrCl}_6$ . *J. Phys. Chem. Solids* **1974**, *35*, 373–381.
- (2) Maniv, S.; Low, W.; Gabay, A. EPR Spectrum of  $\text{W}^{5+}$  in Single Crystals of  $\text{Cs}_2\text{ZrCl}_6$  and  $\text{Cs}_2\text{HfCl}_6$ . *J. Phys. Chem. Solids* **1971**, *32*, 815–817.
- (3) Reinberg, A. R.; Parker, S. G. Sharp-Line luminescence of  $\text{Re}^{4+}$  in cubic single crystals of  $\text{Cs}_2\text{ZrCl}_6$  and  $\text{Cs}_2\text{HfCl}_6$ . *Phys. Rev. B: Condens. Matter Mater. Phys.* **1970**, *1*, 2085–2088.
- (4) Douglas, I. N. Optical spectra of  $\text{IrCl}_6^{2-}$  in Single Crystals of  $\text{Cs}_2\text{ZrCl}_6$ ,  $\text{Cs}_2\text{HfCl}_6$ , and  $\text{K}_2\text{SnCl}_6$  at low temperatures. *J. Chem. Phys.* **1969**, *51*, 3066–3073.
- (5) Dorain, P. B.; Patterson, H. H.; Jordan, P. C. Optical spectra of  $\text{Os}^{4+}$  in single cubic crystals at 4.2°K. *J. Chem. Phys.* **1968**, *49*, 3845–3857.
- (6) Hofstadter, R. Alkali Halide Scintillation Counters. *Phys. Rev.* **1948**, *74*, 100.
- (7) Burger, A.; Rowe, E.; Groza, M.; Morales Figueroa, K.; Cherepy, N. J.; Beck, P. R.; Hunter, S.; Payne, S. A. Cesium hafnium chloride: A high light yield, non-hygroscopic cubic crystal scintillator for gamma spectroscopy. *Appl. Phys. Lett.* **2015**, *107*, 143505.
- (8) Saeki, K.; Fujimoto, Y.; Koshimizu, M.; Yanagida, T.; Asai, K. Comparative Study of Scintillation Properties of  $\text{Cs}_2\text{HfCl}_6$  and  $\text{Cs}_2\text{ZrCl}_6$ . *Appl. Phys. Express* **2016**, *9*, 042602.
- (9) Fang, C. M.; Biswas, K. Quaternary Iodides  $\text{A}(\text{BaSr})\text{I}_3\text{:Eu}^{2+}$  (A = K, Cs) as Scintillators for radiation detection. *J. Phys. Chem. C* **2016**, *120*, 1225–1236.
- (10) van Loef, E. V. D.; Dorenbos, P.; Krämer, K.; Güdel, H. U. High-energy-resolution scintillator:  $\text{Ce}^{3+}$  activated  $\text{LaBr}_3$ . *Appl. Phys. Lett.* **2001**, *79*, 1573–1575.
- (11) Cherepy, N. J.; Hull, G.; Drobshoff, A. D.; Payne, S. A.; van Loef, E.; Wilson, C. M.; Shah, K. S.; Roy, U. N.; Burger, A.; Boatner,

- L. A.; et al. Strontium and barium iodide high light yield scintillators. *Appl. Phys. Lett.* **2008**, *92*, 083508.
- (12) Fang, C. M.; Biswas, K. Preferential Eu site occupation and its consequences in the ternary luminescent halides  $AB_2I_3:Eu^{2+}$  (A=Li–Cs; B=Sr, Ba). *Phys. Rev. Appl.* **2015**, *4*, 014012.
- (13) Bourret-Courchesne, E. D.; Bizarri, G.; Borade, R.; Yan, Z.; Hanrahan, S. M.; Gundiah, G.; Chaudhry, A.; Canning, A.; Derenzo, S. E. Nuclear instruments and methods in physics research section A: Accelerators, spectrometers, detectors and associated equipment. *Nucl. Instrum. Methods Phys. Res., Sect. A* **2009**, *612*, 138–142.
- (14) Dorenbos, P.; van't Spijker, J. C.; Frijns, O. W. V.; van Eijk, C. W. E.; Krämer, K.; Güdel, H. U.; Ellens, A. Scintillation Properties of  $RbGd_2Br_7:Ce^{3+}$  Crystals; Fast, Efficient, and High Density Scintillators. *Nucl. Instrum. Methods Phys. Res., Sect. B* **1997**, *132*, 728–731.
- (15) Shah, K. S.; Glodo, J.; Higgins, W.; van Loef, E. V. D.; Moses, W. W.; Derenzo, S. E.; Weber, M. J. *CeBr3 Scintillators for Gamma-Ray Spectroscopy, IEEE Nuclear Science Symposium Conference Record, Rome, Italy, Oct 16–22, 2004*; Seibert, A., Ed.; IEEE, 2004.
- (16) Guillot-Noël, O.; de Haas, J. T. M.; Dorenbos, P.; van Eijk, C. W. E.; Krämer, K.; Güdel, H. U. Optical and Scintillation Properties of Cerium-Doped  $LaCl_3$ ,  $LuBr_3$ , and  $LuCl_3$ . *J. Lumin.* **1999**, *85*, 21–35.
- (17) Kurosawa, S.; Kodama, S.; Yokota, Y.; Horiai, T.; Yamaji, A.; Shoji, Y.; Král, R.; Pejchal, J.; Ohashi, Y.; Kamada, K.; et al. Cesium Hafnium Chloride Scintillator Coupled with an Avalanche Photodiode Photodetector. *J. Instrum.* **2017**, *12*, C02042.
- (18) Koshimizu, M.; Saeki, K.; Fujimoto, Y.; Okada, G.; Yanagida, T.; Yamashita, Sh.; Asai, K. A three-state model for describing the temperature variation of the scintillation properties of  $Cs_2HfCl_6$ . *Jpn. J. Appl. Phys.* **2018**, *57*, 032401.
- (19) Glodo, J.; Hawrami, R.; Shah, K. S. Development of  $Cs_2LiYCl_6$  scintillator. *J. Cryst. Growth* **2013**, *379*, 73–78.
- (20) Ashcroft, N. W.; Mermin, N. D. *Solid State Physics*; Brooks/Cole, Cengage Learning, 1976.
- (21) Kang, B.; Biswas, K. Carrier Self-Trapping and Luminescence in Intrinsically Activated Scintillator: Cesium Hafnium Chloride ( $Cs_2HfCl_6$ ). *J. Phys. Chem. C* **2016**, *120*, 12187–12195.
- (22) *Nanocomposite Ceramic and Thin Film Scintillators*; Nikl, M., Ed.; Pan Stanford Publishing Pte. Ltd: Singapore, 2017.
- (23) Král, R.; Babin, V.; Mihóková, E.; Buryi, M.; Laguta, V. V.; Nitsch, K.; Nikl, M. Luminescence and Charge Trapping in  $Cs_2HfCl_6$  Single Crystals: Optical and Magnetic Resonance Spectroscopy Study. *J. Phys. Chem. C* **2017**, *121*, 12375–12382.
- (24) Nitsch, K.; Cihlár, A.; Málková, Z.; Rodová, M.; Vaněček, M. The purification and preparation of high purity  $PbCl_2$  and ternary alkali lead chloride single crystals. *J. Cryst. Growth* **1993**, *131*, 612–615.
- (25) Král, R.; Nitsch, K.; Babin, V.; Šulc, J.; Jelínková, H.; Yokota, Y.; Yoshikawa, A.; Nikl, M. Growth and optical properties of RE-doped ternary rubidium lead chloride single crystals. *Opt. Mater.* **2013**, *36*, 214–220.
- (26) Takabe, M.; Kishimoto, A.; Kataoka, J.; Sakuragi, S.; Yamasaki, Y. Performance evaluation of newly developed  $SrI_2(Eu)$  scintillator. *Nucl. Instrum. Methods Phys. Res.* **2016**, *831*, 260.
- (27) Stoll, S.; Schweiger, A. EasySpin, a comprehensive software package for spectral simulation and analysis in EPR. *J. Magn. Reson.* **2006**, *178*, 42.
- (28) McKeever, S.W.S. *Thermoluminescence of Solids*; Cambridge University Press: Cambridge, 1985.
- (29) Engel, G. Die kristallstrukturen einiger hexachlorkomplexsalze. *Z. für Kristallogr.—Cryst. Mater.* **1935**, *90*, 341–373.
- (30) Ackerman, J. F. Preparation and Luminescence of Some  $[K_2PtCl_6]$  Materials. *Mater. Res. Bull.* **1984**, *19*, 783–791.
- (31) Hauschild, R.; Priller, H.; Decker, M.; Brückner, J.; Kalt, H.; Klingshirn, C. Temperature dependent band gap and homogeneous line broadening of the exciton emission in  $ZnO$ . *Phys. Status Solidi C* **2006**, *3*, 976–979.
- (32) Wertz, J. E.; Bolton, J. R. *Electron Spin Resonance. Elementary Theory and Practical Applications*, Series in Advanced Chemistry; McGraw-Hill: New York, 1972.
- (33) Laguta, V. V.; Buryi, M.; Nikl, M.; Rosa, J.; Zazubovich, S. Hole capture in  $PbWO_4:Mo,La(Y)$  scintillator crystals. *Phys. Rev. B: Condens. Matter Mater. Phys.* **2011**, *83*, 094123.
- (34) Castner, T. G.; Känzig, W. The Electronic Structure of V Centers. *J. Phys. Chem. Solids* **1957**, *3*, 178–195.
- (35) Maniv, S. Crystal data for  $Cs_2HfCl_6$ . *J. Appl. Crystallogr.* **1976**, *9*, 245.
- (36) Meilman, M. L.; Samoilovich, M. I. *Introduction into EPR Spectroscopy of Activated Crystals*; Atomizdat: Moscow, 1977; pp 126–130 (in Russian).
- (37) Känzig, W.; Woodruff, T. O. The Electronic Structure of an H Center. *J. Phys. Chem. Solids* **1959**, *9*, 70–92.
- (38) Nistor, S. V.; Goovaerts, E.; Schoemaker, D. Direct observation of electron self-trapping in  $PbCl_2$  crystals. *Phys. Rev. B: Condens. Matter Mater. Phys.* **1993**, *48*, 9575–9580.
- (39) Buryi, M.; Laguta, V.; Fasoli, M.; Moretti, F.; Trubitsyn, M.; Volnianskii, M.; Vedda, A.; Nikl, M. Electron self-trapped at molybdenum complex in lead molybdate: An EPR and TSL comparative study. *J. Lumin.* **2017**, *192*, 767–774.
- (40) Nistor, S. V.; Stefan, M.; Ghica, D. Pulse annealing electron paramagnetic resonance with probing transition ions. Application to thermal formation and growth of nano $ZnO$ . *J. Therm. Anal. Calorim.* **2014**, *118*, 1021–1031.
- (41) Pejchal, J.; Buryi, M.; Babin, V.; Prusa, P.; Beitlerova, A.; Barta, J.; Havlak, L.; Kamada, K.; Yoshikawa, A.; Laguta, V.; Nikl, M. Luminescence and scintillation properties of Mg-codoped  $LuAG:Pr$  single crystals annealed in air. *J. Lumin.* **2017**, *181*, 277–285.
- (42) Sellès, O.; Fasoli, M.; Vedda, A.; Martini, M.; Gourier, D. Thermoluminescence study of cerium-doped lanthanum halides. *Phys. Status Solidi C* **2007**, *4*, 1004–1007.
- (43) Spassky, D. A.; Nagirnyi, V.; Mikhailin, V. V.; Savon, A. E.; Belsky, A. N.; Laguta, V. V.; Buryi, M.; Galashov, E. N.; Shlegel, V. N.; Voronina, I. S.; et al. Trap Centers in Molybdates. *Opt. Mater.* **2013**, *35*, 2465–2472.
- (44) Buryi, M.; Spassky, D. A.; Hybler, J.; Laguta, V.; Nikl, M. Electron Spin Resonance study of charge trapping in  $\alpha$ - $ZnMoO_4$  single crystal scintillator. *Opt. Mater.* **2015**, *47*, 244–250.



## Modified vertical Bridgman method: Time and cost effective tool for preparation of Cs<sub>2</sub>HfCl<sub>6</sub> single crystals

V. Vanecek<sup>a,b,\*</sup>, R. Kral<sup>a</sup>, J. Paterek<sup>a,b</sup>, V. Babin<sup>a</sup>, V. Jary<sup>a</sup>, J. Hybler<sup>a</sup>, S. Kodama<sup>c</sup>, S. Kurosawa<sup>d,e</sup>, Y. Yokota<sup>d</sup>, A. Yoshikawa<sup>c,d,f</sup>, M. Nikl<sup>a</sup>

<sup>a</sup> Institute of Physics of the Czech Academy of Science, Cukrovarnická 10/112, 162 00 Prague, Czech Republic

<sup>b</sup> Czech Technical University in Prague, Faculty of Nuclear Sciences and Physical Engineering, Břehová 7, Prague 1, Czech Republic

<sup>c</sup> Institute for Materials Research, Tohoku University, Sendai, Miyagi, Japan

<sup>d</sup> New Industry Creation Hatchery Center, Tohoku University, Sendai, Miyagi, Japan

<sup>e</sup> Faculty of Science, Yamagata University, Yamagata, Japan

<sup>f</sup> C&A Corporation, Sendai, Miyagi, Japan

### ARTICLE INFO

Communicated by R.S. Feigelson

#### Keywords:

A1. Characterization  
A1. Crystal structure  
A2. Bridgman technique  
B1. Halides  
B2. Scintillator materials

### ABSTRACT

Time and cost effective methods are highly desirable in research and development of new scintillators. Modern techniques like micro-pulling down ( $\mu$ -PD) are suitable for material screening but are unfit for the growth of some crystals. These crystals must be grown by different methods that are usually very time demanding. Modification of halide  $\mu$ -PD apparatus by custom made elements allowed us to grow cesium hafnium chloride (Cs<sub>2</sub>HfCl<sub>6</sub>) by vertical Bridgman method (VB) with significantly reduced growth time. Structural and optical properties of samples prepared from as-grown crystals were studied and compared to crystals grown by standard VB method. The X-ray diffraction confirmed the formation of cesium hafnium chloride single-phase and natural cleavage of the crystals along the (1 1 1) crystallographic plane. Photoluminescence emission, excitation, absorption, and radioluminescence spectroscopy revealed that the optical quality of the crystals grown by modified VB method was comparable to the quality of the crystals grown by standard VB method. Therefore we can use samples prepared by modified VB to estimate and optimize the performance of Cs<sub>2</sub>HfCl<sub>6</sub> based crystals in scintillation detectors. This setup allows the time and cost-effective material screening and it is a powerful tool for the development of new halide based single crystal scintillators.

### 1. Introduction

Since its discovery in 1948 the sodium iodide doped with thallium (NaI:Tl) [1] plays a crucial role in the field of detectors of ionizing radiation. Due to a low production cost of large volume single crystals, the moderate density of 3.67 g/cm<sup>3</sup> [2], high  $Z_{eff} = 51$ , high light yield of 45,000 ph/MeV [2], and moderate energy resolution of  $\sim 7\%$  [2] it is still the most widespread scintillator.

In many fields including nuclear medicine, geology, military, and environmental protection there is a need for a scintillator(s) with better properties than those of NaI:Tl. Most importantly the energy resolution that would allow better identification of radionuclides, while keeping the low price. Novel halide scintillators such as SrI<sub>2</sub>:Eu [3], LaBr<sub>3</sub>:Ce [4,5], LuI<sub>3</sub>:Ce have superior scintillation properties compared to those of NaI:Tl, but their price is much higher. Moreover, LaBr<sub>3</sub> and LuI<sub>3</sub> suffer from internal contamination by <sup>138</sup>La and <sup>176</sup>Lu, respectively,

which hinders their performance in low count applications and decreases their energy resolution at low energies [6].

Recently, cesium hafnium chloride of a formula Cs<sub>2</sub>HfCl<sub>6</sub> (CHC) was rediscovered [7] as a promising scintillator for cost-effective gamma spectrometers due to its high  $Z_{eff} = 58$  [7], moderate density of  $\rho = 3.8$  g/cm<sup>3</sup> [7], high light yield up to 54,000 ph/MeV [7], and high energy resolution of 3.3% at 662 keV [7] in undoped crystals. Its low hygroscopicity [8] and scintillation properties make it a prospective candidate for replacement of NaI:Tl in cost-effective gamma spectrometers. The CHC crystallizes in a cubic crystallographic structure (space group  $Fm\bar{3}m$ ) with a lattice parameter  $a = 10.42$  Å [9] and melts congruently at 826 °C [10].

The CHC belongs into a group of compounds with a general formula of A<sub>2</sub>MX<sub>6</sub> (K<sub>2</sub>PtCl<sub>6</sub> structural type), where A = Li, Na, K, Rb, and Cs; M = Hf, Zr, Ti, Pt, Sn and Te, X = Cl, Br, and I. Each element in the CHC structure can be substituted for an alternative element with equal

\* Corresponding author at: Institute of Physics of the Czech Academy of Science, Na Slovance 1999/2, 182 21 Prague 8, Czech Republic.  
E-mail address: [vanecekv@fzu.cz](mailto:vanecekv@fzu.cz) (V. Vanecek).

<https://doi.org/10.1016/j.jcrysgro.2020.125479>

Received 4 September 2019; Received in revised form 18 November 2019; Accepted 3 January 2020

Available online 03 January 2020

0022-0248/ © 2020 Elsevier B.V. All rights reserved.

ionic charge keeping the  $K_2PtCl_6$  structural type unchanged, which makes the  $A_2MX_6$  matrix very flexible. Controlled substitution allows to improve the light yield, energy resolution and fine-tuning of the radioluminescence (RL) emission maxima to match the sensitive region of the detector.

In this paper, we report on the growth of CHC crystals by vertical Bridgman (VB) method using the micro-pulling-down apparatus, so-called “miniaturized-vertical-Bridgman” (mVB). The structural and optical quality of the grown crystal is evaluated and compared to the quality of CHC crystals grown by the standard VB method. The goal of this work is to introduce the time and cost effective method of the single crystal growth that is suitable for screening of  $A_2MX_6$  compounds. We continue in the previous study of the CHC single crystals and characterization of their luminescence properties and charge trapping centers using the electron paramagnetic resonance and thermally stimulated luminescence [11,12].

## 2. Experimental

The CHC crystals were prepared from starting materials of commercially available cesium chloride (CsCl, 99.9%, Alfa Aesar) and hafnium chloride ( $HfCl_4$ , 99.9%, with the content of Zr below 0.5 mol %, Alfa Aesar). The CsCl was purified by a combination of zone melting and the introduction of gaseous halogenating agents into its melt according to [13,14].  $HfCl_4$  was purified by a repeated resublimation under the continuous flow of halogenating agents. Synthesis of CHC was performed by direct reaction of purified CsCl and  $HfCl_4$  mixed in a stoichiometric ratio (2:1) sealed into a quartz ampoule under vacuum and heated above its melting point.

In the case of the standard VB growth of CHC, a two-section furnace with resistive heating was used [13] with the upper and lower furnace sections heated above and below the CHC melting point, respectively, forming a temperature gradient between these sections. The growth itself was performed by lowering the ampoule with molten CHC from the upper section through the temperature gradient (up to 40 K/cm) in the mid-section into the colder lower section with a pulling rate of 0.3–0.7 mm/h. Samples made from crystals prepared by this method will be further on labeled as “CHC-VB”.

The crystal growth in the micro-pulling-down ( $\mu$ -PD) apparatus was achieved using only one inductively heated hot zone containing one graphite tube as a heating element and one surrounding alumina shielding of the same length. The schematic of the apparatus is depicted in Fig. 1. The hot zone design was based on our previous study of  $Cs_2HfCl_6$  single crystals prepared by similar approach, for details see [15,16,17]. The temperature gradient was defined by the position of the induction coil relative to the hot zone and by the length of the heating graphite tube. Its precise value in the mVB setup was not

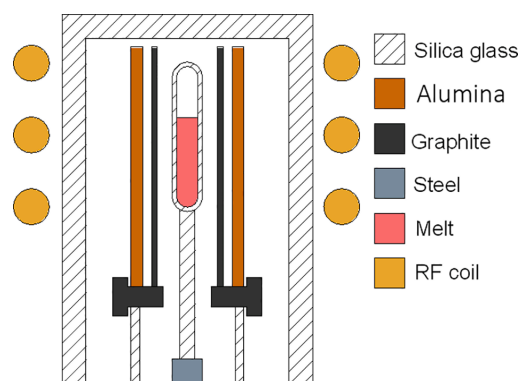


Fig. 1. Schematic of the mVB apparatus.

determined, however, we estimate that it is similar to that of the standard  $\mu$ -PD setup around or below 50 K/mm. The hot zone was placed in the removable chamber, which was connected to a vacuum source and evacuated with a rotary pump to ca. 0.5 Pa. The growth chamber was continuously evacuated during the entire growth. Influence of vibrations on the crystallization front and final crystal quality was not observed. The crystal growth of CHC was performed similarly to the standard VB. CHC was placed and sealed in the quartz ampoule and pulled down into cooler part of the chamber below the hot zone with a rate of 0.6–1.2 mm/h. Samples made from crystals prepared by this method will be further on labeled as “CHC-mVB”.

The X-ray diffraction (XRD) was performed using RigakuMiniFlex 600 (Ni-filtered Cu-K $\alpha$ 1,2 radiation) equipped with the NaI:Tl scintillation detector and XRD patterns were compared to the relevant records in the ICDD PDF-2 database (version 2013). The angular range was 10°–80°, with a step of 0.02° and a scanning speed of 2°/min. The XRD was applied to both cleaved (polished) and powder samples to determine the grain orientation and the phase purity of the grown crystals, respectively.

Photoluminescence emission (PL), photoluminescence excitation (PLE), and radioluminescence (RL) spectra were measured in the spectral range of 190–800 nm at room temperature (RT) using custom-made spectrofluorometer 5000 M, Horiba JobinYvon. The X-ray tube (RL spectra) and deuterium lamp (PL and PLE spectra) were used as the excitation sources, respectively. Detection part of the setup consisted of a single grating monochromator and photon-counting detector TBX-04. Measured spectra were corrected for the spectral dependence of excitation energy (PLE) and spectral dependence of detection sensitivity (PL). Absorption spectra were measured with a Shimadzu 3101 PC spectrometer in the spectral range of 190–800 nm. The scintillation decay curves were obtained with the use of  $^{137}Cs$   $\gamma$ -ray excitation, a Tektronix TDS3052C digital phosphor oscilloscope, and a fast photomultiplier 85 (R7207-01 KA0310, Hamamatsu) working in the current regime. All procedures consisting of quartz ampoules feeding and closure, handling and weighing of all chemicals, and manufacturing of grown crystals were performed in the atmosphere-controlled glovebox (MBraun) with the content of  $O_2$  and  $H_2O$  below 1 ppm.

## 3. Results and discussion

### 3.1. As-grown crystals and structural characteristics

The CHC-VB crystal was easily separated from the ampoule as a single object (see Fig. 2a) not sticking to its surface. The dimensions of the CHC-VB crystals were 12 mm in diameter and 50 mm in length. The as-grown crystal was nontransparent due to the low quality of the surface and surface deposition of  $HfCl_4$  during cooling. The volume of the crystal was transparent without formation of the core. The tail of the crystal was hazy and nontransparent most probably due to non-stoichiometry caused by evaporation of  $HfCl_4$ . Transparent polished plates 1 mm thick were prepared for subsequent optical measurements (see Fig. 2b). The crystal CHC-mVB was removed from the ampoule in three pieces (see Fig. 2c). Its dimensions were 7 mm in diameter and ca. 30 mm in length. The crystal was translucent with visible black impurities on the surface. XRD measurements suggest that the black particles were composed of  $HfO_2$  which most probably originates from thermal decomposition of hydrates and oxychlorides that can be formed during the technological process due to extremely high hygroscopicity of  $HfCl_4$ . The occurrence of black particles on the surfaces of mVB grown crystal is most probably due to difference in used  $HfCl_4$ . In the case of mVB crystal a batch of  $HfCl_4$  of a lower purity was used. Samples for the optical measurements were selected from the middle section of the crystal and 1 mm thick transparent polished plates were prepared (see Fig. 2d).

The XRD measurement was performed on the powder CHC samples (selected from the start of the as-grown crystal) confirming the presence

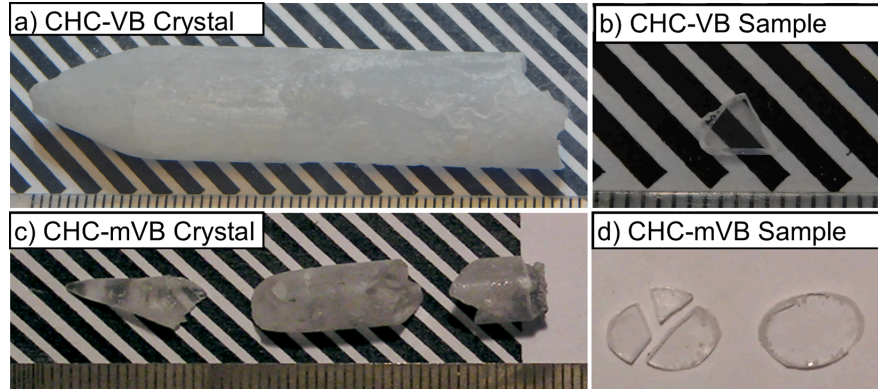


Fig. 2. The as-grown crystals (a and c) and cut and polished specimens (b and d) of the undoped  $\text{Cs}_2\text{HfCl}_6$  crystal prepared by the standard VB and mVB methods, respectively.

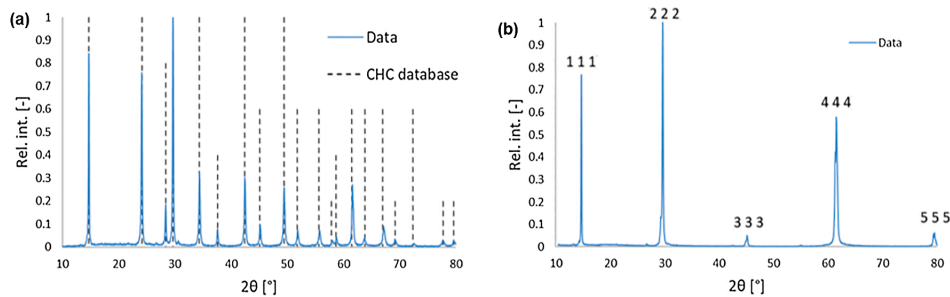


Fig. 3. The XRD pattern of the powder (a) and cut and polished plate (b) samples of the undoped CHC-mVB crystal. A relevant database record is shown in the dashed line.

of a single  $\text{Cs}_2\text{HfCl}_6$  phase (see Fig. 3a). No additional reflections related to different phases were observed. The lattice parameter of  $a = 10.424 \pm 0.003 \text{ \AA}$  (95% confidence interval) is in agreement with [9]. The XRD measured on the 1 mm thick cleaved and polished CHC plate showed only reflections from the (1 1 1) plane and its multiples, see Fig. 3b. Cleavage of the CHC crystal along the (1 1 1) plane is in agreement with results reported in [11].

### 3.2. Optical and luminescence characteristics

The RT absorption spectra of both VB and mVB CHC samples are depicted in Fig. 4. The spectra showed no features in the region of 350–800 nm and therefore this region was omitted from the figure. Both samples showed a similar position of absorption edge at around 250 nm which is due to the onset of excitonic absorption. The course of absorbance is similar as in the case of  $\text{Cs}_2\text{HfCl}_4\text{Br}_2$  (CHCB) [18] and  $\text{Cs}_2\text{HfBr}_6$  (CHB) [19]. For CHCB and CHB, the onset of absorption edge is situated at a longer wavelength (lower energies) due to the upward shift of the valence band edge given by the participation of  $\text{Br}^-$  energy levels.

The RT RL spectra of both the CHC-VB and CHC-mVB crystals are shown in Fig. 5. Their shape was identical for both samples and showed a broad band emission peaking at ca. 375 nm typical for CHC [7,20]. The origin of the emission was attributed to the self-trapping of charge carriers and creation of the  $V_k$  centers in the  $\text{HfCl}_6^{2-}$  octahedra [11,12,21]. Integrals of the RL spectra (scintillation efficiencies) of both samples are comparable and even slightly higher for the CHC-mVB sample. Both integrals were also compared to scintillation efficiency of the  $\text{Bi}_4\text{Ge}_3\text{O}_{12}$  (BGO) standard.

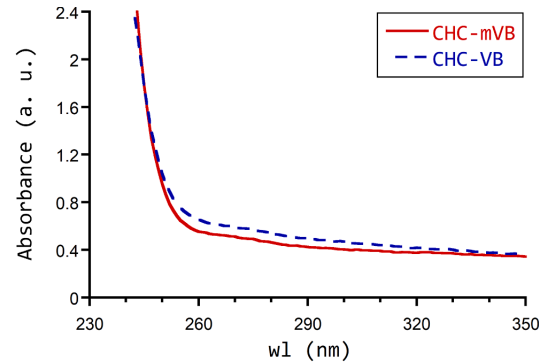


Fig. 4. The RT absorption spectra of the undoped CHC sample grown by mVB (red solid line) and VB (blue dashed line) methods. (For interpretation of the references to colour in this figure legend, the reader is referred to the web version of this article.)

The RT PLE spectra of the undoped CHC-VB and CHC-mVB samples are displayed in Fig. 6. The spectra were recorded at the emission wavelengths corresponding to the high energy part of the RL spectrum (em. 330 nm), its emission maxima (em. 385 nm), and its low energy part (em. 440 nm) showing three excitation bands peaking at 225, 240, and 265 nm. The PLE spectra of both the CHC-VB and CHC-mVB crystals were almost identical. At the high energy of the emission, only one excitation band peaking at 225 nm was clearly observed. At the

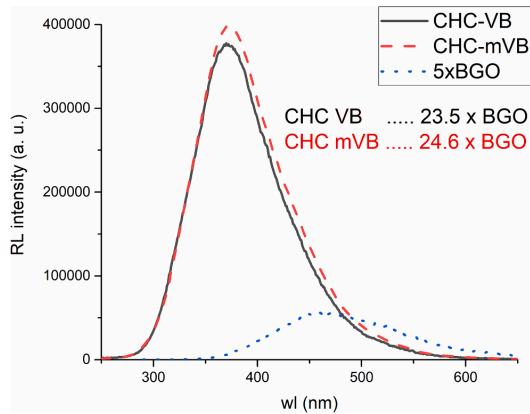


Fig. 5. The RT RL spectra of the undoped CHC-VB (black solid line) and CHC-mVB (red dashed line) samples. The BGO (blue dotted line) was used for comparison as a standard. (For interpretation of the references to colour in this figure legend, the reader is referred to the web version of this article.)

emission of 385 nm the excitation peak at 225 nm was still dominant, but another excitation peak at ca. 265 nm emerged. On the contrary, at the low energy part of the RL spectrum (em. 440 nm) the dominant peak at 240 nm together with a less intense peak at ca. 265 nm was present. The excitation peak at 225 nm was not clearly distinguished from the 240 nm peak, but the slope change in the area is clearly visible. The excitation peaks at 229 and 245 nm in CHC were also observed by Sakei et al. [20].

The photoluminescence emission spectra of the undoped CHC-VB and CHC-mVB samples were measured at excitation wavelengths of 215, 240, and 265 nm (see Fig. 7). The excitation wavelengths were selected based on results of PLE spectra, however, with slight deviations from the PLE maxima in order to better separate the excitation regions. Spectrum excited at 215 nm showed emission from 275 to 500 nm with a maximum at 375 nm (see Fig. 7a). The shape of the spectra was

practically identical for both samples as well as equal to the RL spectrum (see Fig. 5). The spectra of both samples excited at 240 nm (see Fig. 7b) showed a very broad emission from 275 to 650 nm peaking at 420 nm with almost equal shape, slightly different at shorter wavelengths. Interestingly, the excitation at 265 nm (see Fig. 7c) gave a sharper emission at higher energies (maximum at ca. 380 nm), when compared to excitation at 240 nm. The decrease in the line width is expected with a lower Stokes shift (approx. 2.2 eV for 240 nm excitation and 1.4 eV for 265 nm excitation). The shift of the emission peak towards higher energy with longer excitation wavelength is probably caused by the different nature of the involved luminescence center.

The PL decay curves of the undoped CHC (VB and mVB) are shown in Fig. 8. The PL decays were fitted by the convolution of instrumental response and the sum of exponential functions. The PL decay measurement with excitation at 215 nm and emission at 330 nm was selected at lower wavelengths with respect to the corresponding maxima in order to reduce the contribution from other luminescence centers. The curves of both samples (see Fig. 8a) were fitted by single exponentials with decay times of 5.2 and 4.4  $\mu$ s for CHC-VB and CHC-mVB, respectively. In the case of the second PL emission (see Fig. 8b) peak the excitation wavelength was selected at its maximum (240 nm) and the emission at the low energy end (500 nm) to reduce the mentioned contribution. The PL decay curves of both samples CHC-VB and CHC-mVB were fitted by single exponentials with decay times of 12.6 and 13.0  $\mu$ s, respectively. The PL decay of the third emission (see Fig. 8c) center was measured with excitation and emission wavelengths of 265 and 385 nm, respectively. The PL decay of the CHC-VB sample was fitted by two exponential functions due to contribution of the high energy component. The obtained decay times of the fast component were 1.2  $\mu$ s for both samples.

Scintillation decay curves measured in both CHC samples (VB and mVB) under  $^{137}\text{Cs}$  irradiation are depicted in Fig. 9. Both curves were fitted by the convolution of three exponential functions and the instrumental response. The samples showed decay curves with a similar quantity of components with decay times around 1, 5, and 12  $\mu$ s. In the case of the CHC-VB sample (see Fig. 8a), the components accounted for 22% (1.1  $\mu$ s), 62% (5.1  $\mu$ s), and 16% (12.1  $\mu$ s). Similarly, for the CHC-mVB sample (see Fig. 8b) the components of the decay curve were 24%

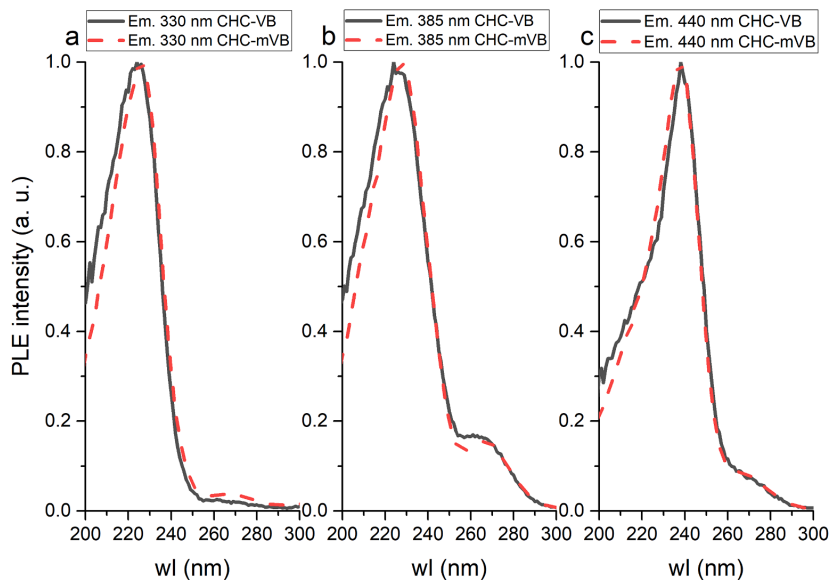


Fig. 6. The RT PLE spectra of the undoped samples CHC-VB and CHC-mVB recorded at ca 330 (a), 385 (b), and 440 nm (c).



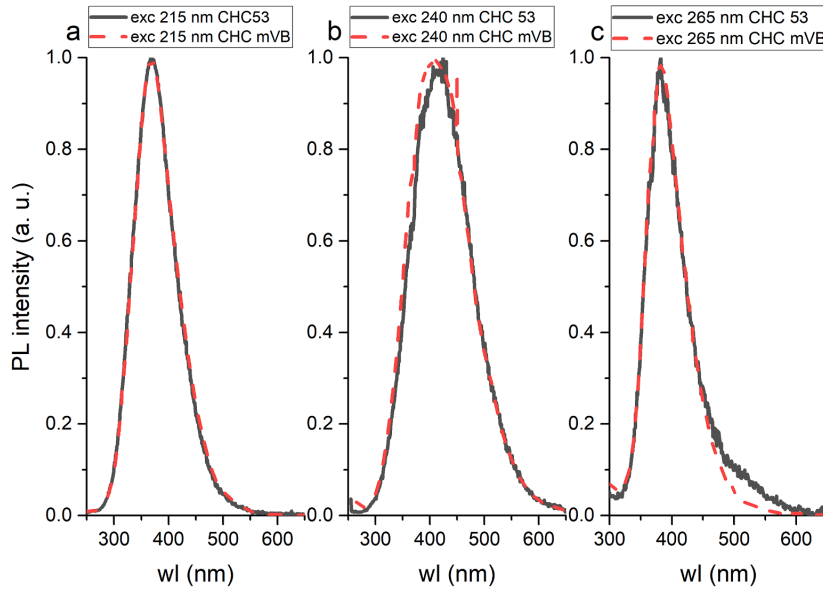


Fig. 7. The RT PL spectra of the CHC-VB and CHC-mVB samples excited at ca 215 (a), 240 (b), and 265 nm (c).

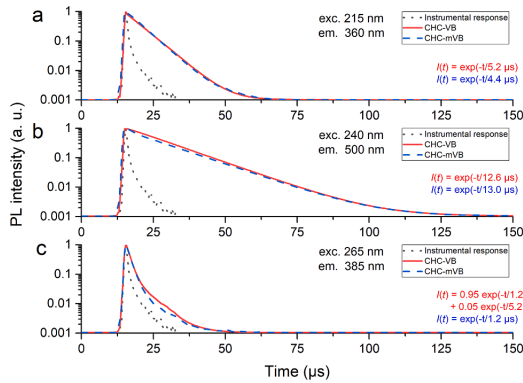


Fig. 8. The RT PL decay curves of the undoped CHC-VB and CHC-mVB samples measured at ex. 215 nm, em. 360 nm (a), ex. 240 nm, em. 500 nm (b); and ex. 265 nm, em. 385 nm (c). For figure clarity, the convolution curves were omitted.

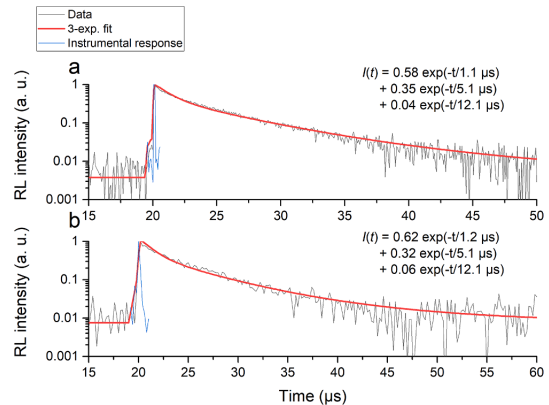


Fig. 9. The RT scintillation decay curves of the undoped CHC-VB (a) and CHC-mVB (b) samples.

(1.2 μs), 53% (5.1 μs) and 23% (12.1 μs). The value of the scintillation decay time of fast component is in a good agreement with PL decay measurements (1.1 μs for CHC-VB and 1.2 μs for CHC-mVB). The middle component shows a scintillation decay time within reasonable departure from the PL decay times (5.1 μs for CHC-VB and 4.4 μs for CHC-mVB). The decay time of the slowest component is somewhat longer compared to PL decay times (12.6 μs for CHC-VB and 13.0 for CHC-mVB), but still within reasonable limits. The presence of three components in decay curves is in agreement with the existence of three excitation-emission centers identified in the PLE and PL spectra. It is supported further by the measurements of the PL kinetics which indicated that emissions with the decay time approx. 1, 5, and 12 μs could be well selectively excited under the 265, 225, and 240 nm excitation wavelengths, respectively.

#### 4. Conclusion

The micro-pulling-down apparatus was successfully modified into the arrangement of the vertical Bridgman method allowing the growth of the CHC crystal. This technique, so-called “miniaturized-vertical-Bridgman” method, enabled the preparation of CHC crystal and polished transparent samples of comparable quality as those prepared by traditional vertical Bridgman method. XRD of grown CHC confirmed the cubic  $K_2PtCl_6$  crystal structure type and showed that natural cleavage plane of the prepared crystal was along (1 1 1). The optical measurements confirmed that the quality of the prepared crystal is comparable to that of crystals grown by the standard vertical Bridgman method and therefore sufficient to estimate its scintillation performance. PL decay time measurements showed that three excitation pathways revealed in the PLE spectra could be assigned to three components of the scintillation decay time. We presented the time and cost effective method to grow single crystals suitable for composition

screening of the  $A_2MX_6$  class of halide scintillators.

#### CRedit authorship contribution statement

**V. Vanecek:** Conceptualization, Methodology, Writing - original draft, Investigation, Formal analysis, Visualization. **R. Kral:** Conceptualization, Methodology, Investigation, Formal analysis, Writing - review & editing, Supervision, Project administration, Funding acquisition. **J. Paterek:** Investigation, Formal analysis, Visualization, Writing - review & editing. **V. Babin:** Investigation, Formal analysis. **V. Jary:** Investigation, Formal analysis, Writing - review & editing. **J. Hybler:** Investigation, Formal analysis. **S. Kodama:** Conceptualization, Methodology, Writing - review & editing. **S. Kurosawa:** Conceptualization, Methodology. **Y. Yokota:** Conceptualization, Methodology, Supervision. **A. Yoshikawa:** Conceptualization, Methodology, Writing - review & editing, Supervision. **M. Nikl:** Conceptualization, Writing - review & editing, Supervision, Project administration, Funding acquisition.

#### Declaration of Competing Interest

The authors declare that they have no known competing financial interests or personal relationships that could have appeared to influence the work reported in this paper.

#### Acknowledgement

Support of the Czech Science Foundation project no. 18-17555Y is gratefully acknowledged. Partial support of the projects from the Ministry of Education, Youth and Sports of the Czech Republic no. LO1409, LM2015088 and CZ.02.1.01/0.0/0.0/16 013/0001406 are also gratefully acknowledged. The authors thank A. Beitlerova and R. Kucerkova, for absorption and radioluminescence measurements, to A. Bystricky and A. Cihlar for starting materials purification and preparation of growth ampoules, and M. Kittler for grinding and polishing of samples for optical measurements.

#### References

- [1] R. Hofstadter, Alkali halide scintillation counters, *Phys. Rev.* 74 (1948) 100–101, <https://doi.org/10.1103/PhysRev.74.100>.
- [2] E. Sakai, Recent measurements on scintillator-photodetector systems, *IEEE Trans. Nucl. Sci.* 34 (1987) 418–422, <https://doi.org/10.1109/TNS.1987.4337375>.
- [3] N.J. Cherepy, G. Hull, A.D. Drobshoff, S.A. Payne, E. van Loef, C.M. Wilson, K.S. Shah, U.N. Roy, A. Burger, L.A. Boatner, W.-S. Choong, W.W. Moses, Strontium and barium iodide high light yield scintillators, *Appl. Phys. Lett.* 92 (2008) 083508, <https://doi.org/10.1063/1.2885728>.
- [4] E.V.D. van Loef, P. Dorenbos, C.W.E. van Eijk, K. Krämer, H.U. Güdel, High-energy-resolution scintillator: Ce<sup>3+</sup> activated LaBr<sub>3</sub>, *Appl. Phys. Lett.* 79 (2001) 1573–1575, <https://doi.org/10.1063/1.1385342>.
- [5] N.J. Cherepy, S.A. Payne, S.J. Asztalos, G. Hull, J.D. Kuntz, T. Niedermayr, S. Pimpulkar, J.J. Roberts, R.D. Sanner, T.M. Tillotson, E. van Loef, C.M. Wilson, K.S. Shah, U.N. Roy, R. Hawrami, A. Burger, L.A. Boatner, W. Choong, W.W. Moses, Scintillators with potential to supersede lanthanum bromide, *IEEE Trans. Nucl. Sci.* 56 (2009) 873–880, <https://doi.org/10.1109/TNS.2009.2020165>.
- [6] B.D. Milbrath, B.J. Choate, J.E. Fast, W.K. Hensley, R.T. Kouzes, J.E. Schweppe, Comparison of LaBr<sub>3</sub>:Ce and NaI(Tl) scintillators for radio-isotope identification devices, *Nucl. Instrum. Methods Phys. Res., Sect. A* 572 (2007) 774–784, <https://doi.org/10.1016/j.nima.2006.12.003>.
- [7] A. Burger, E. Rowe, M. Groza, K. Morales Figueroa, N.J. Cherepy, P.R. Beck, S. Hunter, S.A. Payne, Cesium hafnium chloride: A high light yield, non-hygroscopic cubic crystal scintillator for gamma spectroscopy, *Appl. Phys. Lett.* 107 (2015), <https://doi.org/10.1063/1.4932570>.
- [8] S. Lam, C. Gugushev, A. Burger, M. Hackett, S. Motakef, Crystal growth and scintillation performance of Cs<sub>2</sub>HfCl<sub>6</sub> and Cs<sub>2</sub>HfCl<sub>4</sub>Br<sub>2</sub>, *J. Cryst. Growth* 483 (2018) 121–124, <https://doi.org/10.1016/j.jcrysgro.2017.11.013>.
- [9] S. Maniv, W. Low, A. Gabay, EPR sites of molybdenum ions in single crystals of Cs<sub>2</sub>HfCl<sub>6</sub> and Cs<sub>2</sub>ZrCl<sub>6</sub>, *J. Phys. Chem. Solids* 35 (1974) 373–381, [https://doi.org/10.1016/S0022-3697\(74\)80030-2](https://doi.org/10.1016/S0022-3697(74)80030-2).
- [10] D.A. Asvestas, P. Pint, S.N. Flengas, Some thermodynamic properties of the solutions of ZrCl<sub>4</sub> and HfCl<sub>4</sub> in CsCl melts, *Can. J. Chem.* 55 (1977) 1154–1166, <https://doi.org/10.1139/v77-162>.
- [11] R. Král, V. Babin, E. Mihóková, M. Buryi, V.V. Laguta, K. Nitsch, M. Nikl, Luminescence and charge trapping in Cs<sub>2</sub>HfCl<sub>6</sub> single crystals: optical and magnetic resonance spectroscopy study, *J. Phys. Chem. C* 121 (2017) 12375–12382, <https://doi.org/10.1021/acs.jpcc.7b02327>.
- [12] M. Buryi, R. Král, V. Babin, J. Paterek, V. Vaněček, P. Veverka, M. Kohoutková, V. Laguta, M. Fasoli, I. Villa, F. Cova, A. Vedda, M. Nikl, Trapping and re-combination centers in cesium hafnium chloride single crystals: EPR and TSL study, *acs.jpcc.9b05760*, *J. Phys. Chem. C* (2019), <https://doi.org/10.1021/acs.jpcc.9b05760>.
- [13] K. Nitsch, A. Cihlár, Z. Málková, M. Rodová, M. Vaněček, The purification and preparation of high-purity PbCl<sub>2</sub> and ternary alkali lead chloride single crystals, *J. Cryst. Growth* 131 (1993) 612–615, [https://doi.org/10.1016/0022-0248\(93\)90214-H](https://doi.org/10.1016/0022-0248(93)90214-H).
- [14] K. Nitsch, M. Dušek, M. Nikl, K. Polák, M. Rodová, Ternary alkali lead chlorides: Crystal growth, crystal structure, absorption and emission properties, *Prog. Cryst. Growth Charact. Mater.* 30 (1995) 1–22, [https://doi.org/10.1016/0960-8974\(95\)00012-V](https://doi.org/10.1016/0960-8974(95)00012-V).
- [15] S. Kodama, S. Kurosawa, A. Yamaji, J. Pejchal, R. Král, Y. Ohashi, K. Kamada, Y. Yokota, M. Nikl, A. Yoshikawa, Growth and luminescent properties of Ce and Eu doped Cesium Hafnium Iodide single crystalline scintillators, *J. Cryst. Growth* 492 (2018) 1–5, <https://doi.org/10.1016/j.jcrysgro.2018.03.033>.
- [16] S. Kodama, S. Kurosawa, J. Pejchal, R. Kral, A. Yamaji, Y. Ohashi, Y. Yokota, K. Kamada, M. Nikl, A. Yoshikawa, Growth and luminescent properties of Cs<sub>2</sub>HfCl<sub>6</sub> scintillators doped with alkaline earth metals, *IEEE Trans. Nucl. Sci.* 65 (2018) 2169–2173, <https://doi.org/10.1109/TNS.2018.2848474>.
- [17] S. Kodama, S. Kurosawa, M. Ohno, A. Yamaji, M. Yoshino, J. Pejchal, R. Král, Y. Ohashi, K. Kamada, Y. Yokota, M. Nikl, A. Yoshikawa, Development of a novel red-emitting cesium hafnium iodide scintillator, *Radiat. Meas.* 124 (2019) 54–58, <https://doi.org/10.1016/j.radmeas.2019.03.005>.
- [18] E. Rowe, W.B. Goodwin, P. Bhattacharya, G. Cooper, N. Schley, M. Groza, N.J. Cherepy, S.A. Payne, A. Burger, Preparation, structure and scintillation of cesium hafnium chloride bromide crystals, *J. Cryst. Growth* 509 (2019) 124–128, <https://doi.org/10.1016/j.jcrysgro.2018.08.033>.
- [19] K. Saeki, Y. Fujimoto, M. Koshimizu, D. Nakauchi, H. Tanaka, T. Yanagida, K. Asai, Luminescence and scintillation properties of Cs<sub>2</sub>HfBr<sub>6</sub> and Cs<sub>2</sub>ZrBr<sub>6</sub> crystals, *Jpn. J. Appl. Phys.* 57 (2018) 030310, <https://doi.org/10.7567/JJAP.57.030310>.
- [20] K. Saeki, Y. Fujimoto, M. Koshimizu, T. Yanagida, K. Asai, Comparative study of scintillation properties of Cs<sub>2</sub>HfCl<sub>6</sub> and Cs<sub>2</sub>ZrCl<sub>6</sub>, *Appl. Phys. Express* 9 (2016) 042602, <https://doi.org/10.7567/APEX.9.042602>.
- [21] By. Kang, K. Biswas, Carrier self-trapping and luminescence in intrinsically activated scintillator: cesium hafnium chloride (Cs<sub>2</sub>HfCl<sub>6</sub>), *J. Phys. Chem. C* 120 (2016) 12187–12195, <https://doi.org/10.1021/acs.jpcc.6b02496>.



## Cs<sub>2</sub>HfCl<sub>6</sub> doped with Zr: Influence of tetravalent substitution on scintillation properties

V. Vaněček<sup>a,b,\*</sup>, J. Páterek<sup>a,b</sup>, R. Král<sup>a</sup>, M. Buryi<sup>a</sup>, V. Babin<sup>a</sup>, K. Zlouževá<sup>a,c</sup>, S. Kodama<sup>d</sup>, S. Kurosawa<sup>e,f</sup>, Y. Yokota<sup>e</sup>, A. Yoshikawa<sup>d,e,g</sup>, M. Nikl<sup>a</sup>

<sup>a</sup> FZU - Institute of Physics of the Czech Academy of Sciences, Cukrovarnická 10, Prague, Czech Republic

<sup>b</sup> FNSPE, Czech Technical University in Prague, Břehova 7, Prague, Czech Republic

<sup>c</sup> FCT, University of Chemistry and Technology Prague, Technická 5, Prague 166 28, Czech Republic

<sup>d</sup> IMR, Tohoku University, 2-1-1, Katahira, Aoba-ku, Sendai, Miyagi 980-8577, Japan

<sup>e</sup> NICHe, Tohoku University, 6-6-10 Aza-Aoba, Aoba-ku, Sendai, Miyagi 980-8579, Japan

<sup>f</sup> FS, Yamagata University, 1-4-12 Kojirakawa-machi, Yamagata 990-8560, Japan

<sup>g</sup> C&A Corporation, 6-6-40 Aza-Aoba, Aramaki, Aoba-ku, Sendai, Miyagi 980-8579, Japan

### ARTICLE INFO

Communicated by Gen Sazaki

#### Keywords:

- A1. Characterization
- A1. Crystal structure
- A2. Bridgman technique
- B1. Halides
- B2. Scintillator materials

### ABSTRACT

Homeland security is an emerging application field for inorganic scintillators. Detection and identification of radioactive materials in both individual and cargo transport requires scintillators with excellent energy resolution and high light output. On the other hand, the time characteristics of the scintillation are less crucial. Furthermore, price is a key parameter due to the large volume of the detectors. State-of-the-art halide scintillators e. g. SrI<sub>2</sub>:Eu or LaBr<sub>3</sub>:Ce can satisfy the requirements for light yield and energy resolution, but the production costs are very high due to complicated crystal growth and the high prices of rare earth metals. Cesium hafnium chloride (Cs<sub>2</sub>HfCl<sub>6</sub>) is a promising intrinsic scintillator with high light yield and excellent resolution. Moreover, its low hygroscopicity and cubic crystal structure could allow lower production costs compared to SrI<sub>2</sub> or LaBr<sub>3</sub>. Intrinsic luminescence of Cs<sub>2</sub>HfCl<sub>6</sub> is commonly attributed to self-trapped excitons. However, the luminescence of Cs<sub>2</sub>HfCl<sub>6</sub> shows complex structure and temperature dependence. This might be explained by the presence of zirconium which is a common impurity in hafnium compounds. We present a study of the influence of zirconium doping on the scintillation properties of Cs<sub>2</sub>HfCl<sub>6</sub>. Single crystals of Cs<sub>2</sub>HfCl<sub>6</sub> with zirconium doping from 0 to 1 mol% were grown by the vertical Bridgman method. Their phase purity, radioluminescence, scintillation decay, light yield, and afterglow were evaluated. Results show that zirconium doping can affect the scintillation properties of Cs<sub>2</sub>HfCl<sub>6</sub> even at concentrations comparable to impurity levels of zirconium in hafnium compounds.

### 1. Introduction

Nowadays, the ionizing radiation is used in many fields of human activity including geology, medical imaging, nuclear industry, environment protection, and homeland security [1,2]. The risk of terrorist attacks created an increasing demand for checking both individual and cargo transport. Passive radiation detectors can be used for the screening of cargo at borders or other security controls. These applications require large-scale detectors, therefore, a low price of the detector materials is required. Moreover, scintillators with high light yield, high stopping power, and very good energy resolution have to be used to enable fast readout, high detection efficiency, and radioisotope identification.

Newly developed cerium or europium doped halide scintillators e. g. SrI<sub>2</sub>:Eu [3], (Sr,Ba)(Br,I)<sub>2</sub>:Eu [3–5], CsBa<sub>2</sub>I<sub>5</sub>:Eu [5,6], LaBr<sub>3</sub>:Ce [7,8], LuI<sub>3</sub>:Ce [9] exhibit high light yields up to ~ 100,000 ph/MeV [10] and energy resolution down to 2.0 % [11] (at 662 keV of <sup>137</sup>Cs). However, the production costs of those materials are high due to high hygroscopicity, complicated crystal growth, and the high price of rare earth metals. Therefore, a search for new materials, that would satisfy light yield and energy resolution requirements while keeping low production costs is demanded.

Cesium hafnium chloride of a formula Cs<sub>2</sub>HfCl<sub>6</sub> (CHC) is a promising scintillator for homeland security applications due to its high stopping power ( $Z_{eff} = 58$  [12],  $\rho = 3.8$  g/cm<sup>3</sup> [12]), light yield up to 54 000 ph/

\* Corresponding author.

E-mail address: [vanecekv@fzu.cz](mailto:vanecekv@fzu.cz) (V. Vaněček).

<https://doi.org/10.1016/j.jcrysgr.2021.126307>

Received 24 March 2021; Received in revised form 18 August 2021; Accepted 19 August 2021

Available online 23 August 2021

0022-0248/© 2021 Elsevier B.V. All rights reserved.

MeV [12], and energy resolution down to 2.8% [13] (at 662 keV of  $^{137}\text{Cs}$ ) in undoped crystals. Moreover, its low hygroscopicity [14] and cubic crystal structure (space group  $Fm\bar{3}m$ ) could allow the reduction of crystal growth costs compared to  $\text{SrI}_2$  or  $\text{LaBr}_3$ .

The scintillation mechanism in CHC and other materials from the same  $\text{A}_2\text{MX}_6$  family (where A is an alkali metal cation, M is a tetravalent cation, e.g. Hf, Zr, Se, Te, Sn, etc., and X is a halogen anion) is mostly ascribed to self-trapped exciton (STE) formed by hole trapped at the  $\text{Cl}_2^-$  ( $V_k$  center) and electron at  $\text{Hf}^{3+}$  [15–17]. This is consistent with the observations that  $\text{Ti}^{3+}$  doping is ineffective in CHC at room temperature [18] and substitution on A site induces only a slight shift of radioluminescence (RL) spectra [19–23] which is probably caused by a change in the bandgap. Furthermore,  $\text{Te}^{4+}$  doping on the M site produces a much larger shift of the RL maxima [24] compared to A site substitution. Zirconium substitution on the M site results in a similar shift of the RL maxima in both  $\text{Cs}_2\text{MCl}_6$  [25,26] and  $\text{Cs}_2\text{MBr}_6$  [27] matrices.

The separation of Zr from Hf is difficult due to their similar chemical and physical properties [28]. Therefore, zirconium is a dominant impurity in Hf compounds with concentrations at levels of  $10^{-1}\%$  and vice versa. Such concentrations are comparable to the dopant levels in activator-based scintillators. Thus, the properties of the CHC crystals could be influenced by the Zr impurity level in the  $\text{HfCl}_4$  raw material given by technological processes used by the  $\text{HfCl}_4$  supplier. Zirconium center in CHC was suggested as a reason for the complex nature of CHC RL spectra [15,16]. In this paper, we report on an investigation of low concentration Zr doping (0 – 1 mol%) and its influence on the scintillation properties of CHC single crystals. The goal of the present work is to explain the role of Zr impurity on the scintillation properties of CHC and to get a better insight into the scintillation mechanism in CHC crystals.

## 2. Experimental

The CHC crystals were prepared from starting materials of commercially available cesium chloride ( $\text{CsCl}$ , 99.9 %, Alfa Aesar), hafnium chloride ( $\text{HfCl}_4$ , 99.9%, with the content of Zr below 0.5 %, Alfa Aesar), and zirconium chloride ( $\text{ZrCl}_4$ , 99.9%, Alfa Aesar). The  $\text{CsCl}$  was purified by a combination of zone melting and the introduction of gaseous chlorinating agents into its melt according to [29,30].  $\text{HfCl}_4$  was purified by a multiple-step resublimation under the continuous flow of chlorinating agents. The purification process is mainly focused on the removal of oxidic impurities by a chemical reaction (in  $\text{CsCl}$  melt and in gaseous  $\text{HfCl}_4$ ) or by separation (zone refining of  $\text{CsCl}$  and resublimation of  $\text{HfCl}_4$ ). However, the XRF measurements showed that minor (not significant) separation of  $\text{ZrCl}_4$  and  $\text{HfCl}_4$  was observed. This is in corroboration with results reported by Cardenas et al. [31]. Synthesis of  $\text{Cs}_2\text{Hf}_{1-x}\text{Zr}_x\text{Cl}_6$ , where  $x = 0; 0.001; 0.005; \text{ and } 0.01$ , was performed by direct reaction of purified  $\text{CsCl}$  and  $\text{HfCl}_4/\text{ZrCl}_4$  mixed in a stoichiometric ratio (2:1) and sealed into a quartz ampoule under vacuum and heated above its melting point.

The  $\text{Cs}_2\text{Hf}_{1-x}\text{Zr}_x\text{Cl}_6$  crystals were grown by a single-zone vertical Bridgman method using a micro-pulling-down apparatus [32,33]. The starting charge in the quartz ampoule, when melted, was pulled down with a rate of 0.6 mm/h in all performed crystal growths. For further details see Vaněček et al. [32].

For the X-ray powder diffraction (XRPD) analysis, the crystalline samples were powdered in alumina mortar and pestle. The XRPD was performed using RigakuMiniFlex 600 (Ni-filtered  $\text{Cu-K}\alpha 1,2$  radiation) equipped with the  $\text{NaI:Tl}$  scintillation detector and XRD patterns were compared to the relevant records in the ICDD PDF-2 database (version 2013). The angular range was  $10^\circ - 80^\circ$ , with a step of  $0.02^\circ$  and a scanning speed of  $2^\circ/\text{min}$ . The XRD was measured on powder samples to determine the phase purity of the grown crystals.

Radioluminescence (RL) spectra measured in the spectral range of 190–800 nm at room temperature and afterglow profiles were obtained

using custom-made spectrofluorometer 5000 M, Horiba Jobin Yvon. The afterglow profiles were measured within 5000 ms time window after X-ray excitation cut-off. Tungsten-cathode X-ray tube Seifert was used as the excitation source (at 40 kV, 15 mA). The detection part of the set-up consisted of a single grating monochromator and photon-counting detector TBX-04, Horiba. Measured spectra were corrected for the spectral distortions. The setup for time-resolved spectroscopy of scintillation pulses consisted of fast photomultiplier R375, Hamamatsu working in the current regime and Keysight InfiniiVision DSOX6002A digital oscilloscope. The setup for amplitude spectroscopy consisted of hybrid photomultiplier DEP PPO 475B, spectroscopy amplifier ORTEC 672 (shaping time set to 10  $\mu\text{s}$ ) and multichannel analyzer ORTEC 927TM. The light yield of the examined materials was determined according to Mares et al. [34]. Scintillation pulses were excited by  $^{137}\text{Cs}$   $\gamma$ -rays (662 keV) for both the time-resolved spectroscopy and amplitude spectroscopy of scintillation pulses. The crystals were covered with a thin film of UV/VIS-transparent Fluka immersion oil during all of the conducted measurements to prevent the degradation of the surface due to contact with atmospheric oxygen and moisture.

All procedures consisting of quartz ampoules feeding and valve closure, handling and weighing of all chemicals, and manufacturing of grown crystals was performed in the atmosphere-controlled glovebox (MBraun Labstar) with the content of  $\text{O}_2$  and  $\text{H}_2\text{O}$  below 1 ppm.

## 3. Results and discussion

### 3.1. Sample preparation

In total, four CHC crystals with nominal Zr concentrations of 0, 0.1, 0.5, and 1 mol% were investigated. Throughout this text, the samples from the respective crystal will be denoted as CHC-X%, where X is the nominal Zr concentration. The as-grown crystals were 7 mm in diameter and ca. 30 mm in length. All the crystals were easily separated from the ampoule as a single ingot (see Fig. 1). The surface of the samples was opaque, but the bulk of the crystals was clear and transparent. Black impurities on the surfaces of the crystal are  $\text{ZrO}_2$  or  $\text{HfO}_2$  as reported in [32]. The increasing amount of black impurities with increasing Zr content is most probably due to the higher concentration of the oxidic impurities in as-bought  $\text{ZrCl}_4$  compared to in-house purified  $\text{HfCl}_4$ . Samples for optical measurements were prepared in the form of 1.5 mm thick polished plates as shown in Fig. 2.

### 3.2. Structural analysis

The XRPD analysis was performed on powder samples prepared from the start (first-to-freeze) of the as-grown crystals. The analysis revealed that all prepared crystals were single  $\text{Cs}_2\text{HfCl}_6$  phase ( $\text{K}_2\text{PtCl}_6$  type). No

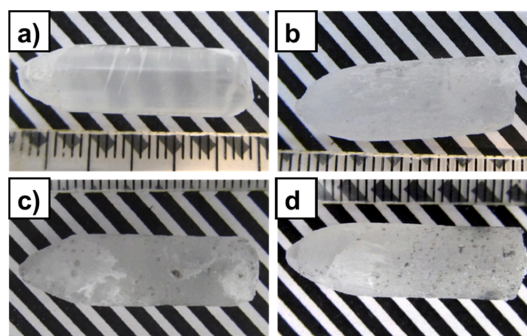


Fig. 1. As-grown crystals a) CHC-0%, b) CHC-0.1%, c) CHC-0.5% and d) CHC-1%.



Fig. 2. Prepared samples for optical measurements in order from left to right: CHC-0%, CHC-0.1%, CHC-0.5%, CHC-1%.

additional reflections related to a different phase were observed (see Fig. 3). Interestingly, we observed an increase in relative intensity of reflections from the (111) crystallographic plane (and its multiples) with increasing Zr content. This can be well observed on the relative intensity of both (111) reflection (at  $14.74^\circ$ ) and (222) reflection (at  $29.70^\circ$ ). The increase of relative intensity of (111) reflection is higher for low Zr concentration and is reaching saturation at the highest concentration. The dependence of relative intensity on Zr concentration follows the same trend for both reflections (Fig. 4). This cannot be explained by the formation of the  $\text{Cs}_2\text{ZrCl}_6$  (CZC) phase since the Zr concentration is too low to create such an effect. Further investigation is necessary to fully explain this phenomenon.

### 3.3. Optical characterization

#### 3.3.1. Radioluminescence

RL spectra of the examined crystals were measured and are shown in Fig. 5 in normalized form. The RL spectra of the undoped CHC-0% as well as other CHC:Zr samples consisted of a broad emission peak with maxima at ca. 380 nm, which is a typical RL spectrum of CHC [25]. However, in the case of Zr-doped CHC-0.5% and CHC-1%, an increased RL signal was observed in the range from 380 to 650 nm. The previously published data state that the trapped exciton (TE) emission of ternary halides with Zr on the site of the tetravalent ion is shifted to lower energies when compared to that with Hf on this position [25,27]. In line with these findings, we ascribe the increased emission of the examined Zr-doped CHC crystals in the range 380–650 nm to additional TE around Zr cation. The effect was not observed in CHC-0.1% suggesting that the actual Zr concentration was too low to support Zr emission or the concentration of Zr impurity in the undoped CHC-0% reaches levels comparable to the concentration of Zr dopant in CHC-0.1%. Therefore, the emission of these crystals observed in the range 380–650 nm is at least partly due to TE around Zr cation. The distortion in the RL spectra at 370 nm was caused by an experimental artifact.

#### 3.3.2. Amplitude spectroscopy of scintillation pulses

Pulse height spectra of the examined materials were measured and the acquired spectra are displayed in Fig. 6. A peak of total absorption as

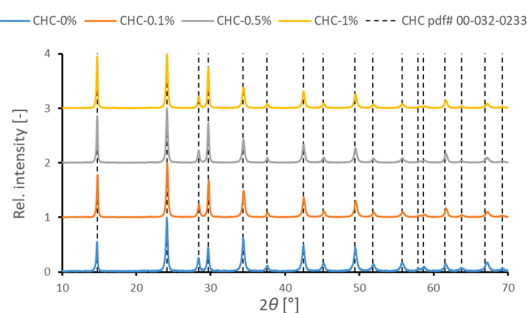


Fig. 3. Powder diffractograms of all prepared CHC:Zr crystals. A relevant database record is shown in the dashed line.

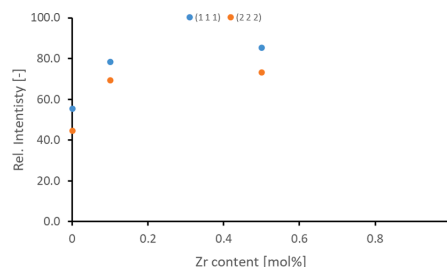


Fig. 4. Dependence of relative intensity of (111) and (222) reflections in CHC:Zr crystals on Zr concentration.

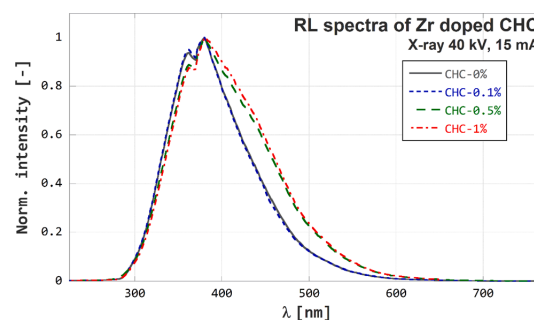


Fig. 5. Normalized RL spectra of CHC:Zr crystals.

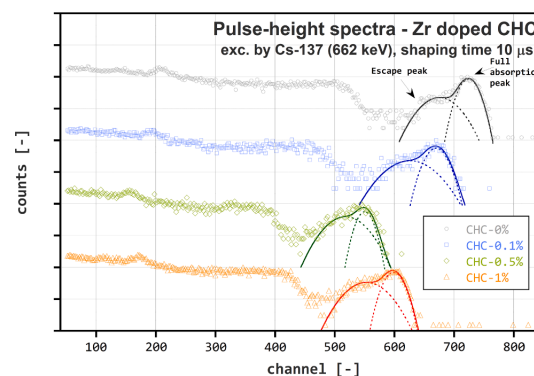


Fig. 6. Pulse height spectra of scintillation pulses of CHC:Zr crystals with the Gaussian fits of the total absorption and the escape peak structures (dashed lines) and their summation (solid lines).

well as escape peak can be observed in the examined materials due to small volume of the samples. The structures composed of these two peaks were approximated with a pair of Gaussian functions and the results of the fit corresponding to the total absorption peak were used to

Table 1  
Light yield, and energy resolution of CHC:Zr crystals.

Label	LY [photos/MeV]	En. resolution [%]
CHC-0%	26,800	4.3
CHC-0.1%	24,700	5.3
CHC-0.5%	20,900	5.0
CHC-1%	22,900	5.4

determine the light yield and the energy resolution. The calculated light yield and energy resolution are listed in Table 1. One can see that both characteristics were slightly impaired for the Zr doped crystals. The light yield of CHC:Zr dropped by 8 to 22 % with respect to the undoped one and their energy resolution ranged between 5.0 and 5.4 %, while that of undoped CHC-0% reaches a superior value of 4.3 %. No dependence of light yield and energy resolution on the dopant concentration was observed.

### 3.3.3. Time-resolved spectroscopy of scintillation pulses

Scintillation decays were measured and the acquired decay curves were fitted with a 3-exponential function. A fine match of the fit function with the data was obtained for decay time values of 1, 5, and 12  $\mu$ s that were previously observed in photoluminescence decays of CHC crystals [32]. Such values are in good agreement with values reported by Buryi et al. [26]. Based on luminescence and EPR measurements [15,16] we assume that the 1 and 5  $\mu$ s components relate to the STEs with hole trapped in two different  $V_k$  centers. The decay curves of the CHC-0% and CHC-0.5% together with the corresponding fit functions are shown in Fig. 7. The parameters of the fit were used to calculate the areas below the decay curve for each of the decay components. The results are listed in Table 2. The scintillation decays of all of the examined samples were dominated by 5 and 12  $\mu$ s components, the contribution of 1  $\mu$ s component was below 10%. An increased contribution of the 12  $\mu$ s component can be observed in all the Zr-doped crystals. The effect is even more pronounced in crystals CHC-0.5% and CHC-1% with a higher Zr content. This suggests that the 12  $\mu$ s component corresponds to TE emission related to the Zr cation. However, further study, engaging materials with higher Zr content and examination of photoluminescence decays, must be conducted to support this statement.

### 3.3.4. Afterglow

Afterglow profiles were measured to study the contribution of very slow components of scintillation pulses in the CHC:Zr crystals. The afterglow profiles are depicted in Fig. 8 and the afterglows at 100 and 1000 ms after the X-ray excitation cut-off are summarized in Table 2. The Zr doped CHC showed a lower contribution of millisecond components at times greater than 1000 ms. The situation is different in the time range up to 1000 ms. In this region, a component with decay time in the range of hundreds of milliseconds can be observed in the afterglow profile of CHC-1%. It induced a higher level of afterglow at 100 ms when compared to that of the undoped CHC-0%. This component was not resolved in the other examined materials.

## 4. Conclusions

A series of zirconium doped (0–1 mol%)  $\text{Cs}_2\text{HfCl}_6$  crystals was investigated to explain the role of natural Zr-impurity in this promising novel scintillator. XRPD analysis revealed that all prepared samples were phase pure and that zirconium influenced the intensity of the reflection from (111) crystallographic planes and its multiples. As mentioned in the introduction the concentration of Zr impurity in raw  $\text{HfCl}_4$  is comparable to the lowest nominal concentration introduced into the CHC:Zr samples. Therefore, the actual concentration of samples CHC-0% and CHC-0.1% might be very similar. Thus, a deviation of CHC-0% from the overall trends could be expected. This study showed that even at low Zr concentrations its substitution for Hf can influence the scintillation properties of  $\text{Cs}_2\text{HfCl}_6$ . This could be caused by exciton trapping around Zr anion groups. For further study, the large concentration interval of Zr substitution in  $\text{Cs}_2\text{Hf}_{1-x}\text{Zr}_x\text{Cl}_6$  should be investigated to obtain a better insight into its influence on energy transfer and trapping processes, which could allow optimization of  $\text{Cs}_2\text{Hf}_{1-x}\text{Zr}_x\text{Cl}_6$  single crystal scintillator.

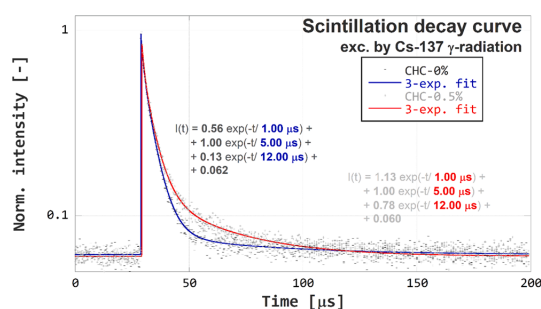


Fig. 7. Scintillation decay curves of the undoped CHC-0% and CHC-0.5% and the corresponding 3-exponential fit functions.

Table 2

Areas of the 1 ( $a_{1\mu\text{s}}$ ), 5 ( $a_{5\mu\text{s}}$ ) and 12 ( $a_{12\mu\text{s}}$ ) components of scintillation decay curves calculated from the parameters of 3-exponential fit and afterglow at 100 and 1000 ms after X-ray excitation cut-off of the CHC:Zr crystals.

Label	$a_{1\mu\text{s}}$	$a_{5\mu\text{s}}$	$a_{12\mu\text{s}}$	afterglow @100 ms	afterglow @1000 ms
CHC-0%	0.079	0.702	0.219	0.030	0.018
CHC-0.1%	0.087	0.597	0.315	0.082	0.011
CHC-0.5%	0.073	0.323	0.604	0.043	0.011
CHC-1%	0.073	0.334	0.593	0.024	0.008

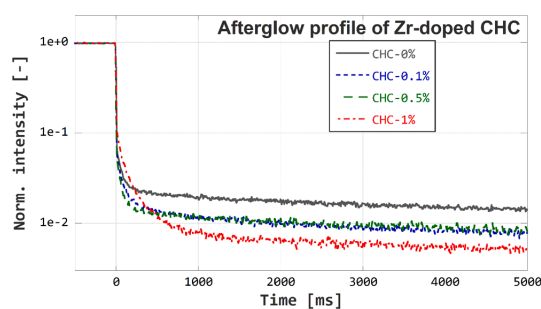


Fig. 8. Afterglow profiles of CHC:Zr crystals.

## CRediT authorship contribution statement

V. Vaněček: Conceptualization, Investigation, Methodology, Writing - original draft. J. Pátek: Investigation, Writing - original draft. R. Král: Conceptualization, Writing - review & editing, Supervision, Funding acquisition. M. Buryi: Investigation, Writing - review & editing. V. Babin: Investigation, Writing - review & editing. K. Zluzovova: Resources, Investigation. S. Kodama: Investigation, Writing - review & editing. S. Kurosawa: Writing - review & editing. Y. Yokota: Writing - review & editing. A. Yoshikawa: Writing - review & editing. M. Nikl: Conceptualization, Supervision, Writing - review & editing, Funding acquisition.

## Declaration of Competing Interest

The authors declare that they have no known competing financial interests or personal relationships that could have appeared to influence the work reported in this paper.

## Acknowledgment

Support of the Czech Science Foundation project no. 18-17555Y and project No. SOLID21 CZ.02.1.01/0.0/0.0/16.019/0000760) of the Operational Programme Research, Development and Education financed by European Structural and Investment Funds and the Czech Ministry of Education, Youth and Sports is gratefully acknowledged. The authors thank to A. Bystrický and A. Cihlar for starting materials purification and preparation of growth ampoules.

## References

- [1] M. Nikl, Scintillation detectors for x-rays, *Meas. Sci. Technol.* 17 (2006) R37–R54, <https://doi.org/10.1088/0957-0233/17/4/R01>.
- [2] M. Nikl, A. Yoshikawa, Recent R&D Trends in Inorganic Single-Crystal Scintillator Materials for Radiation Detection, *Adv. Opt. Mater.* 3 (2015) 463–481, <https://doi.org/10.1002/adom.201400571>.
- [3] N.J. Cherepy, G. Hull, A.D. Drobshoff, S.A. Payne, E. van Loef, C.M. Wilson, K.S. Shah, U.N. Roy, A. Burger, L.A. Boatner, W.-S. Choong, W.W. Moses, Strontium and barium iodide high light yield scintillators, *Appl. Phys. Lett.* 92 (2008), 083508, <https://doi.org/10.1063/1.2885728>.
- [4] G. Gundiah, G. Bizarri, S.M. Hanrahan, M.J. Weber, E.D. Bourret-Courchesne, S.E. Derenzo, Structure and scintillation of Eu<sup>2+</sup>-activated solid solutions in the BaBr<sub>2</sub>-BaI<sub>2</sub> system, *Nuclear Instruments and Methods in Physics Research Section A: Accelerators, Spectrometers, Detectors and Associated Equipment*. 652 (2011) 234–237. 10.1016/j.nima.2010.10.058.
- [5] G. Bizarri, E.D. Bourret-Courchesne, Z. Yan, S.E. Derenzo, Scintillation and Optical Properties of BaBr<sub>1.5</sub>Eu<sub>0.5</sub> and CsBa<sub>2</sub>I<sub>5</sub>Eu<sub>2+</sub>, *IEEE Trans. Nucl. Sci.* 58 (2011) 3403–3410, <https://doi.org/10.1109/TNS.2011.2166999>.
- [6] E.D. Bourret-Courchesne, G. Bizarri, R. Borade, Z. Yan, S.M. Hanrahan, G. Gundiah, A. Chaudhry, A. Canning, S.E. Derenzo, Eu<sup>2+</sup>-doped Ba<sub>2</sub>CsI<sub>5</sub>, a new high-performance scintillator, *Nuclear Instruments and Methods in Physics Research Section A: Accelerators, Spectrometers, Detectors and Associated Equipment*. 612 (2009) 138–142. 10.1016/j.nima.2009.10.146.
- [7] E.V.D. van Loef, P. Dorenbos, C.W.E. van Eijk, K. Krämer, H.U. Güdel, High-energy-resolution scintillator: Ce<sup>3+</sup> activated LaBr<sub>3</sub>, *Appl. Phys. Lett.* 79 (2001) 1573–1575. 10.1063/1.1385342.
- [8] N.J. Cherepy, S.A. Payne, S.J. Asztalos, G. Hull, J.D. Kuntz, T. Niedermayr, S. Pimpitkar, J.J. Roberts, R.D. Sanner, T.M. Tillotson, E. van Loef, C.M. Wilson, K.S. Shah, U.N. Roy, R. Hawrami, A. Burger, L.A. Boatner, W. Choong, W.W. Moses, Scintillators With Potential to Supersede Lanthanum Bromide, *IEEE Trans. Nuclear Sci.* 56 (2009) 873–880. 10.1109/TNS.2009.2020165.
- [9] J. Glodo, K.S. Shah, M. Klugerman, P. Wong, B. Higgins, P. Dorenbos, *Scintillation properties of Lu<sub>3</sub>Ce 537 (1-2) (2005) 279–281*.
- [10] E.V. van Loef, C.M. Wilson, N.J. Cherepy, G. Hull, S.A. Payne, W.-S. Choong, W.W. Moses, K.S. Shah, Crystal Growth and Scintillation Properties of Strontium Iodide Scintillators, *IEEE Trans. Nuclear Sci.* 56 (2009) 869–872. 10.1109/TNS.2009.2013947.
- [11] M.S. Alekhin, J.T.M. de Haas, I.V. Khodyuk, K.W. Krämer, P.R. Menge, V. Ouspenski, P. Dorenbos, Improvement of  $\gamma$ -ray energy resolution of LaBr<sub>3</sub>:Ce<sup>3+</sup> scintillation detectors by Sr<sup>2+</sup> and Ca<sup>2+</sup> co-doping, *Appl. Phys. Lett.* 102 (2013), 161915, <https://doi.org/10.1063/1.4803440>.
- [12] A. Burger, E. Rowe, M. Groza, K. Morales Figueroa, N.J. Cherepy, P.R. Beck, S. Hunter, S.A. Payne, Cesium hafnium chloride: A high light yield, non-hygroscopic cubic crystal scintillator for gamma spectroscopy, *Appl. Phys. Lett.* 107 (2015), 143505, <https://doi.org/10.1063/1.4932570>.
- [13] E. Ariesanti, R. Hawrami, A. Burger, S. Motakef, Improved growth and scintillation properties of intrinsic, non-hygroscopic scintillator Cs<sub>2</sub>HfCl<sub>6</sub>, *J. Lumin.* 217 (2020), 116784, <https://doi.org/10.1016/j.jlumin.2019.116784>.
- [14] S. Lam, C. Gugushev, A. Burger, M. Hackett, S. Motakef, Crystal growth and scintillation performance of Cs<sub>2</sub>HfCl<sub>6</sub> and Cs<sub>2</sub>HfCl<sub>4</sub>Br<sub>2</sub>, *J. Cryst. Growth* 483 (2018) 121–124, <https://doi.org/10.1016/j.jcrysgro.2017.11.013>.
- [15] R. Král, V. Babin, E. Mihoková, M. Buryi, V.V. Laguta, K. Nitsch, M. Nikl, Luminescence and Charge Trapping in Cs<sub>2</sub>HfCl<sub>6</sub> Single Crystals: Optical and Magnetic Resonance Spectroscopy Study, *J. Phys. Chem. C* 121 (2017) 12375–12382, <https://doi.org/10.1021/acs.jpcc.7b02327>.
- [16] M. Buryi, R. Král, V. Babin, J. Paterek, V. Vaněček, P. Veverka, M. Kohoutková, V. Laguta, M. Fasoli, I. Villa, F. Cova, A. Vedda, M. Nikl, Trapping and Recombination Centers in Cesium Hafnium Chloride Single Crystals: EPR and TSL Study, *J. Phys. Chem. C* (2019) acs.jpcc.9b05760. 10.1021/acs.jpcc.9b05760.
- [17] M. Koshimizu, K. Saeki, Y. Fujimoto, G. Okada, T. Yanagida, S. Yamashita, K. Asai, A three-state model for describing the temperature variation of the scintillation properties of Cs<sub>2</sub>HfCl<sub>6</sub>, *Jpn. J. Appl. Phys.* 57 (2018), 032401, <https://doi.org/10.7567/JJAP.57.032401>.
- [18] K. Saeki, Y. Fujimoto, M. Koshimizu, D. Nakauchi, H. Tanaka, T. Yanagida, K. Asai, Luminescence and scintillation properties of Tl- and Ce-doped Cs<sub>2</sub>HfCl<sub>6</sub> crystals, *Jpn. J. Appl. Phys.* 56 (2017), 020307, <https://doi.org/10.7567/JJAP.56.020307>.
- [19] Q.V. Phan, H.J. Kim, G. Rooh, S.H. Kim, Tl<sub>2</sub>ZrCl<sub>6</sub> crystal: Efficient scintillator for X- and  $\gamma$ -ray spectroscopies, *J. Alloy. Compd.* 766 (2018) 326–330, <https://doi.org/10.1016/j.jallcom.2018.06.349>.
- [20] P.Q. Vuong, M. Tyagi, S.H. Kim, H.J. Kim, Crystal growth of a novel and efficient Tl<sub>2</sub>HfCl<sub>6</sub> scintillator with improved scintillation characteristics, *CrystEngComm*. 21 (2019) 5898–5904. 10.1039/C9CE01202H.
- [21] R. Hawrami, E. Ariesanti, V. Buliga, A. Burger, S. Lam, S. Motakef, Tl<sub>2</sub>HfCl<sub>6</sub> and Tl<sub>2</sub>ZrCl<sub>6</sub>: Intrinsic Tl-, Hf-, and Zr-based scintillators, *J. Cryst. Growth* 531 (2020), 125316, <https://doi.org/10.1016/j.jcrysgro.2019.125316>.
- [22] K. Saeki, Y. Wakai, Y. Fujimoto, M. Koshimizu, T. Yanagida, D. Nakauchi, K. Asai, Luminescence and scintillation properties of Rb<sub>2</sub>HfCl<sub>6</sub> crystals, *Jpn. J. Appl. Phys.* 55 (2016), 110311, <https://doi.org/10.7567/JJAP.55.110311>.
- [23] S. Kodama, S. Kurosawa, Y. Morishita, H. Usami, T. Torii, M. Hayashi, M. Sasano, T. Azuma, H. Tanaka, V. Kochurikhin, J. Pejchal, R. Král, M. Yoshino, A. Yamaji, S. Toyoda, H. Sato, Y. Ohashi, Y. Yokota, K. Kamada, M. Nikl, A. Yoshikawa, Growth and Scintillation Properties of a New Red-Emitting Scintillator Rb<sub>2</sub>HfCl<sub>6</sub> for the Fiber-Reading Radiation Monitor, *IEEE Trans. Nucl. Sci.* 67 (2020) 1055–1062. 10.1109/TNS.2020.2976695.
- [24] Y. Fujimoto, K. Saeki, D. Nakauchi, H. Fukuda, T. Yanagida, H. Kawamoto, M. Koshimizu, K. Asai, Photoluminescence, photoacoustic, and scintillation properties of Te<sup>4+</sup>-doped Cs<sub>2</sub>HfCl<sub>6</sub> crystals, *Mater. Res. Bull.* 105 (2018) 291–295, <https://doi.org/10.1016/j.materresbull.2018.04.050>.
- [25] K. Saeki, Y. Fujimoto, M. Koshimizu, T. Yanagida, K. Asai, Comparative study of scintillation properties of Cs<sub>2</sub>HfCl<sub>6</sub> and Cs<sub>2</sub>ZrCl<sub>6</sub>, *Appl. Phys. Express*. 9 (2016), 042602, <https://doi.org/10.7567/APEX.9.042602>.
- [26] M. Buryi, V. Babin, R.A.M. Ligthart, S.S. Nagorny, V.B. Mikhailik, V. Vaněček, L.P. Prochazková, R. Kandel, V.V. Nahorna, P. Wang, Correlation of emission, scintillation and charge trapping properties in Cs<sub>2</sub>HfCl<sub>6</sub> and Cs<sub>2</sub>ZrCl<sub>6</sub> single crystals, *J. Mater. Chem. C* 9 (2021) 2955–2968. 10.1039/D0TC05482H.
- [27] K. Saeki, Y. Fujimoto, M. Koshimizu, D. Nakauchi, H. Tanaka, T. Yanagida, K. Asai, Luminescence and scintillation properties of Cs<sub>2</sub>HfBr<sub>6</sub> and Cs<sub>2</sub>ZrBr<sub>6</sub> crystals, *Jpn. J. Appl. Phys.* 57 (2018), 030310, <https://doi.org/10.7567/JJAP.57.030310>.
- [28] M. Taghizadeh, M. Ghanadi, E. Zolfonoun, Separation of zirconium and hafnium by solvent extraction using mixture of TBP and Cyanex 923, *Journal of Nuclear Materials*. 412 (2011) 334–337. 10.1016/j.jnucmat.2011.03.033.
- [29] K. Nitsch, A. Cihlar, Z. Malková, M. Rodová, M. Vaněček, The purification and preparation of high-purity PbCl<sub>2</sub> and ternary alkali lead chloride single crystals, *Journal of Crystal Growth*. 131 (1993) 612–615. 10.1016/0022-0248(93)90214-H.
- [30] K. Nitsch, M. Dušek, M. Nikl, K. Polák, M. Rodová, Ternary alkali lead chlorides: Crystal growth, crystal structure, absorption and emission properties, *Progress in Crystal Growth and Characterization of Materials*. 30 (1995) 1–22. 10.1016/0960-8974(95)00012-V.
- [31] C. Cardenas, A. Burger, M.L. DiVacri, B. Goodwin, M. Groza, M. Laubenstein, S. Nagorny, S. Nisi, E. Rowe, Internal contamination of the Cs<sub>2</sub>HfCl<sub>6</sub> crystal scintillator, *Nucl. Instrum. Methods Phys. Res., Sect. A* 872 (2017) 23–27, <https://doi.org/10.1016/j.nima.2017.08.006>.
- [32] V. Vaněček, R. Král, J. Paterek, V. Babin, V. Jary, J. Hybler, S. Kodama, S. Kurosawa, Y. Yokota, A. Yoshikawa, M. Nikl, Modified vertical Bridgman method: Time and cost effective tool for preparation of Cs<sub>2</sub>HfCl<sub>6</sub> single crystals, *J. Cryst. Growth* 533 (2020), 125479, <https://doi.org/10.1016/j.jcrysgro.2020.125479>.
- [33] S. Kodama, S. Kurosawa, J. Pejchal, R. Král, A. Yamaji, Y. Ohashi, Y. Yokota, K. Kamada, M. Nikl, A. Yoshikawa, Growth and Luminescent Properties of Cs<sub>2</sub>HfCl<sub>6</sub> Scintillators Doped With Alkaline Earth Metals, *IEEE Transactions on Nuclear Science*. 65 (2018) 2169–2173. 10.1109/TNS.2018.2848474.
- [34] J.A. Mares, M. Nikl, N. Solovieva, C. D'Ambrosio, F. de Notaristefani, K. Blazek, P. Maly, K. Nejezchleb, P. Fabeni, G.P. Pazzi, J.T.M. de Haas, C.W.E. van Eijk, P. Dorenbos, Scintillation and spectroscopic properties of Ce<sup>3+</sup>-doped YAlO<sub>3</sub> and Lu<sub>3</sub>(RE)<sub>1-x</sub>AlO<sub>3</sub>(RE=Y<sup>3+</sup> and Gd<sup>3+</sup>) scintillators, *Nuclear Instruments and Methods in Physics Research Section A: Accelerators, Spectrometers, Detectors and Associated Equipment*. 498 (2003) 312–327. 10.1016/S0168-9002(02)01996-4.



## Thermal analysis of cesium hafnium chloride using DSC–TG under vacuum, nitrogen atmosphere, and in enclosed system

R. Král<sup>1</sup> · P. Zemenová<sup>1</sup> · V. Vaněček<sup>1,2</sup> · A. Bystrický<sup>1</sup> · M. Kohoutková<sup>3</sup> · V. Jary<sup>1</sup> · S. Kodama<sup>4</sup> · S. Kurosawa<sup>5,6</sup> · Y. Yokota<sup>6</sup> · A. Yoshikawa<sup>4,6,7</sup> · M. Nikl<sup>1</sup>

Received: 24 April 2019 / Accepted: 22 November 2019  
© Akadémiai Kiadó, Budapest, Hungary 2019

### Abstract

This paper reports on the preparation of undoped cesium hafnium chloride ( $\text{Cs}_2\text{HfCl}_6$ ) and study of its thermal properties. The  $\text{Cs}_2\text{HfCl}_6$  is considered, due to its excellent scintillation properties, as a promising candidate for cost-effective radiation detectors with potential to replace traditional halide scintillators, e.g., NaI:Tl and CsI:Tl. The  $\text{Cs}_2\text{HfCl}_6$  material was successfully synthesized from a cesium chloride and a hafnium chloride mixed together in stoichiometric ratio. The presence of only one crystalline phase of the  $\text{Cs}_2\text{HfCl}_6$  in the material was confirmed by the X-ray diffraction analysis. The simultaneous non-isothermal differential scanning calorimetry and thermogravimetry (DSC–TG) of the synthesized material under nitrogen atmosphere, vacuum, and in enclosed system was performed. The  $\text{Cs}_2\text{HfCl}_6$  decomposition and melting of CsCl– $\text{Cs}_2\text{HfCl}_6$  mixture under nitrogen and vacuum were observed. On the contrary, the DSC measurement of the cesium hafnium chloride in enclosed system showed only one endothermic peak related to the congruent melting point. Furthermore, the repeated DSC–TG measurements to investigate the materials' stability in enclosed system were carried out as well.

**Keywords** Cesium hafnium chloride · DSC–TG · Thermal stability · Scintillator

### Introduction

The discovery of rare earth halide scintillator family [1, 2] initiated the research of halide radiation detectors such as halide elpasolites [3, 4],  $\text{SrI}_2\cdot\text{Eu}$  [5], and Eu-doped ternary halide compounds [6] for their excellent scintillation properties. Recently, growing interest in a new class of ternary halides such as cesium hafnium chloride ( $\text{Cs}_2\text{HfCl}_6$ ) has appeared as well [7–12]. The  $\text{Cs}_2\text{HfCl}_6$  belongs into a family of ternary halides based on a general formula  $\text{A}_2\text{MX}_6$ , where A is an alkali metal (Li, Na, K, Rb, Cs), M is metal in 4+ valence state (e.g., Ti, Zr, Hf, Pt, Sn, Se, Te), and X is halide (F, Cl, Br, and I) [7]. High effective atomic number of  $Z=58$ , high light yield of 30,000–54,000 photons  $\text{MeV}^{-1}$ , energy resolution of 3.3% at 662 keV, high proportionality, moderate density of  $3.86 \text{ g cm}^{-3}$ , and low hygroscopicity [12] make it a suitable candidate for cost-effective radiation detectors [7].

The  $\text{Cs}_2\text{HfCl}_6$  is formed by cesium chloride (CsCl, m.p. 645 °C) and hafnium chloride ( $\text{HfCl}_4$ , s.p. ~ 320 °C [13]) mixed together in stoichiometric ratio 2:1. This ternary halide melts congruently without any phase transitions at the temperature 826 °C [14], see phase diagram CsCl– $\text{HfCl}_4$

✉ R. Král  
kralr@fzu.cz

- <sup>1</sup> Institute of Physics of the Czech Academy of Sciences, Cukrovarnická 10, 162 00 Prague, Czech Republic
- <sup>2</sup> Faculty of Nuclear Sciences and Physical Engineering, Czech Technical University in Prague, Břehová 7, Prague 1, Czech Republic
- <sup>3</sup> University of Chemistry and Technology Prague, Technická 5, 166 28 Prague, Czech Republic
- <sup>4</sup> Institute for Materials Research, Tohoku University, 2-1-1, Katahira, Aoba-ku, Sendai, Miyagi 980-8577, Japan
- <sup>5</sup> Faculty of Science, Yamagata University, 1-4-12, Kojirakawa-machi, Yamagata 990-8560, Japan
- <sup>6</sup> New Industry Creation Hatchery Center, Tohoku University, 6-6-10 Aza-Aoba, Aramaki, Aoba-ku, Sendai, Miyagi 980-8579, Japan
- <sup>7</sup> C&A Corporation, 6-6-40 Aza-Aoba, Aramaki, Aoba-ku, Sendai, Miyagi 980-8579, Japan



(Fig. 1). The  $\text{Cs}_2\text{HfCl}_6$  crystallizes in a cubic structure with lattice parameters  $a = 10.42 \pm 0.01 \text{ \AA}$  (space group  $\text{Fm}\bar{3}\text{m}$ ) [15], which is isostructural to  $\text{K}_2\text{PtCl}_6$  and analogous to an anti-fluorite  $\text{CaF}_2$  structure [15–19].

The synthesis of the  $\text{Cs}_2\text{HfCl}_6$  material is an uneasy task due to the  $\text{HfCl}_4$  sublimation and its high hygroscopicity [13] and reaction kinetics of the  $\text{CsCl}$  and  $\text{HfCl}_4$  in solid phase [14, 17]. Obtaining high-quality and purity starting  $\text{Cs}_2\text{HfCl}_6$  material requires firstly successful synthesis of  $\text{Cs}_2\text{HfCl}_6$  and secondly removal of oxidic impurities before its crystal growth [10, 21, 22]. Therefore, characterization of  $\text{Cs}_2\text{HfCl}_6$  behavior under thermal treatment can be considered as the first and useful step to improve the technological procedure of its synthesis and crystal growth.

In this work, we focus on the characterization of the pure  $\text{Cs}_2\text{HfCl}_6$  using simultaneous non-isothermal differential scanning calorimetry (DSC) and thermogravimetry (TG). This method is well known and widely used to simultaneously monitor heat flow and mass differences in the sample in dependence on the temperature and time, respectively. The DSC–TG analysis plays irreplaceable role in the characterization of materials' basic thermal properties, for instance melting point and melts' undercooling ( $\text{CsSrBrI}_2\text{:Eu}$  [23],  $\text{CsSr}_{1-x}\text{Ba}_x\text{I}_3\text{:1\% Eu}$  [24]), phase transitions ( $\text{Rb}_2\text{PbCl}_4$ ,  $\text{Cs}_4\text{PbCl}_6$  [25],  $\text{CsCaI}_3\text{:Eu}$  [26]), or decomposition ( $\text{Na}_3\text{Sn}_2\text{F}_6\text{Cl}$  [27]). In the case of the  $\text{Cs}_2\text{HfCl}_6$ , detailed

thermodynamic properties of the  $\text{HfCl}_4$  solution in the  $\text{CsCl}$  melt and measurements of the equilibrium decomposition pressures of the  $\text{HfCl}_4$  over the melt in the temperature range of the undergoing reactions were presented in [14, 17]. Similarly, thermodynamic data for other  $\text{Cs}_2\text{HfCl}_6$  isostructural compounds such as  $\text{K}_2\text{ZrCl}_6$ ,  $\text{Na}_2\text{ZrCl}_6$ ,  $\text{Cs}_2\text{ZrCl}_6$ ,  $\text{Na}_2\text{HfCl}_6$ , and  $\text{K}_2\text{HfCl}_6$  were reported as well [17, 28–30]. In a similar system of the  $\text{K}_2\text{SnBr}_6$ , Galloni et al. [31] described the tetragonal-cubic phase transition by X-ray diffraction analysis (XRD) equipped with electrically heated holder.

The goal of this paper is to describe the stability and thermal behavior of the  $\text{Cs}_2\text{HfCl}_6$  material by the DSC–TG analysis and test the influence of various atmospheres (nitrogen and vacuum) and conditions (enclosed system in a sealed quartz ampule) on its stability. This analysis contributes to the improvement and optimization of the conditions for crystal growth of the  $\text{Cs}_2\text{HfCl}_6$  from the melt by the Bridgman method. To the best of our knowledge, the DSC–TG measurements of the  $\text{Cs}_2\text{HfCl}_6$  material were not reported so far, and in this paper, they are presented for the first time.

## Experimental

### Preparation of $\text{Cs}_2\text{HfCl}_6$ material

The  $\text{Cs}_2\text{HfCl}_6$  material was synthesized by the direct reaction of  $\text{CsCl}$  and  $\text{HfCl}_4$  mixed together in required stoichiometric ratio 2:1. Firstly, removal of oxidic impurities from the starting  $\text{CsCl}$  and  $\text{HfCl}_4$  before planned measurements was of high importance. The  $\text{CsCl}$  (99.9% p.a., Alfa Aesar) was purified from oxy- and hydroxy-impurities in our laboratory via introducing the gaseous mixture of chlorination agents into the melt with subsequent zone refining [21, 32, 33]. Detailed description of the purification procedure containing both methods as well as of undergoing chemical reactions between the agents and oxidic impurities is presented in [21, 33]. The  $\text{HfCl}_4$  (99.9% p.a., Alfa Aesar with content of  $\text{Zr} < 0.5 \text{ at\%}$ ) was resublimed twice in a flow of chlorination agents. Afterward, both  $\text{CsCl}$  and  $\text{HfCl}_4$  (in stoichiometric ratio 2:1) were sealed in a quartz ampule under vacuum and heated above the melting point to form  $\text{Cs}_2\text{HfCl}_6$ . Due to very high vapor pressure (269 MPa at 820 °C [14]) of  $\text{HfCl}_4$ , a high caution was required when heating to prevent any risk of explosion. For comparison, Bloom and Hastie [34] reported that the vapor pressure of  $\text{CsCl}$  at 650 °C is only 0.126 mm. Consequently, zone refining of the  $\text{Cs}_2\text{HfCl}_6$  by 25 passes of molten zone with transition rate of  $30 \text{ mm h}^{-1}$  was applied. Powder samples for further analyses were selected from a second part (ca. 30 mm in length) along the refined ingot.

All procedures including weighing of starting materials, manufacturing, cutting, and sample preparation were

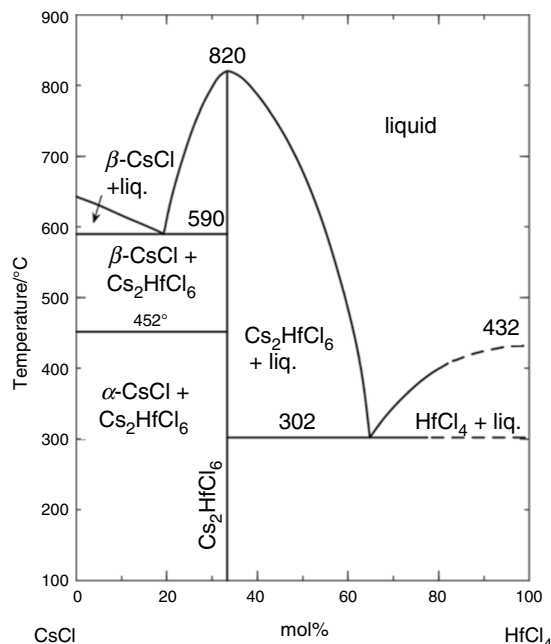


**Fig. 1** Pseudobinary  $\text{CsCl}$ – $\text{HfCl}_4$  phase diagram at normalized pressure [20]

performed in a glove box under inert nitrogen ( $N_2$ ) atmosphere with moisture and oxygen content below 1 ppm.

### Characterization of $Cs_2HfCl_6$ material

The powder XRD of the  $Cs_2HfCl_6$  sample was performed at the room temperature using the powder diffractometer PANalytical X'Pert<sup>3</sup> with the  $CuK\alpha$  radiation ( $\lambda = 1.5418 \text{ \AA}$ ,  $U = 40 \text{ kV}$ ,  $I = 30 \text{ mA}$ ) in the angular range  $5^\circ$ – $100^\circ$   $2\theta$ , step size of  $0.04^\circ$ , and counting time of  $115 \text{ s step}^{-1}$ . The XRD patterns were evaluated using the commercial software PANalytical X'Pert HighScore Plus 3.0e.

The non-isothermal DSC–TG was carried out using Setaram Setsys Evolution 16 apparatus. The nominal charge of about 30 mg of the powder  $Cs_2HfCl_6$  material was placed either into an alumina crucible or sealed in a quartz ampule depending on used atmosphere or conditions, respectively. In the case of the experiments in the alumina crucible, the  $N_2$  atmosphere (purity 5.0 N) and vacuum (3–5 mbar) were used. On the contrary, sealing the  $Cs_2HfCl_6$  powder under vacuum in a small quartz ampule enabled to simulate and monitor heat conditions similar to those present during the  $Cs_2HfCl_6$  crystal growth by Bridgman method.

All DSC–TG experiments were measured with the heating rate  $10 \text{ K min}^{-1}$  in the temperature range  $100$ – $900^\circ\text{C}$  and with an empty alumina crucible or a sealed quartz ampule in alumina crucible as a reference. The DSC–TG apparatus was calibrated in the temperature range of  $25$ – $1300^\circ\text{C}$  using following standards (In, Sn, Zn, Al, Ag, and Au). The standard deviation of performed calibrations was in the range of  $\pm 1 \text{ K}$ . Processing of the obtained data was carried out by the Calisto Processing software.

### Results and discussion

The XRD analysis of the refined  $Cs_2HfCl_6$  ingot (second part) confirmed the presence of only one crystalline phase— $Cs_2HfCl_6$  (PDF card 04-018-4277), see Fig. 2. No other crystalline phases or impurities were detected.

The DSC–TG curves of the  $Cs_2HfCl_6$  measured at  $N_2$  atmosphere (denoted as  $Cs_2HfCl_6$ - $N_2$ ) and vacuum ( $Cs_2HfCl_6$ -VAC) are depicted in Fig. 3a, b, respectively. In both plots, the derivatives of the TG curves further denoted as DTG are displayed as well.

The DSC curve of  $Cs_2HfCl_6$ - $N_2$  showed several endothermic effects in the temperature range of  $100$ – $900^\circ\text{C}$ , see Fig. 3a. As mentioned above, Kipouros and Flengas [17] measured the equilibrium pressure of the  $HfCl_4$  over the  $Cs_2HfCl_6$  with temperature describing the dependence by reactions:

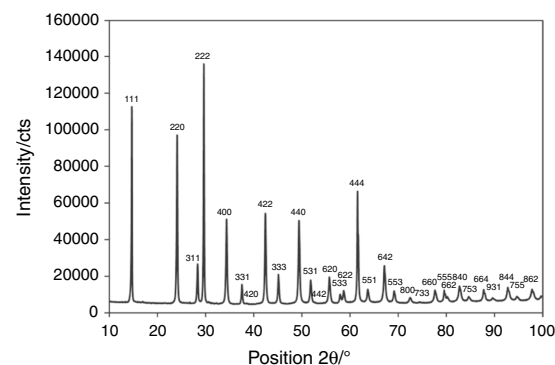


Fig. 2 XRD pattern of the  $Cs_2HfCl_6$  material

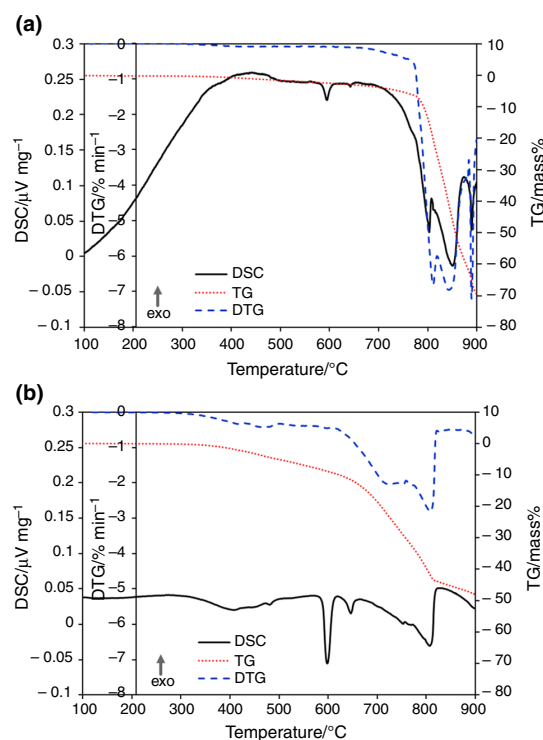
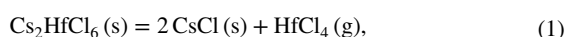


Fig. 3 DSC–TG–DTG curves of  $Cs_2HfCl_6$  measured under  $N_2$  atmosphere (a) and vacuum (b), heating rate  $10 \text{ K min}^{-1}$



undergoing consequently in three temperature intervals: (i) 645–864 K (372–591 °C), (ii) 864–1100 K (591–827 °C), and (iii) 1100–1177 K (827–904 °C). In the following text, the DSC curves will be evaluated according to these intervals; however, the intervals will be adjusted for the purpose of evaluation to better fit the temperature range of the achieved measurements.

In the first interval extended into 100–586 °C, two effects were observed, see Fig. 3a. One very weak barely visible effect at the onset temperature ( $T_{\text{onset}}$ ) of about 476 °C was present. This peak can be ascribed to phase transition of the CsCl from the cubic low-temperature structure (space group  $\text{Pm}\bar{3}\text{m}$ ), further denoted as  $\alpha$ -CsCl, to the cubic high-temperature one ( $\text{Fm}\bar{3}\text{m}$ ), further denoted as  $\beta$ -CsCl [35]. This value is in good agreement with those in the cited literature ranging from 470 to 480 °C [36, 37] and different of 445 °C [38]. Its low intensity points to that the sample contained mainly the  $\text{Cs}_2\text{HfCl}_6$  phase with minimum but still present content of the CsCl. The second effect at 586 °C corresponded to the eutectic melting of  $\text{Cs}_2\text{HfCl}_6$  and CsCl [14, 17, 20]. Both effects were accompanied by mass loss of about 0.7% in temperature range 100–586 °C, which corresponded to low release of  $\text{HfCl}_4$  and its low vapor pressure [17] over the solid  $\text{Cs}_2\text{HfCl}_6$  as a result of the decomposition according to Eq. 1.

The temperature range of the second interval was adjusted as mentioned above according to effects observed in the DSC curve (Fig. 3a) to 586–807 °C. The weak endothermic peak with the  $T_{\text{onset}}$  at 638 °C (Fig. 3a) was ascribed with high probability to continuing decomposition of  $\text{Cs}_2\text{HfCl}_6$  from the solution of the CsCl melt, as shown in Eq. 2 [14, 17]. The mass loss slightly increased to about 3.8%, but in the shorter temperature region 586–775 °C. Even though the decomposition of  $\text{Cs}_2\text{HfCl}_6$  proceeded over the eutectics, the  $\text{Cs}_2\text{HfCl}_6$  still seemed to be stable up to the following intense effect appearing at 775 °C. This is supported by the measurements of Kipouros and Flengas [17] observing only a gradual increase in the  $\text{HfCl}_4$  partial pressure up to ca. 770 °C. Furthermore, according to the phase diagram (Fig. 1) at continuous mass loss of 4.5%, the melting of the remaining solid  $\text{Cs}_2\text{HfCl}_6$  and the molten CsCl– $\text{Cs}_2\text{HfCl}_6$  solution of the corresponding composition on the liquidus line (given by the phase diagram) can be expected around 785 °C. Therefore, following broad endothermic effect consisting probably of multiple peaks with  $T_{\text{onset}}$  distinguishable at 775 and 801 °C can be ascribed to the  $\text{Cs}_2\text{HfCl}_6$  melting accompanied with  $\text{Cs}_2\text{HfCl}_6$  decomposition according to Eqs. 2 or 3. The ongoing mass loss reached 11.3% in the range 775–807 °C. Overlap of the first intense peak on the DTG curve (Fig. 3a) with the DSC curve supports such explanation as well.

In the remaining temperature range modified into 807–900 °C, two effects were present, see Fig. 3a: (i) broad

effect possibly containing three peaks with  $T_{\text{onset}}$  810, 815, and 818 °C with mass loss of 41.1% and (ii) sharper one consisting of two peaks at  $T_{\text{onset}}$  883 and 887 °C and 10.8% mass loss. First effects may be ascribed to final and rapid decomposition of the remaining molten  $\text{Cs}_2\text{HfCl}_6$  via Eq. 3. Significant mass loss exceeded the theoretical content of  $\text{HfCl}_4$  in  $\text{Cs}_2\text{HfCl}_6$  (48.7%) when considering the continuous mass loss (56.9%). Therefore, second effects (882.6 and 887.4 °C) might be related to evaporation of CsCl; however, this assumption is not supported by the shape of the observed peak, as a continuous evaporation is usually presented by a broad peak on a DSC curve.

Conclusively, the DSC curve in the full temperature range contained ten effects and mass loss of 67.7%, which is high above the theoretical content (48.7%) of  $\text{HfCl}_4$  in the  $\text{Cs}_2\text{HfCl}_6$ . It can be assumed that during the DSC–TG experiment not only decomposition of  $\text{Cs}_2\text{HfCl}_6$  phase but also CsCl evaporation (as a reactions' product) occurred. All effects and mass losses according to defined temperature intervals are summarized in Table 1.

The DSC–TG curves of the  $\text{Cs}_2\text{HfCl}_6$  measured under vacuum ( $\text{Cs}_2\text{HfCl}_6$ -VAC) are depicted in Fig. 3b. Similar effects as in the case of the  $\text{Cs}_2\text{HfCl}_6$ - $\text{N}_2$  curve were present; however, their positions were at either equal or lower temperatures. The evaluation of the  $\text{Cs}_2\text{HfCl}_6$ -VAC curve was done with respect to three temperature regions introduced above in the case of the  $\text{Cs}_2\text{HfCl}_6$ - $\text{N}_2$  curve.

In the first region (100–587 °C), a broad peak starting at 316 °C and ending before the eutectic melting was recorded. Similarly, it can be ascribed to the gradual decomposition of the solid  $\text{Cs}_2\text{HfCl}_6$  and continuous release of  $\text{HfCl}_4$  according to Eq. 1. Expectedly, the vacuum significantly supported the decomposition reaction as the mass loss was 8.3%. Such loss resulted in significant composition change in the  $\text{Cs}_2\text{HfCl}_6$  influencing its luminescence and scintillation properties as reported in [9, 39]. The  $\alpha$ - to  $\beta$ -CsCl phase transition [35] was included in the broad peak, and its  $T_{\text{onset}}$  was shifted to 472 °C. Afterward, the peak of the CsCl– $\text{Cs}_2\text{HfCl}_6$  eutectic melting appeared at the approximately same temperature (587 °C) as in  $\text{Cs}_2\text{HfCl}_6$ - $\text{N}_2$ . Its much higher intensity is in agreement with larger release of  $\text{HfCl}_4$  and thus higher content of CsCl present in the remaining sample.

In the second region (587–824 °C), one sharp peak at 632 °C associated with the  $\text{Cs}_2\text{HfCl}_6$  decomposition according to Eq. 2 was present. Due to higher escape of  $\text{HfCl}_4$  during previous effects, the intensity of this effect was higher compared to  $\text{Cs}_2\text{HfCl}_6$ - $\text{N}_2$  curve. Afterward, broad peak in range 667–824 °C, together with distinguishable effects at 773 and 798 °C, was present. Since then, the mass dropped significantly reaching 35.6% (in the range 587–824 °C) highly exceeding the mass loss in the  $\text{Cs}_2\text{HfCl}_6$ - $\text{N}_2$  curve in the same temperature range.

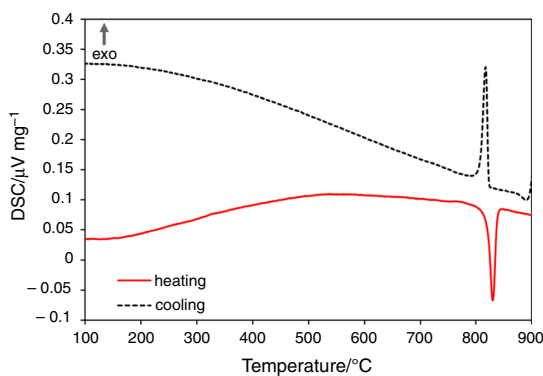
**Table 1** Values of  $T_{\text{onset}}$  and mass losses of ongoing processes in  $\text{Cs}_2\text{HfCl}_6$  material obtained by DSC–TG under  $\text{N}_2$  atmosphere and vacuum

Process	$\text{N}_2$		Vacuum	
	$T_{\text{onset}}/^\circ\text{C}$	Mass loss/%	$T_{\text{onset}}/^\circ\text{C}$	Mass loss/%
Continuous decomposition of solid $\text{Cs}_2\text{HfCl}_6$	–	–	316	–
Solid–solid of $\alpha$ - to $\beta$ - $\text{CsCl}$ phase transition	476	–	472	–
Eutectic melting of $\text{Cs}_2\text{HfCl}_6$ and $\text{CsCl}$ phases	586	0.7 (50–586 $^\circ\text{C}$ )	587	8.3 (50–587 $^\circ\text{C}$ )
Decomposition of $\text{Cs}_2\text{HfCl}_6$ from the $\text{CsCl}$ molten solution	638	3.8 (586–775 $^\circ\text{C}$ )	632 667	21.5 (587–757 $^\circ\text{C}$ )
Melting of $\text{Cs}_2\text{HfCl}_6(\text{s})$ and its continued decomposition	775 801	11.3 (775–807 $^\circ\text{C}$ )	773 798	14.1 (757–824 $^\circ\text{C}$ )
Decomposition of $\text{Cs}_2\text{HfCl}_6(\text{l})$ and evaporation of $\text{CsCl}(\text{l})$	810 815 818	41.1 (807–875 $^\circ\text{C}$ )	–	–
Continuing evaporation of $\text{CsCl}(\text{l})$	883 888	10.8 (875–900 $^\circ\text{C}$ )	–	4.0 (824–900 $^\circ\text{C}$ )

Afterward in the third region (824–900  $^\circ\text{C}$ ), no other effects were observed apart from mass drop of about 4.0%. The total mass loss in all three temperature regions reached 47.9%, which matched very well with the theoretical content of  $\text{HfCl}_4$  in  $\text{Cs}_2\text{HfCl}_6$ . Thus, it can be concluded that even last mass loss can be associated with the  $\text{Cs}_2\text{HfCl}_6$  decomposition. Interestingly, the vacuum did not support the  $\text{CsCl}$  evaporation as could be expected. All onset temperatures related to detected effects as well as mass losses in defined temperature regions are summarized in Table 1.

The DSC measurement of the  $\text{Cs}_2\text{HfCl}_6$  material sealed in a quartz ampule resulted into completely different outcome than in the case of  $\text{Cs}_2\text{HfCl}_6\text{-N}_2$  and  $\text{Cs}_2\text{HfCl}_6\text{-VAC}$ . Firstly, this measurement was unique simulating the conditions similar to those used in  $\text{Cs}_2\text{HfCl}_6$  Bridgman growth. Secondly, the TG curve was impossible to record and omitted from the analysis as the enclosed system prevented any materials' release. Thirdly, the quartz ampule with  $\text{Cs}_2\text{HfCl}_6$  was pressurized during the DSC–TG experiment requiring higher caution when thermally treated. And due to that, the comparison with phase diagram (Fig. 1) is non-reliable.

The DSC heating and cooling curves of the  $\text{Cs}_2\text{HfCl}_6$  material measured in sealed quartz ampule are shown in Fig. 4. Both the heating and cooling curves were repeatedly measured for three times to gain statistical values of observed effects. The heating DSC curve contained only one endothermic peak with  $T_{\text{onset}}$  at 821  $^\circ\text{C}$  as the average value. This effect was ascribed to the congruent melting of  $\text{Cs}_2\text{HfCl}_6$  well matching the value of 820  $^\circ\text{C}$  reported in [20]. However, it is inconsistent with the value of 826  $^\circ\text{C}$  presented by Asvestas et al. [14]. Thus, the sample was remeasured again with 10-cycle repetition to study  $\text{Cs}_2\text{HfCl}_6$  stability and the same one peak with the average  $T_{\text{onset}}$  of 822  $^\circ\text{C}$  was observed, see Fig. 5a. This points to that the effect was stable and no influence

**Fig. 4** DSC heating and cooling curves of  $\text{Cs}_2\text{HfCl}_6$  material in sealed quartz ampule, heating rate 10  $\text{K min}^{-1}$ 

during repeated heating was observed. Even though this value of the melting point was higher than previous one, still it can be considered that the inconsistency was in the range of  $\pm 1$  K deviation of the apparatus and different experimental conditions (ampule position in the crucible). However, the value was still ca. 4  $^\circ\text{C}$  lower than the 826  $^\circ\text{C}$  one. Asvestas et al. [14] suggested that such difference originated in the content of the hafnium oxychlorides and its hydrates in the sample. On the other hand, content of such impurities would deform the shape of the endothermic peak at the onset side (for instance as reported in [40]) and such deformation was not recorded. Another possible explanation might be due to the high pressure in the ampule influencing all the thermal properties (melting point, etc.) of  $\text{Cs}_2\text{HfCl}_6$  at those conditions. Further, no other effects or peaks related to  $\text{Cs}_2\text{HfCl}_6$  decomposition or eutectic melting of  $\text{Cs}_2\text{HfCl}_6$  and  $\text{CsCl}$  were observed on the DSC heating curves.

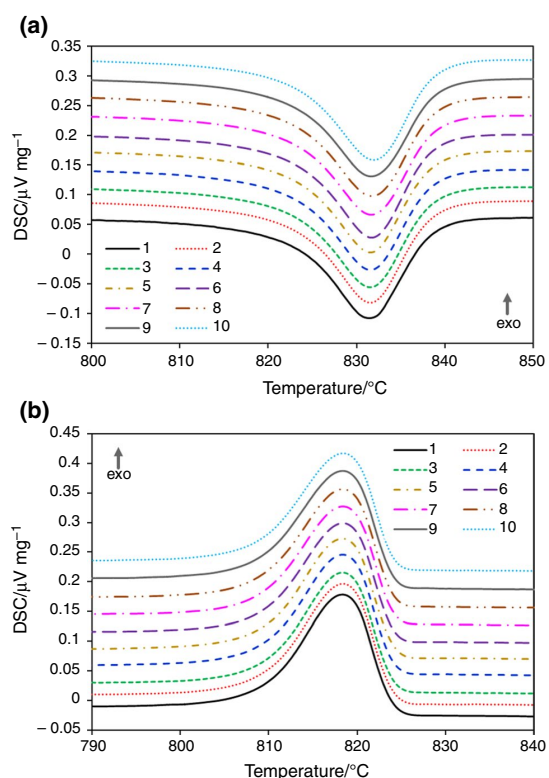


**Fig. 5** DSC curves of repeated (10-cycle) heating (a) and cooling (b) of  $\text{Cs}_2\text{HfCl}_6$  material in sealed quartz ampule, heating rate  $10 \text{ K min}^{-1}$

The cooling curves were measured with 3- and 10-cycle repetition and reached values of  $822$  (Fig. 4) and  $824$  °C (Fig. 5b), respectively. No undercooling was observed as both values were slightly higher for ca.  $1\text{--}2$  °C than the  $T_{\text{onset}}$  in the heating curves. This points to that the solidification appeared at the similar temperature as the  $\text{Cs}_2\text{HfCl}_6$  melting. Such result is not common in halides as high undercooling was observed for instance in  $\text{PbCl}_2$  [41] and  $\text{CsCaI}_3$  [26].

In summary, the DSC–TG measurements of  $\text{Cs}_2\text{HfCl}_6$  material under  $\text{N}_2$  atmosphere and vacuum were very complex containing many effects and thus their curves were very difficult to evaluate. On the contrary, the DSC measurement of  $\text{Cs}_2\text{HfCl}_6$  performed in the sealed quartz ampule was very simple containing only one melting peak.

## Conclusions

The  $\text{Cs}_2\text{HfCl}_6$  was successfully prepared by direct synthesis from starting materials, and its behavior under thermal treatment was studied. The XRD analysis proved the presence

of  $\text{Cs}_2\text{HfCl}_6$  as the only crystalline phase in the prepared material. Its stability and thermal behavior under  $\text{N}_2$  and vacuum atmospheres as well as in the sealed quartz ampule was evaluated by the non-isothermal DSC–TG analysis. The  $\text{Cs}_2\text{HfCl}_6$  showed many endothermic effects and significant mass losses due to  $\text{Cs}_2\text{HfCl}_6$  decomposition under both  $\text{N}_2$  atmosphere and vacuum. However in the  $\text{Cs}_2\text{HfCl}_6\text{--N}_2$  curve, the  $\text{Cs}_2\text{HfCl}_6$  was stable with minimum mass loss until the eutectic temperature at ca.  $586$  °C, which is in agreement with partial pressure measurements in [14, 17]. Above this temperature, the decomposition appeared and mass started to drop significantly at ca.  $775$  °C. Under vacuum, the  $\text{Cs}_2\text{HfCl}_6$  behaved similarly except all effects and mass losses occurred at lower temperatures starting already at ca.  $300$  °C with ca.  $8\%$  loss until the eutectics at  $587$  °C. This limits the  $\text{Cs}_2\text{HfCl}_6$  application as scintillator due to high change in its composition and stoichiometry, its final luminescence and scintillation properties are influenced as reported in [9, 39]. On the contrary, the  $\text{Cs}_2\text{HfCl}_6$  behaved differently in a sealed quartz ampule as only one endothermic peak at ca.  $821\text{--}822$  °C related to the  $\text{Cs}_2\text{HfCl}_6$  melting point was detected. The position of the effect was same even at 10-cycle measurement pointing to reversibility of the observed effect and its stability. Similarly, no undercooling of  $\text{Cs}_2\text{HfCl}_6$  was determined as the solidification occurred at practically similar temperature of ca.  $822\text{--}824$  °C.

**Acknowledgements** This work was performed in the framework of the Czech Science Foundation Project No. 18-17555Y and partial support by Operational Programme Research, Development and Education financed by European Structural and Investment Funds and the Czech Ministry of Education, Youth and Sports (Project No. SOLID21 CZ.0 2.1.01/0.0/0.0/16\_019/0000760). The authors would like to thank Mr. A. Cihlář for quartz ampule preparation.

## References

1. Krämer KW, Dorenbos P, Güdel HU, van Eijk CWE. Development and characterization of highly efficient new cerium doped rare earth halide scintillator materials. *J Mater Chem.* 2006;16:2773–80.
2. Alekhin MS, de Haas JTM, Khodyuk IV, Krämer KW, Menge PR, Ouspenski V, et al. Improvement of  $\gamma$ -ray energy resolution of  $\text{LaBr}_3\text{:Ce}^{3+}$  scintillation detectors by  $\text{Sr}^{2+}$  and  $\text{Ca}^{2+}$  co-doping. *Appl Phys Lett.* 2013;102:161915.
3. Bessiere A, Dorenbos P, van Eijk CWE, Kramer KW, Güdel HU. New thermal neutron scintillators:  $\text{Cs}_2\text{Li}_2\text{YCl}_6\text{:Ce}^{3+}$  and  $\text{Cs}_2\text{Li}_2\text{YBr}_6\text{:Ce}^{3+}$ . *IEEE Trans Nucl Sci.* 2004;51:2970–2.
4. Wei H, Stand L, Zhuravleva M, Meng F, Martin V, Melcher CL. Two new cerium-doped mixed-anion elpasolite scintillators:  $\text{Cs}_2\text{NaYBr}_3\text{I}_3$  and  $\text{Cs}_2\text{NaLaBr}_3\text{I}_3$ . *Opt Mater.* 2014;38:154–60.
5. Cherepy NJ, Hull G, Drobshoff AD, Payne SA, van Loef E, Wilson CM, et al. Strontium and barium iodide high light yield scintillators. *Appl Phys Lett.* 2008;92:083508.
6. Wu Y, Li Q, Chakoumakos BC, Zhuravleva M, Lindsey AC, Johnson JA, et al. Quaternary iodide  $\text{K}(\text{Ca}, \text{Sr})\text{I}_3\text{:Eu}^{2+}$  single-crystal scintillators for radiation detection: crystal structure, electronic

- structure, and optical and scintillation properties. *Adv Opt Mater.* 2016;4:1518–32.
7. Burger A, Rowe E, Groza M, Morales Figueroa K, Cherepy NJ, Beck PR, et al. Cesium hafnium chloride: a high light yield, non-hygroscopic cubic crystal scintillator for gamma spectroscopy. *Appl Phys Lett.* 2015;107:143505.
  8. Kang B, Biswas K. Carrier self-trapping and luminescence in intrinsically activated scintillator: cesium hafnium chloride ( $\text{Cs}_2\text{HfCl}_6$ ). *J Phys Chem C.* 2016;120:12187–95.
  9. Král R, Babin V, Mihóková E, Buryi M, Laguta VV, Nitsch K, et al. Luminescence and charge trapping in  $\text{Cs}_2\text{HfCl}_6$  single crystals: optical and magnetic resonance spectroscopy study. *J Phys Chem C.* 2017;121:12375–82.
  10. Cardenas C, Burger A, DiVacri ML, Goodwin B, Groza M, Laubenstein M, et al. Internal contamination of the  $\text{Cs}_2\text{HfCl}_6$  crystal scintillator. *Nucl Instrum Methods Phys Res Sect Accel Spectrom Detect Assoc Equip.* 2017;872:23–7.
  11. Cardenas C, Burger A, Goodwin B, Groza M, Laubenstein M, Nagorny S, et al. Pulse-shape discrimination with  $\text{Cs}_2\text{HfCl}_6$  crystal scintillator. *Nucl Instrum Methods Phys Res Sect Accel Spectrom Detect Assoc Equip.* 2017;869:63–7.
  12. Lam S, Gugushev C, Burger A, Hackett M, Motakef S. Crystal growth and scintillation performance of  $\text{Cs}_2\text{HfCl}_6$  and  $\text{Cs}_2\text{HfCl}_4\text{Br}_2$ . *J Cryst Growth.* 2018;483:121–4.
  13. Barraud E, Bégin-Colin S, Le Caër G, Villieras F, Barres O. Thermal decomposition of  $\text{HfCl}_4$  as a function of its hydration state. *J Solid State Chem.* 2006;179:1842–51.
  14. Asvestas DA, Pint P, Flengas SN. Some thermodynamic properties of the solutions of  $\text{ZrCl}_4$  and  $\text{HfCl}_4$  in  $\text{CsCl}$  melts. *Can J Chem.* 1977;55:1154–66.
  15. Maniv S. Crystal data for  $\text{Cs}_2\text{HfCl}_6$ . *J Appl Crystallogr.* 1976;9(3):245.
  16. Maniv S, Low W, Gabay A. EPR spectrum of  $\text{W}^{5+}$  in single crystals of  $\text{Cs}_2\text{ZrCl}_6$  and  $\text{Cs}_2\text{HfCl}_6$ . *J Phys Chem Solids.* 1971;32:815–7.
  17. Kipouros GJ, Flengas SN. Equilibrium decomposition pressures of the compounds  $\text{Cs}_2\text{ZrCl}_6$  and  $\text{Cs}_2\text{HfCl}_6$  and X-ray identification of  $\text{Na}_2\text{HfCl}_6$ ,  $\text{K}_2\text{HfCl}_6$ , and  $\text{Cs}_2\text{HfCl}_6$ . *Can J Chem.* 1983;61:2183–8.
  18. Drummen PJH, Donker H, Smit WMA, Blasse G. Jahn-Teller distortion in the excited state of tellurium(IV) in  $\text{Cs}_2\text{MCl}_6$  ( $\text{M}=\text{Zr}, \text{Sn}$ ). *Chem Phys Lett.* 1988;144:460–2.
  19. Ackerman JF. Preparation and luminescence of some  $[\text{K}_2\text{PtCl}_6]$  materials. *Mater Res Bull.* 1984;19:783–91.
  20. Morozov IS, Sun IC. Izucheniye diagramm sostoyaniya sistem  $\text{ZrCl}_4\text{-KCl}$ ,  $\text{ZrCl}_4\text{-CsCl}$ ,  $\text{HfCl}_4\text{-NaCl}$ ,  $\text{HfCl}_4\text{-KCl}$ ,  $\text{HfCl}_4\text{-CsCl}$ . *Zhur Neorg Khim.* 1959;4:678–83.
  21. Nitsch K, Cihlár A, Málková Z, Rodová M, Vaněček M. The purification and preparation of high-purity  $\text{PbCl}_2$  and ternary alkali lead chloride single crystals. *J Cryst Growth.* 1993;131:612–5.
  22. Král R, Nitsch K, Babin V, Šulc J, Jelínková H, Yokota Y, et al. Growth and optical properties of RE-doped ternary rubidium lead chloride single crystals. *Opt Mater.* 2013;36:214–20.
  23. Stand L, Zhuravleva M, Chakoumakos B, Wei H, Johnson J, Martin V, et al. Characterization of mixed halide scintillators:  $\text{CsSrBr}_2\text{:Eu}$ ,  $\text{CsCaBr}_2\text{:Eu}$  and  $\text{CsSrClBr}_2\text{:Eu}$ . *J Lumin.* 2019;207:70–7.
  24. Wei H, Zhuravleva M, Yang K, Blalock B, Melcher CL. Effect of Ba substitution in  $\text{CsSrI}_3\text{:Eu}^{2+}$ . *J Cryst Growth.* 2013;384:27–32.
  25. Nitsch K, Cihlár A, Dušek M, Hamplová V, Nikl M, Rodová M, et al. Growth and characterization of crystals of incongruently melting ternary alkali lead chlorides. *Phys Status Solidi A.* 1993;135:565–71.
  26. Loyd M, Lindsey A, Stand L, Zhuravleva M, Melcher CL, Koschan M. Tuning the structure of  $\text{CsCaI}_3$ : Eu via substitution of bromine for iodine. *Opt Mater.* 2017;68:47–52.
  27. Gong P, Luo S, Huang Q, Yang Y, Jiang X, Liang F, et al. An alkaline tin(II) halide compound  $\text{Na}_3\text{Sn}_2\text{F}_6\text{Cl}$ : synthesis, structure, and characterization. *J Solid State Chem.* 2017;248:104–8.
  28. Kipouros GJ, Flengas SN. Equilibrium decomposition pressures of the compounds  $\text{K}_2\text{ZrCl}_6$  and  $\text{K}_2\text{HfCl}_6$ . *Can J Chem.* 1978;56:1549–54.
  29. Kipouros GJ, Flengas SN. Equilibrium decomposition pressures of the compounds  $\text{Na}_2\text{ZrCl}_6$  and  $\text{Na}_2\text{HfCl}_6$ . *Can J Chem.* 1981;59:990–5.
  30. Lister RL, Flengas SN. On the relationship between equilibrium pressures and the phase diagram of a reactive system: the system:  $\text{NaCl-Na}_2\text{ZrCl}_6$ ,  $\text{KCl-K}_2\text{ZrCl}_6$ ,  $\text{NaCl-KCl-ZrCl}_4$ . *Can J Chem.* 1965;43:2947–69.
  31. Galloni EE, Benyacar MRD, Abeledo MJD. Thermal behavior of potassium bromostannate. *Z Für Krist Cryst Mater.* 1962;117(8):470–2.
  32. Lébl M, Trnka J. Entfernung von sauerstoffhaltigen Anionen aus Alkalihalogeniden. *Z Für Phys.* 1965;186:128–36.
  33. Nitsch K, Dušek M, Nikl M, Polák K, Rodová M. Ternary alkali lead chlorides: crystal growth, crystal structure, absorption and emission properties. *Prog Cryst Growth Charact Mater.* 1995;30:1–22.
  34. Bloom H, Hastie JW. Transpiration vapor pressure measurements for the molten salt systems lead chloride + cesium chloride and cadmium chloride + cesium chloride. *J Phys Chem.* 1968;72:2361–5.
  35. Secco EA, Secco RA. Heats of solution/substitution of  $\text{Ti}^+$ ,  $\text{Rb}^+$ ,  $\text{K}^+$ ,  $\text{Br}^-$ ,  $\text{I}^-$  in crystalline  $\text{CsCl}$  from heats of solid phase transition by differential scanning calorimetry. *J Phys Chem Solids.* 2002;63:1669–75.
  36. Natarajan M, Rao KJ, Rao CNR.  $\text{Pm}3\text{m-Fm}3\text{m}$  transformations of alkali halides Solid solutions of  $\text{CsCl}$  with  $\text{KCl}$ ,  $\text{CsBr}$ ,  $\text{SrCl}_2$ . *Trans Faraday Soc.* 1970;66:2497.
  37. Barin I, Knacke O, Kubaschewski O. Thermochemical properties of inorganic substances. Berlin: Springer; 1977.
  38. Rossini FD, Wagman DD, Evans WH, Levine S, Jaffe I. Selected values of chemical thermodynamic properties. National Bureau of Standards circular, 500. Washington, D.C.: U.S. Govt. Print. Off.; 1952.
  39. Buryi M, Král R, Babin V, Páterek J, Vaněček V, Veverka P, et al. Trapping and recombination centers in cesium hafnium chloride single crystals: EPR and TSL study. *J Phys Chem C.* 2019;123:19402–11.
  40. Rodová M, Cihlár A, Málková Z, Nitsch K. New differential thermal analysis study of lead halides. *Chem Phys Lett.* 1997;268:455–60.
  41. Nitsch K, Cihlár A, Rodová M. Molten state and supercooling of lead halides. *J Cryst Growth.* 2004;264:492–8.

**Publisher's Note** Springer Nature remains neutral with regard to jurisdictional claims in published maps and institutional affiliations.

Cite this: *J. Mater. Chem. C*, 2021,  
9, 2955

## Correlation of emission, scintillation and charge trapping properties in Cs<sub>2</sub>HfCl<sub>6</sub> and Cs<sub>2</sub>ZrCl<sub>6</sub> single crystals

Maksym Buryi,<sup>ib</sup>\*<sup>a</sup> Vladimir Babin,<sup>ib</sup><sup>a</sup> Rian A. M. Ligthart,<sup>b</sup> Serge S. Nagorny,<sup>cd</sup>  
Vitaliy B. Mikhailik,<sup>e</sup> Vojtěch Vaněček,<sup>af</sup> Lenka Prouzová Prochazková,<sup>af</sup>  
Ramjee Kandel,<sup>dg</sup> Viktoriia V. Nahorna<sup>dg</sup> and Peng Wang<sup>ib</sup><sup>dg</sup>

Cs<sub>2</sub>HfCl<sub>6</sub> (CHC) and Cs<sub>2</sub>ZrCl<sub>6</sub> (CZC) single crystals were grown by a vertical Bridgman method. Luminescence and charge trapping properties were studied in CHC crystals by the correlated measurements of electron paramagnetic resonance (EPR), radioluminescence (RL) and thermally stimulated luminescence (TSL) techniques. CZC crystals were studied by the same set of measurements in order to find correlations between CHC and CZC crystals. EPR spectra measured before and after X-ray irradiation in both CHC and CZC samples were attributed with the typical signals of the V<sub>k</sub>(a) hole trapping center (Cl<sub>2</sub><sup>-</sup> pseudomolecular ion), which has recently been reported though the magnitude of the signal was much smaller in the CZC crystal. Besides the V<sub>k</sub>(a) signal, another spectrum was observed in both samples; however, its intensity was at a very low level. It has been tentatively ascribed to the complex HCl-related hole trapping center. TSL glow curves measured in both CHC and CZC samples within the 10–500 K temperature range were composed of 6–8 complex peaks. The dominating peak at about 100–120 K originates from the de-trapping of holes at the V<sub>k</sub>(a) trapping center. Scintillation characteristics of CHC crystal were studied over the temperature range of 9–295 K. Scintillation decay curves were fitted by three components. The CHC crystal demonstrated a much similar light yield of ca. 20 500 ph per MeV at room temperature and 9 K. The temperature dependence of the scintillation light output exhibits an unusual s-shaped character with the drop at around 100 K that correlates well with the decrease in the V<sub>k</sub>(a) EPR signal, evidencing detrapping of holes trapped at the V<sub>k</sub>(a) center in the CHC crystal. Therefore, the V<sub>k</sub>(a) center was assumed to be the part of Hf<sup>3+</sup>–Cl<sub>2</sub><sup>-</sup> self-trapped exciton (STE) that participates in the emission above 100 K becoming “frozen” below 100 K. RL and TSL spectra were complex in the CHC sample composed of two and three overlapping bands, respectively. One of the components peaking at 2.65 eV originated from the Zr-related STE.

Received 22nd November 2020,  
Accepted 19th January 2021

DOI: 10.1039/d0tc05482h

rsc.li/materials-c

### 1. Introduction

Cs<sub>2</sub>HfCl<sub>6</sub> (CHC) and Cs<sub>2</sub>ZrCl<sub>6</sub> (CZC) scintillating crystals are smart materials developed recently for application in gamma

spectroscopy.<sup>1–4</sup> Considering their compositions, these crystals are also highly thought-after for fundamental research aiming at the detection of rare nuclear processes occurring in Hf and Zr isotopes.<sup>5–7</sup> For example, very recently, rare alpha decay of a <sup>174</sup>Hf isotope with  $T_{1/2} = 7 \times 10^{16}$  years half-life has been observed with only 7 g of Cs<sub>2</sub>HfCl<sub>6</sub> scintillating crystal.<sup>7</sup> These crystals demonstrated the stability of mechanical and optical properties, while low hygroscopicity of CHC and CZC facilitates the production of a relatively large crystal volume.<sup>1</sup> Therefore, a reduction in price along with the preservation of spectroscopic parameters can be expected. Initial low-purity grade CsCl and HfCl<sub>4</sub> powders used for the Cs<sub>2</sub>HfCl<sub>6</sub> synthesis could be relatively easily purified, removing the majority of chemical impurities by multistage vacuum sublimation.<sup>1,4</sup> However, it is not easy to remove Zr-residuals from Hf-containing compounds and *vice versa*.<sup>1,3</sup> Due to chemical affinity, Zr is always present

<sup>a</sup> Institute of Physics of the Czech Academy of Sciences, Cukrovarnicka 10/112, 16200 Prague, Czech Republic. E-mail: buryi@fu.cz

<sup>b</sup> Debye Institute for Nanomaterials Science, Utrecht University, Princetonplein 1, Utrecht 3584 CC, The Netherlands

<sup>c</sup> Department of Physics, Engineering Physics and Astronomy, Queen's University Kingston, ON, K7L 3N6, Canada

<sup>d</sup> Arthur B. McDonald Canadian Astroparticle Physics Research Institute, Department of Physics, Engineering Physics and Astronomy, Queen's University, Kingston, ON K7L 3N6, Canada

<sup>e</sup> Diamond Light Source, Harwell Campus, Didcot, OX11 0DE, UK

<sup>f</sup> Czech Technical University in Prague, Faculty of Nuclear Sciences and Physical Engineering, Břehová 7, 115 19, Czech Republic

<sup>g</sup> Chemistry Department, Queen's University Kingston, ON, K7L 3N6, Canada

in  $\text{HfCl}_4$  powders at low percentage levels. Therefore,  $\text{Cs}_2\text{ZrCl}_6$  iso-structures with  $\text{Cs}_2\text{HfCl}_6$  can hardly be fully separated during the CHC crystal growth.<sup>8</sup> Therefore, the origin of emission centers in CHC and CZC remains not fully clear. Several recent works have investigated this point:<sup>9–11</sup> the existence of three different self-trapped excitons was theoretically predicted<sup>9</sup> and experimentally demonstrated.<sup>10</sup> Notably, scintillating pulses in CHC/CZC crystals described by different theoretical models considered several exponential components.<sup>2,3</sup> This can be complemented by the experimental aspects including the origin and types of the emission centers. It was hard to relate luminescence centers unambiguously to Zr or Hf. Moreover, it is unclear to what extent the properties of luminescence centers may be affected by the Zr/Hf content ratio.

Another bottleneck is the presence of defects participating in the energy transfer and charge trapping. Therefore, it is important to find correlations between emission (light output) and trapping states in CHC crystals. Among the typical trapping states in a CHC, one may point out  $\text{Hf}^{3+}/\text{Zr}^{3+}$  – the electron traps and well-known  $V_{\text{K}}$ , H centers<sup>12–17</sup> – hole trapping centers. However, it is not excluded that the trapping centers can be complex, for example,  $\text{HCl}^+$ ,  $\text{HCl}^-$  or  $\text{Cl}_2^- + \text{H}^-$  complexes,<sup>18,19</sup> particularly considering a modest hygroscopicity of CHC/CZC samples. Note that  $\text{LiH}^+$  centers were studied in  $\text{KCl}^{20}$  or  $\text{AgH}^+$  centers were reported in  $\text{MgO}$ .<sup>21</sup> The trapping centers, in turn, affect the light yield by enhancing the afterglow. There are a lot of works dedicated to the light yield measurements reporting 27 000–36 000 ph per MeV values.<sup>2,22–25</sup> The highest light yield of 54 000 ph per MeV<sup>1</sup> was reported in CHC crystals. However, specific processes that influence the light yield value in CHC/CZC crystals are still unclear. Moreover, the luminescence mechanisms in these materials are not completely elucidated. It is expected, therefore, that the combination of EPR, TSL, RL and scintillation measurements could shed light on the mechanisms of emission/scintillation and charge trapping peculiarities (and correlation between them) in  $\text{Cs}_2\text{HfCl}_6$  and  $\text{Cs}_2\text{ZrCl}_6$  scintillating crystals, which is the aim of the present work.

## 2. Samples and experimental

### 2.1. Sample preparation

The polycrystalline  $\text{Cs}_2\text{ZrCl}_6$  and  $\text{Cs}_2\text{HfCl}_6$  samples were synthesized from  $\text{CsCl}$  (Sigma-Aldrich, 99.9 wt%),  $\text{ZrCl}_4$  (Sigma-Aldrich, 99.5 wt%), and  $\text{HfCl}_4$  (Sigma-Aldrich, 98 wt%). A stoichiometric mixture of precursors with 30 g of total mass was sealed in silica ampoules (10 mm ID, 1 mm wall thickness, 250 mm long) under pressure lower than  $1 \times 10^{-4}$  mbar. Subsequently, the ampoules were gradually heated in a tube furnace up to 850 °C for over 24 hours and held at this temperature for another 12 hours before they were cooled down to room temperature at a rate of 60 °C hour<sup>-1</sup>. The synthesized polycrystalline samples were directly used for crystal growth in a single-zone Bridgman furnace equipped with a computer-controlled vertical translation stage. The temperature of the hot zone was 850 °C. The crystal

growth was performed at a rate of 1 mm hour<sup>-1</sup>. The temperature gradient in the Bridgman furnace was estimated to be 12 °C cm<sup>-1</sup>. The grown crystals were extracted after the ampoules fully exited the hot zone. The tip (first to freeze) and heel (last to freeze) parts (~3 mm each) of each crystal ingot were removed along with opaque impurities. The remaining materials were used in the same process of crystal growth again in a fresh ampoule of the same dimensions. Crack-free, transparent crystal ingots were thus obtained.

The symmetry of the CHC and CZC single crystals is cubic  $Fm\bar{3}m$ .<sup>26</sup> The CHC and CZC samples were cleaved along the (111) cleavage plane for EPR and TSL measurements. The approximate size of the samples was  $1 \times 2 \times 6$  mm<sup>3</sup>.

### 2.2. Experimental setup

Both CHC and CZC samples were powdered prior to the X-ray powder diffraction (XRPD) measurement using an alumina mortar and pestle. The XRPD was performed using a Rigaku MiniFlex 600 (Ni-filtered  $\text{Cu-K}\alpha$  1,2 radiation) equipped with a NaI:Tl scintillation detector, and the XRD patterns were compared to the relevant records in the ICDD PDF-2 database (version 2013). The angular range was 10°–80°, with a step of 0.02° and a scanning speed of 2° min<sup>-1</sup>.

X-ray fluorescence (XRF) analysis was performed using an energy-dispersive Niton XL3t 900GOLDD+ series analyzer equipped with a 2 W Ag X-ray tube. The Niton XL3t 900 S GOLDD analyser (Aganode) was used in the Cu/Zn mining mode. The input slot is made of beryllium and 12.7 µm in diameter (AMPTEK Inc.). The acceleration voltage was 30 kV and operating current was 5 µA. An aluminum filter was placed in the beam to decrease the background. The Cu/Zn mining mode was used to record the XRF spectra of the samples in three modes – main (50 kV, 40 µA), low (20 kV, 100 µA) and light range (8 kV, 200 µA). The characteristic lines were compared with the values in the NIST X-ray Transition Energies Database.

The RL and TSL spectra were recorded using a Horiba Jobin-Yvon 5000 M spectrometer equipped with a Janis liquid nitrogen cryostat and a TBX-04 (IBH) photodetector operating in the 200–800 nm spectral range. The spectral resolution of the monochromator was set to 8 nm. In the TSL experiments, the samples were irradiated at 77 K using a Seifert X-ray tube operated at 40 kV and 15 mA with a tungsten target. The X-ray doses delivered to the CHC and CZC samples were regulated by the exposure duration of 1 minute and 120 minutes. All TSL measurements were performed in the temperature range of 77–700 K and a linear heating rate of 0.1 K s<sup>-1</sup>. The RL spectra were recorded at 300 K and 77 K. During the TSL run, the emission spectra were taken every 10 s using a cooled CCD detector of the Ocean Optics QE65000 spectrometer. The TSL and RL amplitudes measured in CHC and CZC single crystals were corrected to the irradiated area of these samples. All the spectra were corrected for experimental distortions caused by the setup.

The scintillation properties were investigated using a multi-photon counting technique, which allows simultaneous measurements of scintillation light output and decay curves



as a function of temperature.<sup>27</sup> It should be noted that this kind of pulse shape analysis method based on waveform recording has been recently identified as an emerging technology that is bound to replace the traditional technique of scintillation detection.<sup>28</sup> A sample of a single crystal was attached to a copper holder inside a He-flow cryostat. Temperature was monitored using a Si-diode sensor and stabilised using a PID controller. The sample was irradiated by <sup>241</sup>Am source and scintillation photons were detected using a multi-alkali photomultiplier tube (PMT) model 9124A (Electron Tube Enterprises). A sequence of photoelectron pulses were produced by PMT during the scintillation event and digitized by a fast ADC with a 10 ns sampling interval that allows us to resolve individual photons. During measurements, many scintillation events (*ca.* 2000) were recorded and then analysed offline using customised software. The software identifies individual photons in the event, calculates the pulse height and then creates their distributions. The histogram of photon arrival times represents a scintillation decay curve, while the distribution of the events by amplitude is the measure of the scintillation yield. The measurements were carried out while cooling the crystal in order to eliminate contribution from thermoluminescence that may lead to erroneous results.

EPR measurements were performed using a commercial Bruker EMX plus spectrometer in the X-band (9.4 GHz) within the 10–296 K temperature range. The spectrometer sensitivity is about  $10^{12}$  spins per mT. Prior to the EPR measurements, the CHC and CZC samples were weighed and the EPR intensity was normalized to 1 g crystal weight. Computer simulations of EPR spectra were carried out using the “Easyspin 5.2.23 toolbox” program.<sup>29</sup> The X-ray irradiation of samples was performed at liquid nitrogen temperature using an ISO-DEBYEFLEX 3003 highly stabilized X-ray equipment for structure analysis (tungsten X-ray tube, 50 kV, 30 mA). The samples were exposed to the same dose of irradiation, about 15 kGy.

### 3. Results and discussion

#### 3.1. Phase and purity of the Cs<sub>2</sub>Hf(Zr)Cl<sub>6</sub> samples

The XRPD measurement confirmed the presence of a single K<sub>2</sub>PtCl<sub>6</sub> type (space group *Fm* $\bar{3}$ *m*). All reflections were matched with the database records of Cs<sub>2</sub>ZrCl<sub>6</sub> (PDF #01-074-1001) and Cs<sub>2</sub>HfCl<sub>6</sub> (PDF #00-032-0233) phases (see Fig. 1). No additional reflections related to any other phases were observed.

The X-ray fluorescence spectra of investigated samples confirmed the presence of all major elements – Cs, Cl and Hf (CHC) or Zr (CZC). In the main mode (Fig. 2A), no other detectable impurities, especially, no Hf, were detected in CZC apart from a few instrumental artefacts: Ag and its Compton scattering peaks around 20.6 and 22.9 keV; Fe, Cu and Ni from filters.

Besides Hf, a significant amount of Zr was also detected in the CHC sample (Fig. 3). No other impurities which might be expected in HfCl<sub>4</sub> precursors (*e.g.*, Al, Bi, Cr, Ir, Pt, Sr and Ti

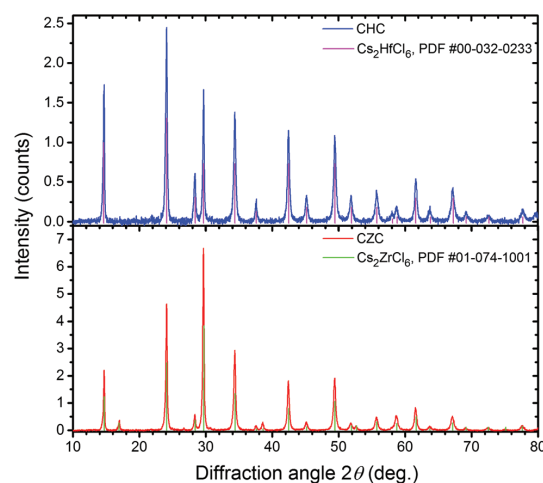


Fig. 1 X-ray diffraction patterns of the CHC and CZC powdered single crystals compared to the ICDD PDF #00-032-0233 (Cs<sub>2</sub>HfCl<sub>6</sub>) and PDF #01-074-1001 (Cs<sub>2</sub>ZrCl<sub>6</sub>) records, respectively.

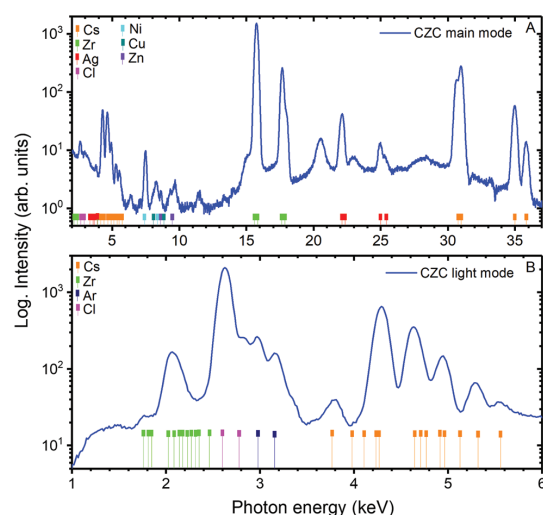


Fig. 2 (A) X-ray fluorescence spectrum of the CZC sample measured in the main mode. (B) X-ray fluorescence spectrum of the CZC sample measured in the light mode.

impurities) were observed in the spectra recorded in the main mode. Only in the light mode, it was possible to detect the characteristic lines of Cl in both samples (Fig. 3), beside Zr and Cs from air.

#### 3.2. EPR characterization of charge trapping processes

Prior to X-ray irradiation, EPR spectra measured in the CHC and CZC samples exhibited no significant EPR signals. The irradiation results in the appearance of new signals in both

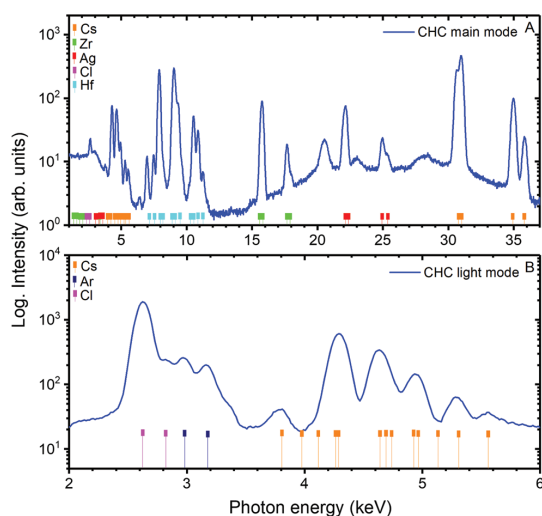


Fig. 3 (A) X-ray fluorescence spectrum of the CHC sample measured in the main mode. (B) X-ray fluorescence spectrum of the CHC sample measured in the light mode.

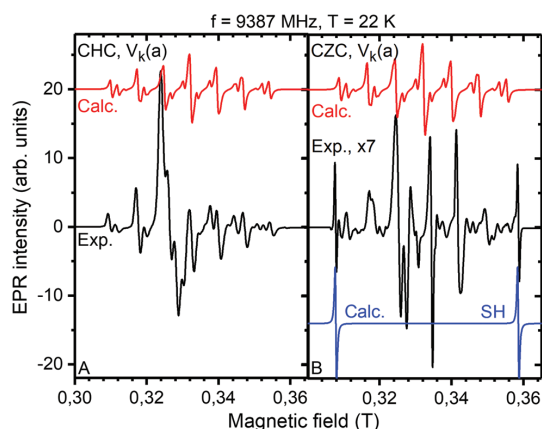


Fig. 4 EPR spectrum of the  $V_k(a)$  trapping center appeared in CHC (A) and CZC (B) single crystals after X-ray irradiation. An external magnetic field is parallel to the (111) axis. "SH" is a hydrogen-related signal.

CHC and CZC samples. The corresponding EPR spectra are shown in Fig. 4 for the orientation of an external magnetic field direction parallel to the (111) crystallographic axis. These two spectra look very similar despite the different composition of materials. They were ascribed to the same  $V_k(a)$  hole self-trapping centers, the  $V_k$  centers of the  $Cl_2^-$  (pseudomolecular ion) origin, reported recently in CHC.<sup>10,11</sup> The intensity of the  $V_k(a)$  EPR signal is approximately seven times larger in the CHC sample than in the CZC sample. In the cubic CHC sample, the  $V_k(a)$  centers exist at six magnetically non-equivalent positions. These positions are structurally the same but with different

mutual orientations in the lattice. They are characterized by the same spin Hamiltonian parameters (tensors) but different orientations of the corresponding principal axes. In order to prove that both the experimental EPR spectra in the CHC and CZC samples shown in Fig. 4 indeed originate from the  $V_k(a)$  center,<sup>10,11</sup> they have been approximated by the calculated ones using the  $\hat{g}$  tensor and  $\hat{A}^{(35,37Cl)}$ , hyperfine tensor, reported in ref. 11. For simplicity, only one magnetically non-equivalent position was considered. The following spin Hamiltonian was used for this purpose

$$\begin{aligned} \hat{H} = & \beta_e \hat{S} \hat{g} \mathbf{B} + \sum_{i=1}^2 \hat{S} \hat{A}_i^{(35Cl)} \hat{I}_i^{(35Cl)} + \sum_{i=1}^2 \hat{S} \hat{A}_i^{(37Cl)} \hat{I}_i^{(37Cl)} \\ & + \hat{S} \hat{A}_1^{(35Cl)} \hat{I}_1^{(35Cl)} + \hat{S} \hat{A}_2^{(37Cl)} \hat{I}_2^{(37Cl)} \\ & + \hat{S} \hat{A}_1^{(37Cl)} \hat{I}_1^{(37Cl)} + \hat{S} \hat{A}_2^{(35Cl)} \hat{I}_2^{(35Cl)}, \end{aligned} \quad (1)$$

where  $\beta_e$  is the Bohr magneton,  $\hat{S}$  is the electron spin operator, and  $\mathbf{B}$  is a magnetic field vector.  $\hat{A}_i^{(35,37Cl)}$  are hyperfine (HF) tensors of the  $^{35,37Cl}$  nuclei ( $i = 1, 2$  for each of chlorine ion creating the  $Cl_2^-$ ) in the following combinations in the pseudomolecular ion:  $^{35Cl}-^{35Cl}$ ,  $^{37Cl}-^{37Cl}$ ,  $^{37Cl}-^{35Cl}$  and  $^{35Cl}-^{37Cl}$ .  $\hat{I}_i^{(35,37Cl)}$  are nuclear spin operators of the  $^{35Cl}$  ( $I = 3/2$ , total abundance  $\sim 76\%$ ) and  $^{37Cl}$  ( $I = 3/2$ ,  $\sim 24\%$  abundance) isotopes. The parameters for the simulations were taken from ref. 11 for both CHC and CZC:  $g_z = g_{\parallel} = 2.003$ ,  $g_{\perp} = 2.046$ ,  $A_z^{(35Cl)} = A_{\parallel}^{(35Cl)} = 85 \times 10^{-4} \text{ cm}^{-1}$ ,  $A_{\perp}^{(35Cl)} = 10^{-3} \text{ cm}^{-1}$ . The principal  $z$  axis is [110]. The other two ( $x, y$ ) belong to the (110) plane. The hyperfine parameters of the  $^{37Cl}$  nucleus can be found as follows:

$A_{\parallel, \perp}^{(37Cl)} = \frac{\nu_L^{(37Cl)}}{\nu_L^{(35Cl)}} A_{\parallel, \perp}^{(35Cl)} = 0.84 A_{\parallel, \perp}^{(35Cl)}$ , where  $\nu_L^{(35,37Cl)}$  are the nuclear Larmor frequencies of the  $^{35,37Cl}$  isotopes.<sup>30</sup> The calculated spectra are shown in Fig. 4 along with the experimental spectra measured in the CHC and CZC samples.

The calculated spectra are in very good agreement with the main experimental resonances in Fig. 4. This also implies that indeed the  $V_k(a)$  center is created by X-ray in the CHC and CZC single crystals.

X-ray irradiation also creates another center in the CZC sample. The corresponding EPR signal marked "SH" in Fig. 4B is isotropic, *i.e.*, orientation-independent. It consists of a doublet of lines with large separation, about  $0.051 T \sim 1400 \text{ MHz}$ . All these indicate (super) hyperfine interaction of an unpaired electron with a nucleus characterized by the nuclear spin  $I = 1/2$  and a large Larmore frequency. Considering the hygroscopicity of CHC and CZC crystals, the nucleus should be  $^1H$  (abundance 100%, nuclear spin  $I = 1/2$ ) with the largest Larmore frequency ever  $\nu_L(^1H) \approx 14.8 \text{ MHz}$ .<sup>30</sup> The SH spectrum has been approximated with the calculated one using the following spin Hamiltonian:

$$\hat{H} = \beta_e \hat{S} g B + \hat{S}_z A(^1H) \hat{I}_z(^1H), \quad (2)$$

where  $g$ ,  $\hat{S}_z$ ,  $\hat{I}_z(^1H)$  and  $A(^1H)$  are  $g$  factor,  $z$  components of electron spin and nuclear spin of the  $^1H$  nucleus, and hyperfine

constant, respectively. The parameters of fit were  $g = 2.0010 \pm 0.0005$  and  $A(^1\text{H}) = 1420 \pm 20$  MHz. All these enabled us to ascribe the SH signal to the OH group. It has also been detected in electron-irradiated ice.<sup>31</sup> However, it is most probably created on the crystal surface.

The observed  $V_k(a)$  signals disappear completely in CHC and CZC samples after annealing at 110 K for four minutes. The annealing also results in a significant increase in the intensity of some other signals, much weaker than the  $V_k(a)$  ones. Very weak, they could also be observed in both CHC and CZC samples immediately after the X-ray irradiation. The corresponding spectra are shown in Fig. 5.

These spectra are multicomponent with very large separations between the resonance lines. They are centered at  $g \approx 2.14$  (0.323 T in Fig. 5) in both samples. Due to the error of the sample orientation in a cryostat, the resonance line positions in CHC slightly differ from those in CZC. The separations between resonance lines in the spectra were:  $A_1 = 0.07$  T,  $A_2 = 0.05$  T, and  $A_3 = 0.04$  T. As one can see, the separations are very large and comparable to the separation within the doublet of the SH spectrum (see Fig. 4B). Along with the  $g$  factor much larger than the 2.0023, the free electron value, hygroscopicity of the CHC and CZC samples and the similarity of the spectra in these samples, one may conclude that the source of the spectra should be some hydrogen-containing complexes such as,  $\text{HCl}^+$ ,  $\text{HCl}^-$  or  $\text{Cl}_2^- + \text{H}^-$  (see ref. 18 and 19) or similar, maybe even more complex. Due to the low intensity of this spectrum, it was difficult to provide rigorous analysis. The source of the spectra (Fig. 5) is expected to be a hole trapping center. For simplicity, further the designation "HC" will be used to refer to the signals in Fig. 5. The intensity of the HC spectrum in CHC was approximately 5 times lower than that in CZC.

The study of thermal stability will provide more evidences for the similarity between the trapping centers observed in CHC

and CZC single crystals. For this purpose, the method known as pulse annealing was used.<sup>32</sup> The EPR spectrum was measured all the time at a chosen temperature during cycles of stepwise annealing at elevated temperatures for a given amount of time (the duration of four minutes in the present case was enough for good thermalization). The dependence of EPR intensity on the annealing temperature can thus be measured. This type of temperature dependences was measured in both CHC and CZC samples after X-ray irradiation (see Fig. 6).

Remarkably, the temperature dependences of the HC signal EPR intensity in both CHC and CZC samples exhibit the increased character within the 60–100 K annealing temperature range. The raising part correlated well with the 60–100 K decay of the  $V_k(a)$  EPR intensity. This allows us to assume that the holes released from  $V_k(a)$  during the pulse annealing processes are partly re-trapped at the HC center. A similar behavior has been observed recently for  $V_k(a)$  and other hole trapping centers (H center<sup>13,16,17</sup>) in  $\text{Cs}_2\text{HfCl}_6$ .<sup>10,11</sup> At the same time, this indicates that the HC center belongs to the CHC and CZC hosts. Moreover, the same charge transfer mechanism should exist in both samples.

All the experimental dependences were fitted by the curves calculated using the following expression for the first-order trapping kinetics:<sup>33</sup>

$$I_{i+1} = I_i \exp\left(-f_0 t \exp\left(-\frac{E_t}{k_B T_i}\right)\right), \quad (3)$$

where  $I_i$  is the EPR intensity in the  $i$ -th cycle of annealing at the given temperature  $T_i$  for  $t = 4$  minutes.  $k_B$  is the Boltzmann constant. The trap depths  $E_t(V_k(a)) = 0.10 \pm 0.02$  eV and  $E_t(\text{HC}) = 0.21 \pm 0.03$  eV, and frequency factors  $f_0(V_k(a)) \sim 10^2 \text{ s}^{-1}$ , and  $f_0(\text{HC}) \sim 10^4 \text{ s}^{-1}$ , were determined for the  $V_k(a)$  and HC centers, respectively, the same, in both CHC and CZC samples. The first-order kinetics of the trapping processes was confirmed by TSL (see below). These measurements suggest that the  $V_k(a)$  and HC centers are, most probably, the same in both CHC and CZC single crystals.

The decay curve of the SH EPR signal intensity was fitted by using the same expression in eqn (3) with the following parameters:  $E_t(\text{SH}) = 0.08 \pm 0.01$  eV and  $f_0(\text{SH}) \sim 10^2 \text{ s}^{-1}$ .

### 3.3. TSL and RL measurements

To create a complete picture of the charge trapping processes in CHC and CZC single crystals and reveal similarities, thermally stimulated luminescence was measured. The corresponding glow curves are shown in Fig. 7.

They were measured after two doses of irradiation (see Section 2.2), which differ by at least two orders of magnitude. This was done to determine the order of trapping kinetics.<sup>34</sup> Since the peak positions did not change after exposure to different doses, this allowed to expect first-order trapping kinetics<sup>34</sup> in both samples. The correlation between some peak positions in CHC and CZC can immediately be seen, namely, CH1=CZ1, CH2=CZ2, CH4=CZ5, CH5=CZ6, CH6=CZ8 (see Fig. 7). Therefore, the presence of similar traps in both CHC and CZC single crystals is expected. To show correlation between EPR and TSL measurements, the corresponding TSL glow curves are shown in Fig. 6 along with the EPR decay

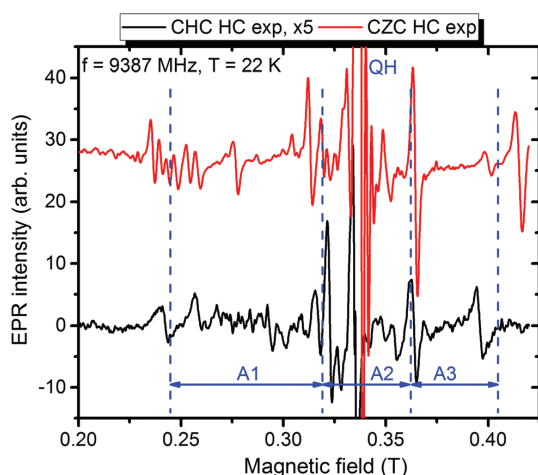


Fig. 5 EPR signals appeared after annealing at 110 K. QH is the signal from the quartz holder. An external magnetic field is approximately parallel to the (111) axis.  $A_i$  ( $i = 1-3$ ) indicates the separations between resonance lines.

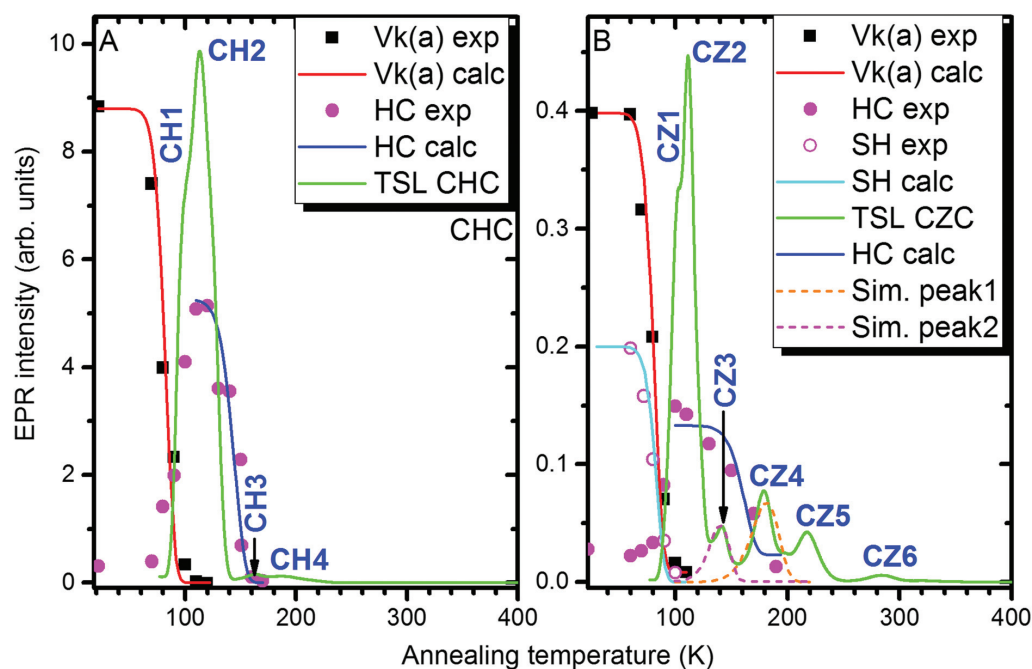


Fig. 6 (A) Experimental decay curves of  $V_k(a)$  and HC EPR signals (dots) measured in the CHC sample at 22 K fitted with calculated ones (solid lines distinguished by color) shown together with the TSL glow curve. The corresponding glow peaks a numbered CH1-4. (B) Experimental decay curves of  $V_k(a)$  and HC EPR signals (dots) measured in the CZC sample at 22 K fitted with the calculated ones (solid lines distinguished by color) shown together with the TSL glow curve. A SH EPR signal decay curve is also plotted. The corresponding glow peaks are numbered CZ1-6. "Sim. peak 1,2" are the glow peaks numerically simulated with the following parameters:  $E_t = 0.22$  eV, and frequency factor  $f_0 = 10^4$  s $^{-1}$  and  $E_t = 0.18$  eV, and frequency factor  $f_0 = 3 \times 10^4$  s $^{-1}$ , respectively.

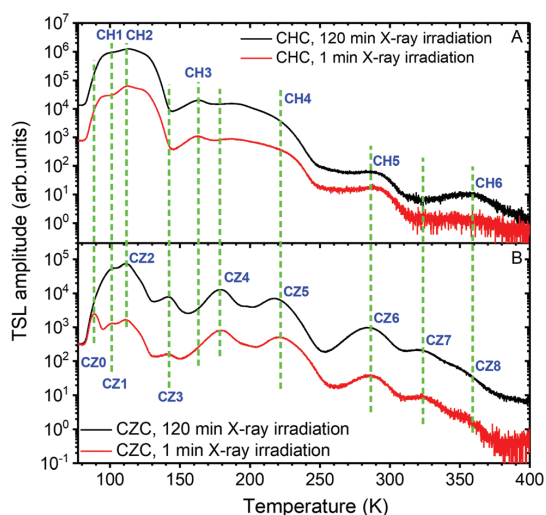


Fig. 7 TSL glow curves measured in CHC (A) and CZC (B) samples after different irradiation doses indicated in legends by the exposure time (1 and 120 min). The observed peaks were numbered CH1-6 in CHC and CZ0-8 in the CZC sample.

curves. The CH1,2 and CZ1,2 peaks were related to the EPR decay curves of the  $V_k(a)$  centers in the CHC and CZC samples,

respectively, based on recent works dedicated to charge trapping phenomena in  $Cs_2HfCl_6$ .<sup>10,11</sup> The CH1,2 peaks are by about one order of magnitude stronger than the CZ1,2 ones. The EPR decay curve of HC center seems to have correlation with the CZ4 glow peak or, probably, even with the CZ3 one in CZC. In general, the glow peaks measured in the CZC above 130–140 K are several orders of magnitude stronger than those observed in the CHC (see Fig. 6 and 7). The weak CH3 peak in the CHC is much weaker than the similar CZ3,4 peaks in the CZC and can probably be correlated with the HC decay curve as well. To check whether the CZ3,4 peaks could be correlated with the decay curve of the HC center in CZC (Fig. 6B), the following kinetic parameters,  $E_t = 0.22$  eV, and frequency factor  $f_0 = 10^4$  s $^{-1}$  (CZ4, "Sim. peak 1" in Fig. 6B) and  $E_t = 0.18$  eV, and frequency factor  $f_0 = 3 \times 10^4$  s $^{-1}$  (CZ3, "Sim. peak 2" in Fig. 6B), respectively, were used in the following expression for the first-order glow peak simulation:<sup>34</sup>

$$I(T) = n_0 f_0 \exp\left(-\frac{E_t}{k_B T}\right) \exp\left(-\frac{f_0}{\beta}\right) \int_{T_0}^T \exp\left(-\frac{E_t}{k_B T}\right) dT, \quad (4)$$

where  $\beta = 0.1$  K s $^{-1}$  is the heating rate in the TSL experiments (Fig. 6 and 7), and  $n_0$  and  $T_0$  are the starting concentration of traps and temperature. The chosen parameters of the

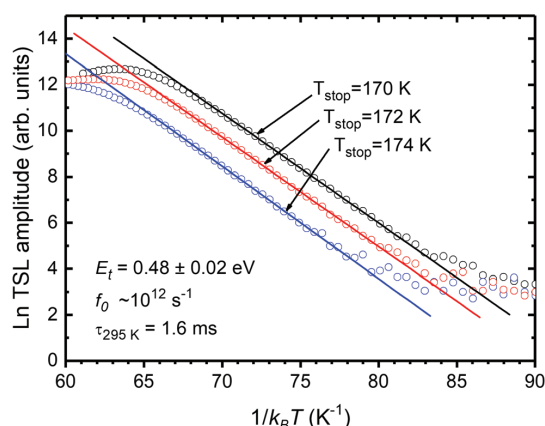


Fig. 8 Arrhenius plots of the TSL glow peak CZ3 in Fig. 7B. Dots are the experimental data whereas solid lines represent the numerical fits. The calculated averaged trap depth, frequency factor and de-trapping time at 295 K are also shown.

simulation are in good agreement with the trap depth  $E_t(\text{HC}) = 0.21 \pm 0.02$  eV, and frequency factor  $f_0(\text{HC}) \sim 10^4 \text{ s}^{-1}$  of the HC center within the given error. The correlation between the simulated peaks and the experimental ones is very good. It can thus be concluded that each of the CZ3,4 glow peaks can, in principle, correspond to the EPR decay curve of HC in the CZC sample. The CH3 glow peak, probably, by analogy can be related to the decay of the HC EPR spectrum in the CHC

sample especially, taking into account that the EPR spectrum of the HC center is stronger in the CZC sample as compared to the CHC sample. The CZ4 peak, the strongest amongst the rest of peaks located above 140 K (Fig. 6B and 7B), was studied using a partial cleaning (PC) procedure followed by initial rise technique both described in detail in ref. 34. The PC procedure was carried out at 170, 172 and 174 K stop temperatures. The corresponding Arrhenius plots are shown in Fig. 8.

The averaged trap depth  $E_t = 0.48 \pm 0.02$  eV, frequency factor  $f_0 \sim 10^{12} \text{ s}^{-1}$  and de-trapping time at 295 K,  $\tau_{295} = 1.6$  ms, were thus determined. As one can see, the listed kinetic parameters are much larger than  $E_t(\text{HC}) = 0.21 \pm 0.03$  eV, and frequency factor  $f_0(\text{HC}) \sim 10^4 \text{ s}^{-1}$  determined for the HC centers in both CHC and CZC samples. Therefore, the relation of the CZ4 peak to the EPR decay curve of the HC signal seems less probable. Based on the above-mentioned analysis, it can be inferred that the HC EPR decay curve can be correlated with the CZ3 and CH3 peaks in the CZC and CHC samples, respectively.

To gain insights into the energy distribution over the emission centers, the TSL and RL spectra measured for the CHC and CZC samples were compared. The corresponding RL spectra measured at 295 K and 77 K in CHC and CZC are plotted in Fig. 9. The spectrum at 77 K seems to be red-shifted by about 0.15 eV in CHC and 0.04 eV in CZC. The CHC spectrum is narrower while the CZC spectrum is broader at 77 K. The spectrum measured in the CZC seems to be single-component, whereas the one measured in the CHC sample is more complex exhibiting at least double-component features. To check this, the spectra (measured at 77 K) were fitted with

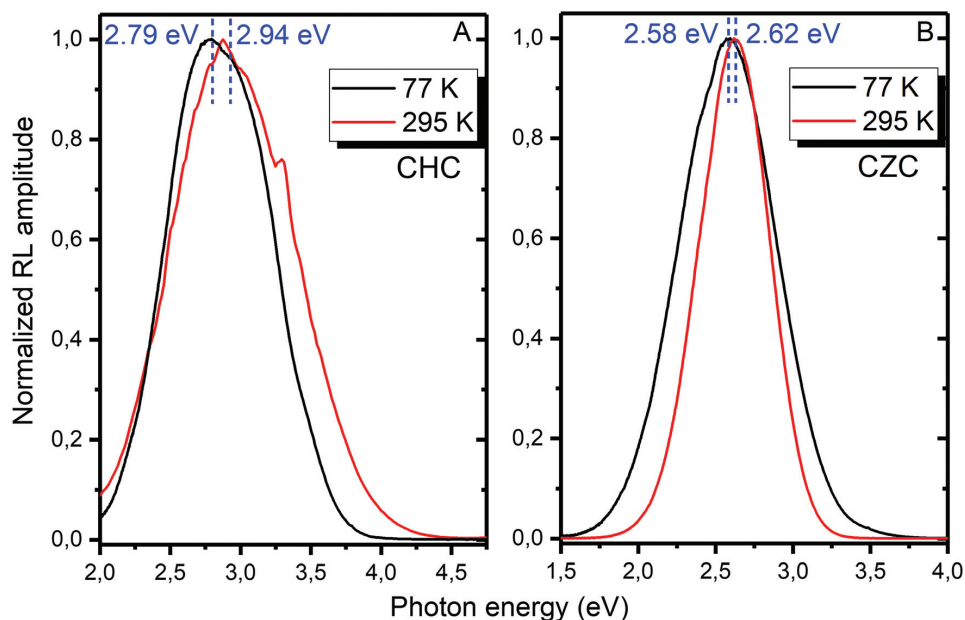


Fig. 9 Experimental RL spectra measured in the CHC (A) and CZC (B) samples at  $T = 295$  K and  $T = 77$  K, respectively. Vertical dashed lines indicate the red-shift upon the decreased temperature.

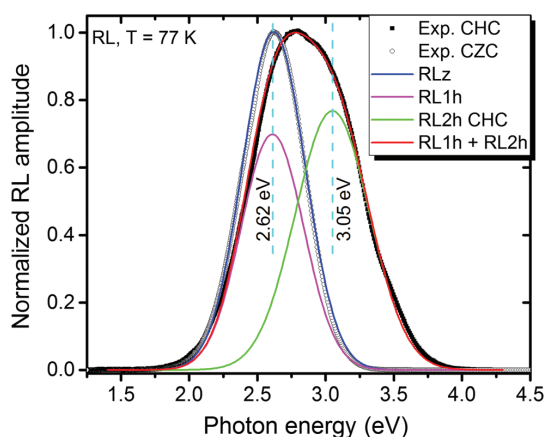


Fig. 10 Experimental RL spectra measured in the CHC and CZC samples at  $T = 77$  K, respectively. Calculated spectra indicated in the legend are as follows: RLz (CZC), RL1h (first component in the CHC spectrum), and RL2h (second component in the CHC spectrum).

the calculated Gaussians using the standard formula (see also Fig. 10):

$$G(E) = A \exp\left(-4 \ln 2 \frac{(E - E_{\max})^2}{\text{FWHM}^2}\right), \quad (5)$$

where FWHM is the full width at half maximum,  $A$  is the amplitude and  $E_{\max}$  is the energy of the maximum intensity. It was found that indeed the CZC RL spectrum is single-component (RLz in Fig. 10). The CHC RL spectrum is composed of two components (RLh1 and RLh2 in Fig. 10). Surprisingly, RLh1 is the same as RLz. Along with the confirmed presence of Zr ions in CHC by XRF (Fig. 3), it allows us to declare that RLh1 is due to the excitons trapped at  $\text{Zr}^{4+}$  in CHC, as it was supposed earlier, e.g., in ref. 8,11. The total set of the fitting parameters is listed in Table 1.

The RLh2 component with the maximum at 2.95 eV should be produced by the Hf-related excitons, as the same photon energy maximum is reported in the TSL spectra of three  $\text{Cs}_2\text{HfCl}_6$  samples recently,<sup>10</sup> where no components with the maximum at 2.62 eV were observed. The TSL spectra appeared to be more complex. The TSL spectra were compared in CZC and CHC samples at 89 K, 118 K, 142 K, 179 K, 217 K and 284 K corresponding to the maxima of TSL peaks measured in CZC (see Fig. 6 and 7). However, there were almost no signals to detect in the CHC sample at  $T = 284$  K, whereas the TSL

Table 1 Spectral parameters of RL spectral components in Fig. 10, including RL emission maxima  $E_{\max 1,2}$ ,  $\text{FWHM}_{1,2}$ , and amplitude  $A_{1,2}$ . Uncertainties of  $E_{\max 1-2}$  and  $\text{FWHM}_{1-2}$  values are equal to 0.05 eV, while for amplitudes  $A_{1-2}$  they are 0.02 a.u. "n.d." means "not determined"

Sample	$E_{\max 1}$ (eV)	$\text{FWHM}_1$ (eV)	$A_1$ (a.u.)	$E_{\max 2}$ (eV)	$\text{FWHM}_2$ (eV)	$A_2$ (a.u.)
CHC	2.62	0.54	0.36	2.95	0.64	0.39
CZC	2.62	0.54	0.52	n.d.	n.d.	n.d.

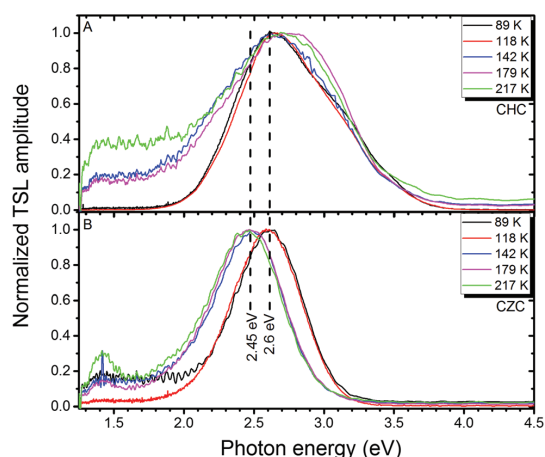


Fig. 11 Experimental TSL spectra measured in the CHC (A) and CZC (B) samples at temperatures given in legends, respectively. Vertical dashed lines indicate the red-shift upon the increased temperature.

spectrum in the CZC at 284 K was very weak and therefore, they are not considered at the moment. The spectra are demonstrated in Fig. 11.

As one can see, again, the TSL spectra of the CZC sample seem to have similarity to the part of the spectra measured in the CHC sample, as it was discussed above for the RL spectra. Moreover, the TSL spectra measured in the CZC sample demonstrated red-shift upon the increased temperature of approximately 0.15 eV, whereas the corresponding RL spectra (Fig. 9) exhibited a much smaller red-shift (0.04 eV). The existence of at least two different Zr-related emission centers in the CZC sample activated at different temperatures while measuring TSL can be assumed. To get clearer image, the TSL spectra of CHC and CZC were fitted with Gaussians in a manner similar to the above-discussed RL spectra processing (eqn (5)). The experimental and calculated TSL spectra of CHC and CZC are shown in Fig. 12 and 13, respectively. The determined fitting parameters (eqn (5)) are listed in Table 2 for CHC and Table 3 for CZC, respectively.

As one can see in Fig. 12, Tables 2 and 3, the G1h component in the CHC has the same properties as the G1z component in the CZC below 142 K similarly to RL discussed above. However, above 142 K, the G1z component shifts to red in the CZC, while the G1h component remains more or less at the constant position in the spectra in the 89–217 K range. This confirms the suggestion that the G1z component originates from different emission centers at different temperatures in the CZC. The G1z component is shifted even more to red at 284 K (2.38 eV) as compared to the spectra at 89 or 118 K (about 2.6 eV), see Tables 2 and 3. Both G1z and G1h components should originate from the Zr-related excitons. These should have the  $\text{Zr}^{3+}-\text{Cl}_2^-$  excited state similarly to the  $\text{Hf}^{3+}-\text{Cl}_2^-$  one discussed in other works.<sup>10,11</sup> The creation of the self-trapped hole ( $\text{Cl}_2^-$ ,  $\text{V}_k(\text{a})$  center) was confirmed by the EPR spectra in both samples (see Fig. 4) surviving at maximum up to 120 K. Therefore, the

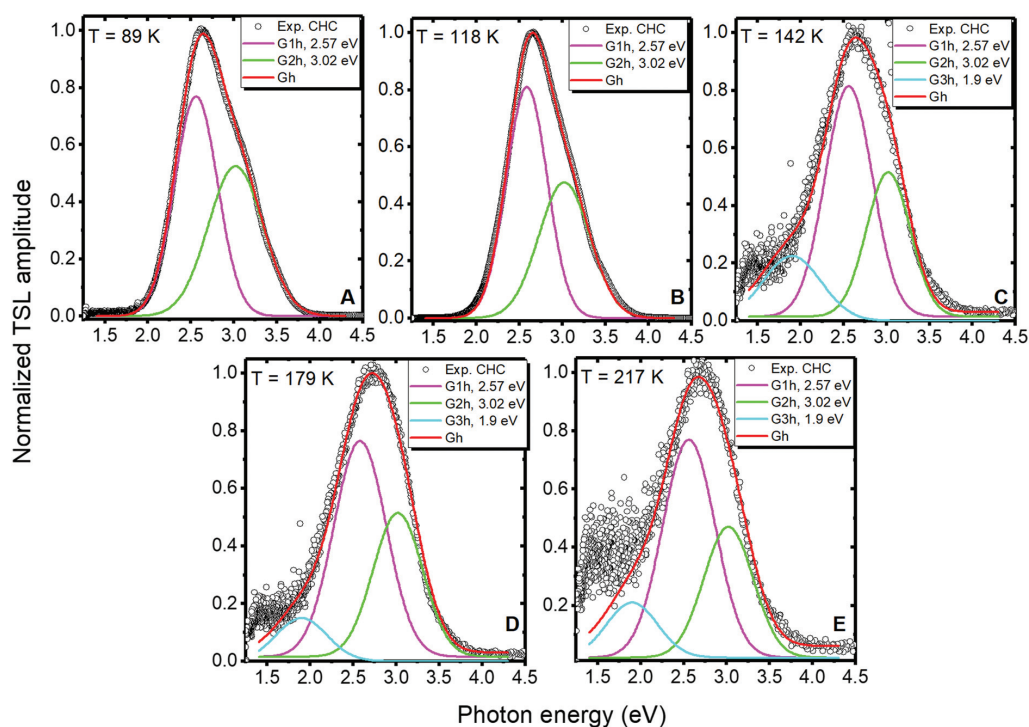


Fig. 12 TSL spectra measured in the CHC sample at 89 K (A), 118 K (B), 142 K (C), 179 K (D) and 217 K (E). Each spectrum was fitted with the sum of single Gaussian components, G1–3h, shown separately. The energy maxima of these bands are listed in legends. Gh is the sum of the corresponding G1–3h components.

emission center activated in the CZC sample below 142 K (G1z component with maxima at around 2.62 eV, see Fig. 10, 12A and B) is, most probably, a self-trapped exciton (not distorted  $Zr^{3+}-Cl_2^-$  state), *i.e.*, an electron and a hole simultaneously trapped in the vicinity of each other. Continuous heating of the sample forces them to mutually recombine. This type of trapping centers was reported in the  $ZnMoO_4$  crystals,<sup>35</sup> where an electron was trapped at  $Mo^{5+}$  and a hole at  $O^-$ . The emission centers were activated above 142 K in the CZC sample (G1z components with maxima at 2.38–2.49 eV, see Fig. 10 and 12C–F), and the excitons should be distorted (stabilized) by some other imperfections nearby, resulting in the observed emission shift (Fig. 10 and 12C–F). The G1h component in the CHC is an impurity-related (Zr is not an intrinsic ion for the CHC) and thus cannot be the part of the self-trapped exciton. This may explain its nearly constant spectral position upon the increased temperature in the CHC as compared to the G1z component in CZC.

The spectral position of the second component ( $E_{max2} = 3.02$  eV in Table 2) in the CHC spectrum remains constant. It can be related to  $Hf^{3+}-Cl_2^-$ , as the component at 3.05 eV has already been discussed in detail in CHC crystals in a recent work.<sup>10</sup> In general, the  $E_{max1,2}$  components in Table 2 (CHC sample) are getting broader above 142 K. This is in agreement with results reported by the previous work.

The third component ( $E_{max3} = 1.99$  eV in Table 2) in the CHC and the second ( $E_{max2} = 1.99$  eV in Table 3) in the CZC sample,

most probably, were related to the increased background level of the detector and used to support the noisiest parts of the spectra to preserve the continuity of the TSL spectra at a low-photon energy edge (see Fig. 12).

### 3.4. Scintillation characterization of $Cs_2HfCl_6$ single crystals

The scintillation properties of CHC were investigated over the temperature range of 9–295 K. The crystal exhibits a very good scintillation response allowing us to detect a clear peak due to  $\alpha$ -particles from  $^{241}Am$  source. The pulse height spectrum of the CHC crystal at room temperatures is displayed in Fig. 14 together with the pulse height spectrum of the  $CaWO_4$  crystal used as a reference. The spectrum features a broad band with a Gaussian shape, attributed to the energy deposited by  $\alpha$ -particles ( $\sim 5.5$  MeV).

The position of this peak is proportional to the scintillation light yield of the crystal. This enables measurements of the temperature dependence of the scintillation light yield by monitoring the peak position as a function of temperature.<sup>27</sup> The temperature dependence of the light output for the CHC measured in this way is displayed in Fig. 15A (represented by solid rectangular dots). The dependence exhibits a quite unusual s-shaped trend, which is distinctively different from the steady rise of scintillation light yield observed at cooling for majority of undoped oxide and halide scintillators.<sup>36,37</sup> With cooling CHC crystals from room temperature, the peak shifts

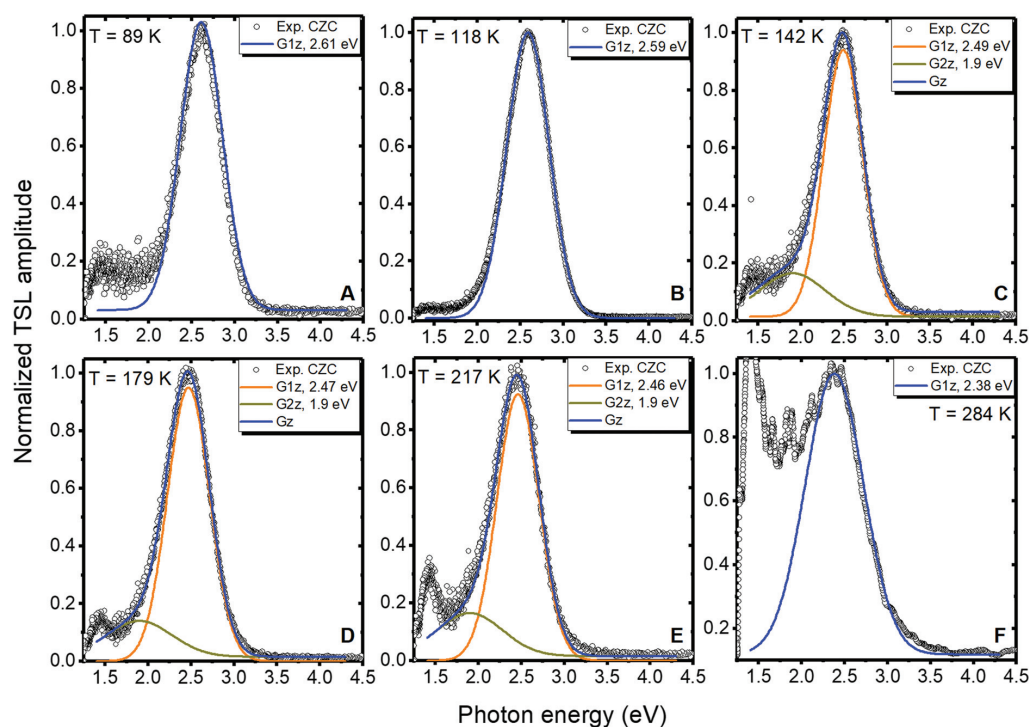


**Fig. 13** TSL spectra measured in the CZC sample at 89 K (A), 118 K (B), 142 K (C), 179 K (D), 217 K (E) and 284 K (F). Each spectrum was fitted with the sum of single Gaussian components, G1,2z, shown separately. The energy maxima of these bands are listed in legends. Gz is the sum of the corresponding G1,2z components.

**Table 2** Spectral parameters of TSL spectral components in Fig. 12 for the CHC sample, including, in general, TSL emission maxima,  $E_{\text{max}1-3}$ , FWHM $_{1-3}$ , and amplitude  $A_{1-3}$ . Uncertainties of  $E_{\text{max}1-3}$  and FWHM $_{1-3}$  values are equal to 0.02 eV, while for amplitudes  $A_{1-3}$  they are 0.02 a.u. "n.d." means "not determined"

T (K)	$E_{\text{max}1}$ (eV)	FWHM $_1$ (eV)	$A_1$ (a.u.)	$E_{\text{max}2}$ (eV)	FWHM $_2$ (eV)	$A_2$ (a.u.)	$E_{\text{max}3}$ (eV)	FWHM $_3$ (eV)	$A_3$ (a.u.)
89	2.57	0.59	0.77	3.02	0.75	0.53	n.d.	n.d.	n.d.
118		0.56	0.81		0.70	0.48	n.d.	n.d.	n.d.
142		0.65	0.80		0.60	0.50	1.90	0.80	0.23
179		0.72	0.75		0.68	0.50		0.70	0.15
217		0.72	0.75		0.68	0.45		0.70	0.19
284	n.d.	n.d.	n.d.	n.d.	n.d.	n.d.	n.d.	n.d.	n.d.

**Table 3** Spectral parameters of TSL spectral components in Fig. 12 for the CZC sample, including, in general, TSL emission maxima,  $E_{\text{max}1,2}$ , FWHM $_{1,2}$ , and amplitude  $A_{1,2}$ . Uncertainties of  $E_{\text{max}1-2}$  and FWHM $_{1-2}$  values are equal to 0.02 eV, while for amplitudes  $A_{1-2}$  they are 0.02 a.u. "n.d." means "not determined"

T (K)	$E_{\text{max}1}$ (eV)	FWHM $_1$ (eV)	$A_1$ (a.u.)	$E_{\text{max}2}$ (eV)	FWHM $_2$ (eV)	$A_2$ (a.u.)
89	2.61	0.58	1.00	n.d.	n.d.	n.d.
118	2.59	0.58	1.00	n.d.	n.d.	n.d.
142	2.49	0.54	0.93	1.90	0.90	0.15
179	2.47	0.58	0.95	1.90	0.90	0.13
217	2.46	0.58	0.93	1.90	0.90	0.15
284	2.38	0.80	1.00	n.d.	n.d.	n.d.

towards a higher amplitude, indicating a rise in the scintillation light output. This trend changes to opposite at *ca.* 225 K, when the scintillation light output starts to decrease. It reaches minimum at *ca.* 100 K and then increases again, so that at  $T = 9$  K the light yield is almost equal to that at room temperature.

These measurements also allowed us to evaluate the scintillation light yields of the CHC crystal. This was done through comparison with the reference  $\text{CaWO}_4$  crystal scintillator measured under the same experimental conditions, which exhibiting a light yield for gamma quanta equal to 15 800 ph per MeV at room temperature.<sup>38</sup> Since in our studies, crystals were irradiated by 5.5 MeV alpha particles, one should take into account the quenching factor ( $\text{QF}_\alpha$ ), which represents the dependence of light output on different types



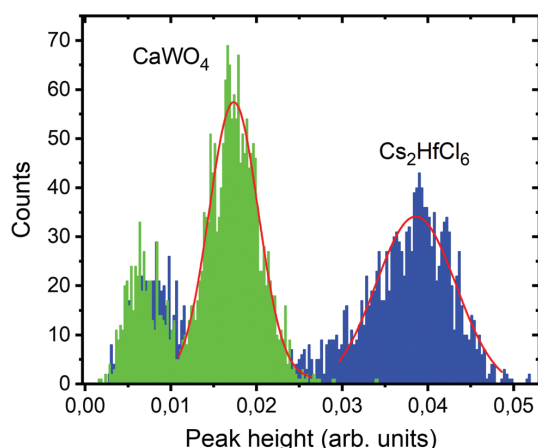


Fig. 14 Pulse height spectra of the CHC crystal measured at excitation by 5.5 MeV alpha particles of  $^{241}\text{Am}$  at room temperature. The figure also displays a pulse height spectrum of the  $\text{CaWO}_4$  crystal used as a reference scintillator. Red lines show a single Gaussian fitting of the peaks.

of irradiation, *i.e.* for alpha particles and gamma quanta. According to experimentally measured energy dependence of the  $\text{QF}_x$  in the  $\text{CaWO}_4$  crystal,<sup>39</sup> it is equal to 0.245(15) for 5.5 MeV alphas. Therefore, our reference light output value is equal to  $3860 \pm 450$  photons

per MeV. Under the assumption of identical light collection efficiency, the measured light output of a crystal  $N_{xi}$  is proportional to the two variables, *i.e.* absolute light yield ( $\text{LY}_x$ ) and emission-weighted detector sensitivity  $\varepsilon_x$ <sup>40,41</sup>

$$N_x \sim \text{LY}_x \times \varepsilon_x \quad (6)$$

The emission-weighted detector sensitivity can be determined from the spectral sensitivity of the detector  $\varepsilon(\lambda)$  and the emission spectra of the crystal  $s(\lambda)$ :

$$\varepsilon_x = \frac{\int \varepsilon(\lambda) s(\lambda) d\lambda}{\int s(\lambda) d\lambda} \quad (7)$$

Thus, the scintillation light yield for alpha particles can be estimated from the measurements of pulse height spectra of the reference  $\text{CaWO}_4$  scintillator and CHC crystal under investigation:

$$\text{LY}_{\text{Cs,HfCl}} = \text{LY}_{\text{CaWO}} \times \frac{N_{\text{Cs,HfCl}}}{N_{\text{CaWO}}} \times \frac{\varepsilon_{\lambda, \text{CaWO}}}{\varepsilon_{\lambda, \text{Cs,HfCl}}} \quad (8)$$

Given that both crystals emit in the blue spectral region, the emission-weighted detector sensitivities  $\varepsilon_x$  are very similar: 0.26 and 0.24 for CHC and  $\text{CaWO}_4$ , respectively. Taking into account the typical value of the absolute light yield of  $\text{CaWO}_4$ , we determined that the light yield of CHC is equal to  $7775 \pm 855$  ph per MeV at 295 K and  $7680 \pm 820$  ph per MeV at 9 K for 5.5 MeV alpha particles. Furthermore, these values of light

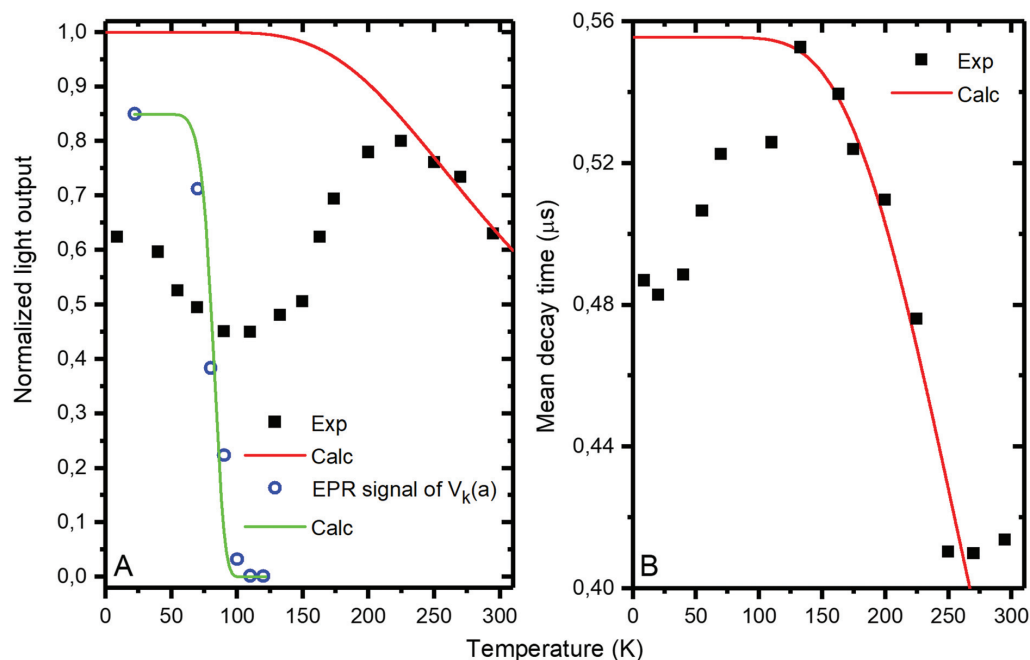


Fig. 15 (A) Temperature dependence of the scintillation light output of CHC measured at excitation by 5.5 MeV alpha particles from  $^{241}\text{Am}$  source. Experimental (hollow circles) and calculated (green solid line)  $V_k(a)$  EPR signals decay curves measured in the CHC sample at 22 K. (B) Temperature dependence of mean decay time constant. Experimental data are shown by solid rectangular dots, whereas the calculated ones are given by red solid lines. The fitting curves of the light output (panel A) and mean decay time (panel B) were calculated simultaneously for both experimental temperature dependences.

Table 4 Scintillation characteristics of the CHC sample measured at 9 K and 295 K

Crystal	Light yield (ph per MeV)		Decay constants ( $\mu\text{s}$ )		Ref.
	$T = 295 \text{ K}$	$T = 9 \text{ K}$	$T = 295 \text{ K}$	$T = 9 \text{ K}$	
CHC	20 460 <sup>a</sup>	20 200 <sup>a</sup>	0.48; 4.5; 14.4 <sup>b</sup>	0.55; 12.6; 73 <sup>b</sup>	This work
	54 000	Not determined	0.3; 4.4	Not determined	1
	27 500		2.2; 8.4		22
	30 000		0.38; 3.9		23
	27 000		0.25; 3.4		2
	—		0.25; 3.8		24
	36 400		0.94; 4.4		25

<sup>a</sup> Light yield was measured under irradiation by 5.5 MeV alpha particles and converted into the light yield corresponding to gamma quanta based on quenching factor's for both the  $\text{CaWO}_4$  reference crystal and the CHC sample. <sup>b</sup> Decay constants and their relative amplitudes were measured under irradiation by 5.5 MeV alpha particles of  $^{241}\text{Am}$  source.

output could be converted to conventional representation of light yield in photons per MeV for the irradiation with gamma quanta adopting the quenching factor measured for the CHC crystal in the range from 4 to 7 MeV.<sup>7</sup> For the 5.5 MeV alphas, the QF is equal to 0.38(3). Therefore, the light yield of the CHC crystal for the irradiation with gamma quanta is equal to  $20\,460 \pm 2450$  ph per MeV at 295 K and  $20\,200 \pm 2400$  ph per MeV at 9 K. This correlates well with the values reported for the CHC scintillator in the literature (see Table 4). A slightly lower value of the light yield could be explained by non-optimized crystal growth technology and by a slight deterioration of the crystal scintillating properties after being stored for a while in ambient atmosphere of the previous measurements.

Fig. 16 displays a set of scintillation decay curves of CHC sample measured in the microsecond time range at different temperatures. We monitored emission in the integral regime, capturing the entire emission spectrum of the scintillator. Hence, the measured decay curve exhibits a complex non-exponential decay that is due to the superposition of a few recombination processes with different types of decay kinetics. Very fast nanosecond component is evident in the decay at any temperature, while the slow component is more pronounced upon cooling the crystal.

For the sake of quantitative representation, the scintillation decay curves are often approximated by the sum of several exponential functions:  $f(t) = y_0 + \sum_i A_i \exp(-t/\tau_i)$  where  $y_0$  is the background,  $A_i$  and  $\tau_i$  are amplitudes and decay time constants. The scintillation decay curves of the CHC sample were fitted using three exponential functions that ensure the best quality of the fit as depicted in Fig. 16B. The results of the fit are summarized in Table 4. Comparative analysis of the results demonstrates that the values of the fast (0.48  $\mu\text{s}$ ) and slow (4.5  $\mu\text{s}$ ) time constants at room temperature correlate very well with what has been reported earlier in a number of studies, where two exponential fits were used.<sup>1,2,22–25,27</sup> Hence, despite the difference in the number of exponentials used in the fit, the results are consistent.

Nonetheless, it should be highlighted that the third component is essential for the analysis of the final part (tail) of the decay curves. This is a distinct feature of the scintillation process in the CHC crystal at any temperature that has been overlooked by earlier studies due to short recording time (typically a few tens of microseconds). The fractional contribution of the long component to the amplitude of scintillation is

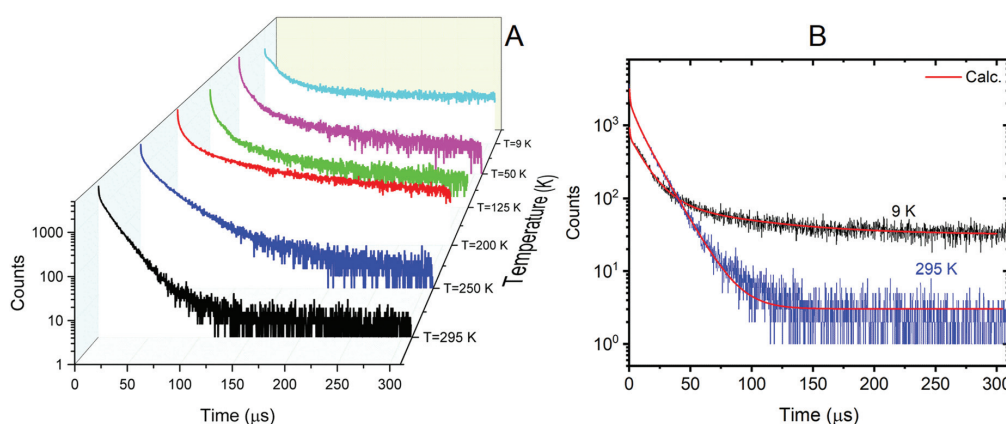


Fig. 16 (A) Scintillation decay curves of the CHC sample measured at different temperatures upon excitation by 5.5 MeV alpha particles from  $^{241}\text{Am}$  source. (B) Chosen scintillation decay curves of CHC at  $T = 9 \text{ K}$  and  $295 \text{ K}$  fitted by three exponential functions (red) in an entire time window of 0–300 microseconds.

ca. 40% at room temperature. The amplitude of this component was reduced with cooling, but due to a concomitant increase in the decay constant, the integrated contribution of the long component to the scintillation event remains significant.

The three-exponential decay curves are expected to originate from (self)-trapped excitons ((S)TE,  $\text{Hf}^{3+}-\text{Cl}_2^-$  and  $\text{Zr}^{3+}-\text{Cl}_2^-$ -like, see RL spectra in Fig. 10), *i.e.*, having very similar emission mechanisms, and therefore, the so-called mean decay time was calculated using the following expression:

$$\tau_{\text{mean}} = \left( \sum_{i=1}^n A_i \tau_i \right)^{-1} \sum_{i=1}^n A_i \tau_i^2, \quad (9)$$

where  $\tau_i$  and  $A_i$  ( $i = 1-3$ ) are the decay time constants and their amplitudes, respectively. Temperature dependence of the mean time is given in Fig. 15B. The following phenomenological model was used to fit the temperature dependence of the mean decay time data (Fig. 16B):<sup>11</sup>

$$\tau_{\text{mean}} = \frac{\tau_r}{1 + K \tau_r \exp\left(-\frac{E}{k_B T}\right)}, \quad (10)$$

where  $\tau$ ,  $\tau_r$ ,  $K$ ,  $E$  and  $k_B$  are the mean decay time at absolute temperature  $T$ , radiative decay time, frequency factor of the nonradiative transitions, corresponding energy threshold and Boltzmann constant, respectively. The total intensity of the emission delivered to a detector after the excitation of CHC with alpha-particles (light output in Fig. 16A) can be expressed as follows:

$$I(T) = N \frac{\tau_{\text{mean}}(T)}{\tau_r} = \frac{N}{1 + K \tau_r \exp\left(-\frac{E}{k_B T}\right)}, \quad (11)$$

where  $N$  is the initial population of the excited state of the (S)TEs set to 1 in the calculation (normalized light output in Fig. 16A);  $\tau_{\text{mean}}(T)$  is from eqn (10). The expressions in eqn (10) and (11) were used to fit simultaneously the normalized light output in Fig. 15A and the mean decay time in Fig. 15B. The following parameters were thus determined:  $\tau_r = 0.56 \pm 0.05 \mu\text{s}$ ,  $K = (3.5 \pm 0.1) \times 10^7 \text{ s}^{-1}$ , and  $E = 0.09 \pm 0.01 \text{ eV}$ . Remarkably, the trap depth of the  $V_k(a)$  center determined from EPR measurements is  $E_t = 0.08 \pm 0.01 \text{ eV}$ . In general, the intensity of emission remains constant until the onset of thermal quenching. Normally, when thermal ionization of the excited state of an emission center happens, liberated holes and electrons can contribute to the delayed emission through re-trapping mechanism. However, in the present case of the temperature dependence of light output (Fig. 16A), the minimum of the dependence at 100 K correlates very well with the drop of the  $V_k(a)$  EPR signal (Fig. 6A and 15A). Therefore, the  $V_k(a)$  center (see Section 3.2) was assumed to be the part of the  $\text{Hf}^{3+}-\text{Cl}_2^-$  STE, which is participating in emission above 100 K. Below 100 K, this state is "frozen" and thus the drop of the light output is observed (Fig. 15A).

## 4. Conclusions

Several experimental techniques have been applied to study the  $\text{Cs}_2\text{HfCl}_6$  and  $\text{Cs}_2\text{ZrCl}_6$  single crystals grown by a vertical Bridgman method. Among them are XRD, XRF, EPR, RL and TSL methods. XRD confirmed the phase purity of the samples. XRF detected no traces of Hf in the CZC sample, whereas some amount of Zr ions was found in the CHC sample. EPR indicated the presence of a  $V_k(a)$  hole trapping center observed previously in CHC single crystals<sup>10,11</sup> in both CHC and CZC samples. Moreover, there were some traces of a new hole trapping center, never detected before. It was related to the hydrogen, which is present, most probably, in the form of OH groups considering a modest hygroscopicity of the samples. Hydrogen should create  $\text{HCl}^+$ ,  $\text{HCl}^-$  or  $\text{Cl}_2^- + \text{H}^-$  (see ref. 18 and 19) or similar complexes in the CHC and CZC samples. Very low intensity of the corresponding EPR spectra did not allow us to analyze them rigorously. TSL glow curves measured in both CHC and CZC samples consisted of 6–8 complex peaks. Their amplitudes were, in general, larger in the CZC crystal above 130–140 K. Oppositely, the peaks at about 100–120 K were stronger in the CHC sample. The strongest peak at about 100–120 K originated from the de-trapping of holes trapped at the  $V_k(a)$  center in both CHC and CZC samples. This is in good correlation with the drop of the scintillation light output at about 100 K measured in the CHC crystal. Therefore, the  $V_k(a)$  center was assumed to be the part of the  $\text{Hf}^{3+}-\text{Cl}_2^-$  self-trapped exciton participating in the emission above 100 K, and "frozen" below 100 K. The trap depths and frequency factors of the  $V_k(a)$  and HCl-related centers were determined from the EPR and TSL study. RL spectra were single-component in the CZC sample, whereas in the CHC sample, they were composed of two overlapping bands. It has been shown that Zr present in the CHC sample participates in the energy transfer. The RL amplitude was larger in the CZC sample than in the CHC sample. TSL spectra had three-component origin in CHC, which is also consistent with the three components identified in the scintillation decay curves. The Zr-related component was found in the CHC sample as well. In general, RL and TSL spectra were expected to be composed mainly of the  $\text{Zr}^{3+}-\text{Cl}_2^-$  exciton-related emission in the CZC sample, whereas in the CHC sample, both  $\text{Zr}^{3+}-\text{Cl}_2^-$  and  $\text{Hf}^{3+}-\text{Cl}_2^-$  emission bands were detected. Based on the presented results, one may point out a certain similarity between the luminescence properties of both CHC and CZC materials. Moreover, the CZC single crystals appear to possess a smaller number of defects as compared to the CHC ones, though this can also be a sample-dependent effect. Based on the results of the studies of scintillation properties of the CHC at low temperatures, we concluded that this material is a perspective cryogenic scintillating material for application in rare nuclear processes search.

## Conflicts of interest

There are no conflicts to declare.

## Acknowledgements

The work is supported by Operational Programme Research, Development and Education financed by European Structural

and Investment Funds and the Czech Ministry of Education, Youth and Sports (Project No. SOLID21 CZ.02.1.01/0.0/0.0/16\_019/0000760) and by the Czech Science Foundation (Project No. 18-17555Y). We also acknowledge the support of the Arthur B. McDonald Canadian Astroparticle Physics Research Institute.

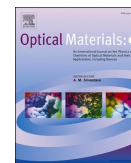
## References

- 1 A. Burger, E. Rowe, M. Groza, K. M. Figueroa, N. J. Cherepy, P. R. Beck, S. Hunter and S. A. Payne, *Appl. Phys. Lett.*, 2015, **107**, 143505.
- 2 E. Ariesanti, R. Hawrami, A. Burger and S. Motakef, *J. Lumin.*, 2020, **217**, 116784.
- 3 C. Cardenas, A. Burger, B. Goodwin, M. Groza, M. Laubenstein, S. Nagorny and E. Rowe, *Nucl. Instrum. Methods*, 2017, **869**, 63–67.
- 4 C. Cardenas, A. Burger, M. L. DiVacri, B. Goodwin, M. Groza, M. Laubenstein, S. Nagorny, S. Nisi and E. Rowe, *Nucl. Instrum. Methods Phys. Res., Sect. A*, 2017, **872**, 23–27.
- 5 P. Belli, R. Bernabei, F. A. Danevich, A. Incicchitti and V. I. Tretyak, *Eur. Phys. J. A*, 2019, **55**, 140.
- 6 F. A. Danevich, M. Hult, D. V. Kasperovych, G. P. Kovtun, K. V. Kovtun, G. Lutter, G. Marissens, O. G. Polischuk, S. P. Stetsenko and V. I. Tretyak, *Eur. Phys. J. A*, 2020, **56**, 5.
- 7 V. Caracciolo, S. S. Nagorny, P. Belli, R. Bernabei, F. Cappella, R. Cerulli, A. Incicchitti, M. Laubenstein, V. Merlo, S. Nisi and P. Wang, *Nucl. Phys. A*, 2020, **1002**, 121941.
- 8 P. S. Bryan and S. A. Ferranti, *J. Lumin.*, 1984, **31&32**, 117–119.
- 9 B. Kang and K. Biswas, *J. Phys. Chem. C*, 2016, **120**, 12187–12195.
- 10 M. Buryi, R. Král, V. Babin, J. Páterek, V. Vaněček, P. Veverka, M. Kohoutková, V. Laguta, M. Fasoli, I. Villa, F. Cova, A. Vedda and M. Nikl, *J. Phys. Chem. C*, 2019, **123**, 19402–19411.
- 11 R. Král, V. Babin, E. Mihoková, M. Buryi, V. V. Laguta, K. Nitsch and M. Nikl, *J. Phys. Chem. C*, 2017, **121**, 12375–12382.
- 12 T. G. Castner and W. Kanzig, *J. Phys. Chem. Solids*, 1957, **3**, 178–195.
- 13 W. Kanzig and T. O. Woodruff, *J. Phys. Chem. Solids*, 1959, **9**, 70–92.
- 14 B. Henderson and A. E. Hughes, in *Defects and Their Structure in Nonmetallic Solids*, ed. D. Schoemaker, Springer, Boston, MA, 1976.
- 15 D. Schoemaker, *Phys. Rev. B: Solid State*, 1973, **7**, 786–801.
- 16 C. R. A. Catlow, K. M. Diller and M. J. Norgett, *J. Phys. C: Solid State Phys.*, 1975, **8**, L34–L36.
- 17 C. R. A. Catlow, K. M. Diller and L. W. Hobbs, *Philos. Mag. A*, 1980, **42**, 123–150.
- 18 A. I. Chichinina, M. Poretskiy, C. Maul and K.-H. Gericke, *Bull. Lebedev Phys. Inst.*, 2018, **45**, 303–307.
- 19 S. P. Morato and F. Luty, *Phys. Rev. B: Condens. Matter Mater. Phys.*, 1980, **22**, 4980–4991.
- 20 L. Schwan, W. Geigle, W. Nagel, R. Bauer and H. Stoll, *J. Phys. Colloq.*, 1980, **41**, C6-408–C6-411.
- 21 V. M. Orera, P. J. Alonso and R. Alcalá, *J. Phys. C: Solid State Phys.*, 1983, **16**, 783–789.
- 22 K. Saeki, Y. Fujimoto, M. Koshimizu, T. Yanagida and K. Asai, *Appl. Phys. Express*, 2016, **9**, 042602.
- 23 S. Lam, C. Gugushev, A. Burger, M. Hackett and S. Motakef, *J. Cryst. Growth*, 2018, **483**, 121–124.
- 24 R. Hawrami, E. Ariesanti, V. Buliga, S. Motakef and A. Burger, *IEEE Trans. Nucl. Sci.*, 2020, **67**, 1020–1026.
- 25 C. Delzer, M. Zhuravleva, L. Stant, C. Melcher, N. Cherepy, S. Payne, R. Sanner and J. P. Hayward, *J. Cryst. Growth*, 2020, **531**, 125336.
- 26 G. Engel, *Z. Kristallogr. – Cryst. Mater.*, 1935, **90**, 341–373.
- 27 H. Kraus, V. B. Mykhaylyk and D. Wahl, *Nucl. Instrum. Methods Phys. Res., Sect. A*, 2005, **553**, 522.
- 28 C. Dujardin, E. Auffray, E. Bourret-Courchesne, P. Dorenbos, P. Lecoq, M. Nikl, A. N. Vasil'ev, A. Yoshikawa and R.-Y. Zhu, *IEEE Trans. Nucl. Sci.*, 2018, **65**, 1977–1997.
- 29 S. Stoll and A. Schweiger, *J. Magn. Reson.*, 2006, **178**, 42.
- 30 NMR Frequency Tables downloaded from [http://kodu.ut.ee/~laurit/AK2/NMR\\_tables\\_Bruker2012.pdf](http://kodu.ut.ee/~laurit/AK2/NMR_tables_Bruker2012.pdf).
- 31 L. H. Piette, R. C. Rempel and H. E. Weaver, *J. Chem. Phys.*, 1959, **30**, 1623.
- 32 S. V. Nistor, M. Stefan and D. Ghica, *J. Therm. Anal. Calorim.*, 2014, **118**, 1021–1031.
- 33 J. Pejchal, M. Buryi, V. Babin, P. Prusa, A. Beitlerova, J. Barta, L. Havlak, K. Kamada, A. Yoshikawa, V. Laguta and M. Nikl, *J. Lumin.*, 2017, **181**, 277–285.
- 34 S. W. S. McKeever, *Thermoluminescence of Solids*, Cambridge University Press, Cambridge, 1985.
- 35 M. Buryi, D. A. Spassky, J. Hybler, V. Laguta and M. Nikl, *Opt. Mater.*, 2015, **47**, 244–250.
- 36 V. B. Mikhailik and H. Kraus, *J. Phys. Stud.*, 2010, **14**, 4201–4206.
- 37 V. B. Mykhaylyk, H. Kraus, V. Kapustianyk, H. J. Kim, P. Mercere, M. Rudko, P. Da Silva, O. Antonyak and M. Dendebera, *Sci. Rep.*, 2020, **10**, 8601.
- 38 M. Moszyński, M. Balcerzyk, W. Czarnacki, A. Nassalski, T. Szczesniak, H. Kraus, V. B. Mikhailik and I. M. Solskii, *Nucl. Instrum. Methods Phys. Res., Sect. A*, 2005, **553**, 578–591.
- 39 Yu. G. Zdesenko, F. T. Avignone III, V. B. Brudanin, F. A. Danevich, S. S. Nagorny, I. M. Solsky and V. I. Tretyak, *Nucl. Instrum. Methods Phys. Res., Sect. A*, 2005, **538**, 657–667.
- 40 B. V. Grinyov, V. D. Ryzhikov, O. T. Sidletskiy, G. M. Onyshchenko, S. N. Galkin, A. I. Ivanov, V. A. Tarasov, O. V. Zelenskaya, D. A. Kurtsev, L. A. Piven and I. M. Zenya, *IEEE Trans. Nucl. Sci.*, 2010, **57**, 1236–1240.
- 41 V. Alenkov, O. A. Buzanov, N. Khanbekov, V. N. Kornoukhov, H. Kraus, V. B. Mikhailik and V. A. Shuvaeva, *J. Instr.*, 2013, **8**, P0600.



Contents lists available at ScienceDirect

## Optical Materials: X

journal homepage: [www.journals.elsevier.com/optical-materials-x](http://www.journals.elsevier.com/optical-materials-x)

Invited Article



## Ultraviolet cross-luminescence in ternary chlorides of alkali and alkaline-earth metals

V. Vaněček<sup>a,b</sup>, J. Páterek<sup>a,b</sup>, R. Král<sup>a</sup>, R. Kučerková<sup>a</sup>, V. Babin<sup>a</sup>, J. Rohlíček<sup>a</sup>, R. Cala<sup>c,d</sup>, N. Kratochvíl<sup>c,e</sup>, E. Auffray<sup>c</sup>, M. Nikl<sup>a,\*</sup><sup>a</sup> FZU, Institute of Physics of the Czech Academy of Sciences, Cukrovarnická 10, Prague, Czech Republic<sup>b</sup> FNSPE, Czech Technical University in Prague, Břehova 7, Prague, Czech Republic<sup>c</sup> CERN, 1211 Geneva 23, Switzerland<sup>d</sup> University of Milano-Bicocca, Piazza dell'Ateneo Nuovo, 1, 20126, Milan, Italy<sup>e</sup> University of Vienna, Universitätsring 1, 1010, Vienna, Austria

## ARTICLE INFO

## Keywords:

Cross-luminescence  
 Auger-free luminescence  
 Core-valence luminescence  
 Alkaline-earth halides  
 Crystal growth  
 Vertical Bridgman method

## ABSTRACT

After the discovery of a cross-luminescence (CL) in BaF<sub>2</sub> in 1982, a large number of CL scintillators were investigated. However, no CL scintillator superior to BaF<sub>2</sub> has been discovered, and the research of CL scintillators has subsided. Recent technological development in medical imaging and high-energy physics created a new demand for ultra-fast scintillators further supported by the development of UV-sensitive semiconductor photodetectors. As a consequence, renewed interest in CL scintillators appeared. To satisfy the requirements of fast timing applications high photo-detection efficiency, e. i. a good spectral match between the scintillator and photodetector must be achieved. Cesium-based ternary chlorides could provide a red-shift (~1.5 eV) of CL towards the sensitive region of the photodetector (PMT or SiPM) while keeping light output and timing characteristics comparable to BaF<sub>2</sub>.

## 1. Introduction

Nowadays ionizing radiation is used in almost all fields of human activity from geology, military, nuclear industry, environment protection, and medicine [1,2] and more and more demand for fast timing properties are requested. Medical imaging is one of the rapidly growing fields. Methods like single-photon emission tomography (SPECT) and positron emission tomography (PET) greatly improved cancer diagnostics and allowed more effective treatment of cancer which is the leading cause of death in modern society. Construction of the time-of-flight positron emission tomography (TOF-PET) scanner is the next important step in the field of medical imaging [3]. The introduction of TOF-PET is mainly motivated by two factors: an increase in signal-to-noise ratio (SNR) and the possibility to determine the position of the annihilation point along the line of response (LOR). Improving the coincidence time resolution (CTR) of the detection system, the ratio of SNR of the PET scanner with TOF and PET scanner without TOF is increasing according to:

$$\frac{SNR_{TOF\ PET}}{SNR_{PET}} = \sqrt{\frac{2 \cdot D}{c \cdot CTR}} \quad (1)$$

where  $D$  is the diameter of the field of view and  $c$  is the speed of light in a vacuum [4,5]. Equation (1) shows that lowering CTR to 100 ps (FWHM) will result in an approximately 8-fold increase in the sensitivity and achieving 10 ps CTR will result in an approximately 25-fold increase in sensitivity of PET scanners. This would allow for a dramatic dose reduction in clinical practice. Moreover, achieving a CTR of 10 ps (FWHM) would allow determining position along LOR with an uncertainty of 1.5 mm [6]. Such spatial resolution is close to an inherent limitation of PET due to the positron mean free path in tissue. However, reaching the 10 ps benchmark is a challenging task and requires significant innovative technological advancements.

A scintillator together with a photodetector and readout electronics constitute the PET detector chain which sets a limit for the timing performance of the detector. Improvement of the scintillator timing characteristics is necessary to achieve CTR well below 100 ps. Several concepts have been developed to either improve conventional scintillators or introduce new scintillators for fast timing applications

\* Corresponding author.

E-mail address: [nikl@fzu.cz](mailto:nikl@fzu.cz) (M. Nikl).<https://doi.org/10.1016/j.omx.2021.100103>

Received 13 July 2021; Received in revised form 6 October 2021; Accepted 7 October 2021

Available online 9 October 2021

2590-1478/© 2021 Published by Elsevier B.V. This is an open access article under the CC BY-NC-ND license (<http://creativecommons.org/licenses/by-nc-nd/4.0/>).

(including PET). Various codoping strategies, direct gap semiconductor nanoscintillators, hot intraband luminescence, Cherenkov radiation [7], and cross-luminescence [8,9] have become of interest [10]. For example, a great improvement of timing characteristics of Pr doped silicates was achieved by codoping and detection of prompt photons [6, 11]. However, the best samples achieved CTR around 100 ps [12] which is still far from the 10 ps desired target. Taking into account the extensive development of the bulk silicate scintillators that led to the materials with such timing characteristics, a further breakthrough is implausible [3]. Hot intraband luminescence (IBL) features very fast decay times estimated to be of the order of 1 ps [13]. However, very low light yields up to 33 ph/MeV [14] and emission in the infrared region severely hinders the application potential of hot IBL. Detection of the prompt Cherenkov photons can be used to improve timing characteristics of conventional scintillators (e. g. YAG, LuAG, LYSO, or BGO) or for the construction of sole Cherenkov radiators. The concept of a sole Cherenkov radiator was first introduced by Ooba et al. [15]. Recently, a CTR of 71 ps was achieved using 5 mm thick PbF<sub>2</sub> crystal [16] and a CTR of 30 ps using 3.2 mm thick black lead glass [17] as a sole Cherenkov radiator. However, those results were obtained using a multichannel plate photomultiplier tube (MCP PMT) resulting in high costs and low detection efficiency. Direct-gap semiconductor nanostructures in the form of quantum dots, rods, and wells can feature very fast intense excitonic luminescence due to the quantum confinement effect. This was demonstrated on a wide variety of materials including ZnO:Ga [18], CsPbBr<sub>3</sub> [19], CdSe/CdS [20]. However, these powder materials suffer from poor light collection due to reabsorption and scattering. Moreover, the low stopping power of semiconductor nanoparticles limits their detection efficiency for 511 keV annihilation photons. This can be possibly solved via composite sampling pixels consisting of a fast nanoscintillator and a high Z<sub>eff</sub> scintillator [21]. However, this technology is at the very early stages of development and reabsorption remains a problem for such nanoscintillators due to their intrinsically small Stokes shift which is inherent to free Wannier exciton luminescence. Cross-luminescence (CL) is a very fast phenomenon that can be exploited for scintillation. It is observed mostly in cesium and barium-based halides. Significant research attention was devoted to CL, mainly in the 1990s [22]. However, most of the work was focused on basic research and no CL scintillator superior to barium fluoride (BaF<sub>2</sub>) was discovered. BaF<sub>2</sub> is currently the only commercially available CL scintillator, but its CL emission within 180–220 nm is not compatible with commonly used alkali metal based photomultiplier tubes (PMTs). Numerical modeling [23,24] in cesium-based ternary chlorides confirms their UV positioned CL reported earlier in experimental works [25–28] better matching the sensitivity of alkali metal based PMTs. In theory, Cs-based cross-luminescence material could produce fast luminescence with sufficient light output for fast timing applications. Moreover, the single crystal form together with the large Stokes shift inherent to CL allows efficient light collection. However, CL materials suffer from low stopping power for high-energy photons due to low effective atomic number (Z<sub>eff</sub>) and densities. Low stopping power results in low sensitivity, because of the requirement for small crystal dimensions in fast timing applications. Therefore, the development of CL scintillators involving heavy elements is necessary for the precise timing detection of high-energy photons. Some of the key material parameters including

density, Z<sub>eff</sub>, attenuation length, and melting point for BaF<sub>2</sub>, CsCaCl<sub>3</sub>, Cs<sub>2</sub>BaCl<sub>4</sub>, and Bi<sub>3</sub>Ge<sub>4</sub>O<sub>12</sub> (BGO) are listed in Table 1. The BGO was added as an example of a classical heavy scintillator.

In this work, we report a study of several novel Cs-based CL halide crystals. All reported crystals were grown by the vertical Bridgman method. Structural, optical, and scintillation properties of prepared crystals were studied using various techniques including X-ray diffraction, radioluminescence, photoluminescence, light yield, and scintillation decay measurements. The application potential is discussed.

## 2. Experimental

All reported crystals were prepared from starting materials of commercially available cesium chloride (CsCl 99.9%, Alfa Aesar), magnesium chloride (MgCl<sub>2</sub>, 99.99% anhydrous, Sigma Aldrich), calcium chloride (CaCl<sub>2</sub>, 99.99% ultradry, Alfa Aesar), strontium chloride (SrCl<sub>2</sub>, 99.99% anhydrous, Sigma Aldrich) and barium chloride (BaCl<sub>2</sub>, 99.99% anhydrous, Sigma Aldrich). All starting chemicals were treated by chlorinating agents according to Refs. [29,30] to remove oxidic anionic impurities. Furthermore, CsCl, MgCl<sub>2</sub>, and CaCl<sub>2</sub> were purified by zone refining [31]. Our setup did not allow zone refining of SrCl<sub>2</sub> and BaCl<sub>2</sub> due to their high melting points. In the case of KCl and RbCl, their high purity as-grown single crystals were used as starting materials. All reported crystals were grown by a single-zone vertical Bridgman method using a micro-pulling-down apparatus. The starting charge (ca. 3–4 g depending on the specific material) was melted in quartz ampoule and subsequently pulled down with a rate of 0.6 mm/h in all performed growth experiments (see Fig. 1). For further details see Vaněček et al. [32]. All procedures consisting of quartz ampoules feeding and valve closure, handling and weighing of all chemicals, and manufacturing of grown crystals was performed in the atmosphere-controlled glovebox (MBraun Labstar) with the content of O<sub>2</sub> and H<sub>2</sub>O below 1 ppm.

For the X-ray powder diffraction (XRPD) analysis, the crystal samples were powdered in alumina mortar and pestle and placed in the Ø 0.5 mm borosilicate-glass capillary in the glovebox. The capillary was sealed with rubber to avoid air contamination. Powder diffraction data were collected using the Debye-Scherrer transmission configuration on the powder diffractometer Empyrean of PANalytical (λ<sub>Cu,Kα</sub> = 1.54184 Å) that was equipped with a focusing mirror, capillary holder, and PIXcel3D detector.

Radioluminescence (RL) spectra measured in the spectral range of 190–800 nm at room temperature were obtained using a custom-made spectrofluorometer 5000 M, Horiba Jobin Yvon. Tungsten-cathode X-ray tube Seifert was used as the excitation source (at 40 kV, 15 mA). The detection part of the set-up consisted of a single grating monochromator and photon-counting detector TBX-04, Horiba IBH Scotland. Measured spectra were corrected for the spectral distortions. A routine spectrally unresolved scintillation decay was measured by means of fast photomultiplier (PMT) R7207-01, Hamamatsu working in the current regime, and Keysight InfiniiVision DSOX6002A digital oscilloscope where the sample was optically coupled directly to the PMT photocathode. Scintillation pulses were excited either by <sup>137</sup>Cs γ-rays (662 keV) or <sup>239</sup>Pu α-particles (5.15 MeV). The pulse-height spectra were collected by hybrid

**Table 1**  
Density, effective atomic number Z<sub>eff</sub>, attenuation length for 511 keV photons l<sub>0</sub>, and melting point T<sub>m</sub> of selected materials.

Chemical formula	Density [g/cm <sup>3</sup> ]	Z <sub>eff</sub> [-]	l <sub>0</sub> (at 511 keV) [mm]	T <sub>m</sub> [°C]
BaF <sub>2</sub>	4.89	51	21	1368
CsCaCl <sub>3</sub>	2.95	42	37	910
Cs <sub>2</sub> BaCl <sub>4</sub>	3.76	49	28	588
Bi <sub>3</sub> Ge <sub>4</sub> O <sub>12</sub>	7.13	71	10	1050

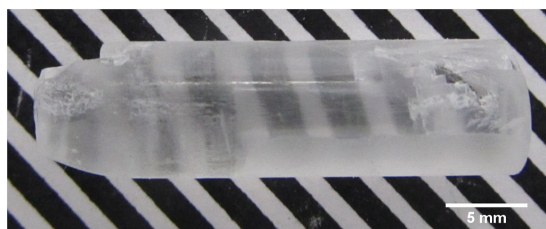


**Fig. 1.** As-grown crystal of CsCaCl<sub>3</sub> prepared by vertical Bridgman method.

photomultiplier DEP PPO 475B, spectroscopy amplifier ORTEC 672 (shaping time set to 1  $\mu$ s), and multichannel analyzer ORTEC 927TM. Scintillation pulses were excited by  $^{137}\text{Cs}$   $\gamma$ -rays (662 keV). The crystals were covered with a thin film of UV/VIS-transparent Fluka immersion oil during all of the conducted measurements to prevent the degradation of the surface due to contact with atmospheric oxygen and moisture. This setup will be labeled “setup no. 1” in the text below.

In the case of the measurements of the fast scintillation decays with high resolution, the samples were excited by picosecond (ps) X-ray tube N5084 from Hamamatsu, operating at 40 kV. The X-ray tube is driven by the ps light pulser equipped with a laser diode operating at 405 nm. The repetition rate can go up to 10 MHz. The adjustable delay generator is triggering the laser pulses and the detector readout. The signal was detected by a hybrid picosecond photon detector HPPD-860 and Fluorohub unit (TCSPC method) from Horiba Scientific. The instrumental response function FWHM of the setup is about 76 ps. Samples are mounted a few centimeters in front of the beryllium window of the X-ray tube with a 45° angle to the incident beam. The luminescence is detected from the same surface by the detector. This setup will be labeled “setup no. 2” in the text below.

The scintillation time distribution of a  $\text{CsCaCl}_3$  sample was measured using a TCSPC setup. A pulse diode laser from PicoQuant is used to excite an X-ray tube from Hamamatsu and produces an X-ray beam which is directed towards the crystal. The light generated by the sample excitation is then detected by a hybrid photomultiplier working in TCSPC mode. The sample under test was placed in such a way that the emitted light is detected from the same surface hit by the X-ray pulse. The instrumental response function of the whole setup is about 180 ps FWHM. The measurement was also repeated placing a 254 nm and a 300 nm optical bandpass filter with 40 nm FWHM in front of the hybrid PMT glass. This setup will be labeled “setup no. 3” in the text below.

The coincidence time resolution of a small  $2 \times 2 \times 3 \text{ mm}^3$   $\text{CsCaCl}_3$  pixel was measured with the setup described in Ref. [33] against a known reference detector. The sample was wrapped in Teflon and Fluka Immersion oil was used between the VUV SiPM ( $3 \times 3 \text{ mm}^2$  active area, Hamamatsu, S13370–3075CN) and crystal to remove the air gap and protect the crystal from air moisture. Only events depositing 511 keV both in the reference detector and the crystal under test were considered [33].

### 3. Results and discussion

#### 3.1. Crystal growth and sample preparation

##### 3.1.1. $(\text{Cs,Rb})\text{MeCl}_3$ ( $\text{Me} = \text{Mg, Ca, Sr}$ )

All as-grown crystals were extracted from the ampoule as a single ingot (See Fig. 1). The crystals were opaque due to the low quality of the surface, but their bulk was clear and transparent. Samples were cut and polished from as-grown crystals into transparent plates of thickness 1.5 mm for further optical evaluation (see Fig. 2).

X-ray powder diffraction measurements showed that  $\text{CsMgCl}_3$  adopts the hexagonal crystal structure (space group  $P6_3/mmc$ , no. 194) isomorphous with  $\text{CsNiCl}_3$  in accordance with literature [23,26,34]. While the  $\text{CsCaCl}_3$  crystallizes in an undistorted simple perovskite structure (space group  $Pm-3m$ , no. 221). The most interesting behavior was observed in the case of  $\text{CsSrCl}_3$ . The diffractogram of  $\text{CsSrCl}_3$

showed a major phase (84 %<sub>w</sub>) with tetragonally distorted perovskite structure (space group  $P_4/mbm$ , no. 127) and a minor phase (16 %<sub>w</sub>) with orthogonally distorted perovskite structure (space group  $Pnma$ , no. 62). This was probably caused by successive phase transitions from cubic to tetragonal and from tetragonal to orthorhombic crystal structure occurring in  $\text{CsSrCl}_3$  upon cooling [35,36] similarly to  $\text{CsPbCl}_3$  [37]. These phase transitions should occur in the temperature region 90–120 °C [36]. Therefore we assume that the used cooling rate did not allow complete phase transformation from tetragonal to orthorhombic phase and the tetragonal phase “frozen” in the  $\text{CsSrCl}_3$  sample. Taking into account that the sample was stored at room temperature for several weeks before the XRPD measurement. A similar phase transition was not observed in  $\text{CsCaCl}_3$  as it occurs below room temperature ( $T = 95 \text{ K}$ ) [38]. X-ray diffraction patterns of  $\text{Cs}_x\text{Rb}_{1-x}\text{CaCl}_3$  ( $x = 0, 0.01, 0.05, 0.5, 1$ ) showed (see Fig. 3) that for low Cs doping i. e. 0, 1, and 5 %<sub>mol</sub> the crystals adopted orthogonally distorted perovskite structure (space group  $Pnma$ , no. 62). However, a sample containing 50 %<sub>mol</sub> of Cs already adopts the same crystal structure as pure  $\text{CsCaCl}_3$  (space group  $Pm-3m$ , no. 221) with reflections positions shifted towards higher angles. The shift is due to the smaller size of  $\text{Rb}^+$  compared to  $\text{Cs}^+$ .

##### 3.1.2. $\text{A}_2\text{BaCl}_4$ ( $\text{A} = \text{K, Rb, Cs}$ )

All three materials from the  $\text{A}_2\text{BaCl}_4$  matrix should, according to the literature [39–41], crystallize in cubic  $\text{Th}_3\text{P}_4$  type crystal structure where  $\text{A}^+$  and  $\text{Ba}^{2+}$  occupy  $\text{Th}^{4+}$  position in stoichiometric ratio 2:1 and  $\text{Cl}^-$  occupies  $\text{P}^{3-}$  position. However, detailed calorimetric studies revealed that these materials crystallize in a slightly off stoichiometric ratio namely  $\text{K}_{2.08}\text{Ba}_{0.96}\text{Cl}_4$  [42] and  $\text{Rb}_{2.07}\text{Ba}_{0.965}\text{Cl}_4$  [43]. Moreover, detailed phase equilibrium diagrams (PED) show the decomposition of the ternary compounds into constituents upon cooling [42]. This was omitted in Ref. [44] where the presence of  $\text{CsCl}$  in the grown crystals is confirmed by XRPD. Our observations support the decomposition of the ternary compound reported in Ref. [42] as crystalline ingots of all three  $\text{A}_2\text{BaCl}_4$  compositions crumbled into powder upon cooling. However, several transparent irregularly shaped grains with dimensions of several mm remained in the ampoule even at room temperature. In the case of  $\text{Rb}_2\text{BaCl}_4$ , a large number of small grains were present in the ingot, which is the reason for the lower optical quality of the prepared sample. Cut and polished plates were prepared from the transparent grains for further optical characterizations (see Fig. 2).

X-ray powder diffraction of  $\text{A}_2\text{BaCl}_4$  samples showed reflections of corresponding phases with cubic  $\text{Th}_3\text{P}_4$  type crystal structure (space group  $I4-3d$ , no. 220). However, each reflection exhibits several satellites which could not be assigned to any record from the PDF4 2021 database. These reflections might be caused by a rhombohedral distortion of the cubic unit cell. Such an effect was proposed as an explanation for additional reflections in diffractograms of  $\text{A}_2\text{BaCl}_4$  and  $\text{A}_2\text{BaBr}_4$  powders [45].

#### 3.2. Scintillation and luminescence characteristics

##### 3.2.1. $(\text{Cs,Rb})\text{MeCl}_3$ ( $\text{Me} = \text{Mg, Ca, Sr}$ )

3.2.1.1. *Scintillation characteristics.* Radioluminescence spectra of  $\text{CsMeCl}_3$  samples are depicted in Fig. 4. The RL spectra show two main features: CL emission in the region 220–310 nm and exciton or defect-

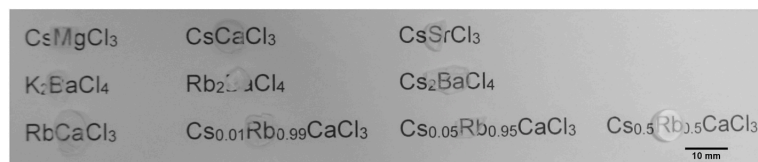
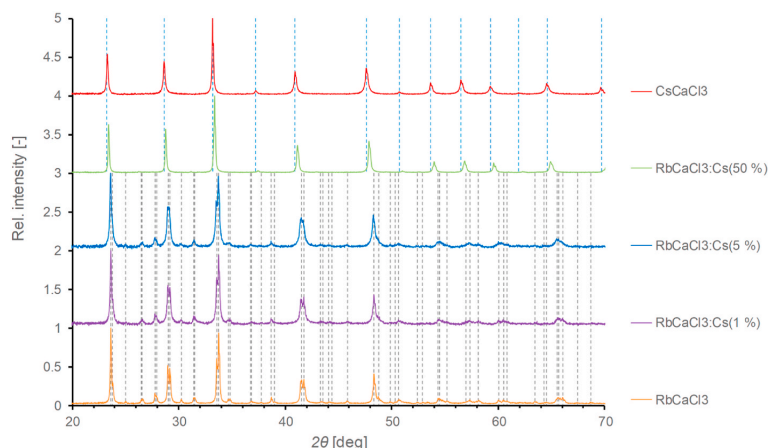
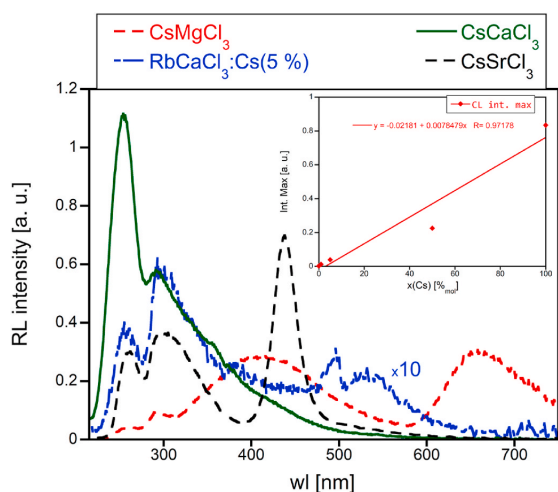


Fig. 2. Cut and polished samples.



**Fig. 3.** Diffraction patterns of  $\text{Cs}_x\text{Rb}_{1-x}\text{CaCl}_3$  ( $x = 0, 0.01, 0.05, 0.5, 1$ ) samples. Gray dashed lines show  $\text{RbCaCl}_3$  (space group  $Pnma$ , no. 62) database record. Blue dashed lines show  $\text{CsCaCl}_3$  (space group  $Pm-3m$ , no. 221) database record. (For interpretation of the references to colour in this figure legend, the reader is referred to the Web version of this article.)



**Fig. 4.** RL spectra of  $(\text{Cs,Rb})\text{MeCl}_3$  ( $\text{Me} = \text{Mg, Ca, Sr}$ ) crystals. The spectrum of  $\text{RbCaCl}_3:\text{Cs}(5\%_{\text{mol}})$  was multiplied by 10 for better clarity. Inset shows the dependence of the intensity of high energy CL band with Cs concentration.

related emission at longer wavelengths. For all  $\text{CsMeCl}_3$  samples, two emissions with maxima around 260 nm and 290 nm can be well observed in the high-energy region. This corroborates with the presumption that the CL in all reported materials originates from the radiative recombination between the hole in the outermost core band consisting of  $5p$  states of  $\text{Cs}^+$  and valence band mainly consisting of  $3p$  states of  $\text{Cl}^-$ . Such presumption is supported by the results of band structure calculations [23,46]. Furthermore, positions of CL emission maxima are in good agreement with values reported in literature for  $\text{CsCaCl}_3$  [25,46–48] and  $\text{CsSrCl}_3$  [26,47,48]. The two-band structure of CL was theoretically predicted via cluster calculation for  $\text{LiBaF}_3$  and  $\text{KMgF}_3$  [47] which have the same coordination sphere (12 anion coordination with  $O_h$  symmetry) of CL active cation. A more complex structure of the CL emission was reported for  $\text{CsMgCl}_3$  [48] which should be the result of the lower symmetry ( $C_3$ ) of the Cs coordination

sphere. However, this was not observed in our study. Most probably due to both low intensity of CL in  $\text{CsMgCl}_3$  and significant overlap with a broad emission band centered at 410. These effects obstruct the resolution of the complex structure of CL emission of  $\text{CsMgCl}_3$ . A similar overlap of the CL emission with excitonic or defect-related emission might be present in the  $\text{CsSrCl}_3$  sample. Such overlap would explain the difference in width of bands centered at 260 nm and 290 nm in  $\text{CsSrCl}_3$ .

Luminescence in the lower-energy part of the RL spectra differs significantly among the  $\text{CsMeCl}_3$  samples. The RL spectrum of  $\text{CsMgCl}_3$  features two broad bands centered at 410 nm and 660 nm. The broad character suggests a defect or excitonic nature of those bands. In the RL spectrum of  $\text{CsCaCl}_3$  no clear emission bands, besides the two ascribed to CL, can be distinguished. However, the long low energy tail of the RL spectrum suggests a contribution of luminescence of different origin that was tentatively ascribed to defect-related emission. In the case of  $\text{CsSrCl}_3$ , one relatively narrow band centered at 440 nm is observed. A very similar band was reported by Takahashi et al. in mixed crystals  $\text{Cs}_{1-x}\text{Rb}_x\text{CaCl}_3$  [49] and  $\text{CsCa}_{1-x}\text{Mg}_x\text{Cl}_3$  [50] and it was ascribed to self-trapped excitons (STE) luminescence in  $\text{CsCaCl}_3$ . However, this is in contradiction with our observation of this band in  $\text{CsSrCl}_3$ .

CL can be induced by Cs doping in CL-free alkali halides. The cesium impurity creates core levels below the valence band which meets the energy conditions for CL. The so-called impurity-induced CL is investigated in several binary [51–53] and ternary halides [46]. To investigate impurity-induced CL and to assess its potential for fast timing applications a series of  $\text{Cs}_x\text{Rb}_{1-x}\text{CaCl}_3$  crystals were studied. Radio-luminescence spectra of two samples ( $x = 0.05$  and 1) from the  $\text{Cs}_x\text{Rb}_{1-x}\text{CaCl}_3$  series are presented in Fig. 4. The values in the spectrum for sample  $\text{RbCaCl}_3:\text{Cs}(5\%_{\text{mol}})$  are multiplied by 10 for better clarity. All Cs containing  $\text{Cs}_x\text{Rb}_{1-x}\text{CaCl}_3$  samples feature emissions centered at 260 nm and 290 nm which we ascribe to CL. The intensity of the CL emission increases monotonically with increasing Cs concentration. The difference in the intensity ratio of 260 nm and 290 nm emission among  $\text{Cs}_x\text{Rb}_{1-x}\text{CaCl}_3$  samples is most probably due to the overlap of low energy CL emission (at 290 nm) with emission of different nature. Such emissions have most probably a different, if any, dependence of emission intensity on Cs content. Therefore, the intensity of the high energy emission (at 260 nm), which should be only very slightly perturbed, was used to examine the influence of Cs content on the intensity of CL in  $\text{Cs}_x\text{Rb}_{1-x}\text{CaCl}_3$ . The dependence of the intensity of the high energy CL emission (at 260 nm) with Cs concentration appears to be reasonably well fitted ( $R^2 = 0.944$ ) with linear dependence (see inset of Fig. 4). The



linear dependence of LY of fast emission on Cs concentration in  $\text{Cs}_x\text{Rb}_{1-x}\text{CaCl}_3$  was reported by Takahashi et al. [49]. However, the number of experimental points and their distribution within the examined concentration range in this study is not sufficient to make clear conclusions. The difference in RL intensity in the region approximately 320–540 nm is most probably due to defect-related luminescence. This assumption is based on the observation that RL intensity in this region is strongly dependent on the crystal quality. The RL spectra of the Cs free sample features only very weak (approx. 100 times less intense than BGO standard) overlying unresolved bands.

Scintillation decay profiles measured with setup no. 1 (see Fig. 5a) of all  $\text{CsMeCl}_3$  samples can be well fitted by the convolution of the IRF with two exponential components. In the short time window (150 ns) a majority of the scintillation light (>99%) is emitted with decay times around 2 ns, which we ascribe to CL. However, increased background points toward the presence of slow components which were not resolved in the fast time window. Such slow components could be related to excitonic or defect emissions. A higher concentration of defects is to be expected for newly developed materials. Optimization of the crystal growth should result in the suppression of such defects. The contribution of slow components in  $\text{CsMeCl}_3$  crystals was studied in a long time window (1500 ns) under excitation with  $\alpha$  radiation of  $^{239}\text{Pu}$ . Since alpha radiation does not effectively excite CL [54,55] it is convenient for the study of the kinetics of slow scintillation components in CL scintillators. All three  $\text{CsMeCl}_3$  show very similar scintillation kinetics under  $\alpha$  irradiation. The majority (>97%) of the scintillation light is emitted with decay times around 40 ns. While the rest of the scintillation light is emitted with decay times from 200 to 400 ns. Parameters of the fit together with light yields of the  $\text{CsMeCl}_3$  samples are summarized in Table 2.

Fast scintillation decay kinetics of  $\text{Cs}_{1-x}\text{Rb}_x\text{CaCl}_3$  samples were studied using pico X-ray apparatus (setup no. 2). Fig. 5b depicts decay curves of samples containing 1, 5, and 100 %mol of Cs measured in the short time window (30 ns) together with mean decay times calculated from 2 exponential fitting of the decay curves. Acceleration of the scintillation decay with decreasing Cs content can be clearly seen. This effect could be explained by competition of CL and Auger recombination for the holes in the conduction band. However, this acceleration of scintillation decay is connected with a decrease in the intensity of CL emission.

From preliminary results,  $\text{CsCaCl}_3$  emerged as the best candidate from materials in this study. Therefore, more detailed measurements were carried out to assess the potential of this material for fast timing applications. These involved measurements of fast scintillation decay

(setup no. 3) and CTR. Fig. 6 depicts fast spectrally unresolved scintillation decays of  $\text{CsCaCl}_3$ . The decay curve is well fitted with the convolution of IRF and two exponential functions. First very fast component with a decay time of 151 ps and the second slower component with a decay time of 2.212 ns accounting for 6.47% and 93.53% of the scintillation light respectively. Moreover, one exponential component was used in the deconvolution to account for the scintillation rise time. The measured rise time was not resolvable within the resolution of the system and is most likely in the range of 0–50 ps.

Spectrally resolved scintillation decay curves were measured (setup no. 3) to further investigate scintillation kinetics in  $\text{CsCaCl}_3$ . Bandpass filters with center wavelengths (CWL) at  $254 \pm 20$  and  $300 \pm 20$  nm were used to separate the two emission bands (See Fig. 7). Scintillation decay curve measured with 250 nm CWL shows a single exponential decay of 2.158 ns. This value is in good agreement with the slower component in spectrally unresolved measurement. On the other hand, scintillation decay curve measured with 300 nm, CWL shows two exponential decay with values close to those for spectrally unresolved measurement ( $t_{d1} = 266$  ps,  $t_{d2} = 2.144$  ns). Therefore, we ascribe the  $\sim 2$  ns component to CL in  $\text{CsCaCl}_3$  and the  $\sim 200$  ps component to a heavily quenched excitonic or defect-related emission.

Measurements of the CTR were challenging due to the hygroscopic nature of  $\text{CsCaCl}_3$ , for which the test bench was not designed. The transparency of employed oil was very low (below 280 nm) and only light above 280 nm was able to fully reach the SiPM, resulting in a significant light loss. Nevertheless, even with such unoptimized conditions, the measured CTR of  $\text{CsCaCl}_3$  was  $148 \pm 12$  ps FWHM, compared to  $164 \pm 12$  ps obtained with  $\text{BaF}_2$  measured under the same conditions of optical coupling and SiPM (though the emission of  $\text{BaF}_2$  is deeper in the UV, suffering more from the coupling agent). Based on the measured scintillation properties of  $\text{CsCaCl}_3$  and the first CTR measurements presented in this study, the expected timing performance should be similar to the one of  $\text{BaF}_2$ . With optimal conditions of wrapping, optical coupling, and SiPM (better PDE) a CTR close to 50 ps may be expected as obtained in  $\text{BaF}_2$  [9].

**3.2.1.2. Photoluminescence characteristics.** The PL spectroscopy of  $\text{CsMgCl}_3$  revealed the emission observed in the RL spectrum centered at 410 nm originates from at least two separate centers with their maxima at 356 and 460 nm and the corresponding excitation bands centered at 266 and 286 nm, respectively, see Fig. 8a. The decay kinetics of the center at 356 nm consists of a fast component with 1.2 and 5.6 ns decay times and another component with 234 ns decay time, while the decay of the center with emission at 460 nm has two components with 21 and 51

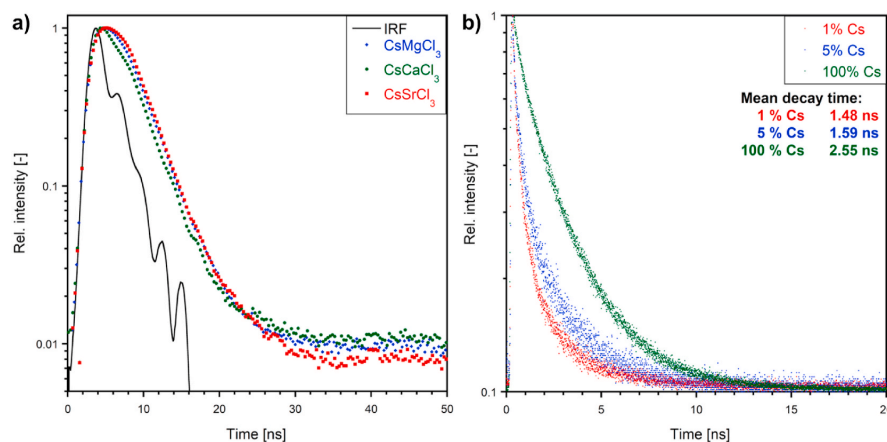
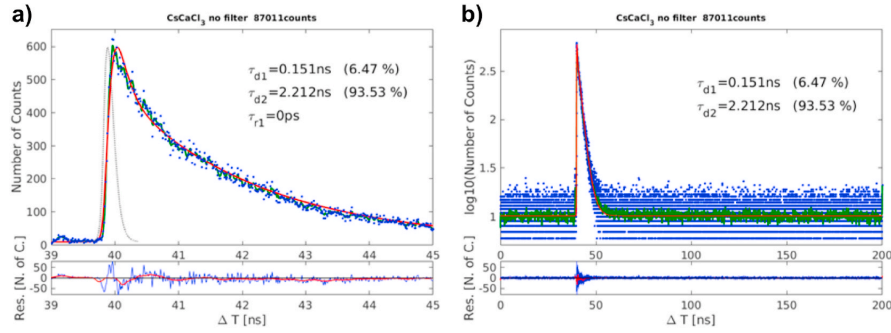


Fig. 5. Scintillation decay curves of a)  $\text{CsMeCl}_3$  samples (setup no. 1) and b) fast scintillation decay curves of  $\text{Cs}_{1-x}\text{Rb}_x\text{CaCl}_3$  samples (setup no. 2).

**Table 2**  
Scintillation decay times  $T_i$  and relative abundance  $P_i$  of the  $i$ -th component of scintillation decay profile together with light yield for all presented materials.

Excitation source:	$^{137}\text{Cs}$					$^{239}\text{Pu}$					
	Ly [ph/MeV]	$T_1$ [ns]	$P_1$ [%]	$T_2$ [ns]	$P_2$ [%]	$T_1$ [ns]	$P_1$ [%]	$T_2$ [ $\mu\text{s}$ ]	$P_2$ [%]	$T_3$ [ $\mu\text{s}$ ]	$P_3$ [%]
CsMgCl <sub>3</sub>	1113	2.36	99.7	178	0.3	43.4	97.3	0.402	2.7	x	x
CsCaCl <sub>3</sub>	1371	2.47	99.8	72.7	0.2	34.6	97.9	0.242	2.1	x	x
CsSrCl <sub>3</sub>	889	2.07	99.6	230	0.4	37.3	97.5	0.235	2.5	x	x
K <sub>2</sub> BaCl <sub>4</sub>	817	x	x	x	x	76	95.2	2.04	4.4	30.0	0.4
Rb <sub>2</sub> BaCl <sub>4</sub>	1181	x	x	x	x	52.9	90.6	2.83	9.0	29.9	0.4
Cs <sub>2</sub> BaCl <sub>4</sub>	1369	1.68	99.3	140	0.7	50.9	96.7	2.20	2.8	27.4	0.5
BGO (ref.)	7311										



**Fig. 6.** Fast spectrally unresolved scintillation decays of CsCaCl<sub>3</sub> measured in a) short and b) long time window (setup no. 3).

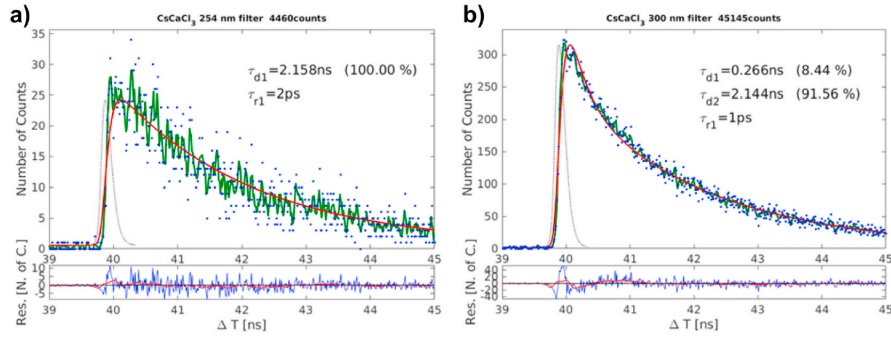


**Fig. 7.** Fast scintillation decays of CsCaCl<sub>3</sub> measured with a) 254 nm and b) 300 nm bandpass filters respectively (setup no. 3).

$\mu\text{s}$  lifetimes, see Fig. 9. A complex structure of excitation bands can be seen below 250 nm. Excitation in this range leads to complex emission ranging from 250 to 650 nm. A similar emission structure can be seen under excitation below 250 nm either in the case of CsCaCl<sub>3</sub> and CsSrCl<sub>3</sub>. In both cases, multiple emission bands span over the range 250–650 nm, and the spectra are dominated by the band with the maxima at 300 nm matching the emission observed in RL spectra. The spectra are not shown here for clarity. No other excitation bands were observed in CsCaCl<sub>3</sub> PL excitation spectra. The PL excitation spectrum of CaSrCl<sub>3</sub> with the emission set to the maximum of the narrow band at 434 nm seen in the RL spectrum reveals a pair of excitation bands with the maxima at 340 and 375 nm, see Fig. 8b. The decay kinetics measured with the emission fixed at 434 nm and excitation at 340 and 375 nm are dominated by 1.6 and 2.1  $\mu\text{s}$  components, respectively. A slower component with a lifetime of about 6  $\mu\text{s}$  is present in both cases.

### 3.2.2. $A_2\text{BaCl}_4$ ( $A = \text{K}, \text{Rb}, \text{Cs}$ )

**3.2.2.1. Scintillation characteristics.** Fig. 10 depicts normalized RL spectra of the  $A_2\text{BaCl}_4$  ( $A = \text{K}, \text{Rb}, \text{Cs}$ ) samples. The inset of Fig. 10 shows the spectral dependence of the integral of RL intensity. All  $A_2\text{BaCl}_4$  samples feature a very similar broad band centered at approx. 400 nm. The low energy side of this band shows a slight red-shift with an increasing atomic number of the  $A^+$  kation. This suggests a similar nature of the emission center in all  $A_2\text{BaCl}_4$  materials. Based on the position and width of this band we tentatively ascribe it to trapped excitons (TE). Furthermore, the Cs<sub>2</sub>BaCl<sub>4</sub> sample features two bands centered at 260 nm and 290 nm respectively. The position of these bands is in good agreement with CL bands in CsMeCl<sub>3</sub> samples. This again corroborates with the presumption that CL in Cs<sub>2</sub>BaCl<sub>4</sub> and CsMeCl<sub>3</sub> originates from the radiative recombination between the hole in the 5p state of Cs<sup>+</sup> and the electron in the 3p states of Cl<sup>-</sup>. The difference in the intensity ratio of 260 nm and 290 nm emissions in CsCaCl<sub>3</sub> and Cs<sub>2</sub>BaCl<sub>4</sub> is caused by the overlap of CL and TE emissions in Cs<sub>2</sub>BaCl<sub>4</sub>. The fact that we do not

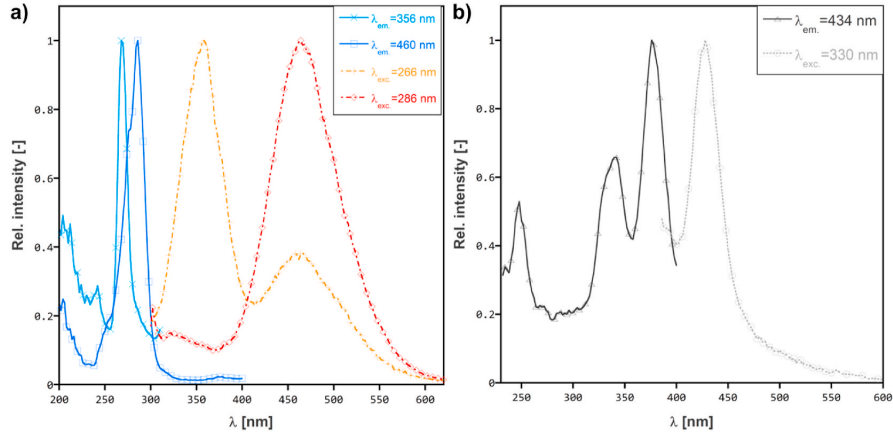


Fig. 8. Normalized PL and PL excitation spectra of a) CsMgCl<sub>3</sub> and b) CsSrCl<sub>3</sub> crystals.

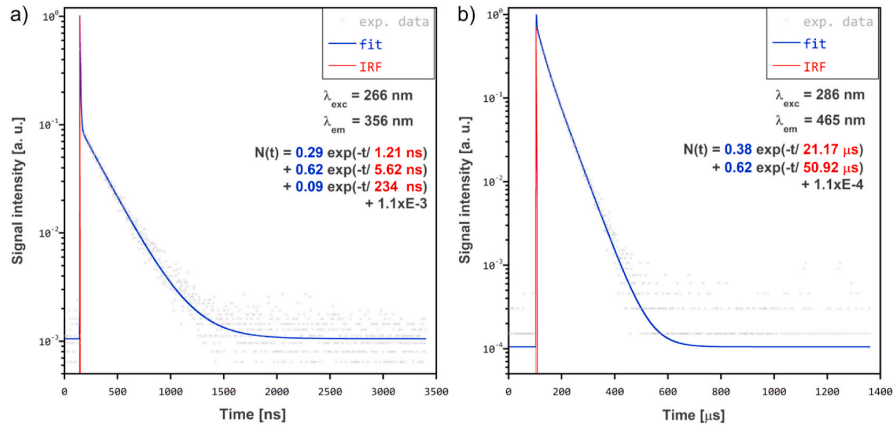


Fig. 9. PL decay curves of CsMgCl<sub>3</sub> excited with a) nanoLED and b) pulse Xe lamp.

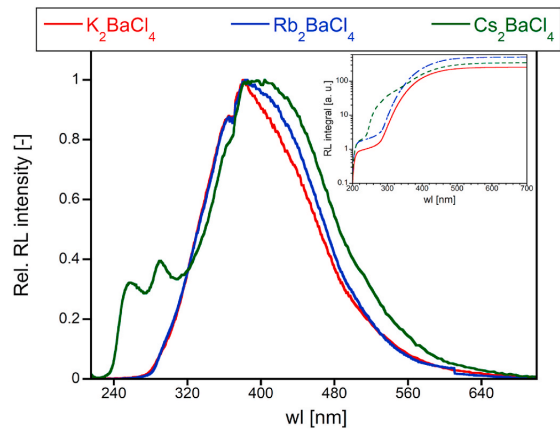
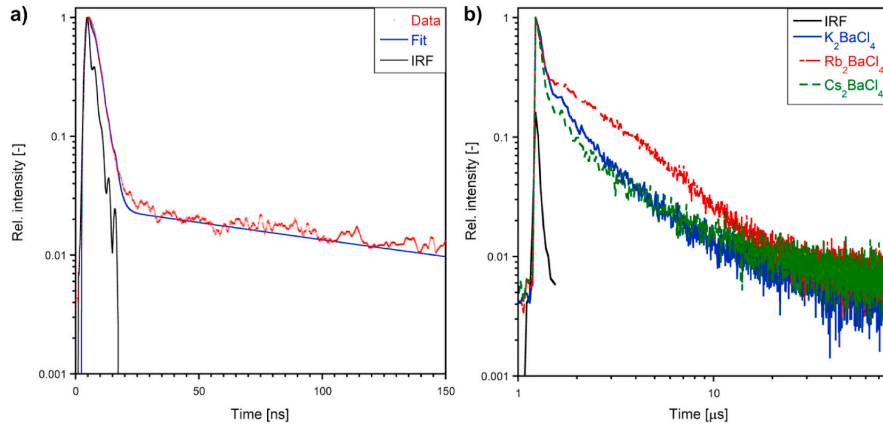


Fig. 10. Normalized RL spectra of A<sub>2</sub>BaCl<sub>4</sub> crystals. The inset shows the spectral dependence of the integral of RL intensity.

observe CL emission in K<sub>2</sub>BaCl<sub>4</sub> and Rb<sub>2</sub>BaCl<sub>4</sub> is in agreement with the results reported in the literature. On one hand, K<sub>2</sub>BaCl<sub>4</sub> is not expected to exhibit CL since KCl does not satisfy the CL condition [47] i. e. the band gap is smaller than the energy difference between the uppermost core band and bottom of the valence band. On the other hand, the Rb<sub>2</sub>BaCl<sub>4</sub> might satisfy the CL condition since it is satisfied in RbCl at low temperatures [47]. However, the CL in RbCl was observed only with very low intensity [56] due to significant self-absorption. Moreover, the CL emission in RbCl is reported at 190 nm which is at the very limit of our detection system. Both these facts prohibit the observation of CL in Rb<sub>2</sub>BaCl<sub>4</sub> in our conditions.

Measurements of scintillation decay kinetics of the A<sub>2</sub>BaCl<sub>4</sub> samples using setup no. 1 showed that only Cs<sub>2</sub>BaCl<sub>4</sub> exhibits fast ~ ns emission. This corroborates with observations from steady-state measurements above. Fig. 11a depicts the scintillation decay curve of the Cs<sub>2</sub>BaCl<sub>4</sub> sample together with two exponential fit (convolution with IRF) and IRF. The timing characteristics are similar to CsMeCl<sub>3</sub> with the majority (>99%) of the scintillation light emitted with 1.68 ns day time. This supports the ascription of 250 nm and 290 nm bands in the RL spectrum of Cs<sub>2</sub>BaCl<sub>4</sub> to CL. The slow components of the scintillation decay were examined with α excitation in the long time window (80 μs). Scintillation decay curves of all three A<sub>2</sub>BaCl<sub>4</sub> samples (see Fig. 11b) were well



**Fig. 11.** Scintillation decay curves of a) Cs<sub>2</sub>BaCl<sub>4</sub> excited with <sup>137</sup>Cs measured in the short time window and b) all three A<sub>2</sub>BaCl<sub>4</sub> samples excited with <sup>239</sup>Pu measured in the long time window.

fitted with three exponential components with similar decay times (see Tab 2). Short component with decay times 50–70 ns accounting for most of the scintillation light (>90%) and two slower components in the microsecond range with decays around 2.5 and 30 μs (See Table 2 for details). Increased contribution of the 2.83 μs component in Rb<sub>2</sub>BaCl<sub>4</sub> could be caused by a higher concentration of the corresponding defect due to lower crystal quality compared to K<sub>2</sub>BaCl<sub>4</sub> and Cs<sub>2</sub>BaCl<sub>4</sub>.

**3.2.2.2. Photoluminescence characteristics.** The PL spectroscopy of A<sub>2</sub>BaCl<sub>4</sub> samples reveals the complex structure of emission centers of these materials. Fig. 12a shows the PL excitation spectra of all examined A<sub>2</sub>BaCl<sub>4</sub> samples measured with the emission wavelength fixed around the maxima of their RL spectra. A dominant excitation band centered at 245–250 nm is present in all samples, as well as a set of excitation bands above 260 nm. The complexity of the PL excitation spectra suggests the presence of multiple emission centers or an emission center with multiple configurations. Fig. 12b shows the PL spectra of the A<sub>2</sub>BaCl<sub>4</sub> measured with excitation wavelength at about 250 nm. All the materials show a wide emission composed of multiple bands. The complexity of excited states is supported also by the measurement of PL decay kinetics. The PL decay kinetics of Cs<sub>2</sub>BaCl<sub>4</sub> measured under excitation at about 250 nm and emission at 350 (360) nm in nanosecond and microsecond

range are shown in Fig. 13. One can see the kinetics of the emission center is composed of several components with lifetimes ranging from 3 ns up to 18 μs. Analogous results were observed for K<sub>2</sub>BaCl<sub>4</sub>. In all of the examined materials, decay times were in the order of tens of microseconds for emission centers in the low-energy part of the spectra (above 400 nm).

#### 4. Conclusions

Scintillation properties of perspective CL scintillators from CsMeCl<sub>3</sub> and A<sub>2</sub>BaCl<sub>4</sub> families were investigated. All Cs containing samples exhibited two UV bands peaking at 260 nm and 290 nm with ns decay times which were ascribed to CL originating from the radiative recombination between the hole in the 5p state of Cs<sup>+</sup> and the electron in the 3p states of Cl<sup>-</sup>. However, emission bands at longer wavelengths were present in all examined materials. Our results suggest that the emission bands at longer wavelengths originate from defects or excitonic effects. A high concentration of defects is expected for newly developed materials. However, optimization of technological processes (e. g. purification of starting materials, crystal growth, sample preparation, etc.) should result in suppression of such unwanted effects.

Impurity-induced CL was observed in RbCaCl<sub>3</sub> upon Cs doping (Cs<sub>1</sub>-

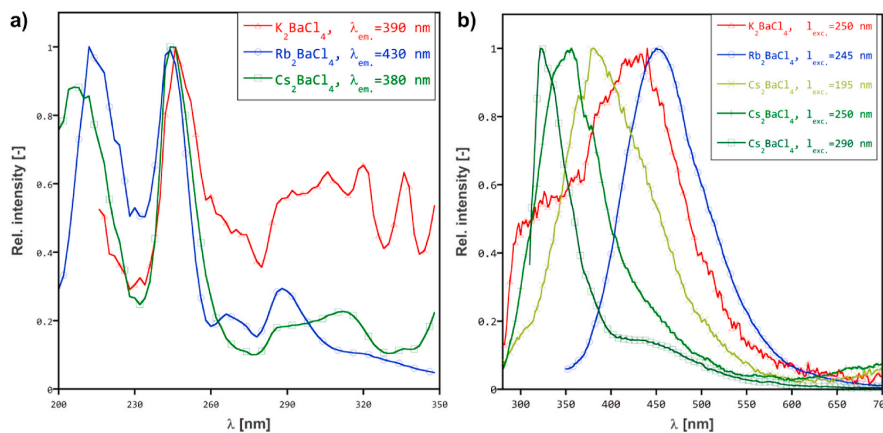


**Fig. 12.** Normalized a) PL excitation and b) PL spectra of A<sub>2</sub>BaCl<sub>4</sub> crystals.

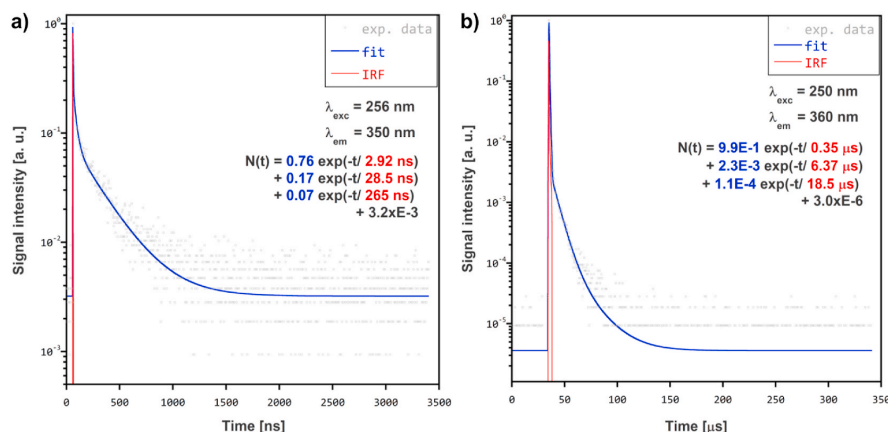


Fig. 13. PL decay curves of  $\text{Cs}_2\text{BaCl}_4$  excited with a) nanoLED and b) pulse Xe lamp.

$x\text{Rb}_x\text{CaCl}_3$ ). We observed acceleration of the scintillation decay with decreasing Cs content. However, this acceleration is connected with a decrease in the intensity of CL. The intensity of the high-energy CL band decreases linearly with decreasing Cs concentration. Based on the reported results we suggest that this behavior is due to competition of Auger recombination (dominant in pure  $\text{RbCaCl}_3$ ) and CL (dominant in  $\text{CsCaCl}_3$ ) for the holes in the core band. This effect might be a perspective for achieving better CTR if the acceleration of scintillation decay kinetics would result in higher initial photon density despite the decrease in intensity due to Auger recombination.

From the preliminary results, the  $\text{CsCaCl}_3$  emerged as the most promising candidate. The best measured samples featured scintillation decay with a mean decay time of 2.55 ns without a presence of slow and components LY close to 1400 ph/MeV. These results demonstrate the possibility of developing CL with properties comparable to  $\text{BaF}_2$  and a better spectral match with the photodetector.

Further research should focus on the suppression of defects via optimization of the technological process of the prospective candidates and exploration of Cs based CL materials containing heavier elements. Such an effort could result in a Cs based CL scintillator that meets requirements for both high CTR and stopping power.

#### Author contribution statement

V. Vaněček: Conceptualization, Methodology, Writing - Original Draft, Investigation, Formal analysis, Visualization.

J. Paterek: Investigation, Formal analysis, Visualization, Writing - Review & Editing.

R. Kral: Conceptualization, Methodology, Investigation, Formal analysis, Writing - Review & Editing, Supervision.

R. Kučerková: Investigation, Formal analysis, Visualization.

V. Babin: Investigation, Formal analysis, Visualization.

J. Rohlíček: Investigation, Formal analysis, Visualization.

R. Čalá: Investigation, Formal analysis, Visualization, Writing - Review & Editing.

N. Kratochvíl: Investigation, Formal analysis, Visualization, Writing - Review & Editing.

E. Auffray: Conceptualization, Supervision, Writing - Review & Editing, Project administration.

M. Nikl: Conceptualization, Writing - Review & Editing, Supervision, Project administration, Funding acquisition.

#### Declaration of competing interest

The authors declare that they have no known competing financial interests or personal relationships that could have appeared to influence the work reported in this paper.

#### Acknowledgment

This project was carried out in the framework of the Crystal Clear Collaboration. Support of project No. SOLID21 CZ.02.1.01/0.0/0.0/16\_019/0000760) of the Operational Programme Research, Development and Education financed by European Structural and Investment Funds and the Czech Ministry of Education, Youth and Sports is gratefully acknowledged. The authors thank A. Bystrický and A. Čihlar for starting materials purification and preparation of growth ampoules.

#### References

- [1] M. Nikl, Scintillation detectors for x-rays, *Meas. Sci. Technol.* 17 (2006), <https://doi.org/10.1088/0957-0233/17/4/R01>. R37–R54.
- [2] M. Nikl, A. Yoshikawa, Recent R&D trends in inorganic single-crystal scintillator materials for radiation detection, *Advanced Optical Materials* 3 (2015) 463–481, <https://doi.org/10.1002/adom.201400571>.
- [3] P. Lecoq, C. Morel, J.O. Prior, D. Visvikis, S. Gundacker, E. Auffray, P. Krizán, R. M. Turtos, D. Thers, E. Charbon, J. Varela, C. de La Taille, A. Rivetti, D. Breton, J.-F. Pratte, J. Nuyts, S. Surti, S. Vandenberghe, P. Marsden, K. Parodi, J.M. Benloch, M. Benoit, Roadmap toward the 10 ps time-of-flight PET challenge, *Phys. Med. Biol.* 65 (2020) 21RM01, <https://doi.org/10.1088/1361-6560/ab9500>.
- [4] W.W. Moses, Time of flight in PET revisited, *IEEE Trans. Nucl. Sci.* 50 (2003) 1325–1330, <https://doi.org/10.1109/TNS.2003.817319>.
- [5] M. Conti, Focus on time-of-flight PET: the benefits of improved time resolution, *Eur. J. Nucl. Med. Mol. Imag.* 38 (2011) 1147–1157, <https://doi.org/10.1007/s00259-010-1711-y>.
- [6] S. Gundacker, R.M. Turtos, E. Auffray, P. Lecoq, Precise rise and decay time measurements of inorganic scintillators by means of X-ray and 511 keV excitation, *Nucl. Instrum. Methods Phys. Res. Sect. A Accel. Spectrom. Detect. Assoc. Equip.* 891 (2018) 42–52, <https://doi.org/10.1016/j.nima.2018.02.074>.
- [7] N. Kratochvíl, S. Gundacker, P. Lecoq, E. Auffray, Pushing Cherenkov PET with BGO via coincidence time resolution classification and correction, *Phys. Med. Biol.* 65 (2020) 115004, <https://doi.org/10.1088/1361-6560/ab87f9>.
- [8] R.H. Pots, E. Auffray, S. Gundacker, Exploiting cross-luminescence in  $\text{BaF}_2$  for ultrafast timing applications using deep-ultraviolet sensitive HPK silicon photomultipliers, *Front. Physiol.* 8 (2020), <https://doi.org/10.3389/fphys.2020.592875>.
- [9] S. Gundacker, R.H. Pots, A. Nepomnyashchikh, E. Radzhabov, R. Shendrik, S. Omelkov, M. Kirm, F. Acerbi, M. Capasso, G. Paternoster, A. Mazzi, A. Gola, J. Chen, E. Auffray, Vacuum ultraviolet silicon photomultipliers applied to  $\text{BaF}_2$  cross-luminescence detection for high-rate ultrafast timing applications, *Phys. Med. Biol.* 66 (2021) 114002, <https://doi.org/10.1088/1361-6560/abf476>.
- [10] C. Dujardin, E. Auffray, E. Bourret-Courchesne, P. Dorenbos, P. Lecoq, M. Nikl, A. N. Vasil'ev, A. Yoshikawa, R.-Y. Zhu, Needs, trends, and advances in inorganic scintillators, *IEEE Trans. Nucl. Sci.* 65 (2018) 1977–1997, <https://doi.org/10.1109/TNS.2018.2840160>.

- [11] S. Gundacker, E. Auffray, K. Pauwels, P. Lecoq, Measurement of intrinsic rise times for various L(Y)SO and LuAG scintillators with a general study of prompt photons to achieve 10 ps in TOF-PET, *Phys. Med. Biol.* 61 (2016) 2802–2837, <https://doi.org/10.1088/0031-9155/61/7/2802>.
- [12] S. Gundacker, R.M. Turtos, E. Auffray, M. Paganoni, P. Lecoq, High-frequency SIPM readout advances measured coincidence time resolution limits in TOF-PET, *Phys. Med. Biol.* 64 (2019), 055012, <https://doi.org/10.1088/1361-6560/aaf452>, <https://www.zotero.org/google-docs/WFuNOs>.
- [13] S.I. Omelkov, V. Nagirnyi, A.N. Vasil'ev, M. Kirm, New features of hot intraband luminescence for fast timing, *J. Lumin.* 176 (2016) 309–317, <https://doi.org/10.1016/j.jlumin.2016.03.039>.
- [14] S.I. Omelkov, V. Nagirnyi, S. Gundacker, D.A. Spassky, E. Auffray, P. Lecoq, M. Kirm, Scintillation yield of hot intraband luminescence, *J. Lumin.* 198 (2018) 260–271, <https://doi.org/10.1016/j.jlumin.2018.02.027>.
- [15] T. Ooba, T. Fukushima, H. Kawai, M. Konishi, H. Nakayama, M. Tabata, I. Adachi, S. Nishida, H. Kishimoto, H. Yokogawa, Proposal of Cherenkov TOPPET with silica aerogel, in: IEEE Symposium Conference Record Nuclear Science 2004, vol. 6, 2004, pp. 3781–3784, <https://doi.org/10.1109/NSSMIC.2004.1466703>.
- [16] R. Ota, K. Nakajima, T. Hasegawa, I. Ogawa, Y. Tamagawa, Timing-performance evaluation of Cherenkov-based radiation detectors, *Nucl. Instrum. Methods Phys. Res. Sect. A Accel. Spectrom. Detect. Assoc. Equip.* 923 (2019) 1–4, <https://doi.org/10.1016/j.nima.2019.01.034>.
- [17] R. Ota, K. Nakajima, I. Ogawa, Y. Tamagawa, H. Shimoi, M. Suyama, T. Hasegawa, Coincidence time resolution of 30xspace0.167Temps FWHM using a pair of Cherenkov-radiator-integrated MCP-PMTs, *Phys. Med. Biol.* 64 (2019), 07LT01, <https://doi.org/10.1088/1361-6560/ab0f0e>.
- [18] L. Procházková, V. Vaněček, V. Čuba, R. Pjatkan, R. Martínez-Turtos, I. Jakubec, M. Buryl, S. Omelkov, E. Auffray, P. Lecoq, E. Mihoková, M. Nikl, Core-shell ZnO:Ga-SiO<sub>2</sub> nanocrystals: limiting particle agglomeration and increasing luminescence via surface defect passivation, *RSC Adv.* 9 (2019) 28946–28952, <https://doi.org/10.1039/C9RA04421C>.
- [19] K. Tomanová, V. Čuba, M.G. Brik, E. Mihoková, R. Martínez Turtos, P. Lecoq, E. Auffray, M. Nikl, On the structure, synthesis, and characterization of ultrafast blue-emitting CsPbBr<sub>3</sub> nanoplatelets, *Appl. Mater.* 7 (2019), 011104, <https://doi.org/10.1063/1.5079300>.
- [20] M.D. Tessier, P. Spinicelli, D. Dupont, G. Patriarche, S. Ithurria, B. Dubertret, Efficient exciton concentrators built from colloidal core/Crown CdSe/Cds semiconductor nanoplatelets, *Nano Lett.* 14 (2014) 207–213, <https://doi.org/10.1021/nl403746p>.
- [21] R.M. Turtos, S. Gundacker, E. Auffray, P. Lecoq, Towards a metamaterial approach for fast timing in PET: experimental proof-of-concept, *Phys. Med. Biol.* 64 (2019) 185018, <https://doi.org/10.1088/1361-6560/ab18b3>.
- [22] P.A. Rodnyi, Core-valence luminescence in scintillators, *Radiat. Meas.* 38 (2004) 343–352, <https://doi.org/10.1016/j.radmeas.2003.11.003>.
- [23] G. Shwetha, V. Kanchana, G. Vaitheeswaran, CsMgCl<sub>3</sub>: a promising cross luminescence material, *J. Solid State Chem.* 227 (2015) 110–116, <https://doi.org/10.1016/j.jssc.2015.03.024>.
- [24] G. Shwetha, V. Kanchana, Impurity induced cross luminescence in KMgCl<sub>3</sub>: an ab initio study, *J. Phys. Condens. Matter* 31 (2019) 115501, <https://doi.org/10.1088/1361-648X/aaf00a>.
- [25] E. Melchakov, P. Rodnyi, B. Rybakov, A. Smakov, M. Terekhin, Radiative core-valence transitions in CsCl and CsCaCl<sub>3</sub>, *Fiz. Tverd. Tela* 31 (1989) 276–278.
- [26] M.A. Macdonald, E.N. Mel'chakov, I.H. Munro, P.A. Rodnyi, A.S. Voloshinovskiy, Radiative core-valence transitions in CsMgCl<sub>3</sub> and CsSrCl<sub>3</sub>, *J. Lumin.* 65 (1995) 19–23, [https://doi.org/10.1016/0022-2313\(95\)00051-Q](https://doi.org/10.1016/0022-2313(95)00051-Q).
- [27] K. Takahashi, M. Arai, M. Koshimizu, Y. Fujimoto, T. Yanagida, K. Asai, Luminescence and scintillation properties of Cs<sub>2</sub>ZnCl<sub>4</sub> and Cs<sub>3</sub>ZnCl<sub>5</sub>, *Jpn. J. Appl. Phys.* 59 (2020), 072002, <https://doi.org/10.35848/1347-4065/ab9655>.
- [28] K. Sugawara, M. Koshimizu, T. Yanagida, Y. Fujimoto, R. Haruki, F. Nishikido, S. Kishimoto, K. Asai, Luminescence and scintillation properties of Ce-doped Cs<sub>2</sub>ZnCl<sub>4</sub> crystals, *Opt. Mater.* 41 (2014), <https://doi.org/10.1016/j.optmat.2014.10.053>.
- [29] K. Nitsch, A. Čihlář, Z. Málková, M. Rodová, M. Vaněček, The purification and preparation of high-purity PbCl<sub>2</sub> and ternary alkali lead chloride single crystals, *J. Cryst. Growth* 131 (1993) 612–615, [https://doi.org/10.1016/0022-0248\(93\)90214-H](https://doi.org/10.1016/0022-0248(93)90214-H).
- [30] K. Nitsch, M. Dušek, M. Nikl, K. Polák, M. Rodová, Ternary alkali lead chlorides: crystal growth, crystal structure, absorption and emission properties, *Prog. Cryst. Growth Char. Mater.* 30 (1995) 1–22, [https://doi.org/10.1016/0960-8974\(95\)00012-V](https://doi.org/10.1016/0960-8974(95)00012-V).
- [31] W.G. Pfann, Principles of Zone Melting, vol. 194, Transactions of the American Institute of Mining and Metallurgical Engineers, 1952, pp. 747–753.
- [32] V. Vanecek, R. Kral, J. Paterek, V. Babin, V. Jary, J. Hybler, S. Kodama, S. Kurosawa, Y. Yokota, A. Yoshikawa, M. Nikl, Modified vertical Bridgman method: time and cost effective tool for preparation of Cs<sub>2</sub>HfCl<sub>6</sub> single crystals, *J. Cryst. Growth* 533 (2020) 125479, <https://doi.org/10.1016/j.jcrysgro.2020.125479>.
- [33] S. Gundacker, R.M. Turtos, N. Kratochwil, R.H. Pots, M. Paganoni, P. Lecoq, E. Auffray, Experimental time resolution limits of modern SiPMs and TOF-PET detectors exploring different scintillators and Cherenkov emission, *Phys. Med. Biol.* 65 (2020), 025001, <https://doi.org/10.1088/1361-6560/ab63b4>.
- [34] M.H. Brooker, C.-H. Huang, Raman spectroscopic investigations on the structures of CsMgCl<sub>3</sub> and Cs<sub>3</sub>MgCl<sub>5</sub>, *Mater. Res. Bull.* 15 (1980) 9–16, [https://doi.org/10.1016/0025-5408\(80\)90154-3](https://doi.org/10.1016/0025-5408(80)90154-3).
- [35] K.S. Alexandrov, B.V. Besnosikov, L.A. Posdnjakova, Successive phase transitions in perovskites. II. Structures of distorted phases, *Ferroelectrics* 12 (1976) 197–198, <https://doi.org/10.1080/00150197608241424>.
- [36] M. Midorikawa, Y. Ishibashi, Y. Takagi, Dilatometric and pressure studies of phase transitions in CsSrCl<sub>3</sub>, *J. Phys. Soc. Jpn.* 41 (1976) 2001–2004, <https://doi.org/10.1143/JPSJ.41.2001>.
- [37] S. Hirotsu, Experimental studies of structural phase transitions in CsPbCl<sub>3</sub>, *J. Phys. Soc. Jpn.* 31 (1971) 552–560, <https://doi.org/10.1143/JPSJ.31.552>.
- [38] Y. Vaills, J.Y. Buzaré, A. Gibaud, Ch Launay, X-ray investigations of the cubic to tetragonal phase transition in CsCaCl<sub>3</sub> at T<sub>c</sub> = 95 K, *Solid State Commun.* 60 (1986) 139–141, [https://doi.org/10.1016/0038-1098\(86\)90546-6](https://doi.org/10.1016/0038-1098(86)90546-6).
- [39] P. Villars, K. Cenzual, K<sub>2</sub>BaCl<sub>4</sub> Crystal Structure: Datasheet from "PAULING FILE Multinaries Edition – 2012" in SpringerMaterials ([https://materials.springer.com/isp/crystallographic/docs/sd\\_1822690](https://materials.springer.com/isp/crystallographic/docs/sd_1822690)), Springer-Verlag Berlin Heidelberg & Material Phases Data System (MPDS), Switzerland & National Institute for Materials Science (NIMS), Japan, n.d. [https://materials.springer.com/isp/crystallographic/docs/sd\\_1822690](https://materials.springer.com/isp/crystallographic/docs/sd_1822690).
- [40] P. Villars, K. Cenzual, Rb<sub>2</sub>BaCl<sub>4</sub> Crystal Structure: Datasheet from "PAULING FILE Multinaries Edition – 2012" in SpringerMaterials ([https://materials.springer.com/isp/crystallographic/docs/sd\\_1829066](https://materials.springer.com/isp/crystallographic/docs/sd_1829066)), Springer-Verlag Berlin Heidelberg & Material Phases Data System (MPDS), Switzerland & National Institute for Materials Science (NIMS), Japan, n.d. [https://materials.springer.com/isp/crystallographic/docs/sd\\_1829066](https://materials.springer.com/isp/crystallographic/docs/sd_1829066).
- [41] P. Villars, K. Cenzual, Cs<sub>2</sub>BaCl<sub>4</sub> Crystal Structure: Datasheet from "PAULING FILE Multinaries Edition – 2012" in SpringerMaterials ([https://materials.springer.com/isp/crystallographic/docs/sd\\_1829065](https://materials.springer.com/isp/crystallographic/docs/sd_1829065)), Springer-Verlag Berlin Heidelberg & Material Phases Data System (MPDS), Switzerland & National Institute for Materials Science (NIMS), Japan, n.d. [https://materials.springer.com/isp/crystallographic/docs/sd\\_1829065](https://materials.springer.com/isp/crystallographic/docs/sd_1829065).
- [42] H.J. Seifert, G. Thiel, Thermal analysis for generating phase diagrams of systems alkali metal chloride/divalent metal chloride, *Thermochim. Acta* 100 (1986) 81–107, [https://doi.org/10.1016/0040-6031\(86\)87052-6](https://doi.org/10.1016/0040-6031(86)87052-6).
- [43] G. Thiel, J. Sandrock, H.J. Seifert, Thermal analysis by emf-measurements on solid electrolytes- the system RbCl with earth alkaline metalchlorides, *Thermochim. Acta* 72 (1984) 245–250, [https://doi.org/10.1016/0040-6031\(84\)85081-9](https://doi.org/10.1016/0040-6031(84)85081-9).
- [44] K. Takahashi, M. Arai, M. Koshimizu, Y. Fujimoto, T. Yanagida, K. Asai, Luminescence characteristics of Cs<sub>2</sub>BaCl<sub>4</sub>, *Jpn. J. Appl. Phys.* 59 (2020), 032003, <https://doi.org/10.35848/1347-4065/ab762b>.
- [45] G.A. Appleby, A. Edgar, G.V.M. Williams, Structure and photostimulated luminescent properties of Eu-doped M<sub>2</sub>BaX<sub>4</sub> (M=Cs, Rb; X=Br, Cl), *J. Appl. Phys.* 96 (2004) 6281–6285, <https://doi.org/10.1063/1.1814171>.
- [46] Y. Chornodolskyy, G. Stryganyuk, S. Szyrotyuk, A. Voloshinovskii, P. Rodnyi, Features of the core-valence luminescence and electron energy band structure of A<sub>1-x</sub>Cs<sub>x</sub>CaCl<sub>3</sub> (A = K,Rb) crystals, *J. Phys. Condens. Matter* 19 (2007) 476211, <https://doi.org/10.1088/0953-8984/19/47/476211>.
- [47] C.W.E. van Eijk, Cross-luminescence, *J. Lumin.* 60–61 (1994) 936–941, [https://doi.org/10.1016/0022-2313\(94\)90316-6](https://doi.org/10.1016/0022-2313(94)90316-6).
- [48] J. Jansons, Z. Rachko, J. Valbis, J. Andriessen, P. Dorenbos, C.W.E. van Eijk, N. M. Khaidukov, Cross-luminescence of complex halide crystals, *J. Phys. Condens. Matter* 5 (1993) 1589–1596, <https://doi.org/10.1088/0953-8984/5/10/015>.
- [49] K. Takahashi, M. Koshimizu, Y. Fujimoto, T. Yanagida, K. Asai, Auger-free luminescence characteristics of Rb<sub>1-x</sub>Cs<sub>x</sub>CaCl<sub>3</sub>, *J. Ceram. Soc. Japan.* 126 (2018) 755–760, <https://doi.org/10.2109/jcersj2.18051>.
- [50] K. Takahashi, M. Koshimizu, Y. Fujimoto, T. Yanagida, K. Asai, Auger-free luminescence characteristics of Cs(Ca<sub>1-x</sub>Mg<sub>x</sub>)Cl<sub>3</sub>, *Nucl. Instrum. Methods Phys. Res. Sect. A Accel. Spectrom. Detect. Assoc. Equip.* 954 (2020) 161842, <https://doi.org/10.1016/j.nima.2019.01.068>.
- [51] M. Itoh, N. Ohno, H. Yoshida, S. Hashimoto, K. Kan'no, M. Kamada, Auger-free luminescence in mixed alkali halides, *J. Electron. Spectrosc. Relat. Phenom.* 79 (1996) 117–120, [https://doi.org/10.1016/0368-2048\(96\)02816-2](https://doi.org/10.1016/0368-2048(96)02816-2).
- [52] V.B. Mikhailik, A.S. Voloshinovskii, G. Zimmerer, Core luminescence as a method of studying the relaxation processes in the outermost core of crystals, *J. Alloys Compd.* 286 (1999) 128–136, [https://doi.org/10.1016/S0925-8388\(98\)00992-X](https://doi.org/10.1016/S0925-8388(98)00992-X).
- [53] A. Voloshinovskii, Decay of 5pCs-core excitations in halide crystals with core valence luminescence, *Radiat. Meas.* 33 (2001) 565–569, [https://doi.org/10.1016/S1350-4487\(01\)00060-9](https://doi.org/10.1016/S1350-4487(01)00060-9).
- [54] M.J. Knitel, P. Dorenbos, J.T.M. de Haas, C.W.E. van Eijk, LiBaF<sub>3</sub>, a thermal neutron scintillator with optimal n-γ discrimination, *Nucl. Instrum. Methods Phys. Res. Sect. A Accel. Spectrom. Detect. Assoc. Equip.* 374 (1996) 197–201, [https://doi.org/10.1016/0168-9002\(96\)00076-9](https://doi.org/10.1016/0168-9002(96)00076-9).
- [55] P.A. Rodnyi, V.B. Mikhailik, G.B. Stryganyuk, A.S. Voloshinovskii, C.W.E. van Eijk, G.F. Zimmerer, Luminescence properties of Ce-doped Cs<sub>2</sub>LiLaCl<sub>6</sub> crystals, *J. Lumin.* 86 (2000) 161–166, [https://doi.org/10.1016/S0022-2313\(99\)00181-7](https://doi.org/10.1016/S0022-2313(99)00181-7).
- [56] J.L. Jansons, V.J. Krums, Z.A. Rachko, J.A. Valbis, Luminescence due to radiative transitions between valence band and upper core band in ionic crystals (crossluminescence), *Phys. Status Solidi* 144 (1987) 835–844, <https://doi.org/10.1002/pssb.2221440244>.